University of Texas at Arlington

MavMatrix

2022

PERFORMANCE EVALUATION AND RETROFITTING OPTIONS OF A PRECAST PRESTRESSED CONCRETE BRIDGE WITH DECK PANEL FAILURE

Ahmed Abdullah Alateeq

Follow this and additional works at: https://mavmatrix.uta.edu/civilengineering_dissertations

 Part of the Civil Engineering Commons

PERFORMANCE EVALUATION AND RETROFITTING OPTIONS OF A PRECAST PRESTRESSED CONCRETE BRIDGE WITH DECK PANEL FAILURE

by

Ahmed Abdullah Alateeq

Presented to the Faculty of the Graduate School of The University of Texas at Arlington in

Partial Fulfillment of the requirements for the Degree of

DOCTOR OF PHILOSOPHY

The University of Texas at Arlington (UTA)

August 2022

Acknowledgements

Abstract

Performance Evaluation and Retrofitting Options of Precast Prestressed Concrete Bridge with Deck Panel Failures

Ahmed Abdullah Alateeq, PhD

The University of Texas at Arlington, 2022

Supervising Professor: Dr. Nur Yazdani

Bridges play a crucial role in the worldwide transportation infrastructure. According to the 2021 America's Infrastructure Report Card, there are more than 617,000 bridges across the Nation, of which, 42% are at least 50 years old, and 7.5% are rated as structurally deficient. Repetitive loading from heavy trucks is one of the reasons that could compromise the structural integrity of bridges. The heavy trucks have a negative impact on the bridge deck as a bridge's first line of defense is to resist the applied load. The Las Lomas Bridge [Eastbound (EB) and Westbound (WB)] carrying IH-20 over Las Lomas Pkwy, which is located in Terrel, TX, experienced deck panel failure. The bridge includes a cast-in-place (CIP) concrete deck over precast concrete panels (PCPs), and four PCPs exhibited evidence of water staining and hairline cracks with efflorescence also in addition to minor alligator cracking in the bridge, which resulted in a localized deck failure. Typically, the PCPs and CIP deck act compositely to resist the traffic load. As the two bridges were built in 1987, their decks experienced several cracks.

To accurately evaluate the bridge performance, field load tests and Non-Destructive Evaluation (NDE) were conducted. NDE is a useful tool to precisely predict the bridge deck current condition and involves using Ground Penetrating Radar (GPR) and Impact Echo (IE). From GPR data, the bridge deck scanning revealed that the deck top rebar cover differed from what was included in the as-built drawings. In addition, two bridge decks greatly suffered from severe delamination, which reduced the deck moment capacity. To assess the overall bridge performance

in regards to composite action and load carrying capacity, a field load test was conducted by instrumenting the bridge with strain gage and rotational tiltmeter sensors.

To conduct a more comprehensive study, a Finite Element Model (FEM) was prepared in ABAQUS. Since the EB and WB bridges demonstrated similar defect types, only one span of the EB bridge was considered during the FE preparation. The FE model was calibrated with field load test data to reflect the actual structure response. Various retrofitting options were carried out to investigate their effectiveness in increasing the bridge composite action and load carrying capacity.

Table of Contents

List of Figures

List of Tables

Chapter 1
INTRODUCTION

1.1 Background

According to the 2021 America's Infrastructure Report Card, $125 billion is currently needed to correct the deficiencies in bridges in the United States. Spending on bridge rehabilitation should be increased from $14.4 billion annually to $22.7 billion annually to improve the bridge conditions. Among the structural components of bridges, the deck experiences deterioration at a faster rate since it is the first line of defense against traffic and environmental exposure. For instance, severely deteriorated bridge decks account for more than 60% of the structurally deficient bridge elements in Oklahoma. Moreover, bridge decks are currently the costliest and most labor-intensive element in bridge systems (Ley et al. 2010). Therefore, the nation's Departments of Transportation (DOTs) must provide vital economical and durable bridge systems in a timely manner. Accordingly, one bridge element that could significantly benefit from precast construction is the bridge deck.

Conventional construction of bridge decks involves plywood forms with supports that are used in the interior and overhang sections to help place the concrete on the top of formwork [Figure1-1(a)]. Currently, two types of bridge deck construction systems are commonly used: partial depth (PD) and full depth precast bridge decks (FD). The PD bridge deck [Figure 1-1(b)] is composed of precast concrete deck panels (PCPs) and is used in the interior portion of the span for approximately half of the deck depth. Top mild reinforcing steels are added to the top of panels (Figure 1-2), and cast-in-place (CIP) concrete deck is used to complete the bridge. In the state of Texas, roughly 85% of bridges use PCPs rather than the conventional method (Merrill 2002) as bridge decks built with PCPs are stronger than conventional bridge decks. Tsui et al. (1986) moreover concluded that PCPs have a crack-resistant advantage over fully CIP concrete decks.

The FD bridge decks [Figure 1-1(c)], on the other hand, consist of thick concrete planks, covering the entire width of the bridge deck and are placed on the beams below. Since the PD and FD bridge decks also have benefits as well as drawbacks, some features of both systems could be combined in a hybrid system that offers significant improvements. The new hybrid system was developed and implemented by the Texas Department of Transportation's (TxDOT) Fort Worth District, with the help of researchers from Oklahoma State University, Texas A&M University, and Austin Prestressed Company (Ley et al. 2010).

The hybrid system is used in the overhang portion of bridge deck [Figures 1-1(d) and 1-1(e)] and uses PCPs and CIP concrete decks. TxDOT estimates that the new hybrid system will result in significant savings in cost and time, including more than one week of construction time per bridge span.
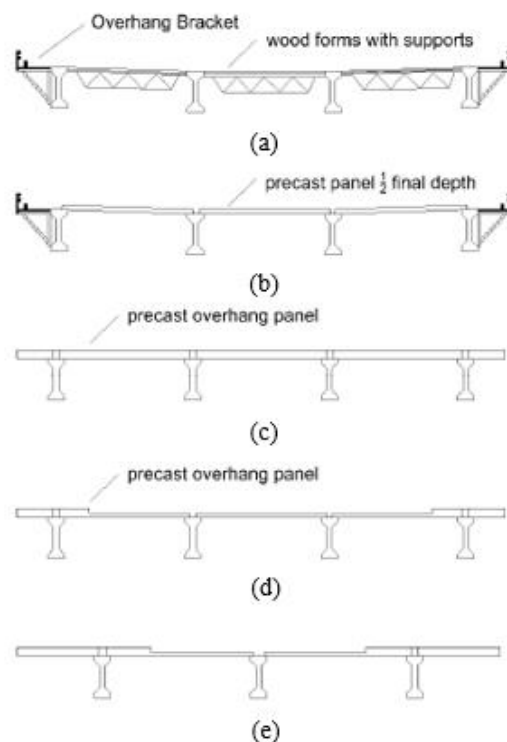
Figure 1-1 Deck Systems (Ley et al. 2010): (a) Conventional forming;(b) PD;(c) FD;(d) Overhang with PD; (e) Extended overhang
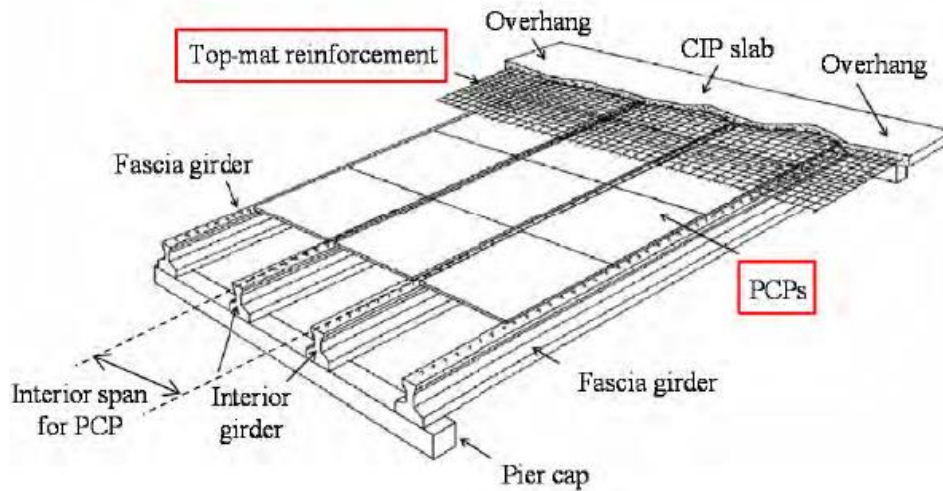
Figure 1-2: Typical CIP-PCP bridge deck (Buth et al. 1972)

Among all of the construction of bridge deck systems, a CIP bridge deck on PCPs system (Figures 1-2 and 1-3) has been widely used around the world(Goldberg 1987) since it was first introduced in a bridge on the Illinois Tollway project in the 1950s (Barker 1975). The CIP bridge deck on PCPs system has many applications, one of which is for bridges located over water where access for construction is limited. Even though PCPs are beneficial in numerous applications, PCPs are susceptible to cracks and failure. Gualtero (2004) found that the cracks occurred at the interface of the CIP deck, and PCPs were caused by shrinkage in the CIP deck portion and creep induced in the PCPs due to prestress force (Figure 1-4). Furthermore, the longitudinal cracks produced transverse cracks that passed through the thickness of the CIP concrete. Additional longitudinal cracking was also associated with panels supported on the negative bedding strips, as shown in Figure 1-4. The cracking additionally caused the shear failure of the CIP concrete. Although using PCPs has some advantages as mentioned above, their propensity for deterioration and/or the possibility of construction errors during installation also have to be considered.
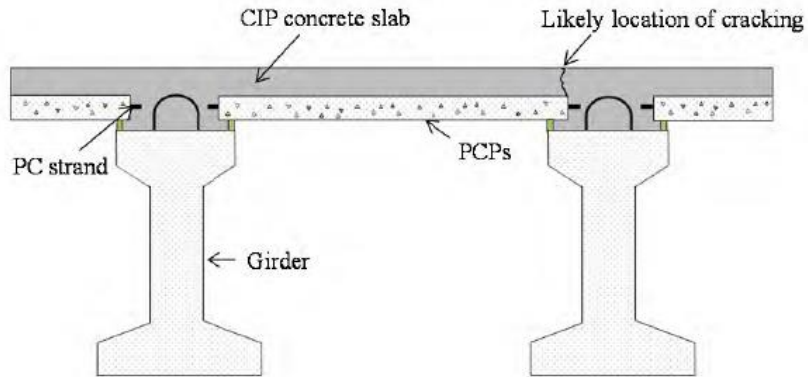
Figure 1-3: CIP-PCP bridge deck (section view) (Bayrak et al. 2013)
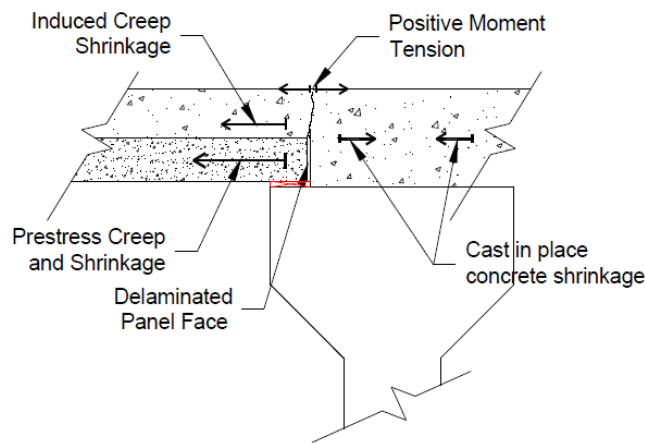
Figure 1-4: Longitudinal/transverse cracks due to creep and shrinkage (Gualtero 2004)

1.2 Problem Statement

Repetitive traffic loading, especially from heavy trucks, is one of the most serious risks to the integrity and safety of bridges. Therefore, the PCPs and CIP deck act compositely to resist the traffic load. Despite the ability of CIP and PCPs to withstand live load, many of the bridges built in the United States have developed cracks in PCPs, CIP deck, or both (Buckner 1983). As a result, the Federal Highway Administration (FHWA) requires an inspection every two years to assess each bridge's components (FHWA 2012).

On May 22, 2018, two inspection reports were prepared by the TxDOT Dallas District on the eastbound (EB) and westbound (WB) Las Lomas Bridge. The reports indicated that the PCPs

between girders C and D showed evidence of water staining and hairline cracks with efflorescence as well as minor alligator cracking in the WB bridge. The cracks were located below a small patch of span 2 at the top surface of the deck of the EB bridge and the center lane of span 4 for the WB bridge, which caused a localized CIP deck failure.

The localized CIP deck failure in the EB bridge, measuring 7 x 15 ft, had exposed rebars [Figure 1-5(a)]. The deck failure resulted from the failure of four PCPs on June 18, 2018, near the mid-span diaphragm of span 2 EB [Figure 1-5(b)]. Consequently, the TxDOT Dallas District contacted the UTA team regarding the PCP failures and the patched holes on the sides of the bridges. A full-depth emergency repair was then performed on the two bridges [Figures 1-6(a-c)].

NOTE: Photo taken by TxDOT

(a)

NOTE: Photo taken by TxDOT

(b)

Figure 1-5 Failure patterns in span 2 of EB bridge (TxDOT): (a) CIP deck; (b) PCPs
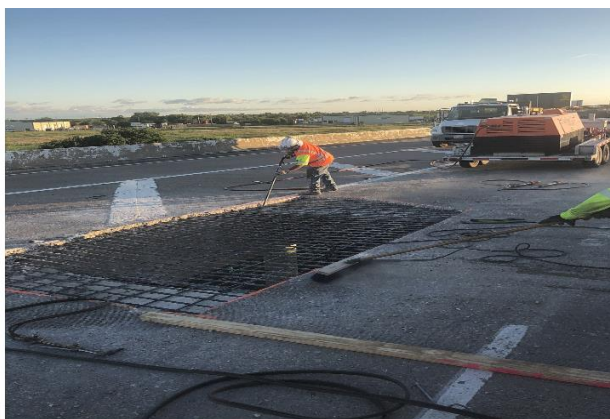
NOTE: Photo taken by TxDOT

(a)

(b)

(c)

Figure 1-6 Full-depth repairs (TxDOT): (a) Span 2 EB;(b) Span 4 WB; (c) Bottom view of WB

1.3 Methodology and Objectives

The present study explores a PCP crack defect that caused a localized CIP failure and additionally aims to investigate the possible mechanism or cause of failure. The study then presents ways to minimize this type of defect in the future. During the study, specific approaches/methodologies were considered to assist the researcher in achieving the primary research objectives.

➢ **Methodology:**

✓ Evaluate the residual capacity of the bridge by performing sensor instrumentation and load testing.

✓ Evaluate the bridge deck and concenrates on the affected deck area by conducting a non-destructive evaluation (NDE) that includes Ground Penetrating Radar (GPR) and Impact Echo (IE) that determine the top rebar cover and deck delamination condition, respectively.

✓ Evaluate the current bridge load rating factor using the field load test and NDE data.

✓ Evaluate the existing composite action between CIP and Girder from strain data.

5

➤ **Primary Objectives:**

  ✓ Develop a realistic 3-D-finite element model (FEM) of the EB bridge for the targeted span where the defect occurred and use the material proerties, geometric dimensions, and boundary conidition mentioned in the as-built drawing and visual inspection.

  ✓ Calibrate the developed FE model with the experimental/field load test data until the FE matches the actual bridge behaviour.

  ✓ Invesitagate the PCP failure mechanism by reviewing the inspection reports and previous relevant research.

  ✓ Suggest future retrofitting/design or construction changes that may eliminate this type of failure and increase the bridge live load carrying capacity that leads to an increase in the bridge load rating and composite action.

  ✓ Select the suitable retrofitting/design or construction options by conducting a cost-benefit analysis.

1.4 Organization of the Dissertation

The dissertation is organized into eight chapters. Each chapter is divided into various sub-sections. The dissertation chapters are organized and summarized as follows:

Chapter 1-Introduction

Composite bridge concrete deck background, problem statements, and objectives are covered in this chapter.

Chapter 2: Literature Reviews

It includes a history of composite bridge deck failure, rehabilitation of composite bridge decks, prior bridge load tests, NDE evaluation, load rating, and FE modeling. Furthermore, the chapter covers previous applications performed using the bridge retrofitting options.

Chapter 3: Bridge Description

The Las Lomas bridge descriptions, location, year built, deck type, bridge conditions, deck replacement, materials properties, and as-built details are covered in this chapter.

Chapter 4: Experimental Procedures

Testing instruments, Las Lomas bridge instrumentation plan, bridge load testing, and NDE scanning procedures are discussed in Chapter 4.

Chapter 5: Finite Element Modeling (FEM)

Initial FE modeling of span 2, concrete and steel properties, prestressing strands, losses, and loading conditions are discussed in this chapter.

Chapter 6: Results and Discussions

This chapter discusses load test results, including strain and rotation bridge responses as well as Neutral Axis (N.A.). NDE scanning results, GPR, IE, and bridge load rating are also discussed. Finally, mesh sensitivity and FE model calibration with field load test data are included in this chapter as well as the PCP failure potential mechanism (based on inspection reports and IE data).

Chapter 7: Bridge Retrofitting

Different retrofitting options to mitigate the PCP failure are discussed in this chapter. Load carrying capacity, composite actions, and cost-benefit analysis of retrofitted options are included as well.

Chapter 8: Conclusions and Recommendations

This chapter discusses the findings related to load test and NDE scanning and also examines suitable retrofitting options.

Chapter 2

LITERATURE REVIEWS

2.1 Composite Bridge Decks Failures

Alvi et al. (2012) conducted research on 127 deck panel bridges with longitudinal, transverse, spalling, and shear cracking. The shear cracks were caused by the diagonal tension of the CIP concrete and extended to the top surface of the CIP, producing longitudinal cracks (Figure 2-1).

Figure 2-1: Longitudinal crack caused by shear (right crack) (Alvi et al. 2012)

Gualtero (2004) studied the deterioration process of deck failures in Florida and concluded that the deterioration began with longitudinal cracking, continued to spalling failure, and eventually caused localized deck failure.

Alvi (2010) investigated the deck failures that occurred in Florida in 2007. Table 2-1 illustrates the localized deck failure, and Figures 2-2(a) and 2-2(b) represent the collapse of bridge #100332. The failure was located within the boundaries of the previous repair patch and on the edge of the PCP and girder.

Table 2-1: Localized deck failures following USF study in 2005 (Alvi, 2010)

Bridge No.	District / Bridge Location	Year Built / Failure Date	Age at Failure (Years)	NBI Rating Before Failure	Days Since Last Insp.	Rain 7 Days Prior to Fail (in.)	ADT / %Trucks	Failure Size (Inches)	Loc. in Panel	Comment
	7	1980		5			23,000			
100332	Tampa, Cross-town Viaduct WB Span 39	3/5/2007	27	(Fair)	565	0.21	8%	18 x 8	Edge	Failed localized patch repair
	7	1983		5			46,250			
100436	I-75 over E. Broadway Ave., CR 574 and CSX Railroad	9/11/2007	24	(Fair)	685	0.54	8%	12 x 24	Edge	Failed localized patch repair

(a)

(b)

Figure 2-2 Bridge No. 100332, span 39 failure (Alvi, 2010): (a) Top view; (b) Bottom view

9

Alvi (2010) suggested that multiple factors, such as massive rainfall events, light-to-moderate wear, minor multi-directional cracks, and minor associated spalls, contributed to the failures that occurred on top of the bridge. A minor delamination in a 1.5 ft. x 3 in. area along the construction joints was observed. Figures 2-3(a) and 2-3(b) depict the failure of bridge #100436, with the same failure pattern as bridge #100332.
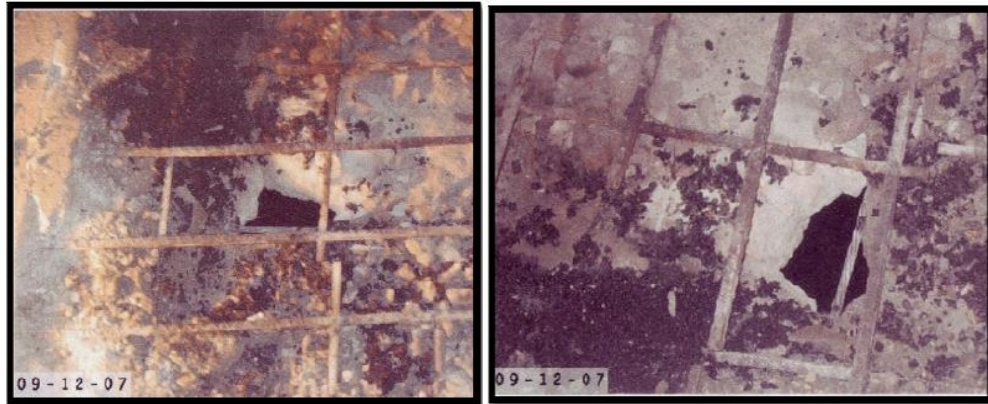
(a)
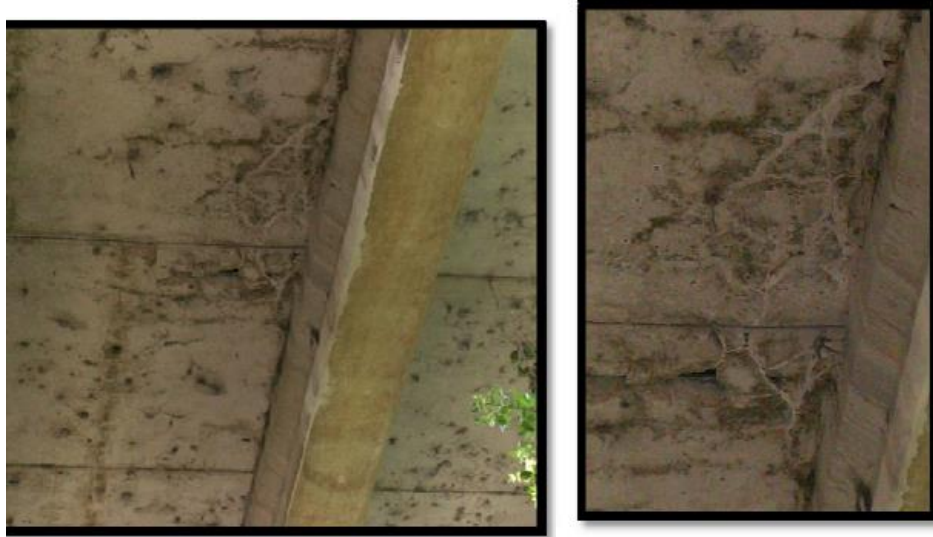
(b)

Figure 2-3 Bridge No. 100436, span 4 failure (Alvi 2010): (a) Top view; (b) Bottom view

Based on the field inspection of both bridges, numerous patches made from an epoxy-type material were found in the field on top of the bridge (Alvi 2010). Alvi (2010) then concluded that longitudinal cracks, with a maximum crack width of 1/16 in., were observed along the edge of the

girder. Additionally, the researcher detected transverse cracks, with a maximum crack width of 1/8 in. up to 12 ft. long, over the PCP joints in all of the spans.

Hays et al. (1976) investigated the shear cracking that occurred on I-75 (on the Peace River Bridge deck) at the fiberboard strip placed at the end of the PCP. The increase in shear stress was caused by creep in the PCP, as observed by Gualtero (2004). In addition, the differential shrinkage between the PCPs and CIP caused cracks on the top of the deck.

Fagundo et al. (1983) conducted a follow-up evaluation for the I-75 bridge to assess the potential for shear fatigue failure of the panel bridges that lacked positive bedding strips. Composite decks, constructed without positive bedding strips, acted as simply supported beams, with maximum positive moment in the mid-span and negative moment at the ends. Fagundo et al. (1983) concluded that using grout as bedding strips would be beneficial in reducing the shear stresses at the end of PCPs.

Durham et al. (2004) developed a field manual to classify 19 ft. precast non-prestressed channel beams without shear reinforcement and identified the beams that exhibited deficient structural behavior. The researchers observed corrosion and concrete spalling (Figure 2-4) in some of the precast channel beams.

Figure 2-4: Deterioration of Jenkins' Ferry Bridge (Durham et al. 2004)

11

Durham et al. (2004) concluded that the corrosion of the longitudinal reinforcing steel was caused by the presence of water and oxygen. The water and oxygen resulted in the expansion of the reinforcing steel, which initiated the cracks. The consequences of the corrosion were the loss of the concrete cover as well as the loss of the bond between the concrete and steel (Figure 2-5).
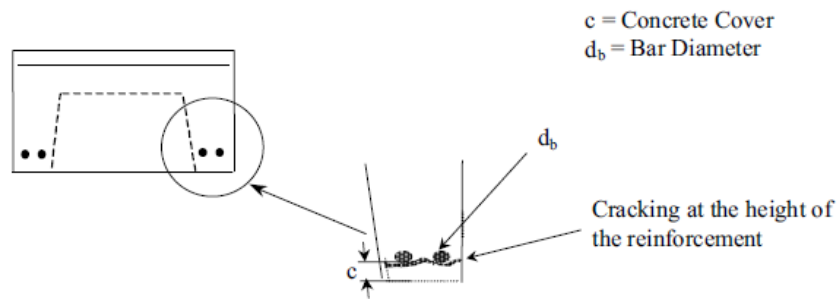
Figure 2-5: Corrosion-induced cracking (Durham et al. 2004)

Merrill (2002) posited that when using PCPs, most of the obstacles were related to longitudinal and transverse cracking. In his (2002) study, Merrill observed significant longitudinal cracking along the panel edge over the concrete girders [Figure 2-6(a)], which caused a reduction in deck stiffness over the girders. This cracking might have resulted from insufficient size, condition, or position of the bedding strips located under the PCPs that are meant to sustain the live load. Additionally, transverse cracking could have been caused by the shrinkage of the concrete as well as the gap between adjacent PCPs [Figure 2-6(b)].

(a)

12

CIP Concrete

PCP Panel   PCP Panel

(b)

Figure 2-6 Cracks in PCPs: (a) Longitudinal crack; (b)Transverse crack (Merrill 2002)

2.2 Rehabilitation of Composite Bridge Decks

Alvi et al. (2012) listed the eight main repair methods used at the intersection of deteriorated CIP and PCPs [Figures 2-7(a-d)]. The repair methods in their study included crack repair, maintenance spall patching, localized spall repair, grout packing, M1 repair, full-span M1 repair with grout packing, M2 repair, and full-depth bay replacement. Alvi et al. (2012) mentioned that simple cracks could be easily repaired by epoxy injections or sealants that were intended to restore the structural strength of the deck. The sealants penetrated and covered the cracks to avoid the entry of water and other impurities into the deck. In addition, epoxy injection was not effective if the cracks were active under loading because epoxy was not flexible as sealant. Additionally, the maintenance spall of the CIP portion of a deck was repaired by patching with asphaltic concrete [Figure 2-7(a)]. This repair method was a temporary solution until the maintenance crew permanently repaired the spalls. Grout packing repair was mainly focused on replacing the fiber board with grout [Figure 2-7(b)]. In M1 repair, the entire affected area was removed and replaced with repair material, and the depth of M1 went to the top of the PCP [Figure 2-7(c)].

Full-span M1 repair with grout packing was the modification of only M1 repair and was used to repair longitudinal spalling along the edge of a beam. The process involved removing the CIP concrete portion above the precast beam and additional steel was added to the area. The fiberboard was replaced with non-shrink cement grout. This repair was extended longitudinally throughout the length of the span. Another repair method was M2 Repair, which developed to

13

address PCP deficiencies and was used along the transverse joints of the PCP. The undesired material was eradicated approximately 6 in. on each side of the transverse joints to form an inverted T-beam with specific dimension requirements [Figure 2-7(d)]. Among all the repair method, full-depth bay replacement was the most common repair method that the District Structures Maintenance Office used. The repair involved the transverse distance between two girders and extends throughout the length of the span [Figure 2-7(e)].

Full-depth Bay replacement also involved demolishing the CIP deck and PCP of the affected area while keeping the original reinforcing steel grid for the purpose of continuity. A new bottom steel mat was designed and placed as an alternate to the PCP [Figure 2-7(f)]. According to Alvi et al. (2012), these repair methods had a common factor, which was the failure of applying the requirements of the composite actions between the PCPs and CIP. PCP with no overhang at its sides was observed and considered one of the failures detected by the researcher (Figure 2-8). Figure 2-8 also shows that an extended strand, from the PCP into the CIP concrete, should be installed as well.

(a)

Replace Fiber Board with Grout   Replace Fiber Board with Grout

(b)

EXISTING #5 @ 8"
EXISTING #5 @ 5¾"
NONSHRINK GROUT

(c)

EXISTING #5 @ 5⅜" O.C.
EXISTING #5 @ 8" O.C.
STIRRUP #3 @ 4.5" O.C.
MINIMUM 12"
CONCRETE TOPPING
PRECAST PANEL
PRESTRESSING STRAND
#5 @ 9" O.C.
#5 @ 18" O.C.
4 # 5
6"
Existing #3
MINIMUM 24"
3 # 5

(d)

15
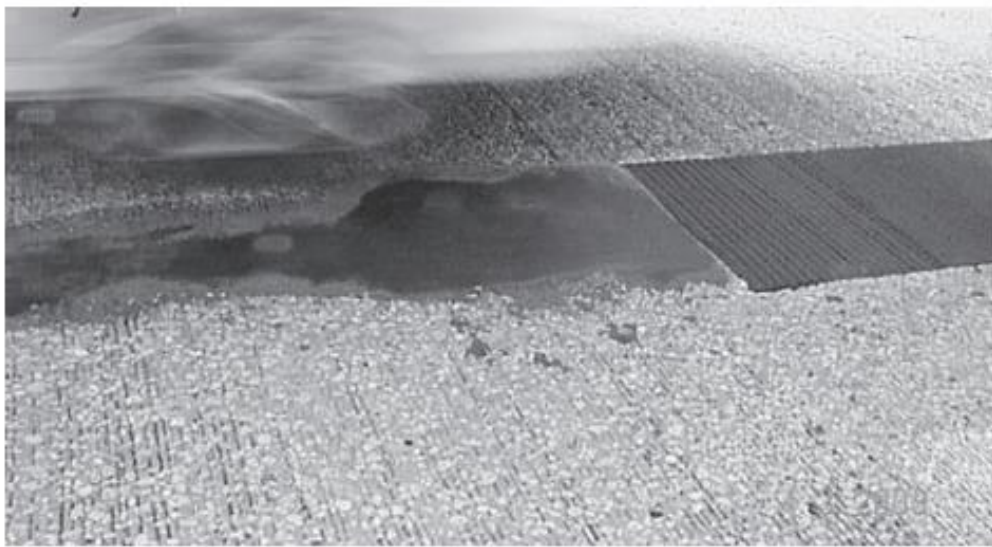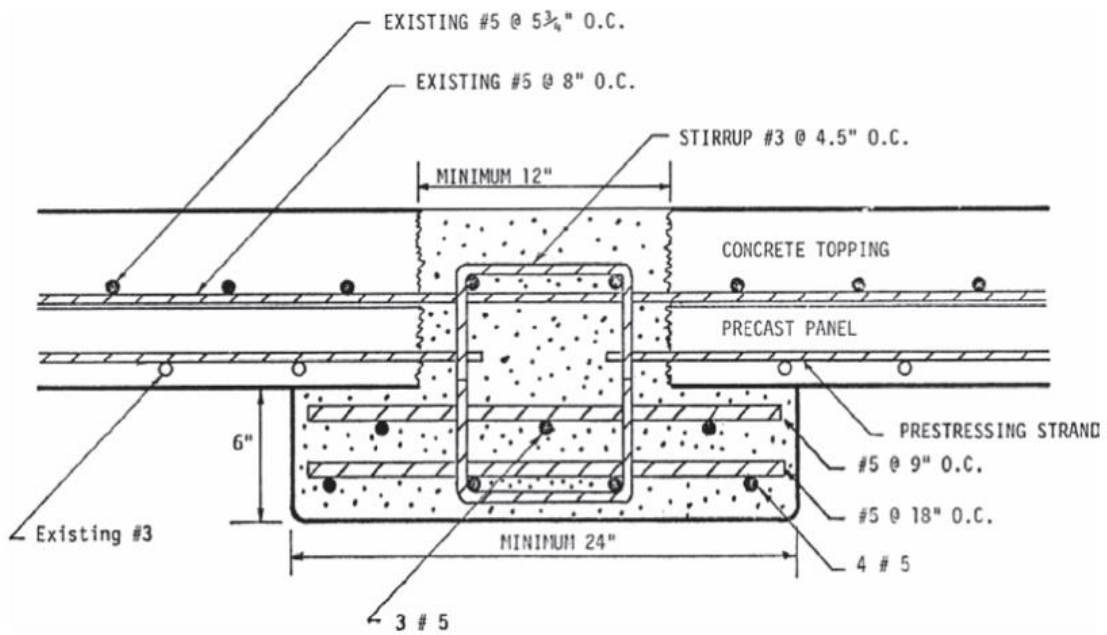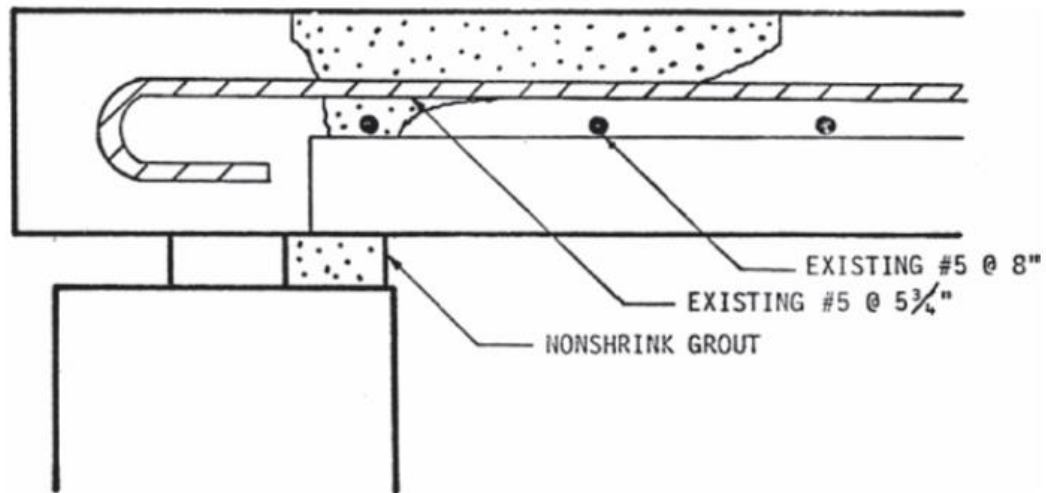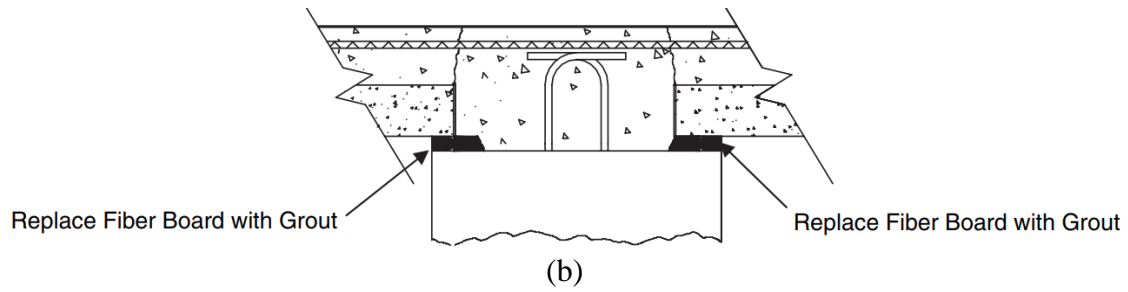
<div style="text-align:center">(e)   (f)</div>

Figure 2-7 Repair methods (Alvi et al. 2012): (a) Maintenance spall patching;(b) Grout packing;(c) M1; (d) M2; (e) Existing full-depth bay replacement; (f) Full-depth Bay replacement with new steel
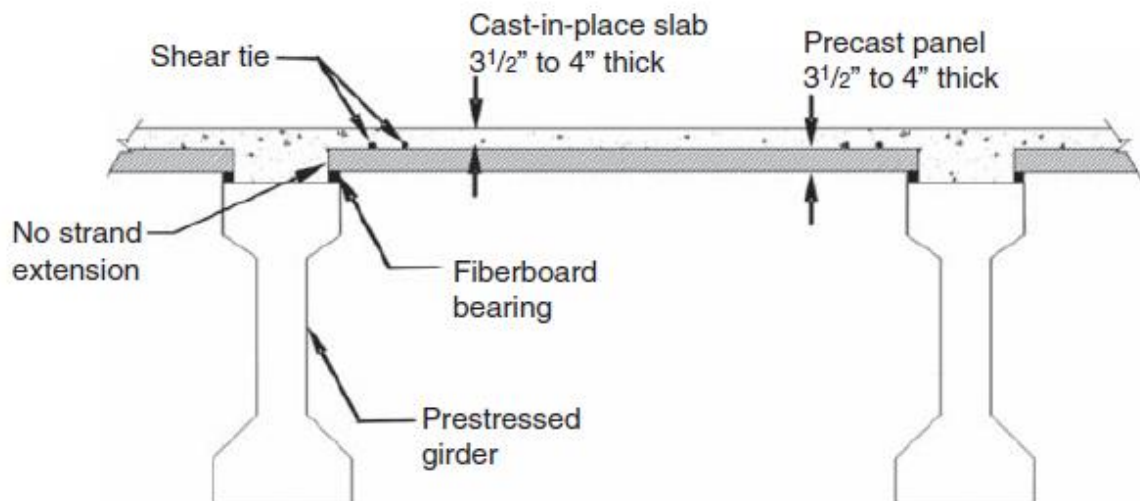
<div style="text-align:center">Figure 2-8: Cross section of CIP and precast panels (Alvi et al. 2012)</div>

Alvi et al. (2012) evaluated all of the advantages and disadvantages of the previous repair methods and concluded that the most effective method was a full replacement of the bridge deck with CIP concrete. The replacement eliminated the potential separation between the CIP and PCP, which causes a non-composite action.

2.3 Non-Destructive Evaluation (NDE)

Kien Dinh et al. (2018) developed an algorithm that allows for an automatic picking and identification of reinforcing steel rebars. Figure 2-9 shows the algorithm picking process. The proposed algorithm was implemented on raw GPR data from two concrete bridge decks and showed a good agreement when compared to the manual rebar picking. For example, the Elkton Bridge located in Maryland consists of a bare concrete deck. The deck thickness is 8 in. and was tested in July 2013. Figures 2-10(a) and 2-10(b) display both the automatic and manual steel rebar picking of the Elkton Bridge. The automatic algorithm was able to pick 2,733 rebars out of 2,772. The accuracy of the proposed method was around 98.09%. Another bridge example was Pequea Bridge, located in Conestoga, Pennsylvania, which also has a bare concrete deck. The algorithm was able to pick 6,834 rebars out of 6,867 with an accuracy of 99.21%. Figure 2-11(a) and 2-11(b) display both the automatic and manual steel rebar picking of Pequea Bridge.
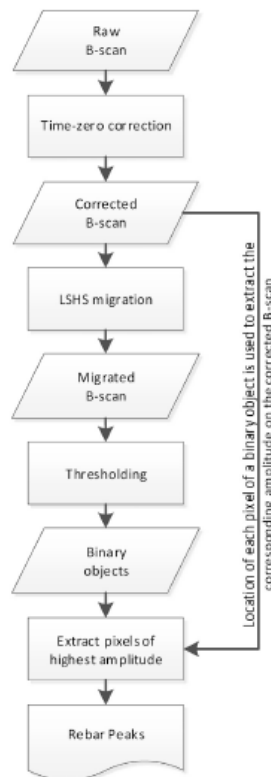
Figure 2-9: Algorithm picking process (Kien Dinh et al. 2018)
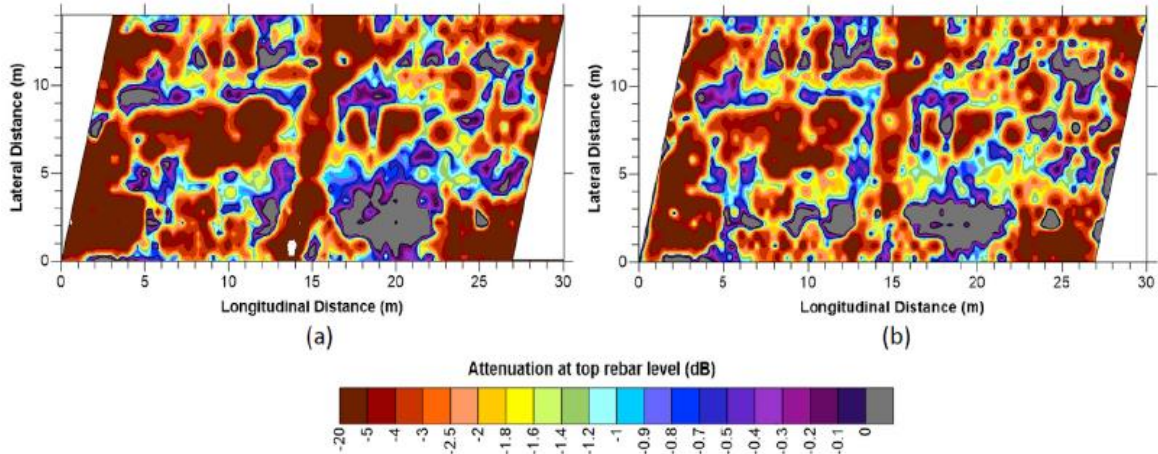
Figure 2-10 GPR contour maps of the Elkton Bridge deck (Kien Dinh et al. 2018): (a) Manual; (b) Automated rebar picking
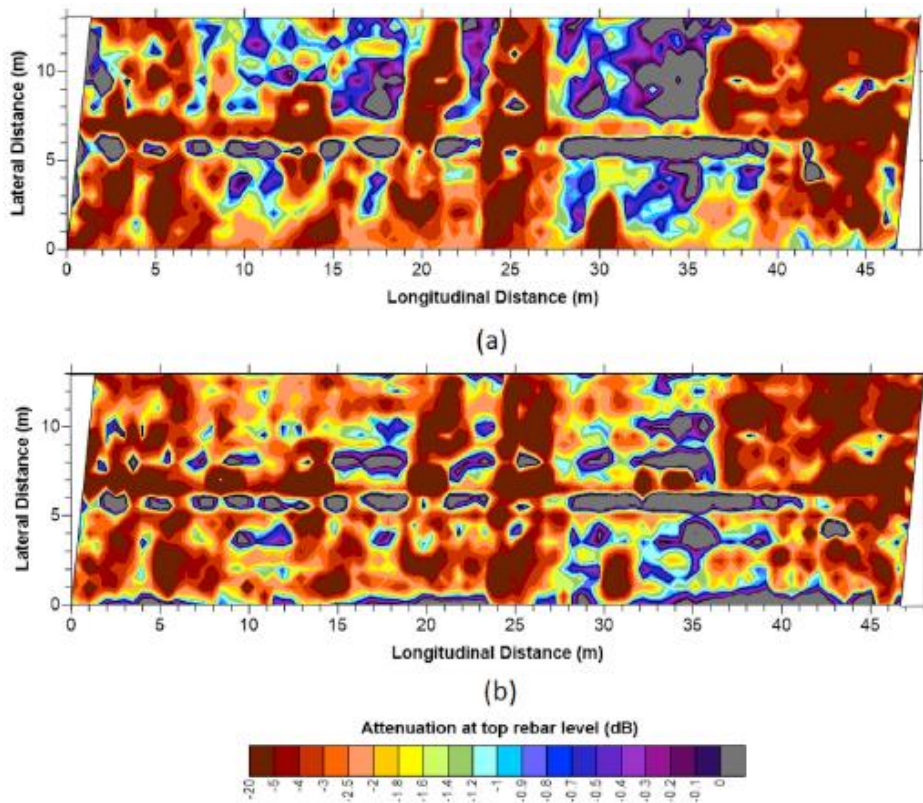
Figure 2-11 GPR contour maps of the Pequea Bridge deck (Kien Dinh et al. 2018): (a) Manual; (b) Automated rebar picking

Kien Dinh et al. (2018) developed a new and completely automated method using MATLAB to simulate the concrete bridge deck by integrating certain techniques. In addition, the researchers used interpolation algorithms in the simulation and produced an amplitude map where

18

two pieces of information can be observed simultaneously. Rebar locations and their corresponding corrosion were able to be detected as having the strongest reflectors of electromagnetic energy and low amplitude rebar reflection, respectively. To validate the proposed algorithm, Kien Dinh et al. (2018) used the new technique to test two bare concrete bridge decks and two concrete bridge decks with asphalt overlays in the U.S. and Canada. The two deck results were then compared using other evaluation methods, such as electrical resistivity (ER), half-cell potential (HCP), and visual inspection. The new method was able to designate the areas affected by corrosion. The Elkton Bridge used three NDE techniques: GPR, HCP, and ER. In the study, the deck area was 27 m. long x 14 m. wide. Figures 2-12(a-c) display the test results for the three NDE technologies. The deck areas with low amplitude in Figure 2-12(a) matched the deck areas with low ER in Figure 2-12(b), and there was a high likelihood of corrosion from HCP as presented Figure 2-12(c). The novel GPR method provides more details related to reinforcing steel position, a possible corrosion area of each rebar, and the locations of deck joint. The algorithm is unable to numerically determine the severity of the corrosion. Figures 2-13(a-c) displays the test results for the three NDE technologies used on the Pequea bridge deck. The GPR map in Figure 2-13(a) matched the ER [Figure 2-13(b)] and HCP [Figure 2-13(c)] by indicating the deck areas with corrosion issues.
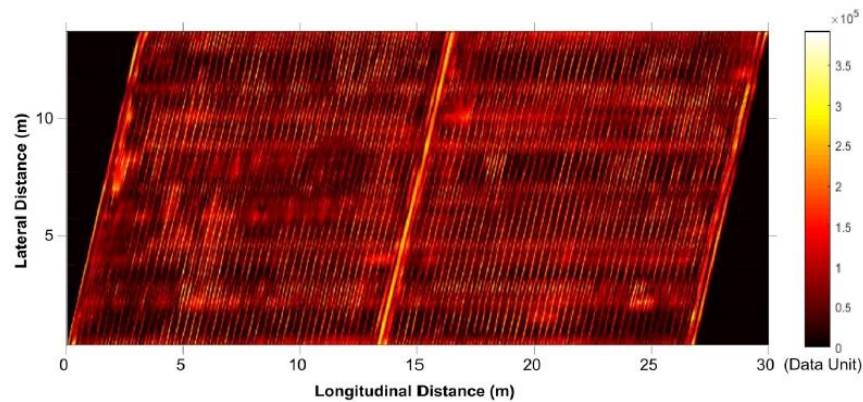
(a)
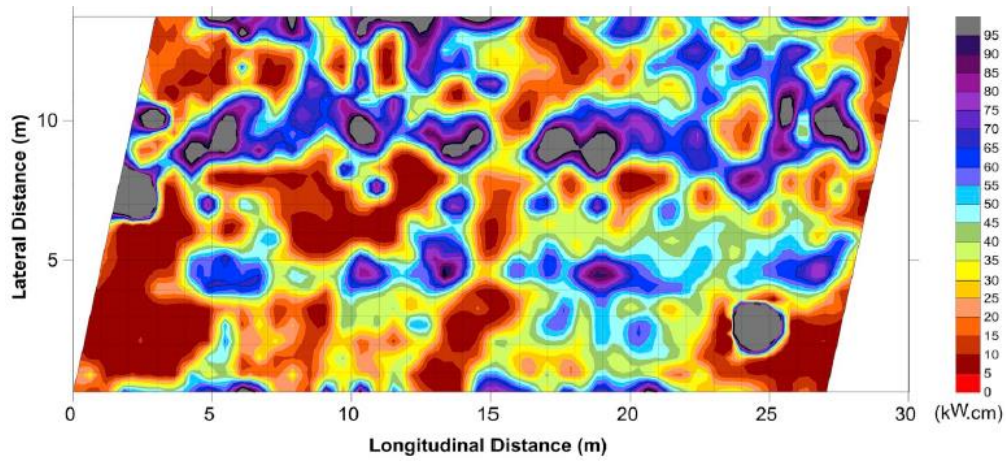
(b)
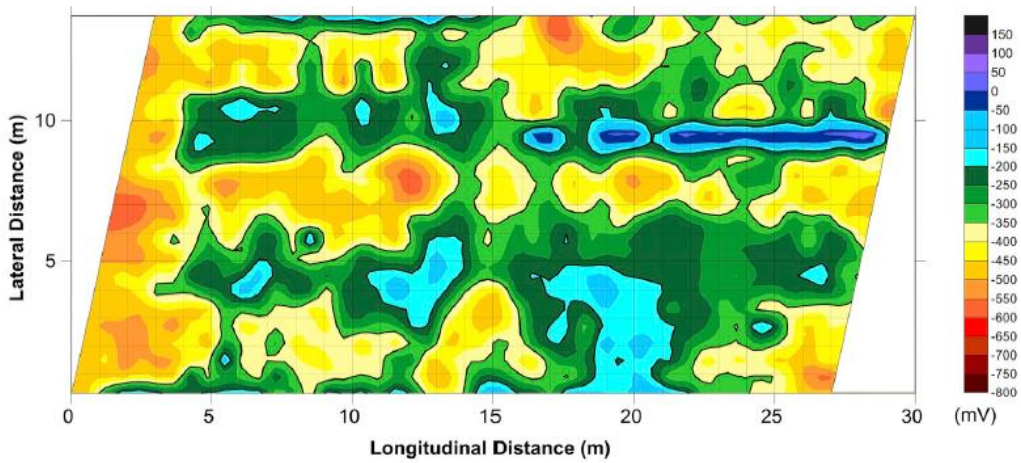
(c)

Figure 2-12 Condition maps of Elkton Bridge deck (Kien Dinh et al. 2018): (a) the proposed method; (b) ER; (c) HCP

(a)

(b)

(c)
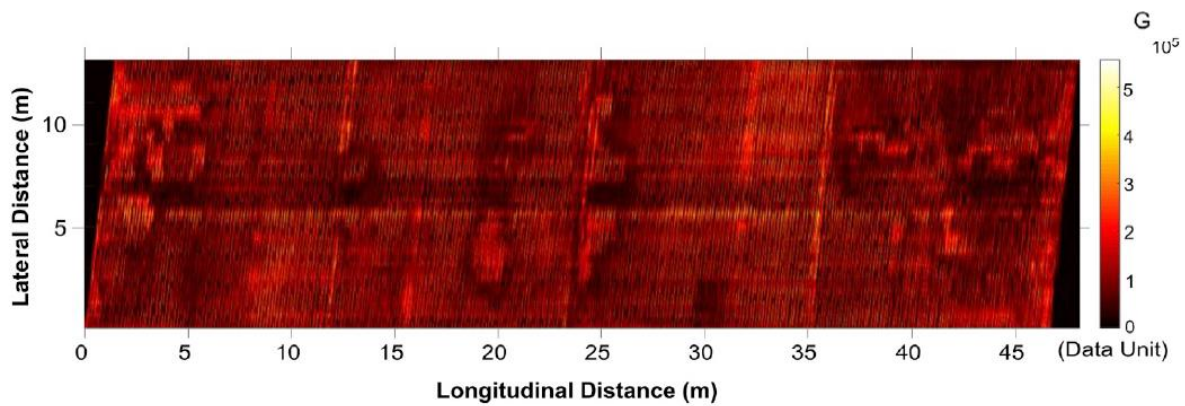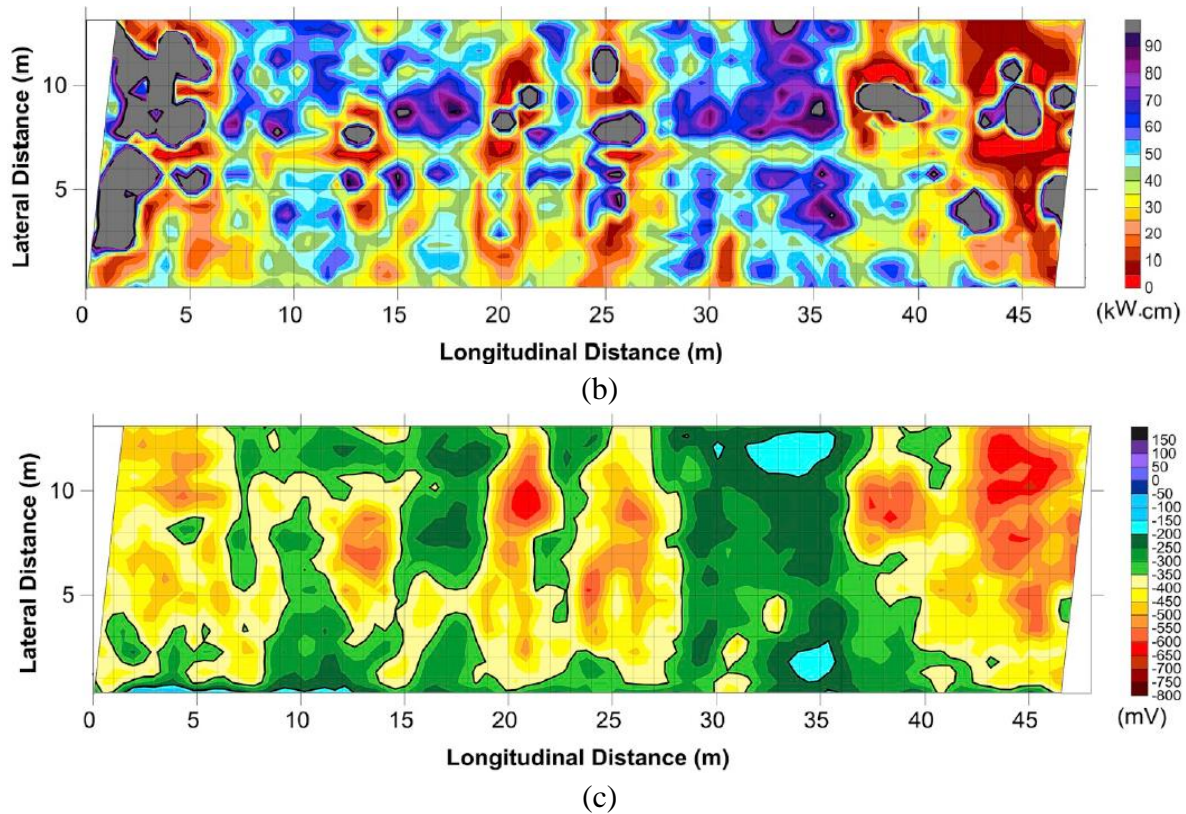
Figure 2-13 Condition maps of the Pequea Bridge deck (Kien Dinh et al. 2018): (a) the proposed method; (b) ER; (c) HCP

Parrillo and Roberts (2017) used a GPR system to evaluate an asphalt overlaid bridge deck deterioration condition on a bridge that was located in Lewiston, Maine. The evaluation was a joint effort between Geophysical Survey Systems and the Maine Department of Transportation (MaineDOT or MDOT). The deterioration map found from the GPR system was compared to the visual inspection from both the top and bottom of the bridge deck. The data indicated that over 50% of the scanned deck area was severely deteriorated.

Figures 2-14(a) and 2-14(b) show the top view of the bridge deck and the associated bridge deck deterioration contour map, respectively. The reflection amplitude data of each rebar location was used as an indication of the deterioration condition. In Figure 2-14(b) the color legend becomes a dark redness as the deterioration condition increases

(a)
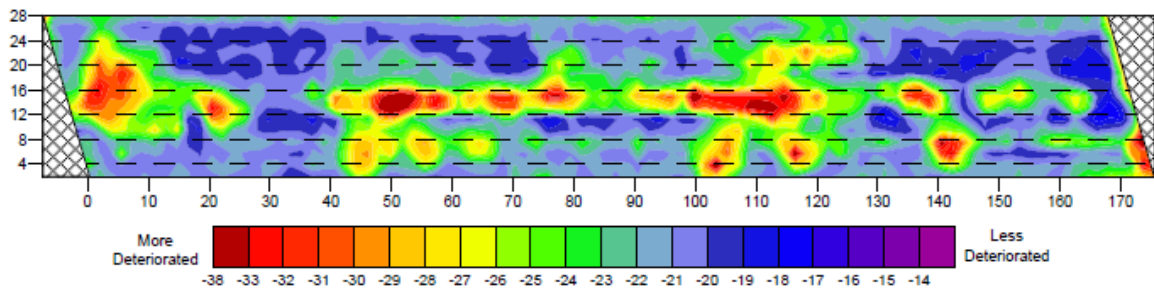
(b)

Figure 2-14 Bridge Deck (Parrillo and Roberts 2017): (a) GPR data collection; (b) Deterioration map

Gucunski et al. (2016) investigated a bridge concrete deck located in Haymarket, Virginia using five NDE techniques, including IE. The IE was performed to determine the deck delamination. The deck was scanned at different time intervals in September 2009, August 2011, October 2014, and June 2015. The scanning grid had a spacing of 2 ft. x 2 ft. Figures 2-15 and 2-16 show the actual grid scanning at the bridge site and delamination map, respectively.

Figure 2-15: NDE technologies during data collection (Gucunski et al. 2016)
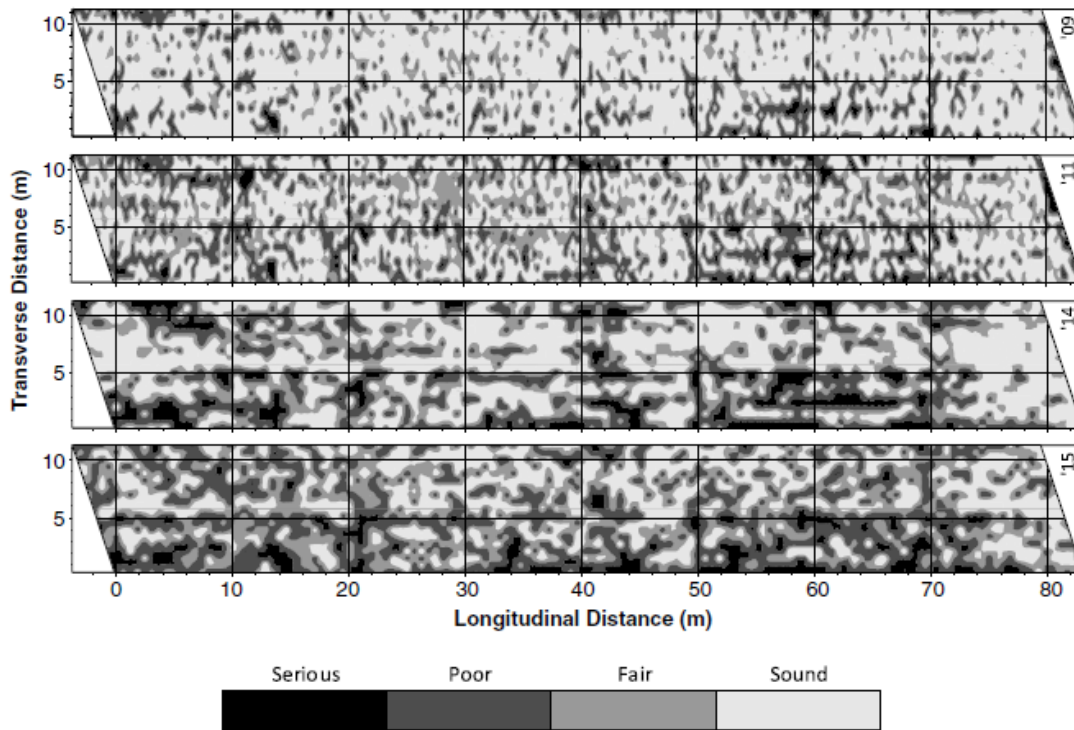
Figure 2-16: Delamination map found from IE from 2009 to 2015 (Gucunski et al. 2016)

2.4 Non-Destructive Load Testing

Peiris and Harik (2016) performed a load rating based on diagnostic testing of three single-span steel girder bridges in Kentucky. The investigation used advanced sensor technologies, such as magnetic and reusable strain gages as well as linear variable displacement transducers (LVDTs). All dimensions and material characteristics were based on field measurement and estimates since the as-built plans for the bridges were not sufficient. Except for one bridge with no end fixity, the other bridges demonstrated an unexpected composite action and end fixity. The field test data provided a higher rating factor than the data from American Association of State Highway and Transportation Officials' (AASHTO) MBE (2018). The bridges were load posted as rating factor magnitude was less than one, but the field load testing demonstrated an acceptable load rating factor.

On a multi-span concrete repaired bridge, Dong et al. (2020) performed dynamic and static load testing. The live load distribution factor (LLDF), the dynamic impact factor (IM), structural frequencies, mode shapes, load-rating factor (RF), and serviceability by way of deflection limits were all calculated using displacement transducers and strain gages. Dong et al.'s (2020) findings indicated that the LLDF and IM factors were much lower than those estimated by the AASHTO LRFD (2020). Per the testing conducted by Dong et al., the greatest deflections were within the permissible limit.

Sanayei et al. (2016) studied three different approaches of conducting a load rating on the Powder Mill Bridge in Barre, Massachusetts, that has a three-span continuous bridge with steel girders/bridge deck composite behavior. The approaches were based on the load and resistance factor rating equation (LRFR) and included a conventional method that used a simplified line girder-by-girder analysis with collected strain data from the field test to determine the actual LLDF. Sanayei et al. (2016) additionally used a finite-element (FE) model for load rating

24

purposes.. The conventional method was fast, easy to use, and inexpensive while also providing a conservative load rating compared to the rating using the filed load test. Although the field load test method was easily implemented and also provided the current in-situ condition of the bridge,, it was costly.. FE required experience but can be more accurate.

Schwarz and Laman (2001) conducted a diagnostic load test on three prestressed concrete I-girder bridges to determine the actual LLDF, IM, and service-level stress. An FE model was also developed for comparison reasons. The researchers concluded that IM decreased as maximum static live load increased and that IM was not affected by the number of vehicle axles or the bridge span length. LLDFs from the diagnostic load test were also lower than the ones specified in AASHTO LRFD [1] and Standard Specification [2]. Finally, the FE model was consistent with the load test results.

Barr et al. (2001) examined the LLDFs for multiple three span prestressed concrete girder bridges. The evaluation involved an FEM that was calibrated with the static live-load test. Then, the FEM was used to evaluate the effects of various factors, such as intermediate diaphragms, end diaphragms, continuity, skew angle, and load type on the bridge LLDFs. Using the tested bridge geometry, the LLDFs found from FE differed by 28% when compared to AASHTO LRFD (1994). LLDFs were significantly reduced due to end diaphragms, skew angle, and load type factors, whereas continuity and intermediate diaphragms had the smallest effect. Barr et al. (2001) concluded that the concrete release strength could be reduced to 1000 psi or live load could be increased by 39% if the bridge was designed using the LLDFs obtained from FE and not from AASHTO LRFD (1994).

2.5 Numerical Studies

Ren et al. (2014) conducted a non-linear 3D FEM approach to investigate the structural behavior of a hybrid PCP. The study used the non-linear damage plasticity model in ABAQUS for the concrete. In a hybrid PCP, two prestressing tendons, either epoxy-coated steel or carbon fiber reinforced polymer (CFRP), were used at the panel edges. Six full-size PCPs were then modeled and validated with the experimental data. The load versus mid-span displacement and effects of damage plasticity parameters on the FEM results were also investigated. Theses parameters were the dilation angle and viscosity parameters. The researchers concluded that the numerical error of the failure load and mid-span displacement were within 6 % and 10 %, respectively. The displacement capacity and failure load also significantly increased as the dilation angle increased. Conversely, decreasing the viscosity parameter increased the FE data accuracy when compared to the experimental data. The detailed non-linear properties of concrete and steel are described in sections 2.5.1 and 2.5.2, respectively.

2.5.1 Inelastic Properties of Concrete

Wahalathantri et al. (2011) used two numerical material models that only incorporated the ultimate compressive strength of the concrete. The models were modified to be used with the damaged plasticity model and then were validated with the experimental results under flexural loading. Moreover, the damaged plasticity model in ABAQUS is divided into two categories, compressive and tensile concrete behaviors.

Concrete Compressive Behavior

Hsu and Hsu's (1994) model was adopted as a complete stress-strain curve of concrete under uniaxial compression. The model can also be applicable for a high compressive strength up to 62 MPa (8.9 ksi). Figure 2-17 illustrates the stress-strain curve of compressive concrete.
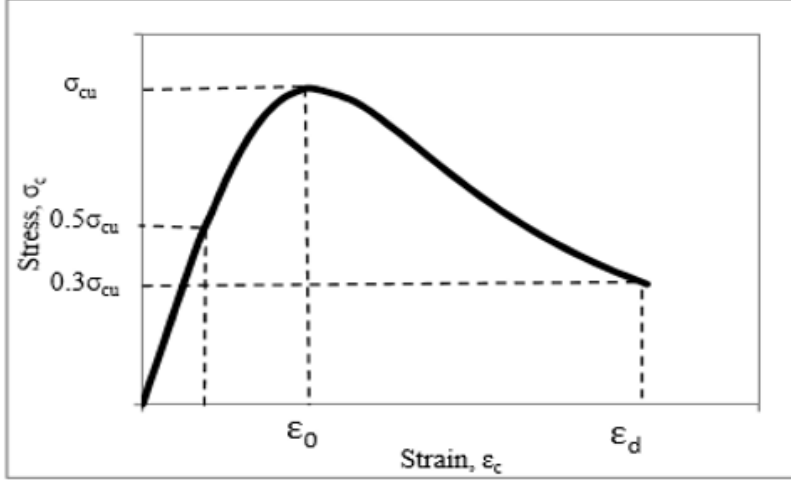
Figure 2-17: Stress-Strain Curve of Compressive Concrete (Wahalathantri et al. 2011)

From Figure 2-17, the ultimate compressive strength of the concrete was defined by σ_{cu} with ε_o as the corresponding strain. The elastic stress-strain curve extends up to 0.5 (σ_{cu}) in the ascending portion, where Hooke's law is applicable. The stress values in the non-linear stage can be computed using Equation 2-1:

$$\sigma_c = \left(\frac{\beta * \left(\frac{\varepsilon_c}{\varepsilon_o} \right)}{\beta - 1 + \left(\frac{\varepsilon_c}{\varepsilon_o} \right)^\beta} \right) * \sigma_{cu} \tag{2-1}$$

β is the parameter that relies on the shape of the stress-strain curve and can be calculated based on Equation 2-2.

$$\beta = \left(\frac{1}{1 - \frac{\sigma_{cu}}{\varepsilon_o * E_o}} \right) \tag{2-2}$$

E_o is the initial tangential modulus, and ε_o is the corresponding strain of the ultimate compressive strength. Both are calculated using Equation 2-3.

$$E_o = 1.2431 * 10^2 \, \sigma_{cu} + 3.28312 * 10^3 \text{ (ksi)} \tag{2-3}$$

$$\varepsilon_o = 8.9 * 10^{-5} \, \sigma_{cu} + 2.114 * 10^{-3}$$

The inelastic strain (ε_{in}) is the total strain (ε_c) subtracted from the elastic deformation defined by Hooke's law. The damage parameter of the concrete is calculated using Equation 2-4.

$$\varepsilon_{in} = \varepsilon_c - \frac{\sigma_c}{E_0} \qquad (2\text{-}4)$$

$$d = 1 - \frac{\sigma}{\sigma_{peak}}$$

σ_{peak} has the same value as (σ_{cu}). The damage parameter (d_c) can be applied to the stress values beyond the ultimate compressive strength, and the concrete compression damage in FEM includes both the damage parameter and the inelastic strain.

Concrete Tensile Behavior

Concrete tensile behavior requires three main failure stages: tension stiffening, tension softening, and reinforcement interaction with concrete. Concrete tensile behavior in FEM includes Young's modulus (E_o), stress (σ_t), cracking strain (ε_{crack}), and the damage parameter (d_t), as shown in Figure 2-18(a).

Wahalathantri et al. (2011) modified the tension stiffening model developed by Nayal and Rasheed (2006) to include three stages: the elastic, primary cracking, and secondary cracking stages. All the tensile stresses and corresponding strains of the three stages are illustrated in Figure 2-18(b).
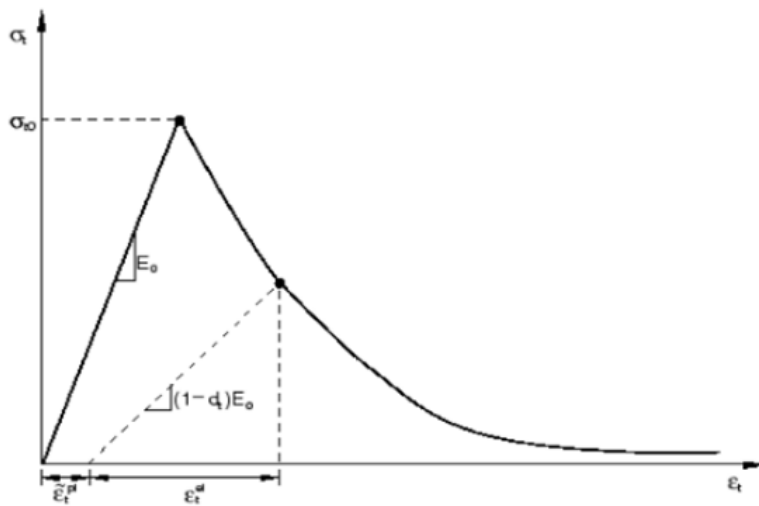
(a)
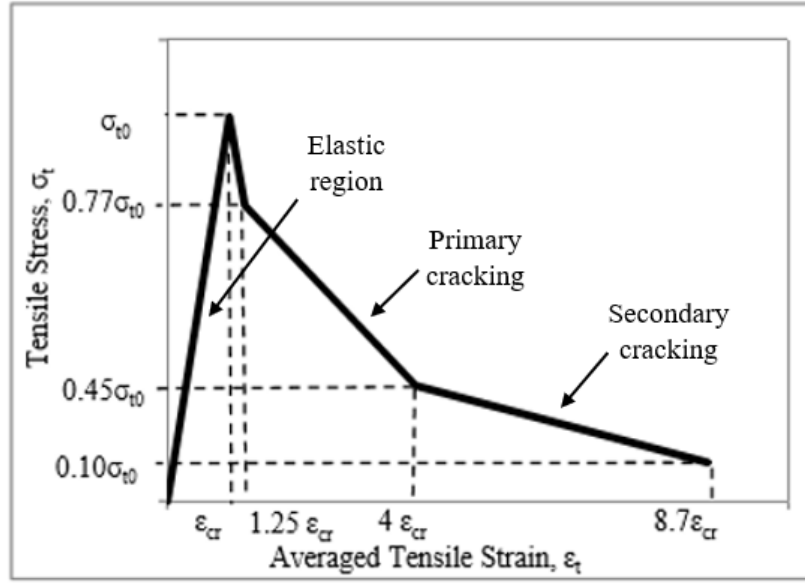
(b)

Figure 2-18 Concrete tensile loading: (a) ABAQUS Dassault Simulia (2013); (b) Modified model

The ultimate splitting tensile stress (σ_{to}) of the concrete can be calculated according to ACI Committee 318 2014, which is given in Equation 2-5.

$$\sigma_{to} = 6.7 \sqrt{f_{cm}} \tag{2-5}$$

f_{cm} represents the measured average compressive strength. The value of critical tensile strain was calculated based on dividing the ultimate tensile stress by the initial tangential modulus (E_o). The calculation of the damage parameters of concrete tensile behavior was the same as those of concrete compression behavior.

2.5.2 Inelastic Properties of Steel

The steel tensile behavior consists of elastic and non-elastic portions. The primary objective of non-elastic behavior was to identify the non-elastic properties, yield stresses, and plastic strains. A uniaxial tensile test was used to determine the yielding stresses and their corresponding total strains. The plastic deformation can be calculated using Equation 2-6.

$$\varepsilon_{plastic} = \varepsilon_{total} - \frac{\sigma}{E_s} \tag{2-6}$$

σ represents the value of stresses on the stress-strain curve of the tested steel specimens, starting from the yielding stress, with the corresponding strain values defined as ϵ_{total}. E_s is known as the modulus of elasticity for steel, which has a magnitude of 29000 ksi.

2.6 Strengthening of Bridge Structures

Bridge structures are normally designed to fulfill their service lifetime. However, some bridge structures are prone to minor or major defects, such as localized deck failure or collapse due to a defect in one of the major structural parts in the bridge, such as a column. The following subsections include an overview of the common repair techniques performed on composite bridge concrete decks.

2.6.1 Fiber Reinforced Concrete (FRB)

Over the last decades, fiber-reinforced concrete (FRC) has been commonly used in bridge deck overlays or newly constructed bridge decks to enhance bridge performance (Figure 2-19). The main objective of utilizing FRC in bridge decks is to reduce deck cracking as well as the crack width. All bridge decks in several states, including as California, Oregon, and Delaware, used the macrofiber reinforcement, whereas bridge deck overlay using FRC materials is the most common application (Amirkhanian and Roesler, 2019).

Naaman and Chandrangsu (2004) explored the feasibility of using high-performance, fiber-reinforced concrete composite in bridge decks. According to AASHTO LRFD, the suggested deck design required a 1.28% steel reinforcement by volume. The researchers additionally assessed the efficacy of a hybrid design by using 0.4% reinforcing steel and 1.5% high-density polyethylene macrofibers by volume. While the proposed hybrid design demonstrated a lower peak load capacity, a 60% increase in post-peak load capacity was measured.

Shafei et al. (2021) investigated the use of FRC in a bridge deck at three different stages. In the first stage, the researchers investigated numerous binder compositions and subsequently selected the most optimal binder that resulted in a reduction in plastic shrinkage. Shafei et al. (2021) then added multiple dosages of microfibers to mixtures to increase the tensile concrete strength and reduce cracking. Next, the researchers measured the mechanical concrete properties, such as compressive and splitting tensile strength. Shafei et al. (2021) additionally explored drying shrinkage and rapid chloride migration. Finally, three types of macrofibres, Polypropylene (PP), Alkali-resistant (AR) glass, and Polyvinyl alcohol (PVA), in addition to the microfibers were utilized in the study to improve the post-peak strength of concrete. Post-peak mechanical properties included measuring toughness and residual flexural strength, whereas pre-peak mechanical properties included compressive, splitting tensile, and concrete flexural strength.
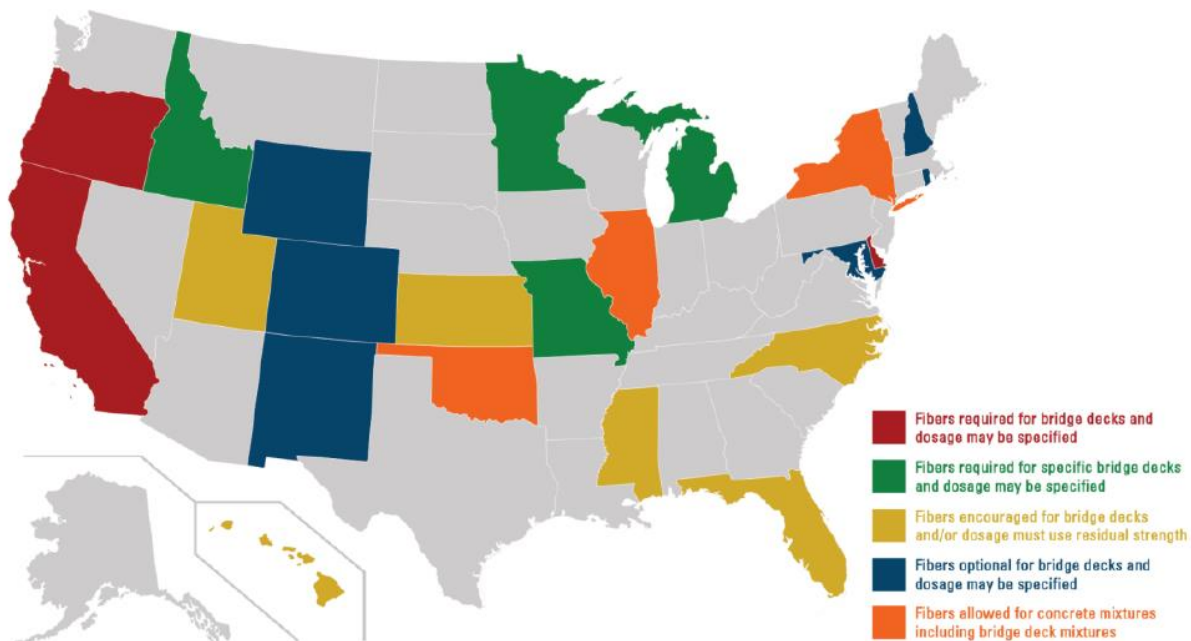
Figure 2-19: State DOTs with fiber specifications and the level of detail in the specifications (Amirkhanian and Roesler, 2019)

2.6.2 Fiber Reinforced Polymer (FRP)

Gar et al. (2013) conducted an experimental study on a full-scale bridge deck slab that consisted of full-depth PCPs. The PCP specimens were composed of three different types of rebars: aramid-fiber-reinforced polymer (AFRP), steel, and strand. One specimen was reinforced and prestressed with (AFRP) rebars in both directions (Figure 2-20). The second specimen, which served as a control specimen, was reinforced with a steel and a prestressing strand. The study investigated the load capacity, crack pattern, and failure mode under different load cases, numbered from 1 to 5. The load cases were applied to the interior span and overhang [Figure 2-21(a)]. Figure 2-21(b) shows the test set-up.
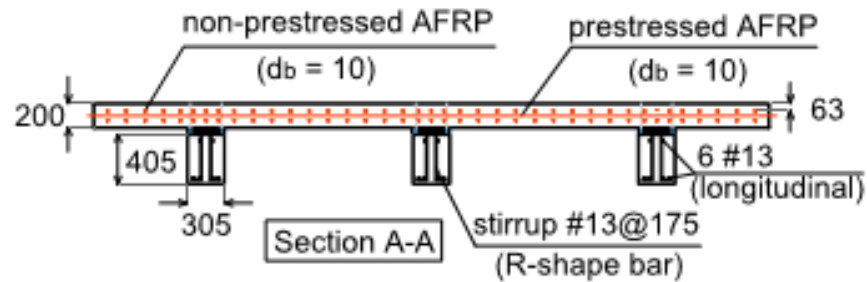
Figure 2-20: Plan view of the bridge deck slab (Gar et al. 2013)

(a)
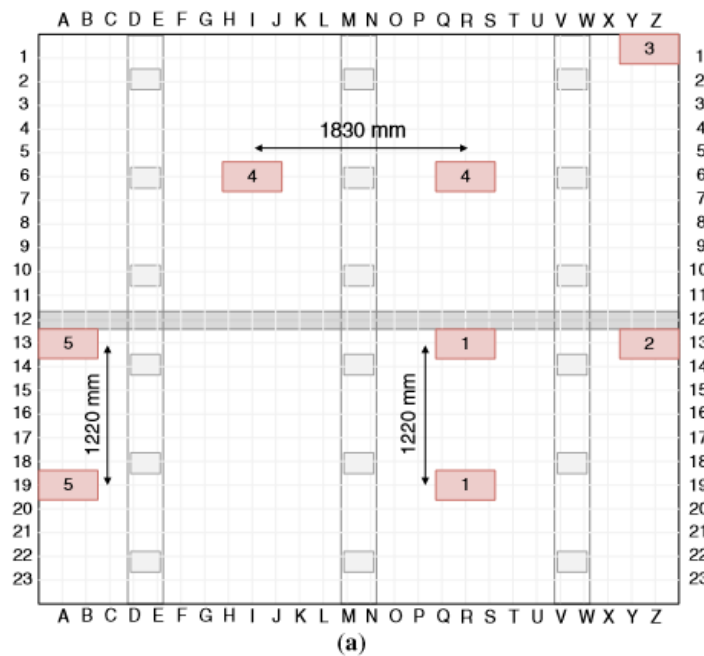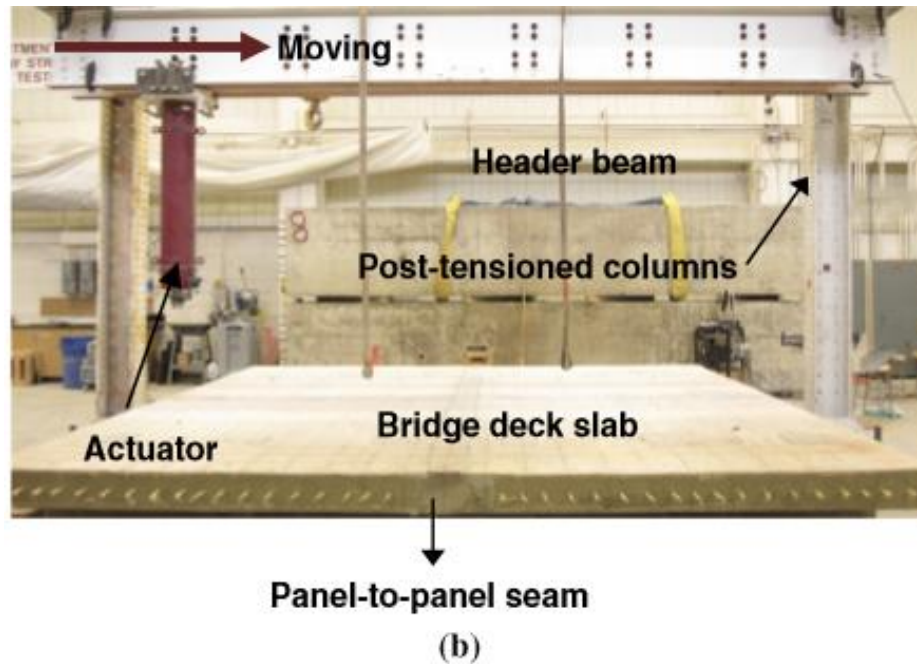
Figure 2-21 Deck slab (Gar et al. 2013): (a) Load cases 1, 2, 3, 4, and 5; (b) Test set-up

Figures 2-22 (a-d) show the applied load versus deflection curves of both rebars. The average failure load in the AFRP rebars of the interior span and overhang was approximately 3.7 and 1.4 times the AASHTO maximum factored load, respectively. Load case 1 [Figure 2-22(a)] shows that the AFRP has more load capacity (700 kN [157 kips]) compared to the capacity of the steel and prestressing strands (550 kN [112 kips]). In load case 4 [Figure 2-22(b)], the opposite is true as the load capacities of the AFRP and steel rebars are 770 kN (173 kips) and 859 kN (193 kips), respectively. The AFRP load capacity decreased when the truck axle load was applied to the same interior span and was even lower when applied to the overhang portion of the PCP [Figures 2-22(c) and 2-22(d)].
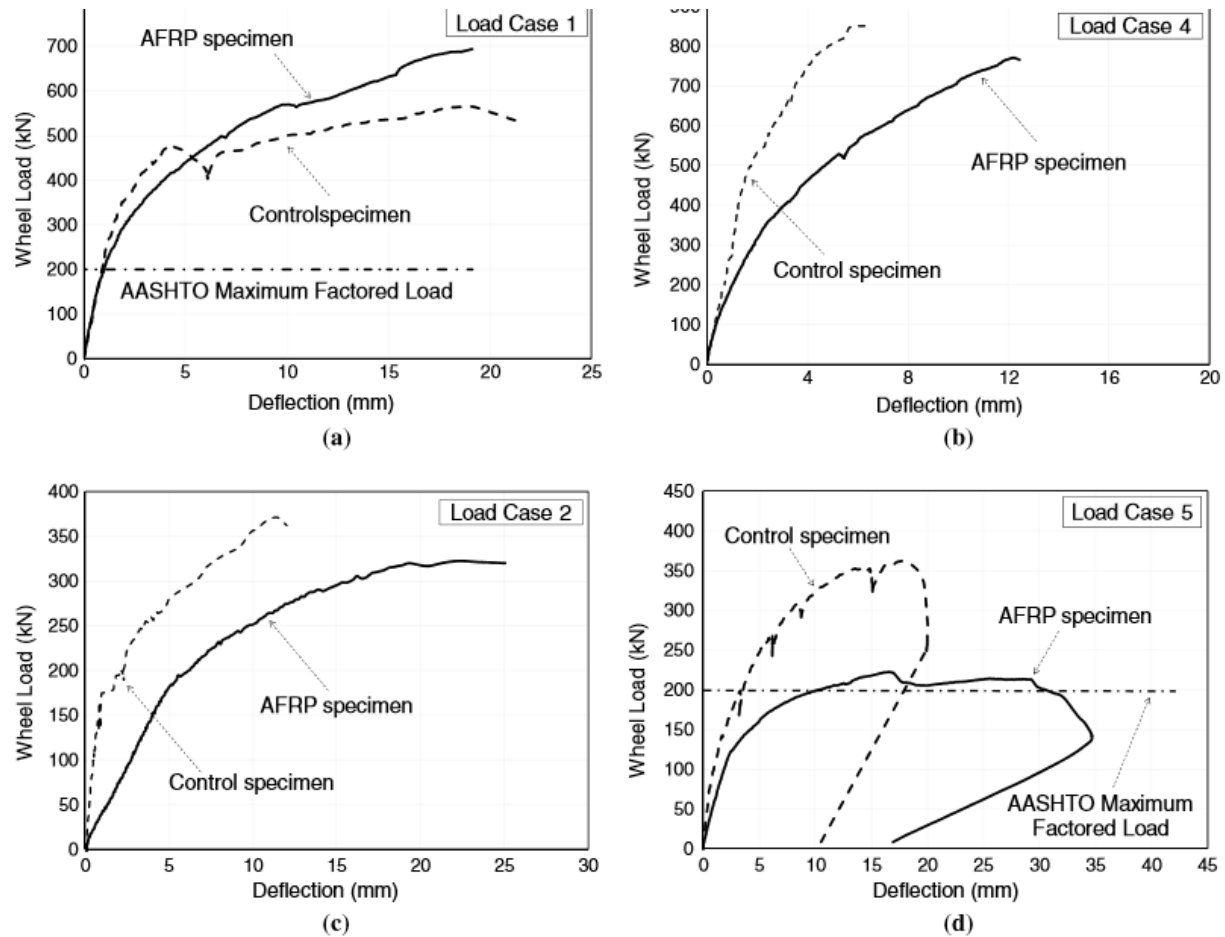
Figure 2-22 Load-deflection curves (Gar et al. 2013): (a) Case 1; (b) Case 4; (c) Case 2; (d) Case 5

Sim et al. (2006) conducted an experimental study to evaluate the failure patterns of bridge decks that were strengthened using various materials, including carbon fiber sheets (CF), glass fiber sheets (GF), carbon fiber reinforced polymer grids (CFR-G), and steel plates (SP). In the study, 10 PCPs were tested, and one PCP without strengthening material served as a control specimen. Figures 2-23(a-d) show the typical failure pattern of the PCPs. Panel 1 was the reference panel, Panel 3 was strengthened with SP, Panel 6 was strengthened with CF, and Panel 10 was strengthened with CFR-G.

The researchers concluded that the panel strengthened with SP exhibited an increase in stiffness but failed in brittle failure mode due to over-strengthening [Figure 2-24(a)]. The panel reinforced with fiber reinforced polymer (FRP) failed mostly in a ductile mode after the yielding

of the rebars. CF and CFRP-G [Figure 2-24(b)] were the most effective strengthening materials for PCPs that were not severely deteriorated. Overall, decks strengthened using these materials exhibited greatly increased strength and improved ductility.
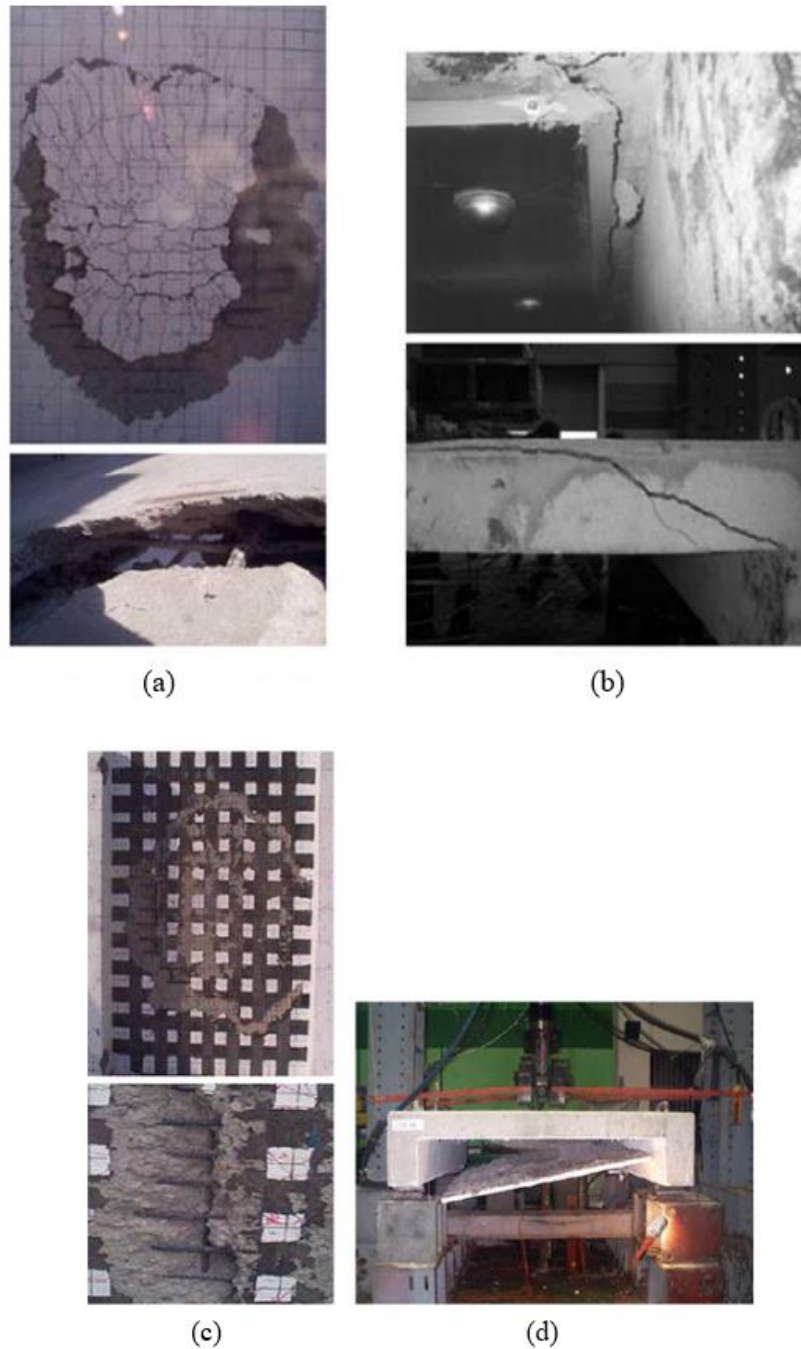
Figure 2-23 Failure patterns (Sim et al. 2006): (a) Panel 1;(b) Panel 3;(c) Panel 6; (d) Panel 10
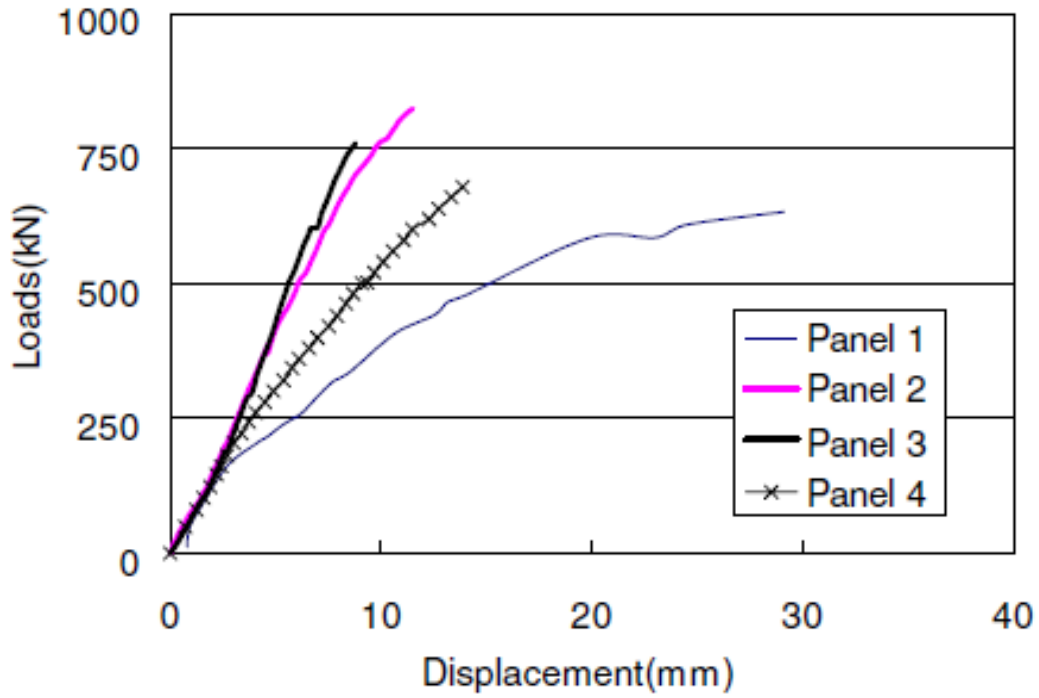
(a)
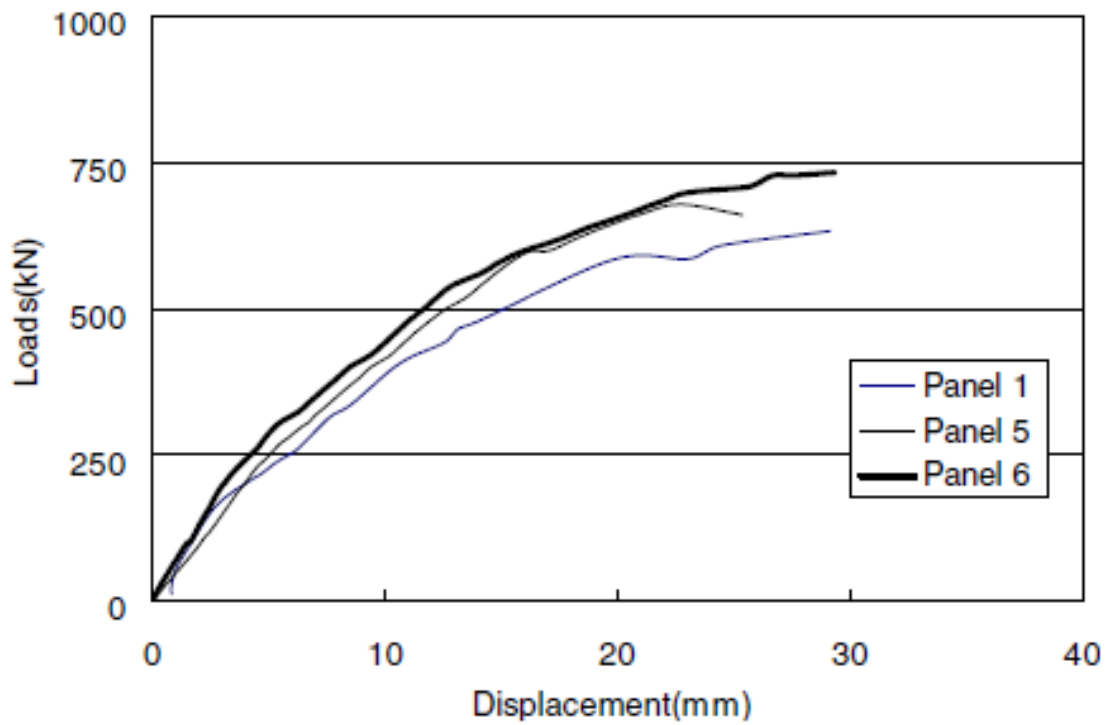
(b)

Figure 2-24 Load–displacement curves of PCPs (Sim et al. 2006): (a) Panel 3 (SP); (b) Panel 6 (CF)

Chapter 3

BRIDGE DESCRIPTION

3.1 Las Lomas Bridge

Las Lomas Bridge consists of EB and WB bridges, structures No. 378 and No. 377, respectively. The bridges were built in 1987 and are located in Terrel, Texas [Figures 3-1(a) and 3-1(b)]. The two bridges carry IH-20 over Las Lomas Parkway and have four simple spans that consist of prestressed Type C girders resting on concrete bent caps. The deck was constructed of CIP concrete over PCPs. Each span measures 70 ft., with a total bridge length of 280 ft. Both EB and WB total composite bridge decks were recently replaced in 2019 and 2020, respectively. Subsections 3.1.1 and 3.1.2 provide a summary of the main features for both bridges, including the construction sequence of the replaced composite bridge decks.
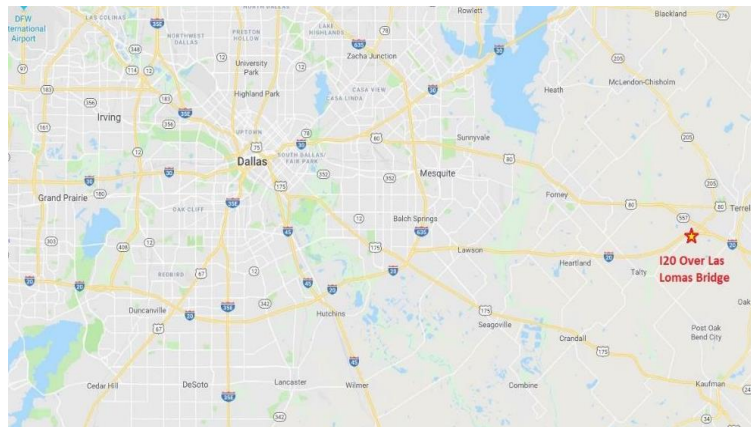
(a)
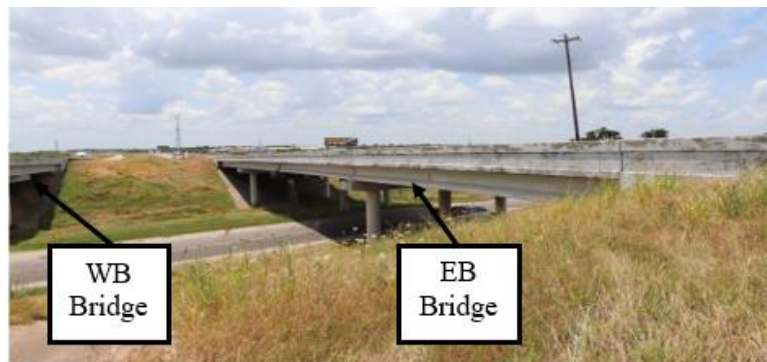
(b)

Figure 3-1: Las Lomas Bridge: (a) Location map; (b) Street view

37

3.1.1 EB Bridge

Span 2 in the EB bridge is comprised of eight Type C prestressed concrete girders, as illustrated in Figure 3-2(a). Since the total EB bridge composite deck was recently reconstructed, this section describes both the original and replaced composite decks. The typical transverse section of the bridge deck for span 2 is shown in Figure 3-2(a). The transverse section indicates the total deck thickness as well as the reinforcement details of the original and replaced decks. The PCP plan and its transverse section are depicted in Figures 3-2(b) and 3-2(d), respectively. Figure 3-2(c) illustrates the physical dimensions of the typical Type C girder.
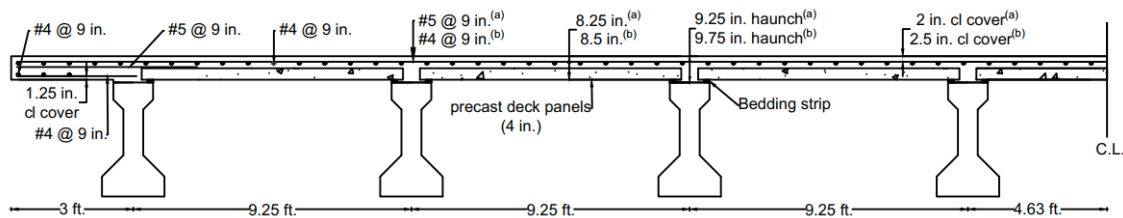
(a)

(Note: $^{(a)}$&$^{(b)}$ represent the EB original and replaced bridge composite decks)

(b)   (c)
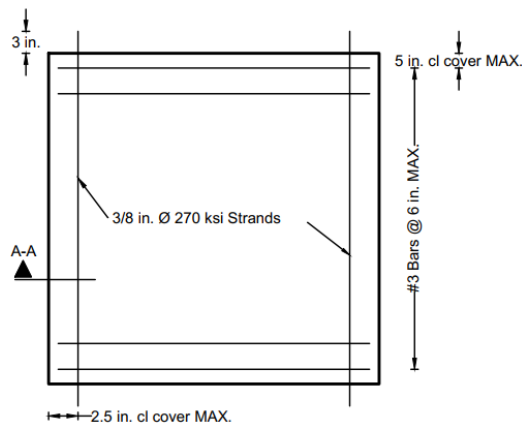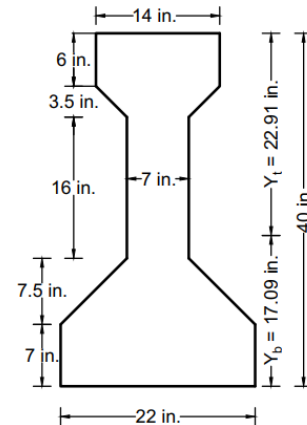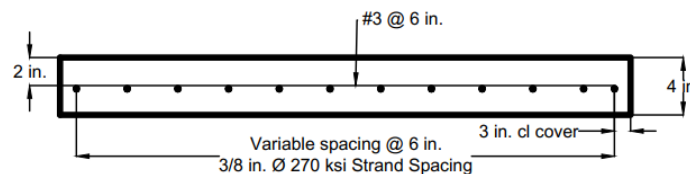
(d)

Figure 3-2 Span 2 details: (a) Typical deck transverse section;(b) PCP plan; (c) Type C dimensions; (d) PCP cross section

Table 3-1 shows the section properties of Type C girders. The sequence of removing the EB original concrete deck was performed in two phases, according to as-built drawings provided by TxDOT [Figures 3-3(a) and 3-3(b)]. The two phases were separated by a break line at Girder D, as shown in Figure 3-3(a). The new deck was then constructed in two stages according to as-built drawings provided by TxDOT. The two stages intersected at Girder C where the construction joint exists [Figure 3-3(b)]. The new deck was designed for HS20-44 AASHTO standard specifications with a design speed of 70 mph. The Type T501 bridge barrier was also replaced with a Type SSTR barrier. The final configuration of the new deck is shown in Figure 3-4.

Table 3-1: Section properties for girders and CIP deck

Girder Type	Area (in^2)	Moment of inertia (I) (in^4)	Weight (lb./ft)
Type C	494.9	82.602	516

(a)

(b)
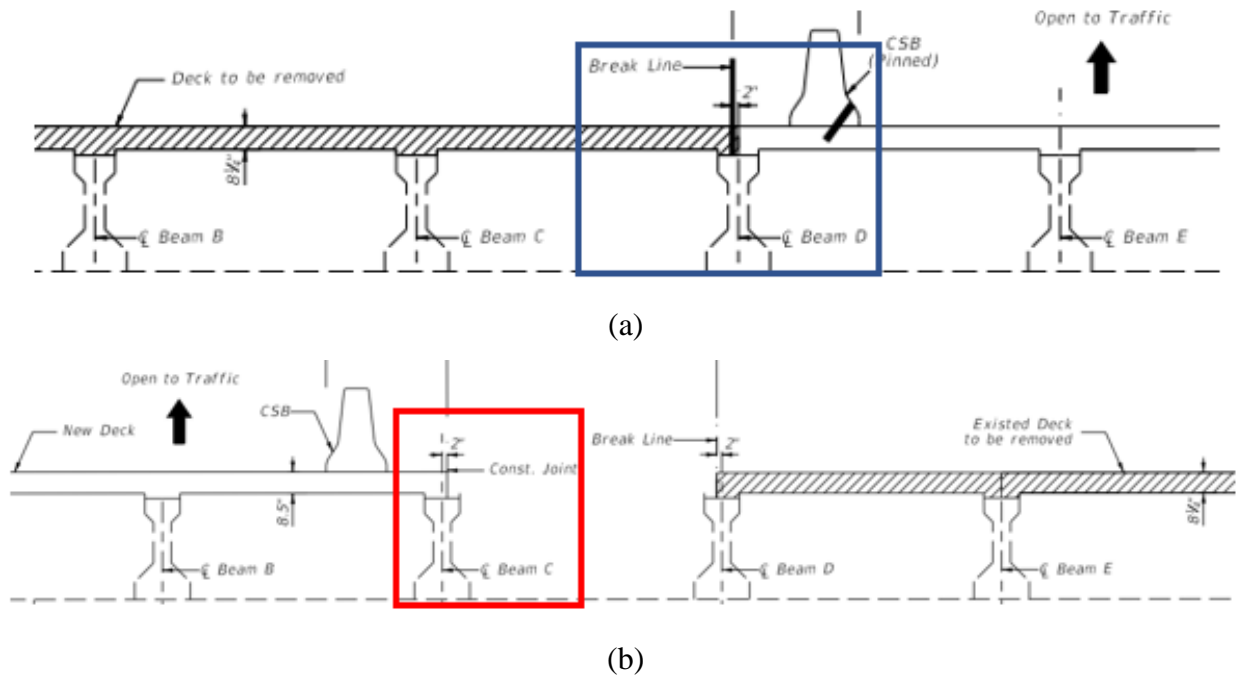
Figure 3-3 Sequence of original EB deck removal: (a) Phase 1;(b) Phase 2
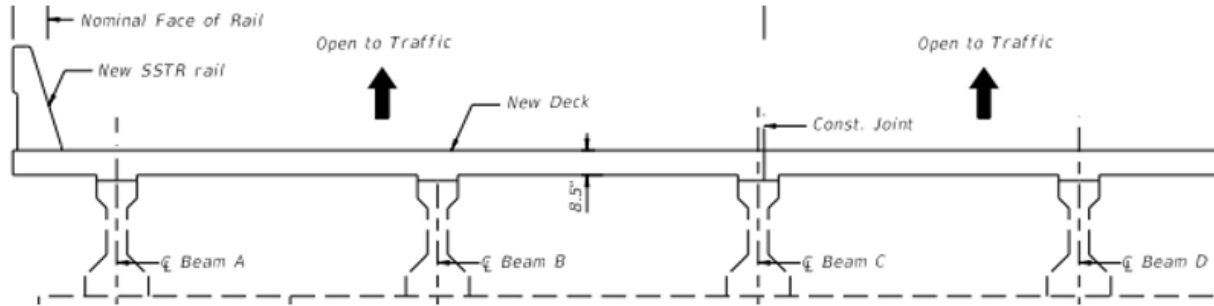
Figure 3-4: Final configuration of the new deck

Material Properties of EB Bridge

The compressive strengths of the CIP concrete deck and PCPs are 4 and 5 ksi, respectively. The strand diameters of girders and PCPs are 0.5 and 0.375 in. with 270 ksi low relaxation steel strands.

The EB bridge material properties of Type C girders span 2 as per the as-built drawing are given in Table 3-2. The girder spacings are shown in Table 3-3.

Table 3-2: Material properties for EB Type C girder

Properties	Girder (A-F)	Girder (G)	Girder (H)
Concrete compressive strength (f_c', girder) (ksi)	5.8	5.1	5.3
Number of prestressing strands in each girder	36	30	32

Table 3-3: Type C girder spacing for span 2

Girder	Spacing (ft.)
A-F	9.25
F-G	8 (average)
G-H	7.72 (average)

3.1.2 WB Bridge

Span 4 is comprised of six Type C prestressed concrete girders, as illustrated in Figure 3-5. The typical transverse section of the WB bridge deck for span 4 has the same reinforcement details as the original EB deck as mentioned in Figure 3-2(a) but with a different number of girders, total deck thickness, haunch height, and girder spacing. Figure 3-5 illustrates the typical section of span 4.
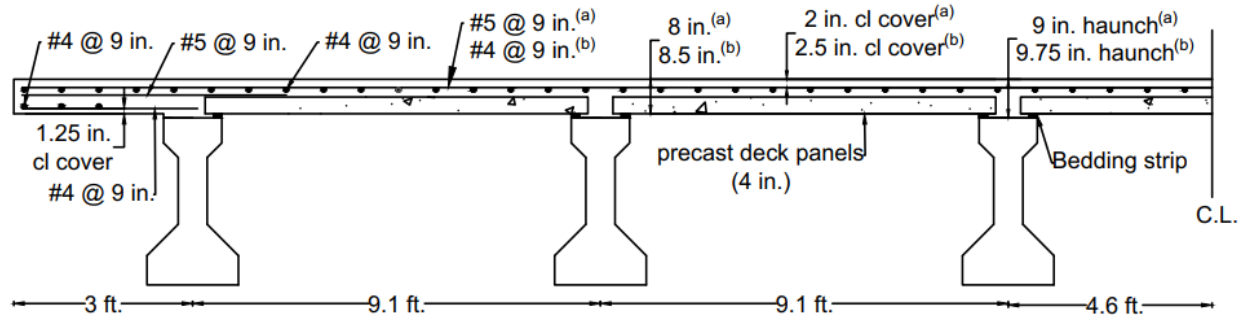
Figure 3-5: Typical transverse section for span 4 of the WB (Note: (a)&(b) represent the WB original and replaced bridge composite decks)

The sequence of removing the WB original concrete deck was performed in the same manner as the original EB deck, and the deck removal was achieved in two phases according to as-built drawings provided by TxDOT.

Material Properties of WB Bridge

The WB Bridge deck has the same compressive strengths of the CIP concrete deck and PCPs as the EB bridge deck. The strand diameters of the girders and PCPs are also the same as those in span 2 of the EB bridge. The WB bridge material properties of Type C girders in span 4, as per the as-built drawing, are given in Table 3-4. The average girder spacing in span 4 is 9.1 ft.

Table 3-4: Material properties of girders in WB Bridge

Properties	Values
Concrete compressive strength (f_c', girder) (ksi)	5.5
Number of prestressing strands in each girder	34

Chapter 4

EXPERIMENTAL PROCEDURES

4.1 Testing Instruments

The sensors used to instrument the bridge to obtain the required data and Data Acquisition (DAQ) used during the field load test are described in the following subsections.

4.1.1 Strain Gage

The strain gage was used to measure the structural member elongation. The strain gages used in the bridge testing consist of non-reusable and reusable/wireless strain gages. The non-reusable gages are a resistance-based foil strain equipped with different gage-length factors. Since the bridge involved a Type C girder made of concrete, a longer gage length of 2.4 in. (60 mm) or longer is optimal due to the non-homogenous nature and crack susceptibility. The non-reusable gages are manufactured by Tokoyo-Sokki, and their types are PL-60-11-3LJCT-F [Figure 4-1(a)]. The gage factor can vary among gages with a range between 2.08 to 2.12, while the gage resistance usually depends on the tested material types. For concrete, the resistance gage is 120 Ω. The reusable gage, ST350, is used for most material types, including steel, concrete, timber, and fiber-reinforced polymer (FRP), which has a gage length of 3 in. (76.2 mm) [Figure 4-1(b)]. ST350 also can measure strain up to 4000 $\mu\varepsilon$, which is suitable for bridge testing.

(a)	(b)

Figure 4-1 Concrete strain gage: (a) Non reusable; (b) Reusable/wireless gage

The installation process of non-reusable and reusable strain gages on the concrete surface consisted of the following steps:

➢ The optimal gage locations were determined on the bottom flange, mid-web, and top flange of the concrete surfaces.

➢ The concrete surface was smoothed by the grinding machine which was connected to a generator as a source of power and was subsequently cleaned with acetone and water.

➢ Non-reusable gages were installed on the concrete surface using CNE adhesive, while the reusable/wireless gages used Loctite 410 epoxy and Loctite accelerator with the assistance of a man-lift [Figure 4-3 (e) and 4-3(f)].

➢ White rope was used to tie the gage wires to the bridge diaphragms near the instrumented girder.

4.1.2 Rotational Tiltmeter:

The T500 tiltmeter is an electrolytic fluid-based tilt sensor that can be used for precision rotation measurements. The angle measurement ranges from $\pm 5^\circ$ to $\pm 60^\circ$ and it used in bridge slabs, beams, and piers to measure the end rotation due to live load. Figure 4-2 shows the tiltmeter sensor configuration.
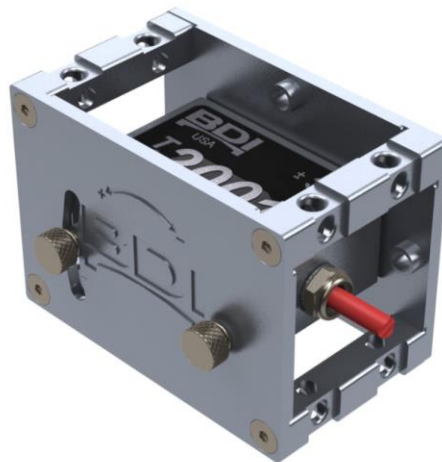
Figure 4-2: Rotational tiltmeter

The installation process of the rotational tiltmeter on the concrete surface is the same as reusable strain gages. The sequence of installing rotational tiltmeters and the reusable/wireless strain gages is shown in Figures 4-3(a-h).

(a) Sanding the surface

(b) Cleaning surface with acetone

(c) Measuring 2 ft. from CL of bent 2

(d) Measuring mid-point of girder

(e) Applying Loctite 410 on steel plate

(f) Applying Loctite accelerator

(g) Holding tiltmeter for 10-15 seconds   (h) Attached rotational tiltmeter

Figure 4-3: Installation sequence of rotational tiltmeters and reusable strain gages

4.1.3 Data Acquisition (DAQ)

The objective of the DAQ is to collect the desirable data from strain gage and rotational tiltmeter sensors. Two DAQs, Tokyo Sokki DS 50A and STS4 Base Station, were used during the load test. Data from non-reusable strain gages was then collected using Tokyo Sokki DS 50A while reusable/wireless strain gages and tiltmeters used STS4 Base Station to collect the data.

Both DAQs are functioned in a unique way. Tokyo Sokki DS 50A requires a cable used to transmit data from DS 50A to the laptop using a software called Strain Smart. DS 50A consists of 4 units in which every unit has 10 channels [Figure 4-4(a)]. Each non-reusable strain gage was connected to a specific channel number. The software allows users to change the gage calibration coefficient based on the recommendation from the manufacturer. STS4 Base Station, on the other hand, communicates wirelessly with STS nodes connected to reusable gages and tiltmeters through a router and transmits the collected data to a connected laptop [Figure 4-4(b)]. The sampling rate used was 10 data/ second. Figure 4-4(c) represents the full field equipment set-up ready for data collection.

(a)   (b)

(c)
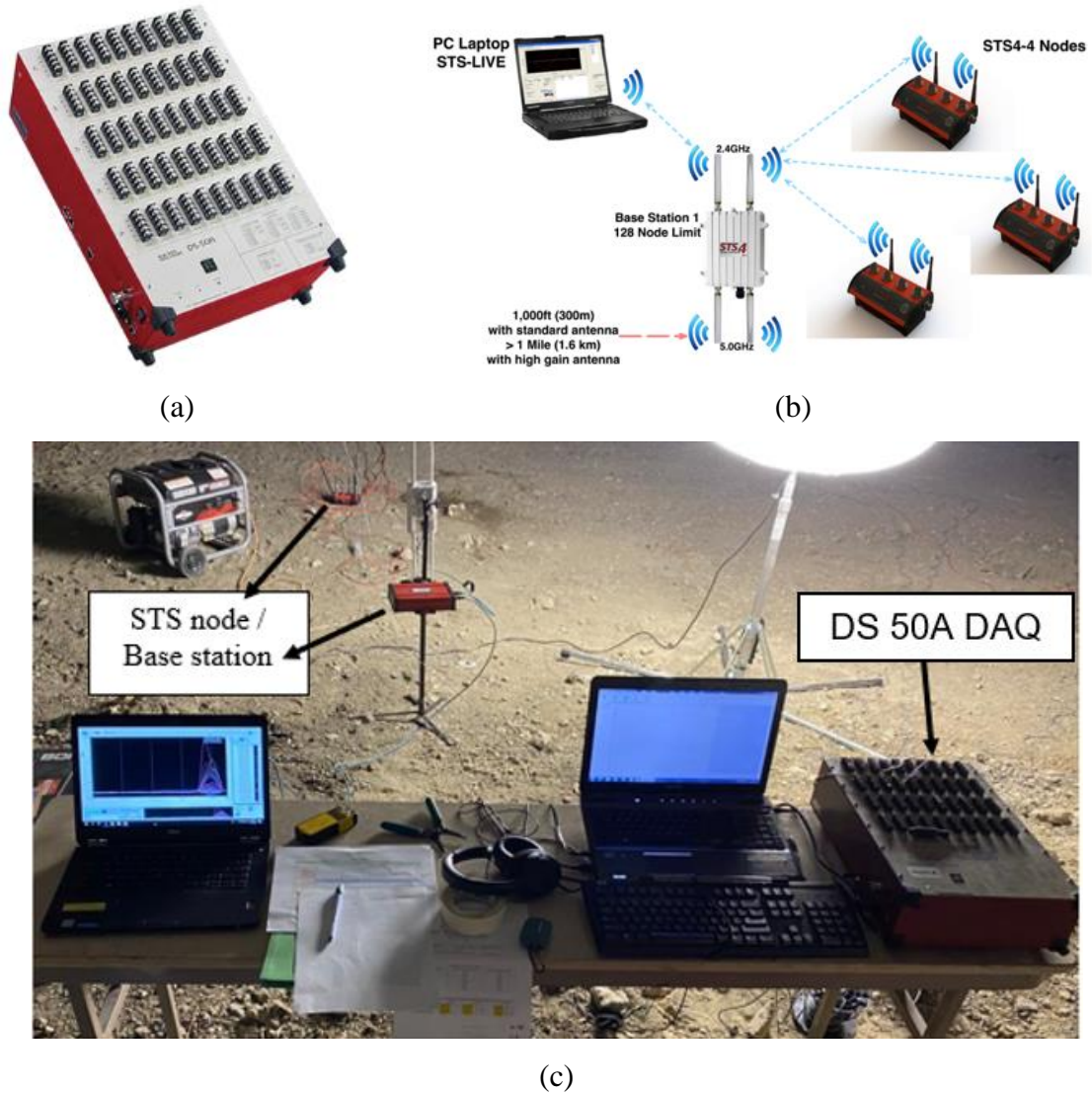
Figure 4-4 Equipment set-up: (a) DS 50A DAQ; (b) STS base station function [BDI]; (c) Full

set-up

4.2 Las Lomas Bridge Instrumentation

The Las Lomas bridge instrumentation included both EB and WB bridges. A follow-up of

EB evaluation was also conducted after the removal of the original bridge deck. Therefore, section

4.2 involved two phases. Phase 1 contains the bridge instrumentation of the original EB and WB

bridge decks, while Phase 2 only involves the follow-up bridge instrumentation of the replaced EB

deck.

4.2.1 Phase 1: Original EB and WB Decks

A detailed plan was prepared for the instrumentation and static load testing of IH-20 over the Las Lomas EB and WB bridges. Spans 2 and 4 were selected for the load test to optimize instrumentation, and only the superstructure behavior was investigated. A total of 25 and 28 non-reusable strain gages for EB and WB bridges, respectively, were installed on the girder surfaces for each bridge along with 12 rotational tiltmeters. The locations of the non-reusable strain gages and tiltmeters as well as DAQ are shown in Figures 4-5(a) and 4-5(b). The top gages were installed 3 in. below the top flange, while the bottom gages were installed at the center of the bottom flange. The tiltmeters were installed 2 ft. from the centerline of bents 2 and 3 for EB while bent 4 and abutment 5 were installed for WB. All of the girders were instrumented with both top and bottom strain gages and performed in two different sections along the length of the girders [Figures 4-5(a) and 4-5(b)]. Critical girders, near the patch area, were instrumented with top, middle, and bottom strain gages. Figures 4-6(a) and 4-6(b) and Figures 4-7(a) and 4-7(b) show strain gages and rotational tiltmeters attached to the girder, respectively.
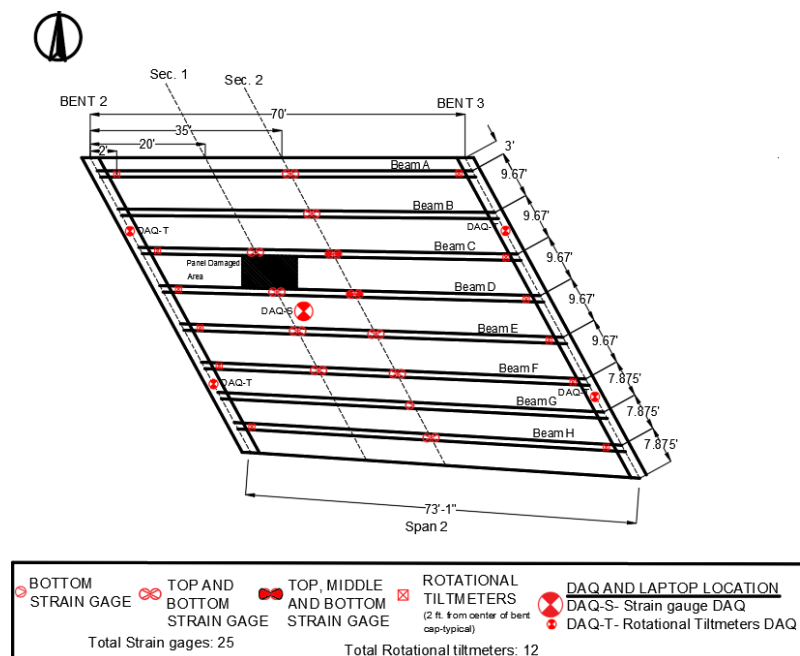
(a)
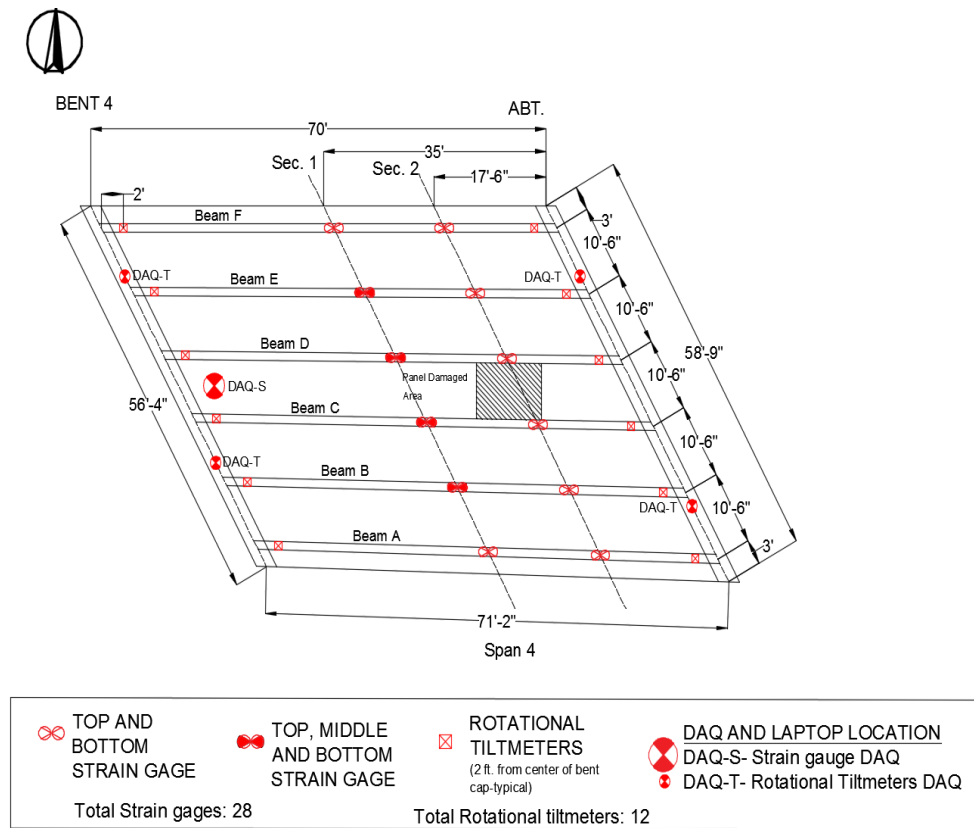
(b)

Figure 4-5 Instrumentation plan for load testing: (a) EB bridge; and (b) WB bridge

(a)   (b)

Figure 4-6 Attached non-reusable strain gages: (a) EB bridge; (b) WB bridge

<table>
<tr><td>(a)</td><td>(b)</td></tr>
</table>

Figure 4-7 Attached tiltmeters: (a) EB bridge; (b) WB bridge

4.2.2 Phase 2: EB Replaced Deck

The main objective of Phase 2 was to investigate whether the load carrying capacity of the replaced bridge deck increased and was able to withstand the induced live load. As a result, a follow-up detailed plan for the bridge instrumentation was prepared. For the load test, span 2 was selected to establish a base reference to compare the follow- up results with the previous EB load test. The primary instrumentation of the bridge consists of tiltmeters as well as reusable/wireless and non-reusable strain gage sensors attached to the girder surfaces.

The instrumentation on the original and replaced decks was almost identical, with additional strain gages attached near the construction joint of the replaced deck (denoted in orange colors). The location of the sensors is depicted in Figure 4-8. At sections 1 and 2, 20 ft. and 35 ft. (mid-span) measured from bent 2, strain gages were installed on four and eight girders, respectively. The transverse cross section of bridge instrumentation at the mid span of girders is shown in Figure 4-9. A minimum of two gages were placed at the top and bottom girder surfaces at each instrumentation point, with additional gages attached at the center of the girder web on girders C and D (denoted in green colors). Reusable wireless gages were used in the bridge instrumentation of the replaced deck [Figures 4-10(a) and 4-10(b)]. Due to the lack of reusable

wireless gages during Phase 1 instrumentation, non-reusable gages were only used on the previous deck. The replaced bridge decks used a total of 41 reusable strain gages. The tiltmeters attached to the girder are shown in Figures 4-10(c). Table 4-1 shows the location of the strain gages and rotational tiltmeters.
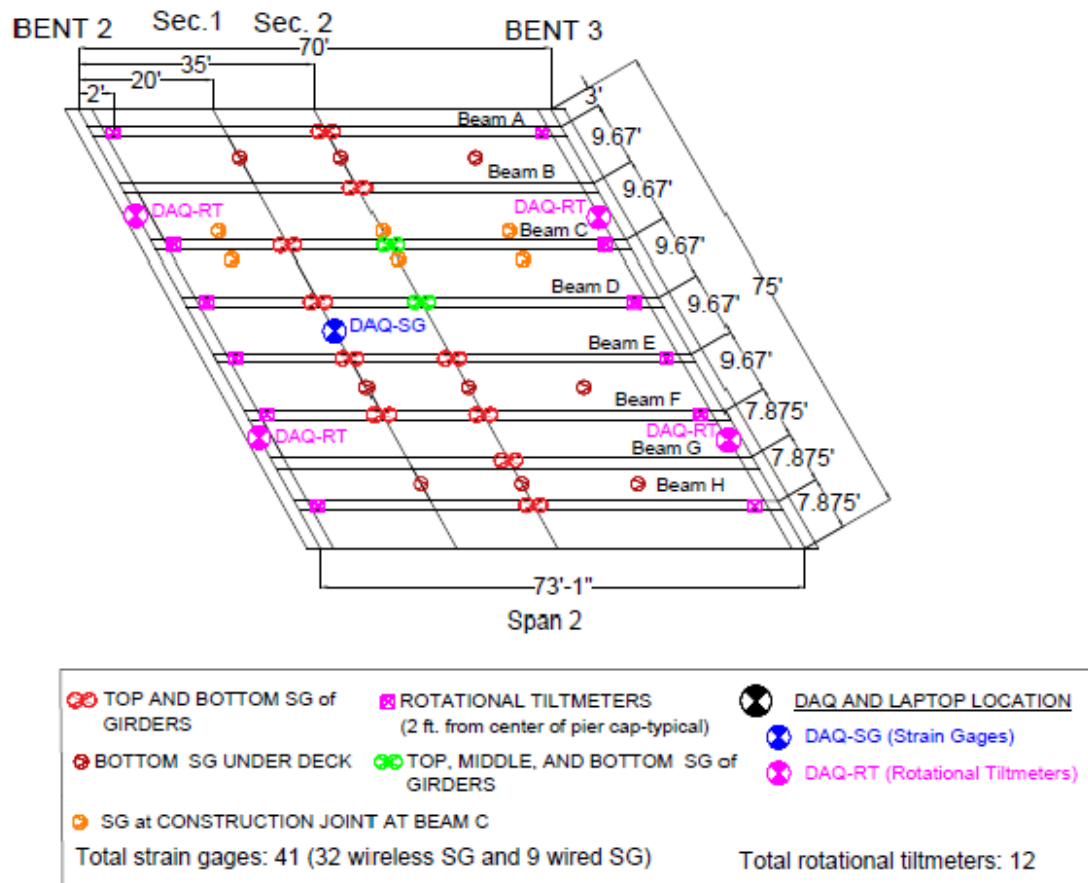
Figure 4-8: Follow up Instrumentation plan for load testing of EB replaced deck
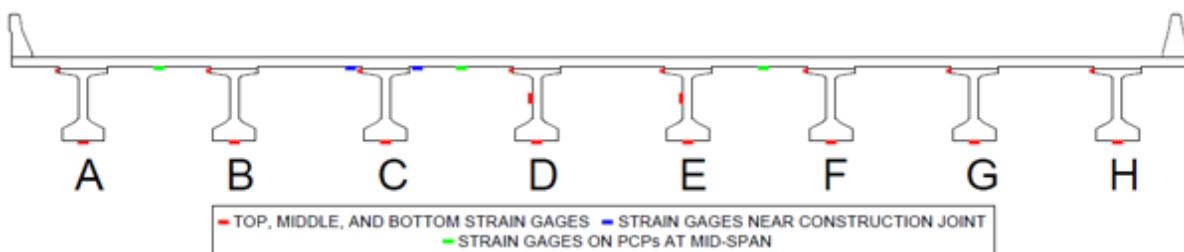
Figure 4- 9: Transverse cross section of bridge instrumentation

Table 4-1: Bridge Instrumentation Sensors

Device	Quantity	Location
Wireless strain gages	32	26 on 8 girders in span 2 6 near construction joints (Girder C)
Rotational tiltmeters	12	Near bents 2 and 3
Wired/foil strain gages	9	Deck Bottom
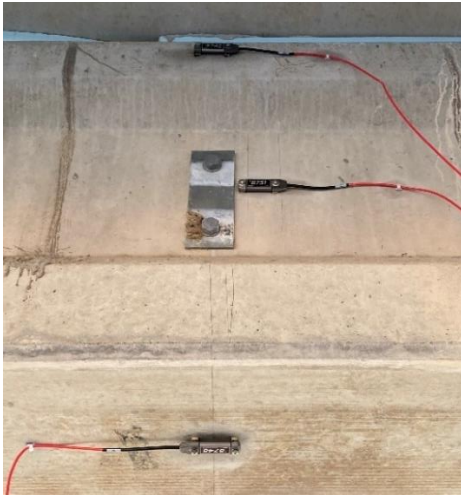
(a)
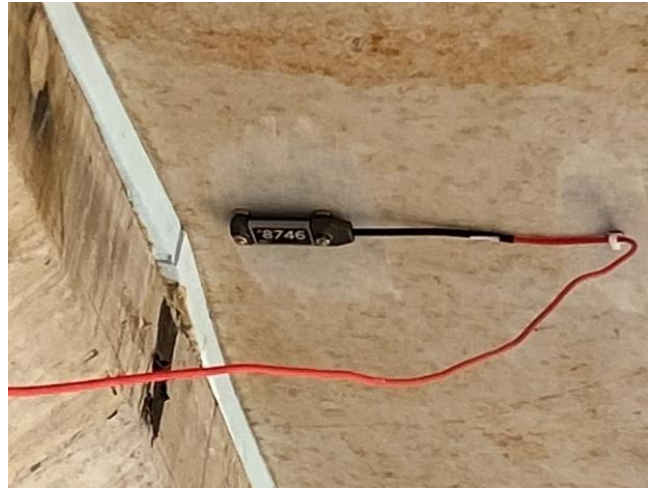
(b)
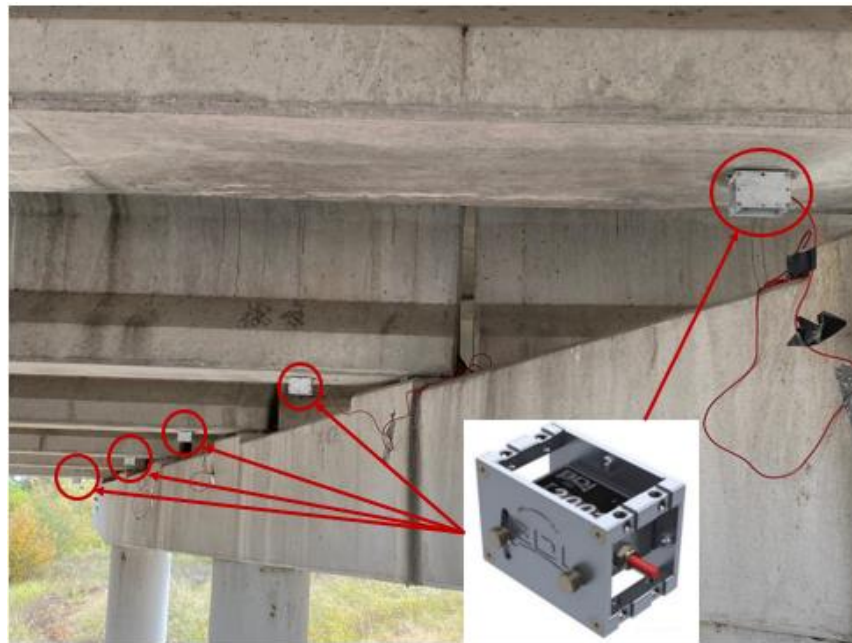
(c)

Figure 4-10 Attached sensors: (a) Strain gages on girder surface; (b) Strain gages near construction joint at girder C; (c) Tiltmeters on girder ends

4.3 Las Lomas Bridge Load Testing

The objective of the load test was to evaluate the composite action between girders and the composite concrete deck, to find the capacity of the bridge decks including the replaced EB bridge deck, and to conduct load rating. The acquired test data also helped to verify the accuracy of the proposed numerical model. Typical load test consists of multiple major parts. Among these parts are testing vehicles and loading paths. As the loading paths were different between the previous and follow-up EB load tests, Load paths were divided into two phases, Phases 1 and 2, respectively. The following subsections cover the testing vehicles and loading paths with more details.

4.3.1 Testing Vehicles

Two fully loaded dump trucks, Trucks A and B, were used to apply the live load on the bridge deck. The TxDOT Area Office provided the trucks, which were then operated by a contractor hired by the office. Figure 4-11(a) shows the distance between the front and first rear wheel axles as well as the distance between the two rear wheel axles of truck A for the previous and follow-up tests after the deck replacement. For the sake of previous EB result comparisons, the truck weight in the follow-up EB load test almost matched the previous test. The two trucks were pre-weighted before the load test to check whether the applied load was sufficient. Figure 4-11(b) shows the dimensions of Truck A used in the WB load test. Table 4-2 shows the weights of each truck axle. The static load test took around 10 seconds to finish since span 2 has a length of 70 ft. and the static speed was around 5 mph, whereas the dynamic test took around 1.2 seconds to finish the test per load path.
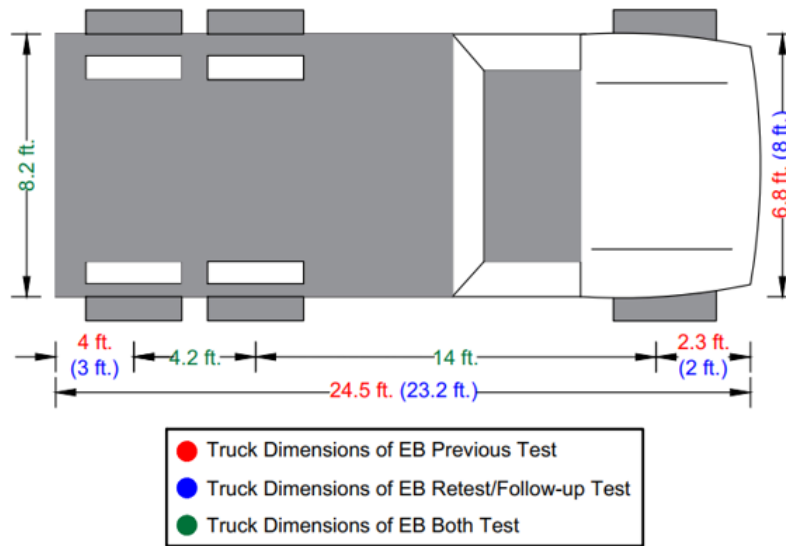
(a)
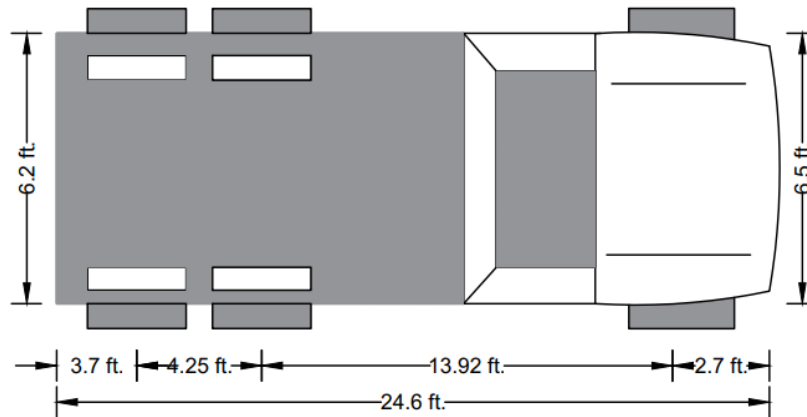
(b)

Figure 4-11 Dimensions of Truck A: (a) EB- previous and follow-up load tests; (b) WB load test

Table 4-2: Truck axle weights of Las Lomas Bridge

| Weights | Las Lomas Bridge | | | | | |
| | WB-Previous Test | | EB-Previous Test | | EB-Follow-up Test | |
	Truck A (kip)	Truck B (kip)	Truck A (kip)	Truck B (kip)	Truck A (kip)	Truck B (kip)
Gross vehicle weight (GVW)	52.9	52.4	52.3	50.9	54.72	54.06
Axle 1 (Front)	12.1	12.1	12.4	12.0	12.97	12.81
Axle 2 (Middle)	22.0	20.3	20.4	20.3	21.34	21.1
Axle 3 (Rear)	18.8	20.0	19.5	18.6	20.4	20.15

4.3.2 Loading Paths

Before conducting every load test, the necessary truck paths on the bridge decks were marked with spray paint. The selection of truck paths relied on two objectives: (1) find the bridge maximum strain and rotational responses; and (2) collect more useful data about bridge performance. For the two objectives, sensors were installed on each girder. Therefore, the marked truck paths were directly located on top of each girder. Truck drivers were informed that at least one of the truck tires should be driven on top of each path because the truck width did not match the girder spacing.

4.3.2.1 Phase 1: Original EB and WB Decks

Different load test scenarios (static and stop location load testing) were considered. Static load test consists of various number of load cases or paths [Figures 4-12(a) and 4-12(b)]. The load test of the previous EB and WB bridge decks had four and three static paths, respectively. The static load test, commonly known as the crawl load test, was conducted utilizing a single and maximum weighted truck moving at a speed of less than 5 mph, while the stop location test used two trucks that stopped for around 25 seconds at the mid-span of bridge girder, according to AASHTO (2020). The objective of stop location is to generate the maximum moments in the girders, as they are simply supported.
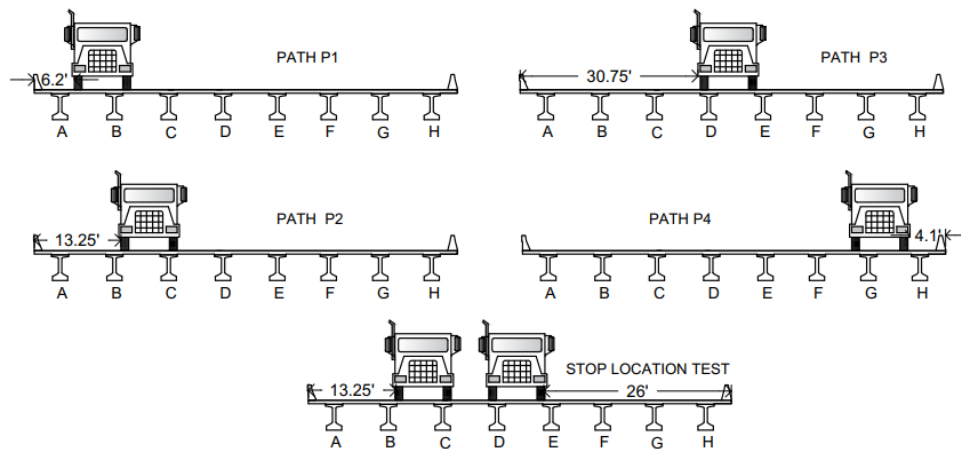
(a)
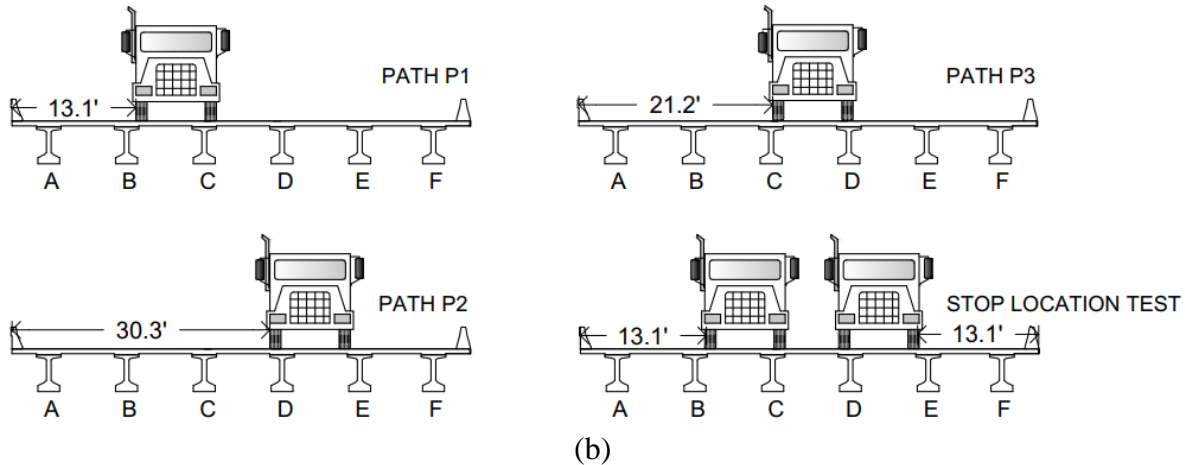
Figure 4-12 Load test paths of previous tests: (a) EB; (b) WB

4.3.2.2 Phase 2: Replaced EB Deck

The follow-up load test involved a comprehensive bridge investigation to obtain insight into bridge performance in terms of composite action and load carrying capacity. A dynamic load test and additional static load test paths were included, when compared to phase 1 to reasonably evaluate the responses of all the girders. Stop location test was the same as in phase 1. As a result, the replaced deck test had six static paths and one dynamic path. The dynamic test was conducted using the same procedure as the crawl test utilizing the heavier truck A but at a speed of 40 mph. The proposed load paths in a follow-up test are depicted in Figures 4-13(a) and 4-13(b).

(a)

(b)
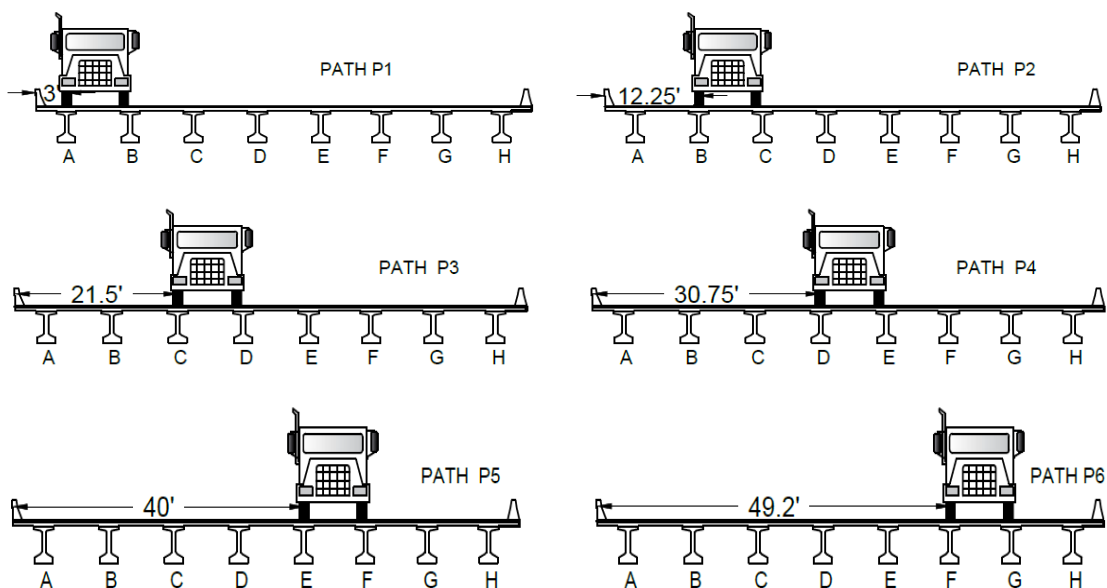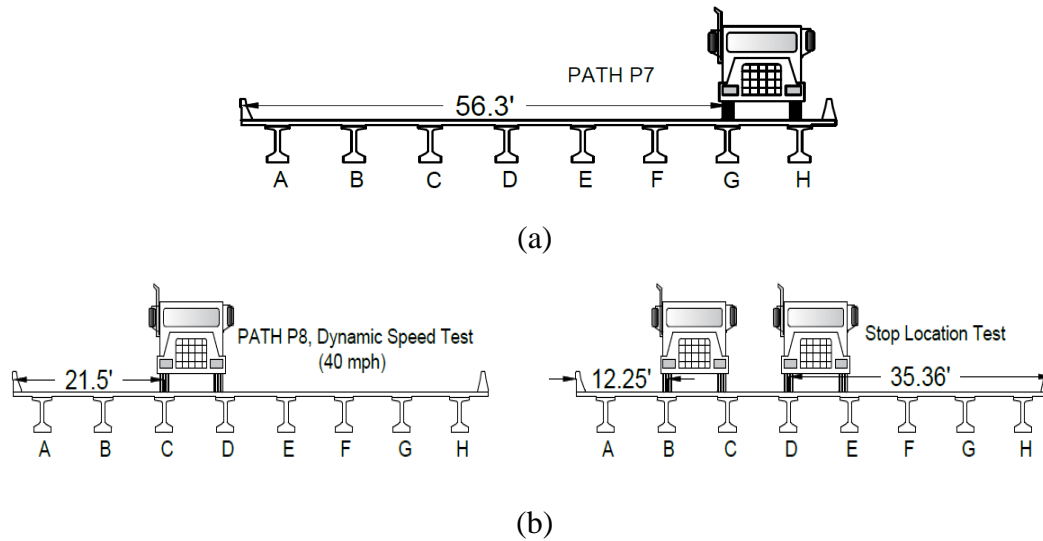
Figure 4-13 Follow-up test paths: (a) Crawl speed; (b) Dynamic and stop location

4.3.3 Load Test Day

Figures 4-14(a) and 4-14(b) show the typical two-truck and one-truck configuration during the load test, respectively. Each load test lasted for 2 to 2.5 hours after the necessary sensor connections were completed. Additionally, the load tests were held from 10:00 pm to 12:30 am due to high traffic on IH-20 during the daytime. The load testing also involved rolling traffic closure as the bridge lanes were closed for 15 minutes, and then the traffic was resumed for approximately 15-20 minutes. After the load test was complete, the reusable sensors were removed from the girder surfaces with the assistance of a man-lift.

(a)

56

(b)

Figure 4-14: Typical dump trucks

4.4 Las Lomas Bridge NDE Scanning

The NDE scanning used on bridge decks involved two NDE devices that can accurately assess the deck condition. NDE alone may only be used for bridge deck, but girder performance should be obtained from load test data, as girders are usually not prone to corrosion and delamination. Moreover, the NDE equipment consists of GPR and IE. The GPR and IE devices are discussed in more details in subsections 4.4.1 and 4.4.2, while subsection 4.4.3 summarizes the general deck scanning procedures. Both devices were used scan WB and EB bridges. As the EB bridge deck was recently replaced, EB bridge deck was scanned twice before and after deck replacement. Therefore, Phase 1 includes all NDE scanning performed for original EB and WB bridge decks, whereas phase 2 includes the follow-up deck scanning of the EB replaced deck.

4.4.1 Ground Penetrating Radar (GPR)

Ground penetrating radar (GPR) is a high-end geophysical device that uses radar pulses to produce images of the rebar subsurface. In a bridge evaluation project, GPR is used to detect rebars, concrete covers, and not delamination since multiple factors affect the detectability of delamination by GPR. First, the strength of waveform reflected from concrete delamination is affected mainly by the thickness of the delamination, the material within the tested concrete.

Second, the depth of delamination and its location relative to adjacent steel bars might impact its detectability in GPR images. Antennae with higher frequency (e.g., 2.6 GHz) are used for low-depth analysis (0-12 in.), while lower frequency (e.g., 270 MHz) are used for higher depth evaluation (0-18 ft.). Figures 4-15(a) and 4-15(b) show a cart mounted GPR and 2.6 GHz antenna as a hand scanner, respectively.

(a)   (b)

Figure 4-15 Ground penetrating radar (GPR): (a) Cart-mounted GPR; (b) 2.6 GHz antenna

➢ **Phase 1**

GSSI SIR-30 GPR was utilized to scan the bridge deck. A truck-mounted GPR used multiple-frequency antennae: two 2.6 GHz [Figure 4-16] and one 400 MHz. These antennae cover a range of depths. The scans using truck-mounted GPR were performed at a speed of less than 5 mph, which saved a significant amount of time compared to a tri-wheel push-cart GPR with a single antenna. As the original EB and WB bridge deck experienced a localized CIP deck failure, the affected deck area was patched. As a result, to increase the accuracy of the scan, the tri-wheel [Figure 4-15(a)] was only used on the patched areas in both bridge decks. A square scanning grid was additionally used for GPR, and the grid was spaced at 2.5 ft. for the full bridge deck (Figure 4-16), with the exception of the patched area which was spaced at 1.0 ft.
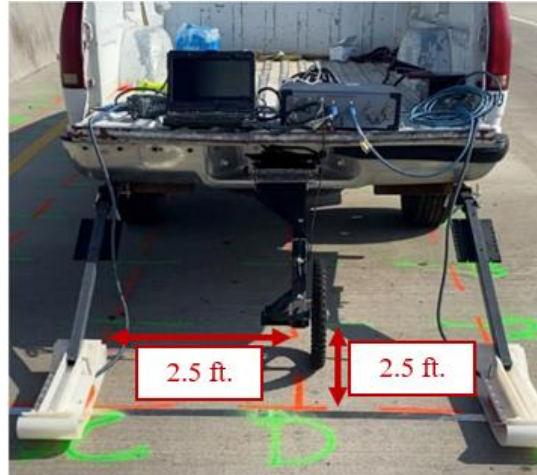
Figure 4-16: Truck-mounted GRP

The GPR scanning was performed in both bridges towards the direction of traffic. Figures 4-17(a) and 4-17(b) show the scanning grid of the original bridge decks.
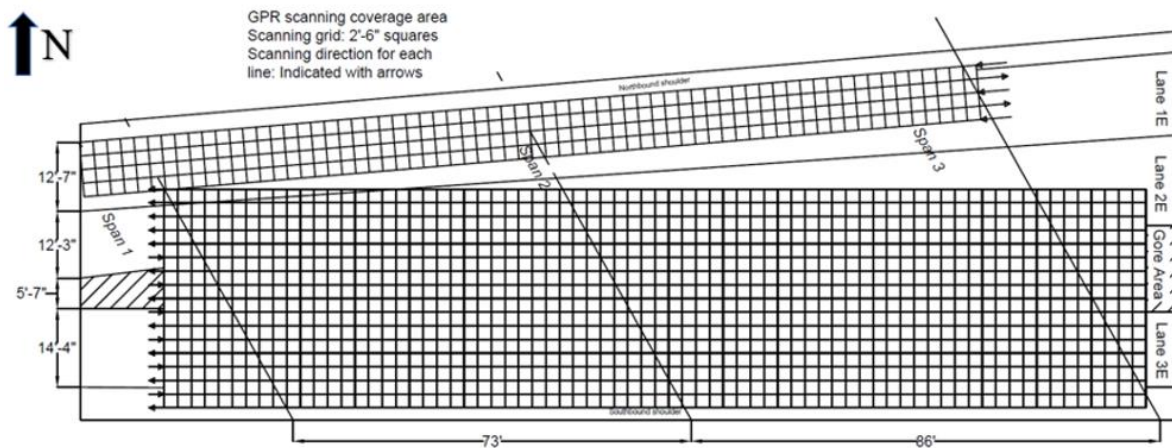
(a)
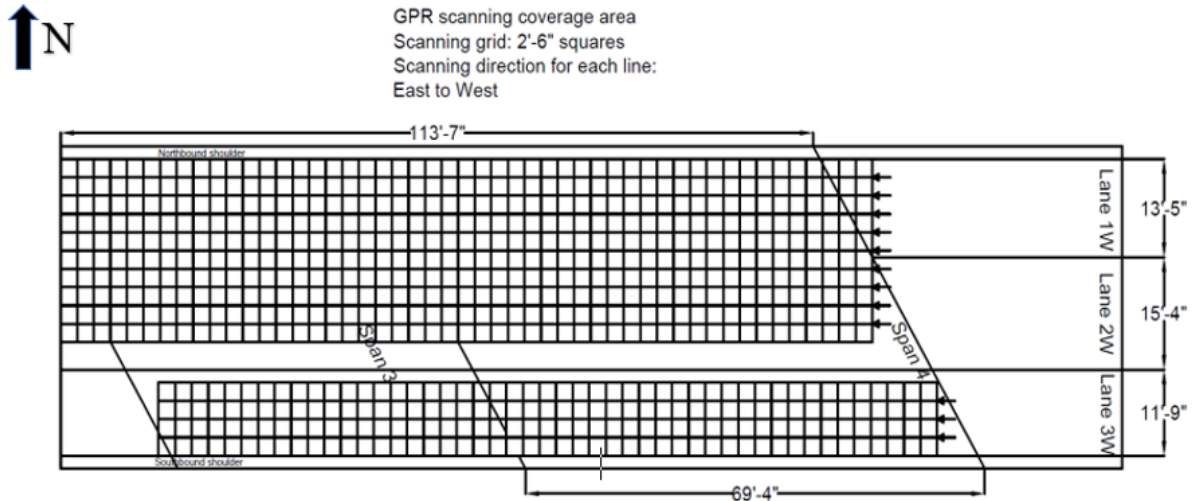
(b)

Figure 4-17 GPR scanning grids: (a) EB bridge; (b) WB bridge

➢ **Phase 2**

Only truck-mounted GPR with two antennae with high frequency (2.6 GHz) was used as the bridge deck was recently constructed in 2019. Figure 4-18 shows the follow-up scanning grid of the EB bridge. The GPR scan was performed on multiple paths and involved all bridge lanes, such as path A-C, path B-D, and path C-E (Figures 4-16 and 4-18). Figure 4-19 shows the actual field scanning grid used for GPR. These grids were used during the GPR scans. Gridlines parallel to the direction of traffic and denoted in orange color were utilized for the GPR scanning (Figures 4-19).
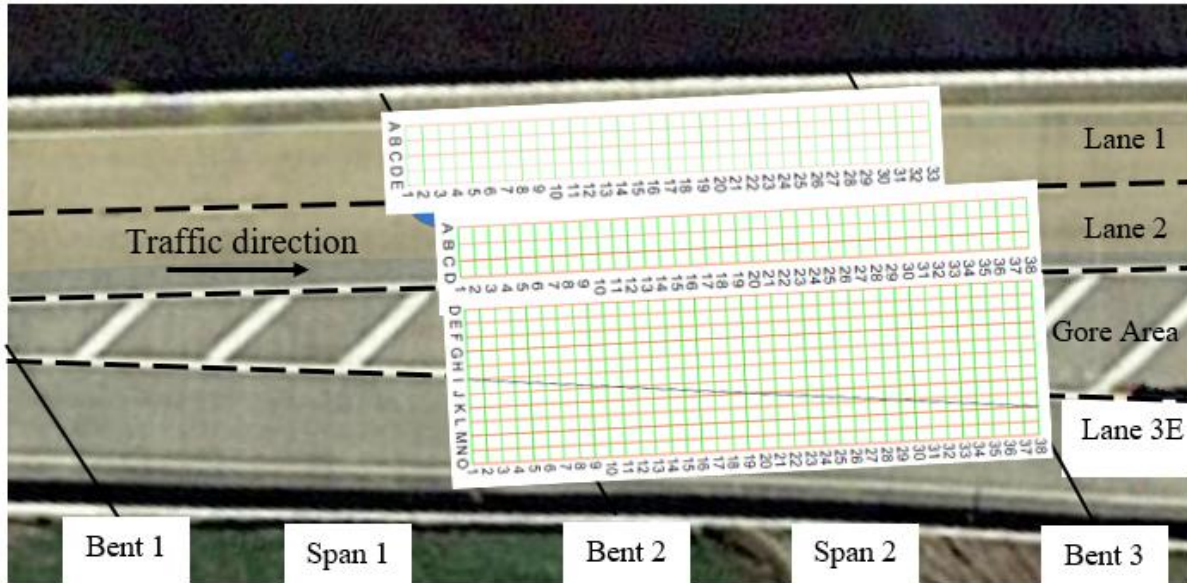
Figure 4- 18: Follow-up GPR scanning grid

Figure 4-19: GPR and IE scanning grids

4.4.2 Impact Echo (IE)

The IE is commonly used to determine the deck delamination condition as well as any voids, honeycombs, or cracks on the deck surface. The IE device additionally determines the

thickness based on Impact Echo (IE) principle. The IE creates an impact at a certain point on the deck surface. At each specific point, the device captures two impact/data and then the average between these two-impact data appears on the IE monitor, and the user has the option to either accept or reject the data if it is within the tested deck thickness or far away from the anticipated deck thickness, respectively. The created impact reflects if delamination presents within the concrete deck thickness. The IE device is only scanned one point at a time and is not a continuous scan as is the case with the GPR device. The IE scanned points are identified as the intersection of the longitudinal and transverse grids, which are denoted in orange and green colors, respectively (Figure 4-19). The IE scanning followed ASTM Standard C1383, and scanning was performed at multiple points on the bridge deck. Figures 4-20(a) and 4-20(b) show the IE configuration.

(a)   (b)

Figure 4-20 IE device: (a) NDE 360 platform; (b) Hand-held

The IE scanning was performed in both bridges. Figures 4-21(a) and 4-21(b) show the scanning grids of the original bridge decks. The replaced deck used the same scanning approach as the original bridge (Figure 4-19).
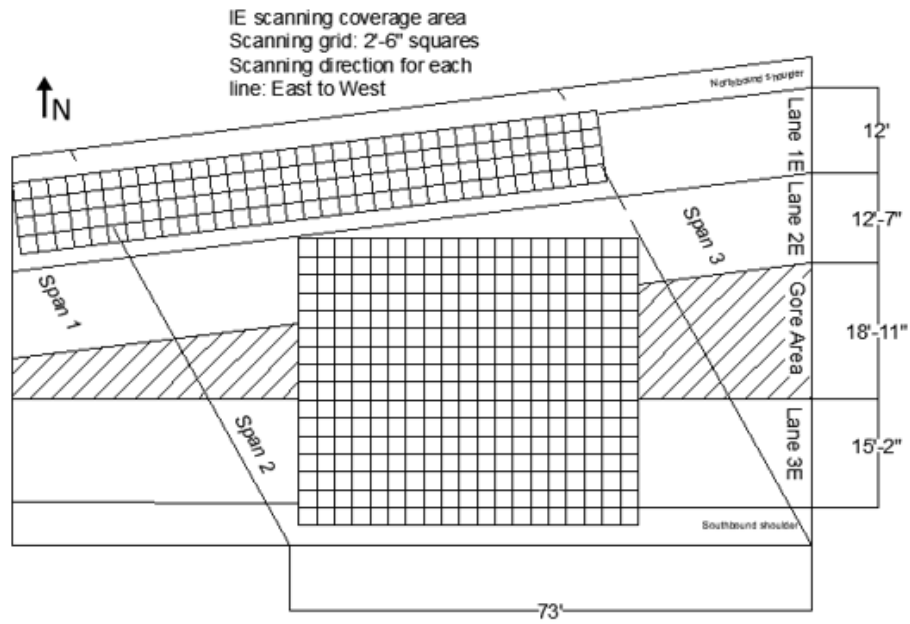
(a)
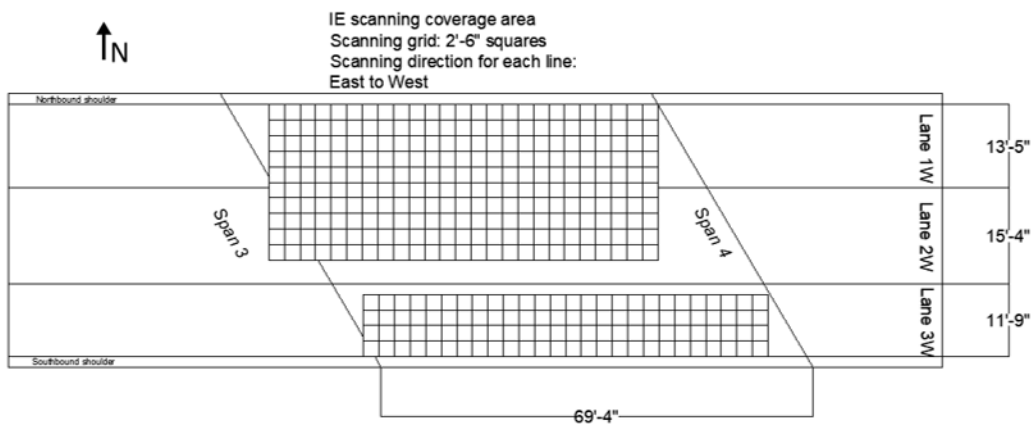
(b)

Figure 4-21 IE scanning grids: (a) EB bridge; and (b) WB bridge

4.4.3 NDE Scanning

The NDE scanning was conducted from 9:00 am to 3:00 pm over a five-day period. Lane

closure was provided on the top of spans 2 and 4 to facilitate the work.

Chapter 5

FINITE ELEMENT MODELING (FEM)

Chapter 5 only covered the initial and developed FE model of the previous EB bridge deck but included modeling of all the structural elements, concrete, mild reinforcing steel, prestressing strands, prestress losses, and loading conditions. Chapter 5 also involved the initial material properties as well as all the assumptions made to model each element in FE.

5.1 Initial Numerical Modeling

The initial FEM was modeled using ABAQUS (2018) and involved creating a 3D geometric model of span 2, defining material properties, interactions, and boundary conditions. Figure 5-1 shows the model view of the targeted span. The model employed 8-node linear brick elements (C3D8) for the concrete and 2-node linear truss elements (B21) for the reinforcements and prestressing strands, as these can carry only tensile forces. Moreover, simple support boundary condition was assumed for all of the girders. The reinforcements and prestressing strands were then embedded in the concrete, using the embedded region constraint option. The reinforcements were the embedded elements, and the girders, PCPs, and CIP deck concrete were the host elements. The interactions between the PCPs, CIP deck, bedding strips, and girders were initially simulated using a tie constraint option. The bedding strips, modeled in FE, have dimensions of 1 in. height and 2 in. width, so the total deck thickness above the girder flange is 9.25 in above the girder flange.
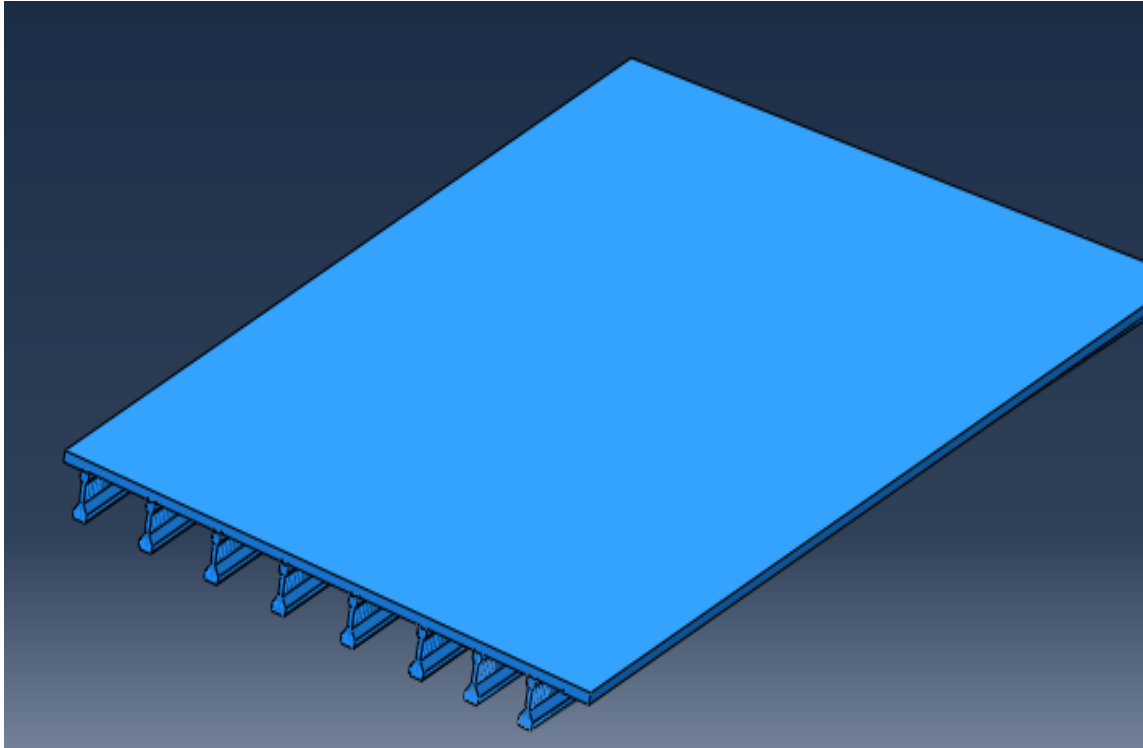
Figure 5-1 FEM views of span 2 EB bridge

5.1.1 Type C Girder

Girders A through F, G, and H include prestressing and depressed strands, as specified in Table 3-2. Two girders, G and H, are flared where the girder spacing varies along the length of the girders. Figures 5-2(a) and 5-2(b) show the FEM views of a girder and embedded reinforcement, respectively. The material properties for Type C girders A-H, as provided to the FE, are mentioned in Table 3-2. Figures 5-3(a-c) show the model views of the prestressing strand profile in FE for each girder, represented with small black dots. Figure 5-3(d) displays the cross section of the Type C girder showing the strand profile. Additionally, the height of the Type C girder cross section is divided into multiple strand rows spaced at 2 in. The width of the Type C girder, shown in Figure 5-3(d), includes nine spacings in one row at the bottom, which fits up to 10 prestressing strands. The two spacings in the middle, lettered A-A, were assigned for the depressed prestressing strands.

65
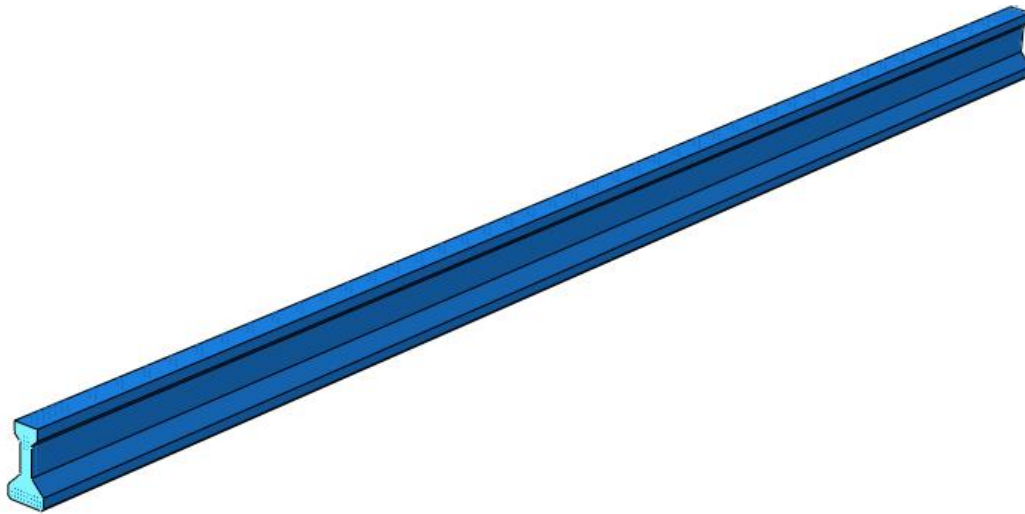
(a)
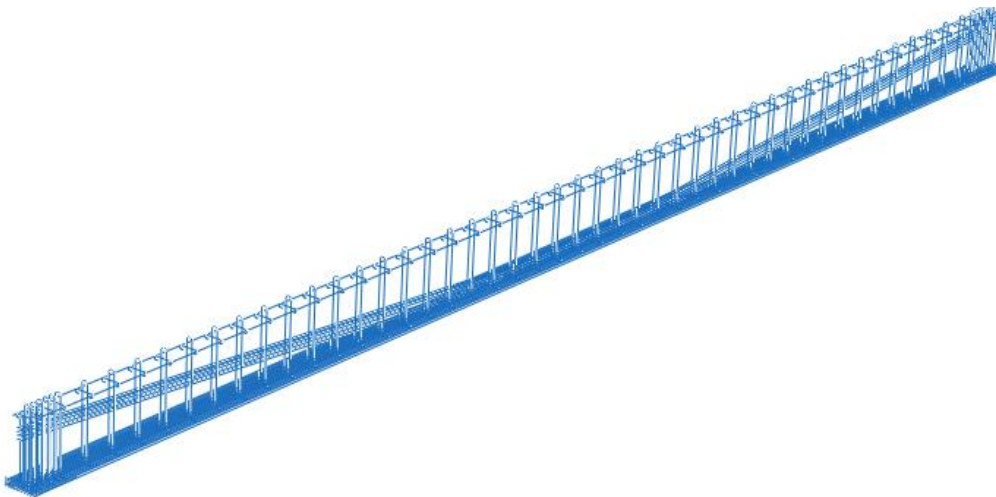
(b)

Figure 5-2 FEM view: (a) Type C girder; (b) Embedded Reinforcements
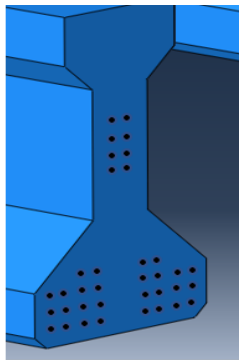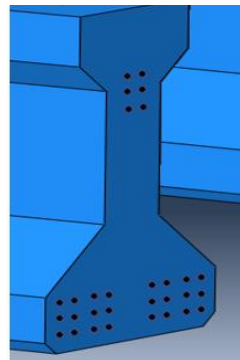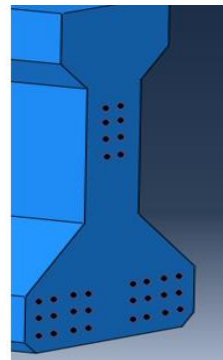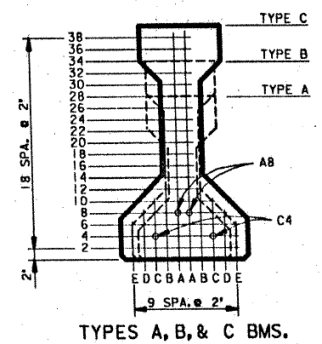
| (a) | (b) | (c) | (d) |

Figure 5-3 FEM view: (a) Girder A-F;(b) Girder G;(c) Girder H; (d) Typical cross-section

5.1.2 Precast Concrete Panels (PCPs)

Span 2 consists of 26 PCPs that are 4 in. thick. Figure 5-4(a) shows the PCP detail plan of the targeted span. Figure 5-4(b) shows the modeled PCPs placed on Type C girders. The PCPs were placed away from the end of the girders on both sides, as shown in Figures 5-4(a) and 5-4(b). Typical precast panel reinforcement includes prestressing strands and No. 3 steel rebars placed in the transverse and longitudinal directions, respectively, which are set at the mid-depth of the PCPs, as shown in Figures 5-5(a) and 5-5(b). The prestressing strands were then extended 3 in. on both sides into the cast-in-place (CIP) concrete portion, as demonstrated in Figure 5-5(a). Table 5-1 shows the PCP material properties used in the FE.
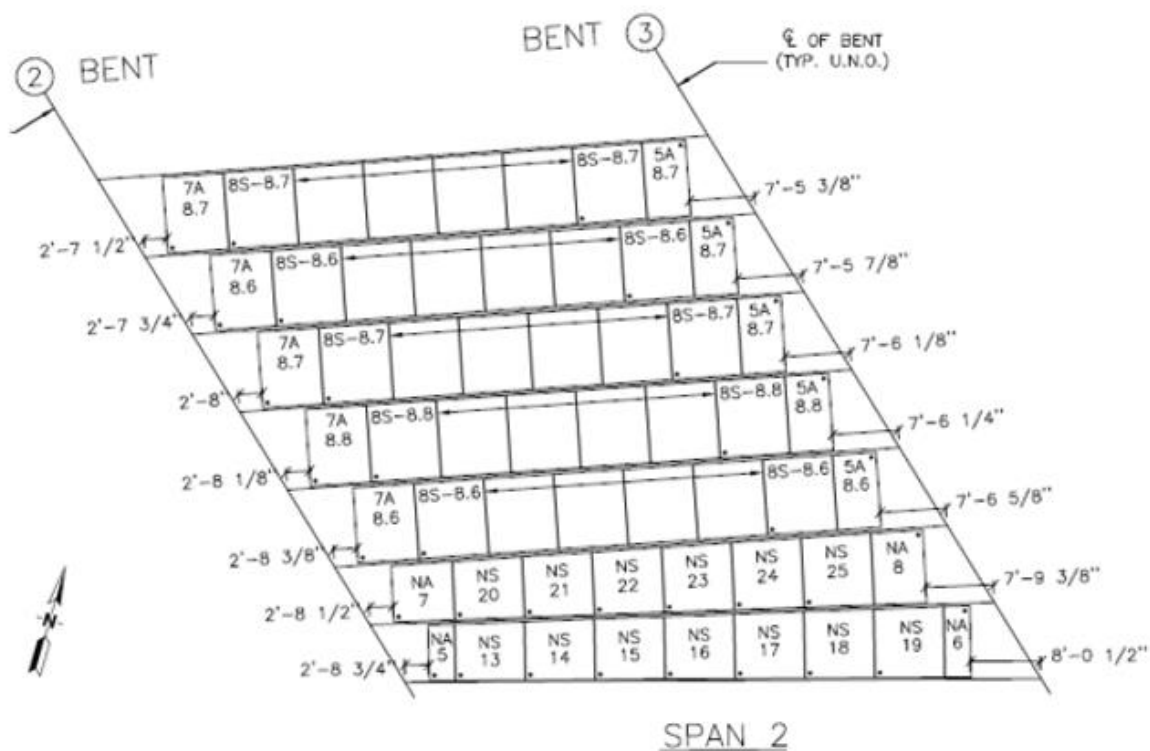
(a)
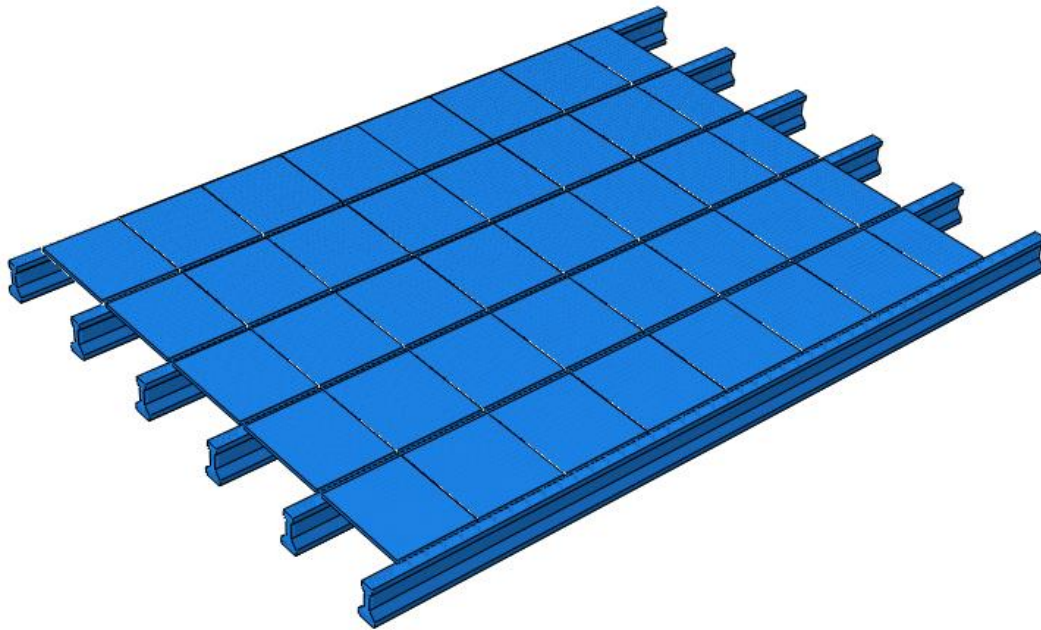
(b)

Figure 5-4 PCP details of Span 2 EB bridge: (a) Plan; (b) Model view
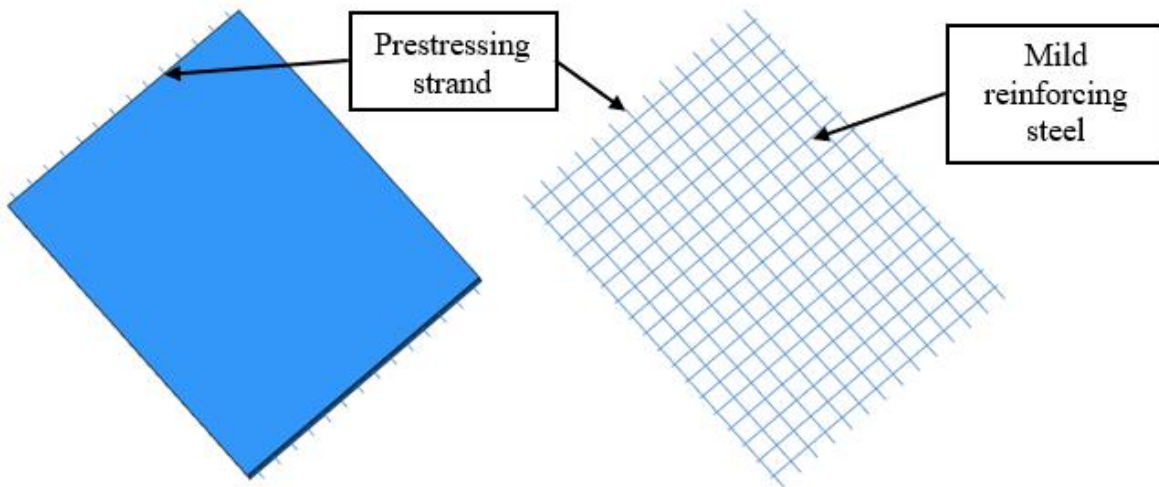
(a)   (b)

Figure 5-5 FEM views: (a) PCP; (b) Reinforcements in PCP

Table 5-1: Material properties of PCPs

Properties	Value
Release compressive strength (f_c') (ksi)	3.5
Compressive strength (28 days) (f_c') (ksi)	5
Strand diameter size (in.)	0.375

5.1.3 Cast-In-Place (CIP) Deck

The CIP concrete deck and the distances next to bents 2 and 3, shown in Figures 5-4(a) and 5-4(b), were modeled in FEM. The extruded option from ABAQUS was used to model these distances, shown in Figure 5-6 with the red arrow, as a part of CIP deck. Figure 5-7(a) shows the typical slab details for spans 2 and 3. No. 4 and No. 5 steel rebars, in the transverse and longitudinal direction of traffic, respectively, were placed at 2 in. from the top surface of CIP and modeled in FE, as shown in Figure 5-7(b). The overhang reinforcement was placed at different depths, according to the TxDOT drawing, as shown in Figure 5-8. Figure 5-7(b) provides a close up view of the overhang reinforcement, which is highlighted in red.
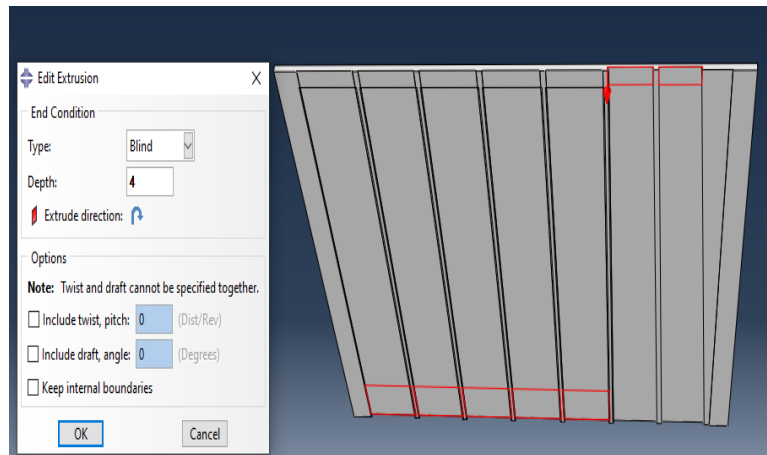
Figure 5-6: Extruded option in FE

(a)

(b)
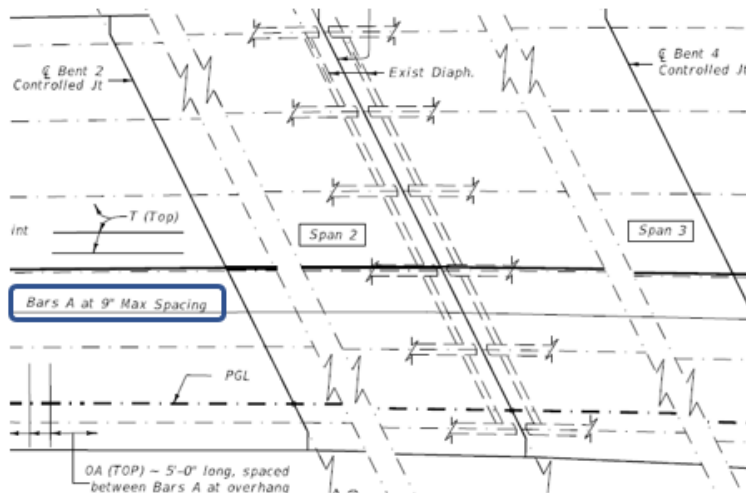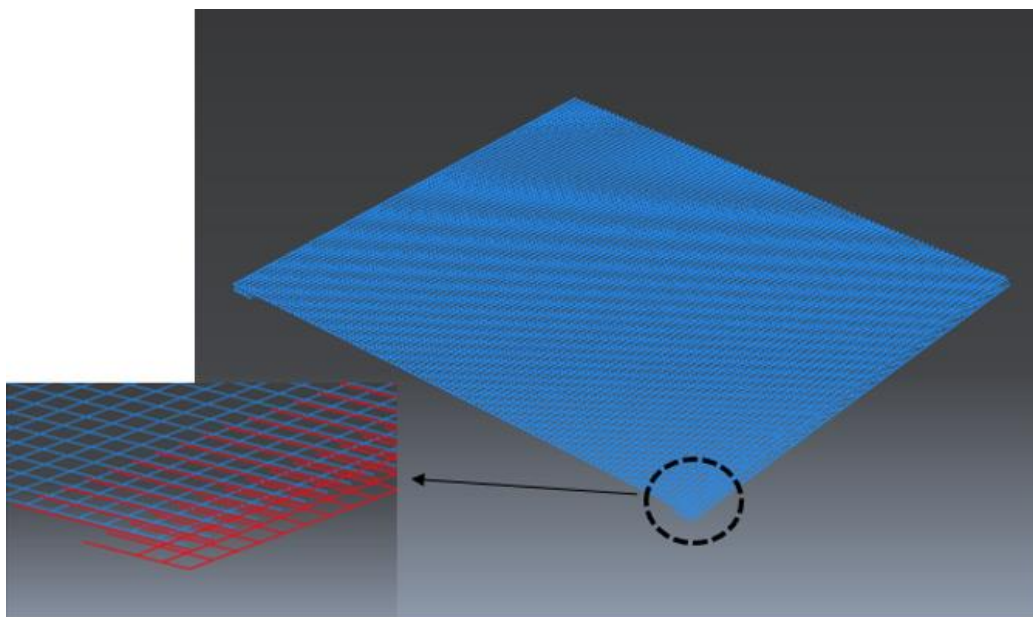
Figure 5-7 Span 2 EB bridge: (a) Slab details; (b) Reinforcement in the CIP deck (model view)

Figure 5-8: Typical cross section of the replaced deck at overhang location
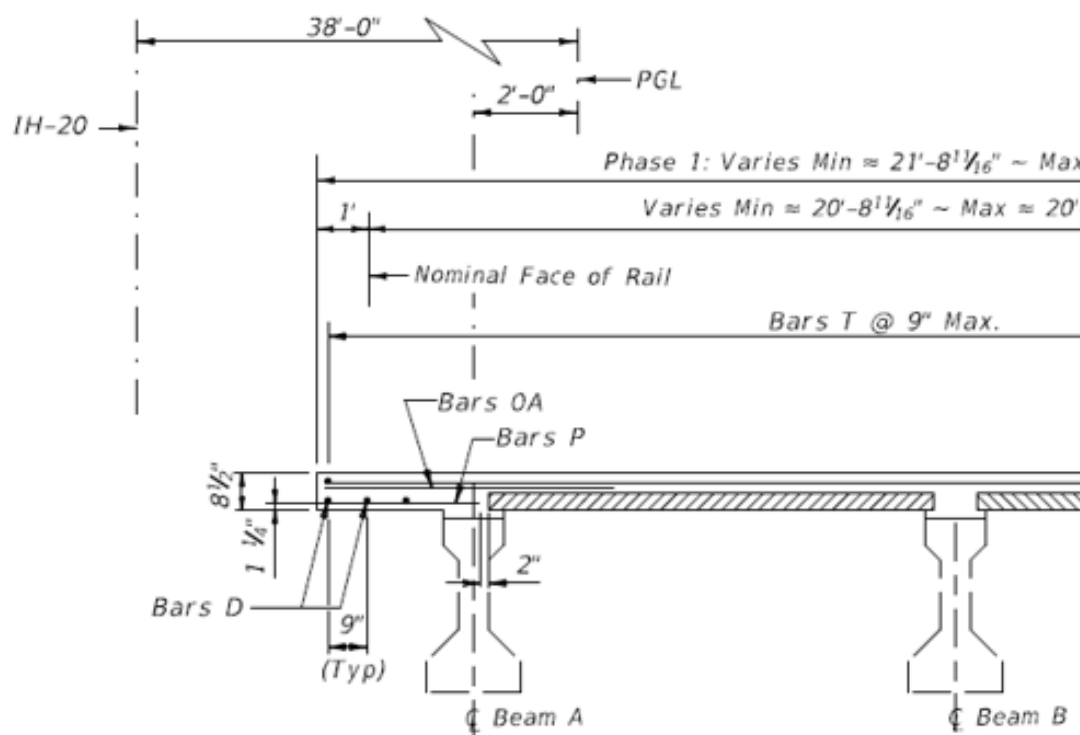
5.1.4 EB Bridge Diaphragm

EB bridge diaphragms in span 2 were modeled according to the as-built drawing. The diaphragms also include a steel channel and steel angle. The steel angle is used to connect the steel channel with girders. Figure 5-9 shows the drawing of the steel channel and angle. Steel channel and angle, measured at C12 x 20.7 and L6 in. x 4 in. x ½ in. x 12 in., were used as specified for the Type C girder. Figures 5-10(a) and 5-10(b) show the modeled diaphragm parts in FE. Two of the diaphragm's nuts located between girders B and C were missing [Figure 5-10(c)]. Figure 5-10(d) shows the bottom view of the span 2 model, including the missing diaphragm in ABAQUS. Table 5-2 shows the physical properties of the steel channel and angle.
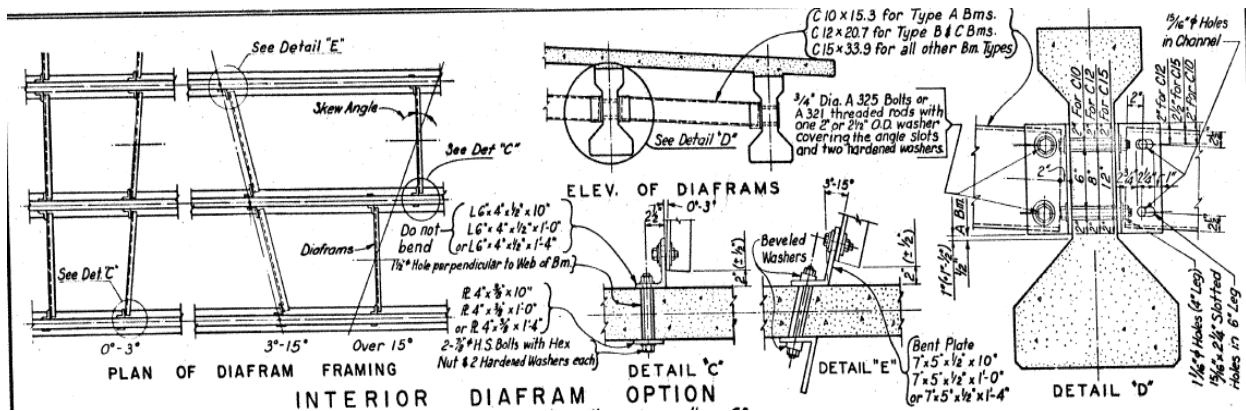
Figure 5-9: Steel channel and angle specifications
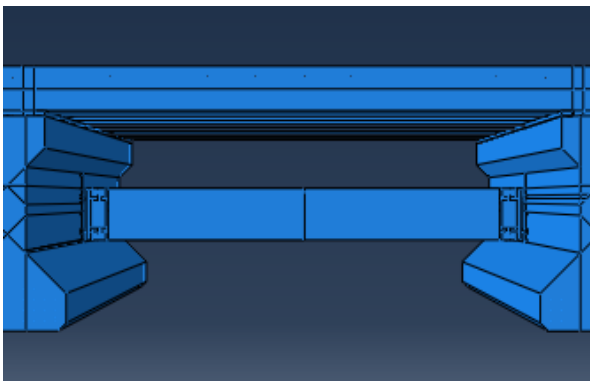
(a)
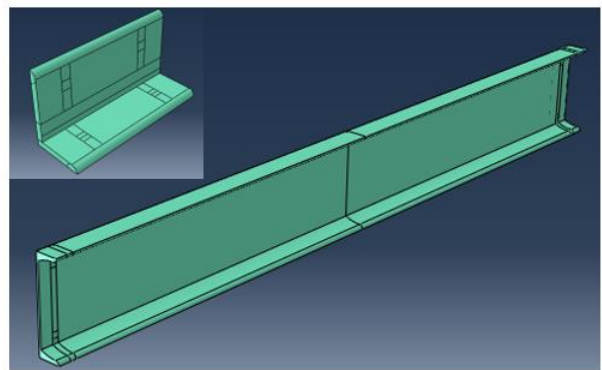
(b)
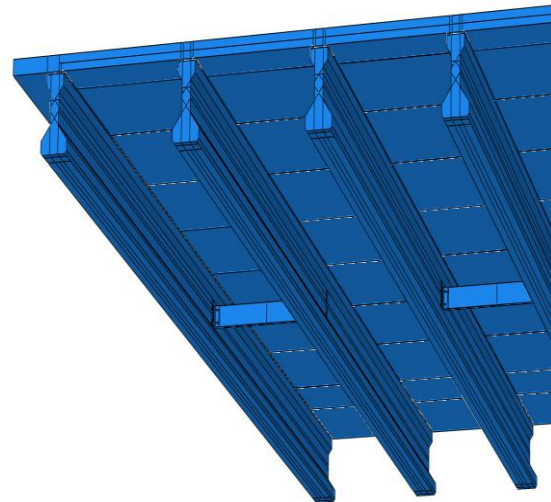
| (c) | (d) |

Figure 5-10: Modeled diaphragm components in FE

Table 5-2: Physical properties of the diaphragm components

Steel components	Height (in.)	Width (in.)	Flange thickness (in.)	Web thickness (in.)	Thickness (in.)	Area (in²)
Channel	12	2.94	0.501	0.282	NA	6.09
Angle	6	4	NA	NA	0.5	4.75

5.2 Concrete and Steel Properties

The non-linear concrete and steel behaviors were previously mentioned in sections 2.5.1, and 2.5.2, respectively, and the initial parameters of concrete damage plasticity used in FE are shown in Table 5-3. Table 5-4 shows the elastic material properties of the concrete and mild reinforcing steel from as-built drawings for all of the structural components of the span 2. The classic elastic perfectly plastic material model was employed for the steel reinforcements.

Table 5-3: Concrete-Damaged Plasticity Parameters

Property	Value
Dilation angle	36°
Flow potential eccentricity	0
Ratio of initial equiaxial to initial uniaxial compressive yield stresses (f_{bo}/f_{co})	1.16
Ratio of the second stress invariant on the tensile meridian to that on the compressive meridian (K_c)	0.667
Viscosity parameter (μ)	0.001

Table 5-4: Elastic properties of concrete and steel from as-built drawing

Material Type	Elastic Property	Value
Concrete	Modulus of Elasticity (E) (ksi)	(3823.68) for CIP deck (4341.0) for Girder (A-F) (4070.61) for Girder (G) (4137.90) for Girder (H) (4030.51) for PCPs
	Poisson's Ratio (ν)	0.15
Steel	Modulus of Elasticity (E) (ksi)	29000
	Poisson's Ratio (ν)	0.3

Concrete compressive strength (f_{cm}) is determined by following a standard test manual, which classifies strength at an age of 28 days. At this age, the desired strength from the as-built drawing is usually achieved. However, concrete continues to gain strength over time. This increase in concrete compressive strength leads to an increase in other material mechanical characteristics (tensile strength, modulus of elasticity, etc.). Therefore, it is critical to consider the change in concrete strength in FE. The AASHTO LRFD (2020) does not address these increments (Corven, 2016). The Comite Euro-Intermationale du Beton/Federation International de la Precontrainte (CEB-FIP) Model Code (1990) (FHWA, 2016) provides the following relationship for the variation in concrete compressive strength over time (Equations 5-1 and 5-2):

$$f_{cm}(t) = \beta_{cc}(t)f_{cm} \tag{5-1}$$

$$\beta_{cc}(t) = exp\left\{s\left[1 - \left(\frac{28}{\frac{t}{t1}}\right)^{\frac{1}{2}}\right]\right\} \tag{5-2}$$

Where:

f $_{cm}$ = 28-day concrete compressive strength

f $_{cm}$ (t) = Concrete compressive strength at time t

β_{cc} (t) = Time-dependent coefficient dependent on the age of concrete

t = Age of concrete at which f $_{cm}$ (t) is computed (days)

$t_1 = 1$ day

s = Cement rate of hardening coefficient

s = 0.20 for rapid-hardening high-strength concretes, 0.25 for normal and rapid-hardening cements, and 0.38 for slow-hardening cements.

Figure 5-11 shows a plot of the ratio of concrete compressive strength to 28-day compressive strength (β_{cc}) for normal hardening cement.
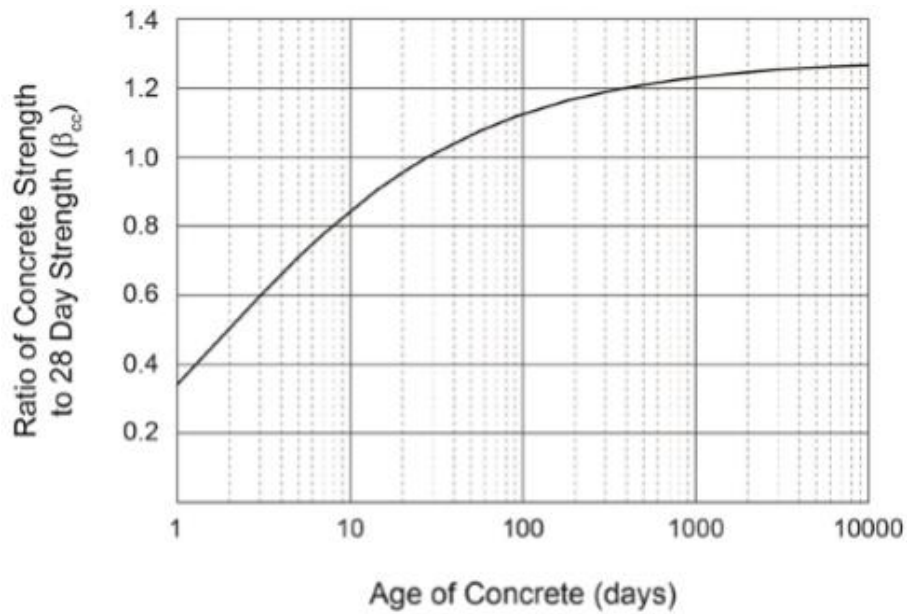
Figure 5-11: Concrete compressive strength with time

The modulus of elasticity (E_{ci}) equation described in AASHTO LRFD (2020) is only used to estimate the 28-day Modulus of Elasticity. As a result, the variation in modulus of elasticity with time is predicted by CEB-FIP Equations 5-3 and 5-4.

$$E_{ci}(t) = \beta_E(t)E_{ci} \tag{5-3}$$

$$\beta_E(t) = \left(\beta_{cc}(t)\right)^{\frac{1}{2}} \tag{5-4}$$

Where:

E_{ci} = Modulus of elasticity of concrete at an age of 28 days

E_{ci} (t) = Modulus of elasticity at time t

β_E(t) = Coefficient depending on the age of concrete at t (days) = 1.13 days

β_{cc} = Coefficient defined by equation 2 = 1.3

Figure 5-12 shows a plot of the ratio of concrete modulus of elasticity to 28-day compressive strength (β_E) for normal hardening cement.
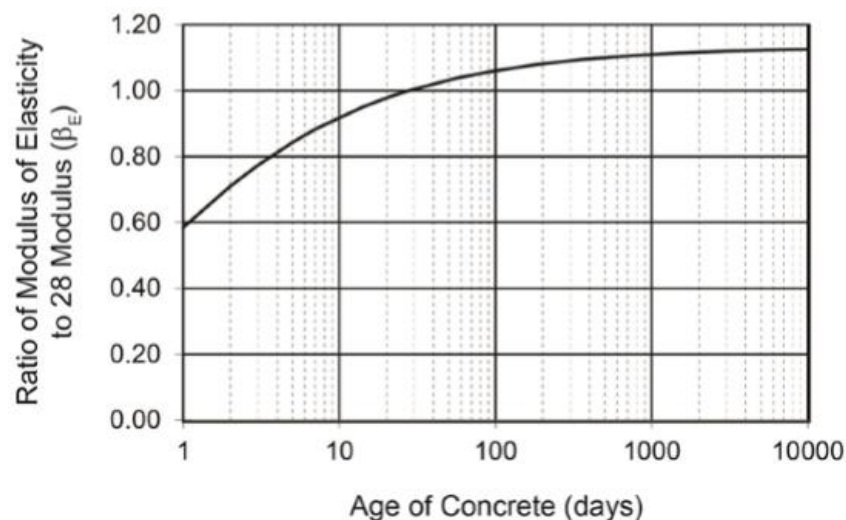
Figure 5- 12: Concrete modulus of elasticity with time

The increased compressive strength and modulus of elasticity of the girders, panels, and the deck of the EB bridge were calculated and are shown in Table 5-5. These concrete material properties were initially incorporated in FEM.

Table 5-5: Compressive strength and modulus of elasticity of the elements of EB bridge

Superstructure elements		f_{cm} from the as-built drawing (ksi)	f_{cm} from CEB-FIP (ksi)	E_{ci} from the as-built drawing (ksi)	E_{ci} from CEB-FIP (ksi)
Girders	A-F	5.8	7.4	4341	4888
	G	5.1	6.5	4070.6	4583.5
	H	5.3	6.7	4137.9	4659.3
Panels		5	6.3	4030.5	4538.4
Deck		4.5	5.7	3823.7	4305.5

5.3 Prestressing Strands

The diameter of the prestressing strands of the girders and PCPs was specified in section 3.1.1. Table 5-6 shows the corresponding jacking, yield, and ultimate stress and strain values. The strain corresponding to each state of stress was calculated using Equation 5-5 (Corven 2016).

Table 5-6: Stress and strain for prestressing strands

	Stress (ksi)	**Strain (in/in)**
Jacking	202.6 (Girders)	0.00711 (Girders)
	169.4 (PCPs)	0.00594 (PCPs)
Yielding	245.1	0.0086
Ultimate	270	0.06

$$\text{For } \varepsilon_{ps} \leq 0.0086: \quad f_{ps} = 28500 * \varepsilon_{ps} \ (\text{ksi})$$

$$\text{For } \varepsilon_{ps} > 0.0086: \quad f_{ps} = 270 - \frac{0.04}{\varepsilon_{ps} - 0.007} \ (\text{ksi}) \tag{5-5}$$

Where:

f_{ps} = Average stress in prestressing steel at nominal resistance (ksi)

ε_{ps} = Strain of average stress in prestressing steel at nominal resistance

The prestressing force in the strand can be applied either as a temperature difference (Ren et al. 2015) or as a cohesive bond between the concrete and the strands (Abdelatif et al. 2015). In this case, the prestressing force was initially applied using the predefined field option in FEM, as the initial force was known. The initial stress option did not work due to an excessive camber of girder, so the temperature difference option was applied using Equation 5-6 (Ren et al. 2015).

$$C = -\frac{P}{c.E.A} \tag{5-6}$$

Where:

P= Prestressing force considering all losses

c= Co-efficient of linear expansion (1×10^{-5})

E= Modulus of elasticity of strands

A= Cross-sectional area of the strands

The final prestressing forces (P) of girder and PCPs should include all prestress losses. Section 5.3.1 illustrates the final prestressing force values and how the user inserts them using the temperature difference option in ABAQUS.

5.3.1 Prestressing Strand Losses

The loss of prestressing force in the girders and PCPs in FEM should be considered. Prestress losses are categorized into short- and long-term losses (AASHTO 2017). The former includes elastic shortening due to the initial compression of released force, while the latter involves time-independent losses, such as creep, shrinkage, and relaxtation. Total losses are the summation of both categories and are expressed in stress terms. Equation 5-7 shows the calculation of the short-term prestress loss; Equation 5-8 shows the calculation of the long-term prestress loss.

$$\Delta f_{PES} = \frac{A_{ps}\, f_{pi}\, (I_g + e_m^2 A_g) - e_m M_g A_g}{A_{ps}(I_g + e_m^2 A_g) + \frac{A_g I_g E_{ci}}{E_{ps}}} \tag{5-7}$$

Where:

Δf_{PES} = Prestress losses due to elastic shortening

A_{ps} = Area of prestressing strand

f_{pi} = Prestressing steel stress immediately prior to transfer

I_g = Moment of inertia of girder/panel

e_m = Eccentricity

A_g = Gross area of girder/deck

M_g = Mid-span moment due to self-weight

E_{ci} = Modulus of elasticity of concrete during release

E_{ps} = Modulus of elasticity of prestressing strand ($E_{ps} = 28{,}500$ ksi)

$$\Delta f_{PLT} = 10 \frac{A_{ps}\, f_{pi}}{A_g} \gamma_h \gamma_{st} + 12\, \gamma_h \gamma_{st} + \Delta f_{PR} \qquad (5\text{-}8)$$

Where:

Δf_{PLT} = Prestress losses due to creep, shrinkage, and relaxlation

A_{ps} = Area of prestressing strand

f_{pi} = Prestressing steel stress immediately prior to transfer

γ_h = Humidity factor ($\gamma_h = 1.7 - 0.01H$)

H = Average annual relative humidity in percentage

γ_{st} = Strength factor ($\gamma_{st} = \frac{5}{1+f'_{ci}}$)

f'_{ci} = Concrete strength during release

A_g = Gross area of girder/deck

Δf_{PR} = 2.5 ksi for low relaxation, 10 ksi for stress relieved

The total losses in the girders and PCPs were 49.66 and 27.46 ksi, respectively; thus, the applied stress in FEM was 152.94 and 141.94 ksi, respectviely, as shown in Figures 5-13(a) and 5-13(b). Appendix C shows a summary of the calculated prestressing losses of girders.
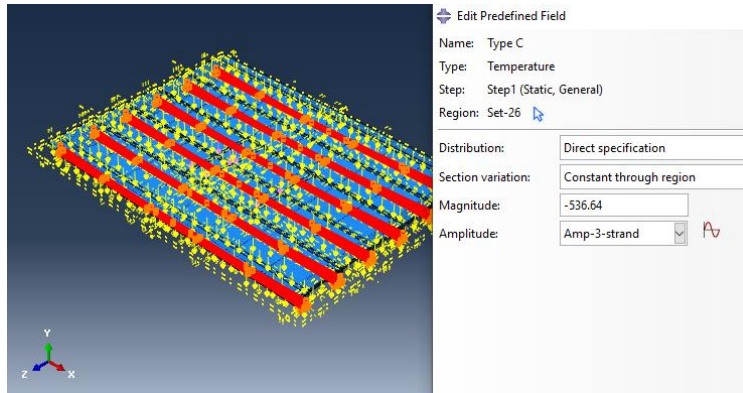
(a)
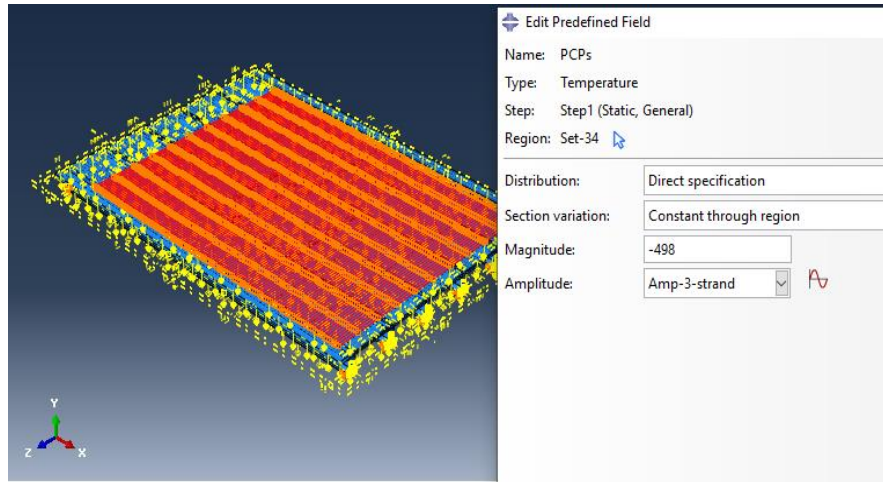
(b)

Figure 5-13 Final stress applied in the strand: (a) Type C girder; and (b) PCPs

5.4 Loading Conditions

The modeling involved applying the truck wheel loads of the original EB bridge shown in Table 4-2 as patch loads over a 200 in^2 area. The tire contract area of a wheel consisting of one or two tires was assumed to be a single rectangle measuring 20 inches wide and 10 inches long (Grubb et al. 2015). The tire pressure was also assumed to act uniformly within the tire contact area. Figure 5-14 shows the loads on the top of girders B and C at mid-span in FEM, simulating the Path 2 (P2) load test condition shown in Figure 4-12(a).
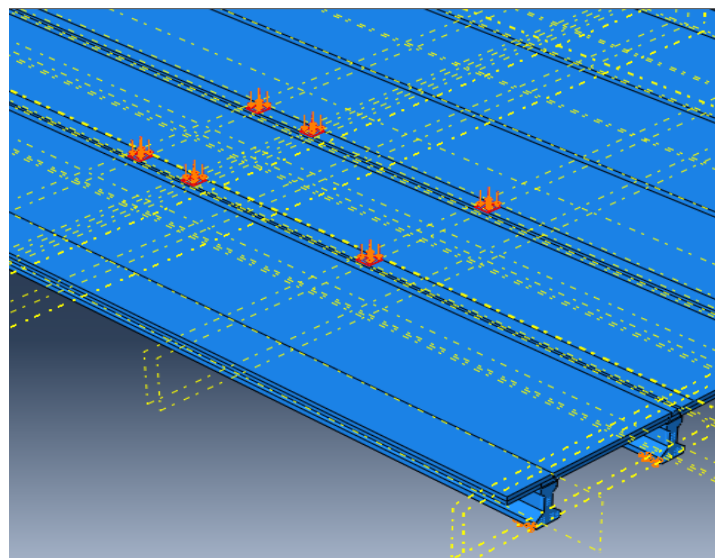
Figure 5-14: Wheel loads applied as patch loads

As the girders and PCPs consists of prestressing strands, the prestress force is initially applied before considering the dead and live loads. Since the applied loads in ABAQUS do not occur simultaneously, they were divided into different stages based on the order of load action. Figure 5-15 shows the different stages of applied loads. Amplitude of 0 means that a specific load has not been applied yet, and 1 means that a specific load has been completely applied and has reached its maximum. For calibration purpose discussed in Chapter 6, the net live load is required and can be obtained by subtracting the load value at $t = 0.75$ seconds from the one at $t = 0.5$ seconds.
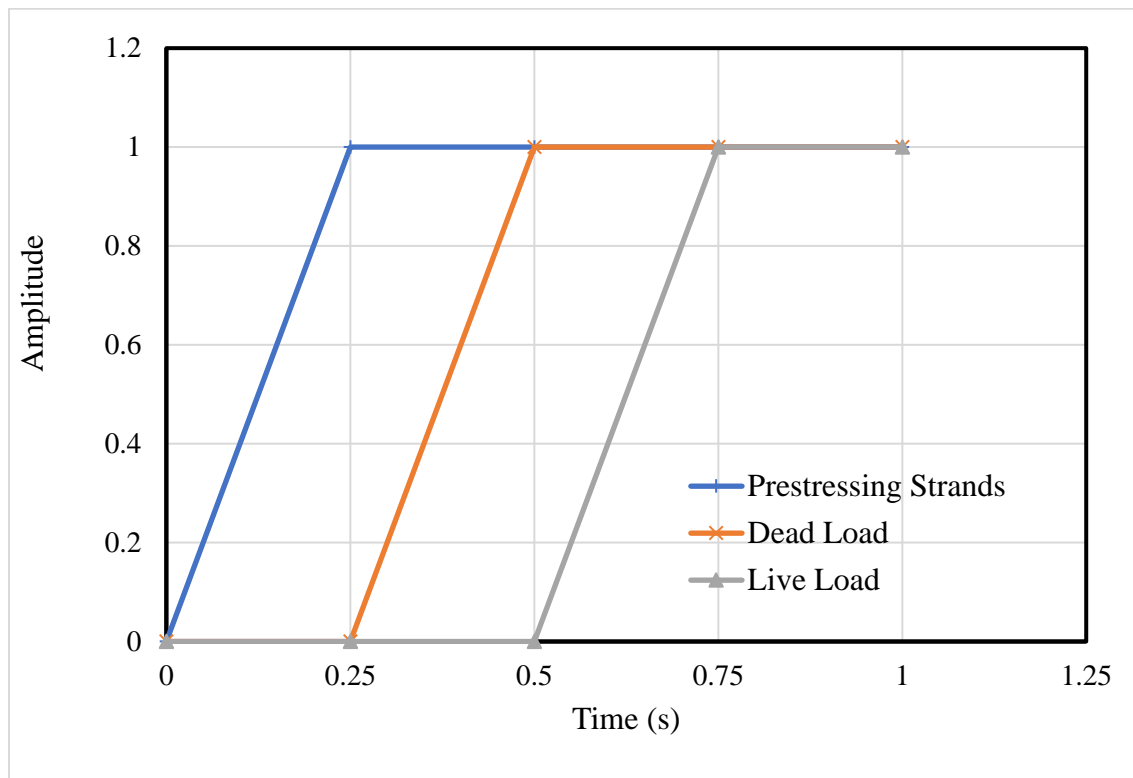
Figure 5-15: Consequence of applied loads

Chapter 6

RESULTS AND DISCUSSIONS

6.1 Load Test

The Las Lomas bridge load test included the non-reusable, reusable/wireless strain gages, and rotational tiltmeters. Each sensor was comprehensively discussed in section 4.1. The original WB bridge deck was discussed in subsection 6.1.1. Since the EB bridge had two load tests before and after deck removal, the related results were divided into two phases, respectively.

6.1.1 Original WB Deck

The strain gage and the rotational tiltmeter data were analyzed to evaluate the bridge response due to the induced truck load. The legend of strain gage results (Figure 6-1) was designated as follows: the 1st letter denotes the girder (A-H), the 2nd number shows the section (1, 2), and the last letter shows the location (T-top, M-Middle, and B-bottom). The bottom strain gages were subjected to tensile stress, whereas the top gages were subjected to compressive stress, resulting in a negative reading. The middle gages should have no or little strain readings depending on their location from the girder neutral axis (N.A.). The non-reusable strain and rotational tiltmeter responses exhibited noise and vibration during the load test. The data was then refined using the moving average between 10 points. Figure 6-1 shows the raw strain response for Path 3 Run 1.
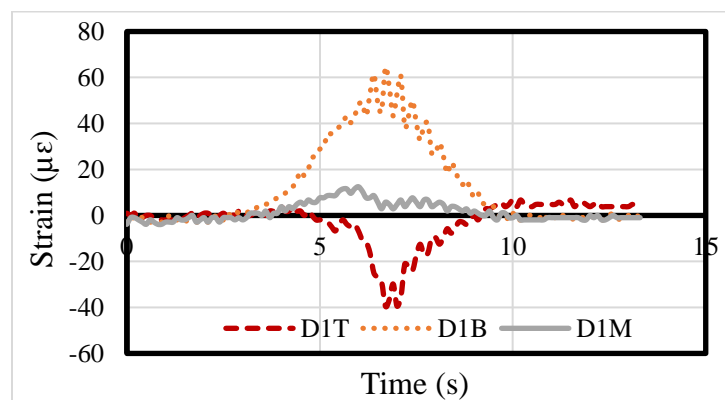
Figure 6-1: Raw strain data for Path 3 Run 1 of WB bridge

Figures 6-2(a) and 6-2(b) show the modified strain time history at section 1 for Path 3, Run 1, and Run 2, respectively. From Figures 6-2(a) and 6-2(b), the strain responses at girders C and D are the maximum, as the truck was directly on top of the girders. Therefore, the position of the truck caused a gradual increase in the strain response. The top gage responses exhibited a great deal of elongation, ranging from 40 $\mu\varepsilon$ to 60 $\mu\varepsilon$. The excess elongation led to lower a N.A. value between CIP and the girder, which affected the degree of composite action (DCA).
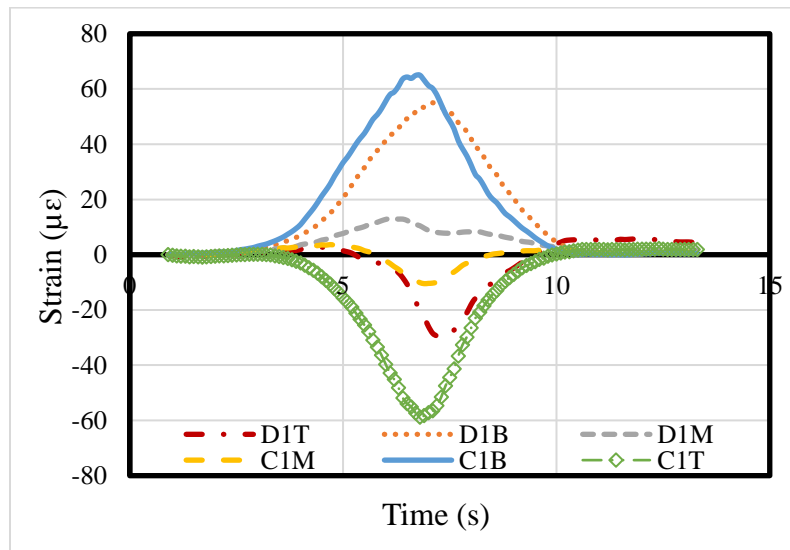
(a)
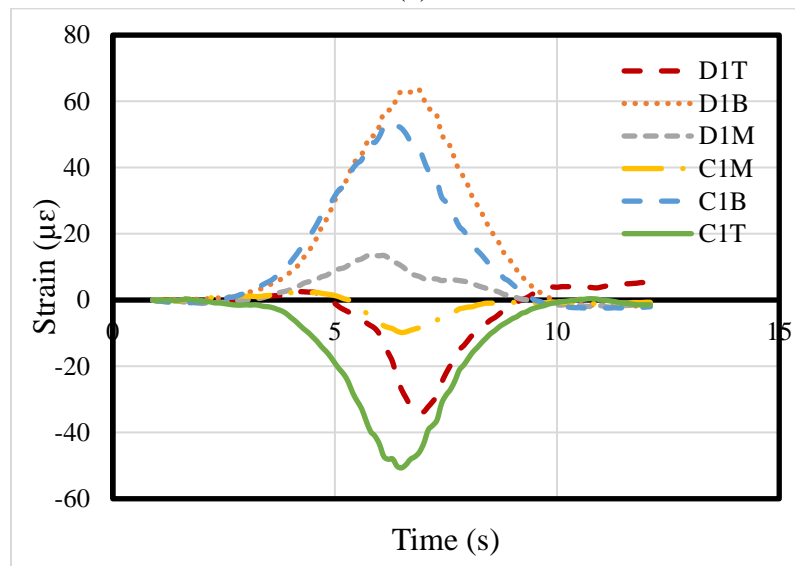
(b)

Figure 6-2 Modified strain vs time diagram for Path 3 of WB bridge: (a) Run 1; (b) Run 2

To evaluate the bridge composite deck-girder composite action, the actual neutral axis (N.A.) location of each girder from all load tests was used as an indication scale. The N.A. magnitude was estimated from the measured top and bottom strain data, assuming a linear strain profile along the cross-section of the girder (Figure 6-3). This assumption is valid if all strain gage readings returned to almost zero after the load test, which suggests that the bridge was still in the elastic region after the load removal. BDI, a known company for bridge diagnostic, used the same relationship between strain data and N.A. which should have been validated by the company as well. The calculation for the field/experimental neutral axis was performed using Equation 6-1.
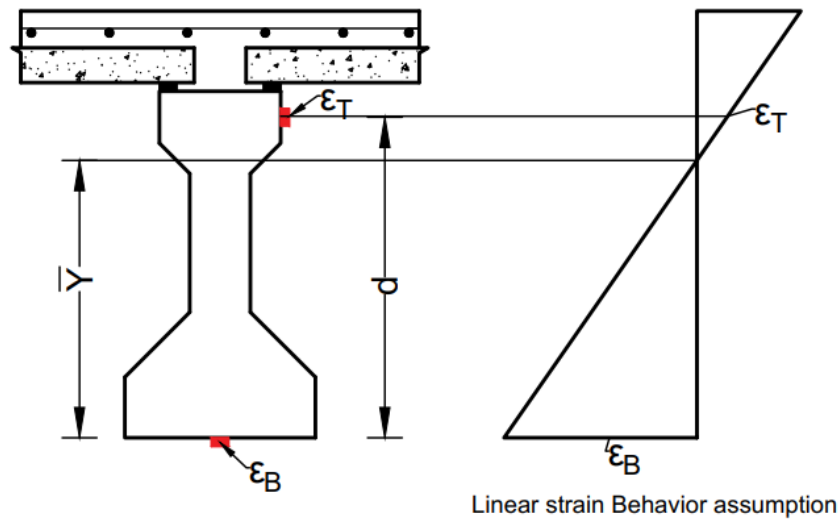
Figure 6-3: Neutral axis (N.A.) calculation

$$Y = \frac{\varepsilon_B * d}{\varepsilon_B + \varepsilon_T} \tag{6-1}$$

Where:

Y = Neutral axis location measured from bottom (in.)

d = Distance between the top and bottom gages (in.)

ε_B = Strain in bottom gage ($\mu\varepsilon$) (absolute value)

ε_T = Strain in top gage ($\mu\varepsilon$) (absolute value)

The theoretical and load test N.A. locations from the WB bridge composite decks for different girders were calculated. Furthermore, The N.A. location for a single girder from load test was found by obtaining the maximum bottom strain gage of a specific girder and its corresponding top strain gage response of the same girder.

Moreover, the N.A. location for a single girder was determined by averaging the locations from all load test paths, except those where the trucks were too far from the girder to make a significant response. The average N.A. location for all the girders was around 28 in. from the bottom flange, as found from the load tests. The average experimental N.A. was between the theoretical full-composite, around 44 in. and non-composite around 17 in., which indicates that there is partial composite action between the girders and composite deck. Based on the N.A. locations, only 41% composite action was calculated between the girders and the deck. The moment capacity of the girders was reduced by about 2.0% because of the loss of composite action (calculation shown in Appendix A).

The serviceability limit state by the means of deflection limit should be satisfied to ensure that the bridge structure is in good standing and performance. The deflection check should not exceed the permissible live load deflection, which is L/800, where L is the bridge span length. One of the methods for deflection check is rotational tiltmeter sensors as it is difficult to place LVDTs because of the bridge height. The legend of the rotational tiltmeter results were as follows: the 1st letter and 2nd digit expressed as either (bent 2 (B2), (B3), (B4), or abutment 5 (A5)), and the 3rd letter was the girder (A-H) in both bridges. Figure 6-4 shows the refined data of rotation vs. time diagram of girder B for WB bridge due to loading on Path 3 Run 1. The average estimated and indirect calculation of deflection at mid-span of girder B was around 0.1 in. compared to AASHTO (2020) permissible live load deflection, 1.05 in.
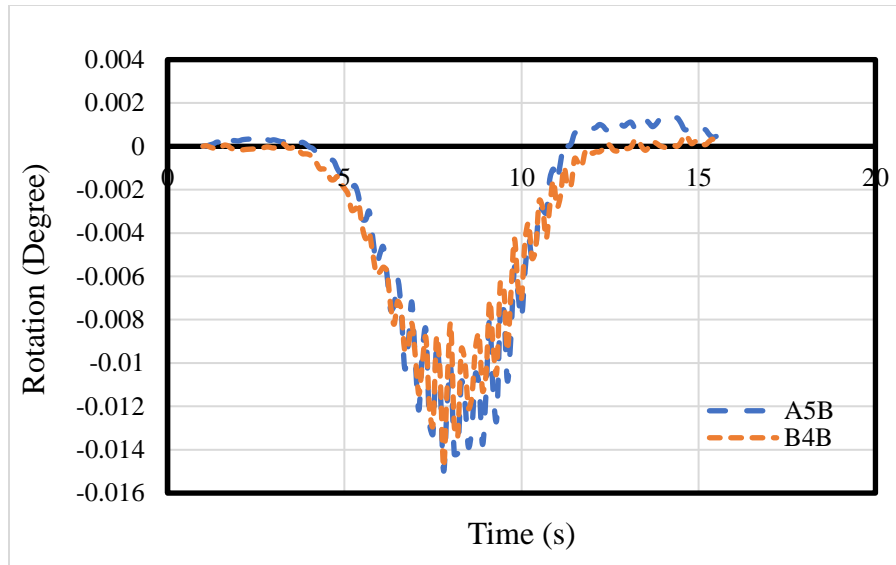
Figure 6-4: Rotation vs time diagram for Path3 of WB bridge Run 1

6.1.2 Original and Replaced EB Decks

This section includes the results on both load tests performed on the EB bridge decks. Phase 1 was discussed the original deck, while Phase 2 was related to the replaced deck. Subsection 6.1.2.3 involved the main result comparisons between the two phases.

6.1.2.1 Phase 1

The objective of Phase 1 was to obtain insight into the overall bridge performance and determine the extent that the localized CIP deck damage influenced the bridge's performance and load carrying capacity. Phase 1 was also served as a decision tool to determine if the bridge deck needed to be replaced. Figures 6-5(a-d) show the strain responses for all tested paths at section 2 located at the mid-span of girders. The top gages displayed different readings, and the maximum readings were at girders C and D, which varied between 26 to 55 µε. As previously mentioned, a similar condition was observed on the WB bridge, but the WB bridge typically demonstrated a slightly more severe condition than the EB bridge. The strain responses exhibited the maximum readings when the truck was above or near the girders, and the response became negligible for the girders as the distance increased from the truck tires [Figures 6-5(a-d)].
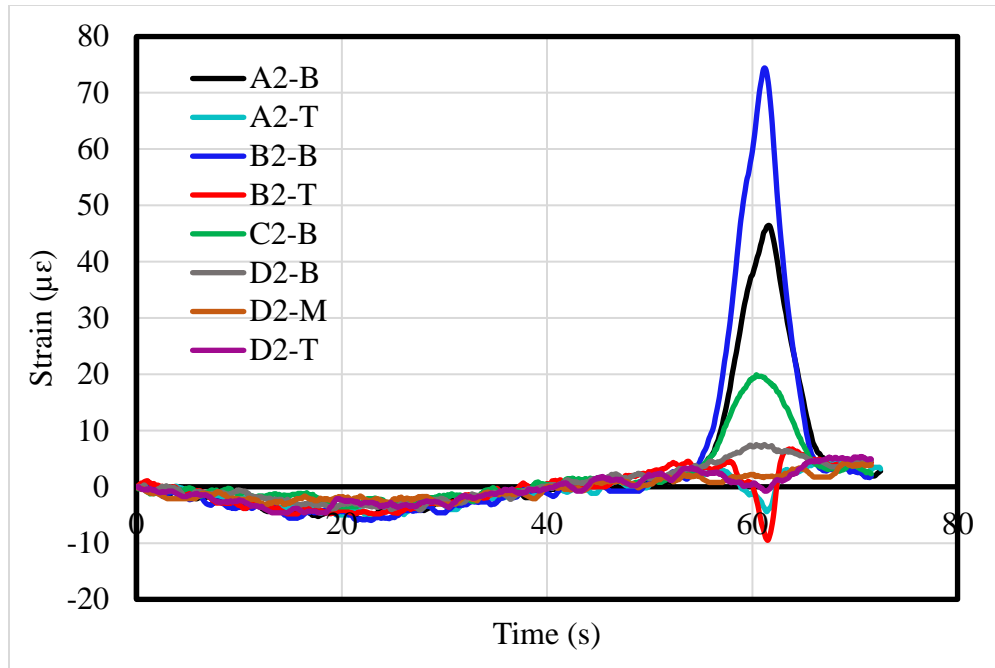
(a)
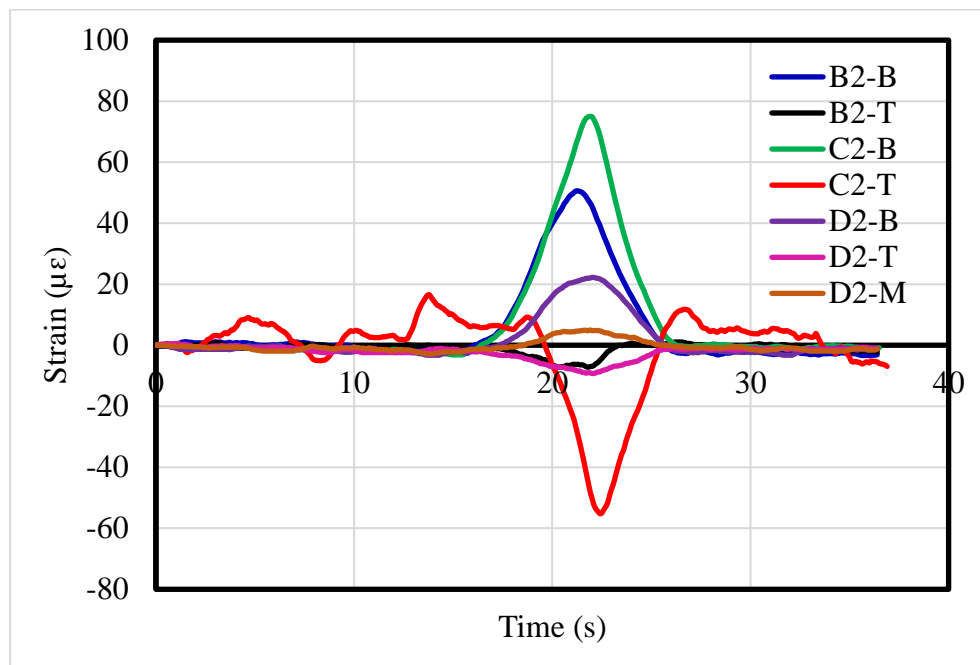
(b)
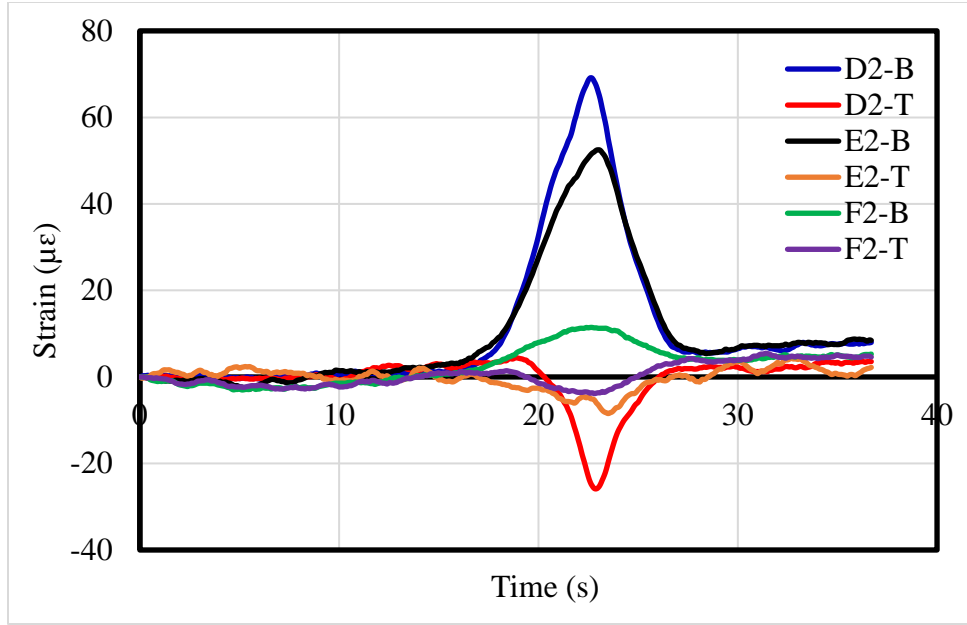
(c)
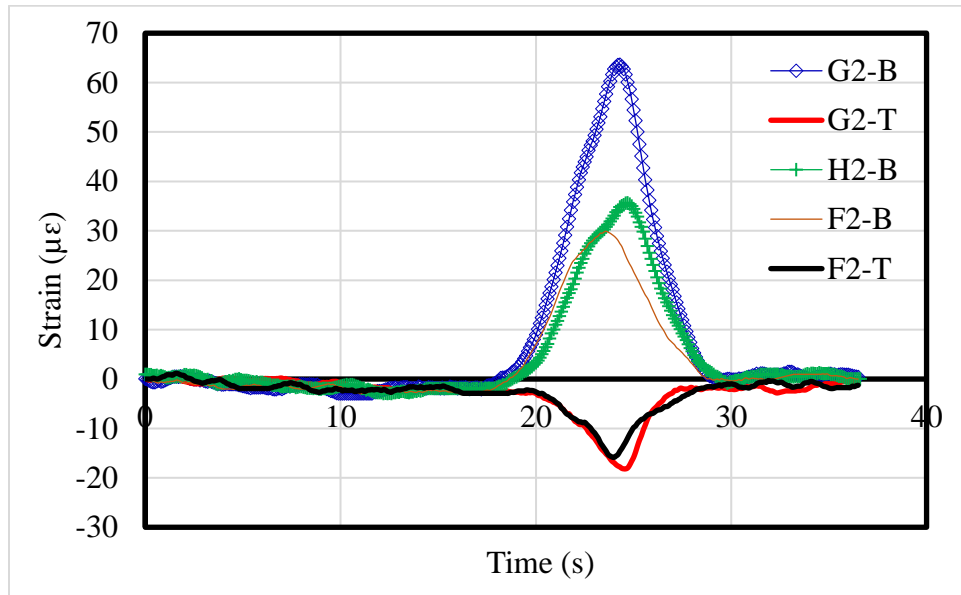
(d)

Figure 6-5 Strain vs. time of original EB bridge deck: (a) Path 1; (b) Path 2; (c) Path 3; (d) Path 4

Two cases of theoretical N.A. calculation were considered, non- and full-composite N.A.

The locations of the theoretical and experimental N.A. of the girders are provided in Table 6-1.

The load tests indicated that the average experimental N.A. location for all the girders was around

30 in., measured from the bottom flange. Therefore, a partial composite action between the girders

and the composite deck was achieved. Based on the N.A. locations, only 48% composite action

was calculated between the girders and the deck. Appendix A shows a sample calculation of N.A.

of EB Bridge.

Table 6-1: N.A. locations for original EB bridge deck

Girder	Theoretical NA from bottom (Non-composite), in.	Theoretical NA from bottom (Composite), in.	Experimental NA from bottom (in.)
A	16.85	43.82	33.79
B	16.85	44.75	32.23
C	16.85	44.75	28.48
D	16.85	44.75	29.23
E	16.85	44.75	32.37
F	16.85	44.43	27.63
G	18.59	44.83	27.11
H	17.85	43.88	**

** Top strain gage was damaged while testing.

Figures 6-6(a) and 6-6(b) show the raw and refined data of rotation vs. time diagram of EB

bridge due to loading on Path P1 Run 1, respectively. The average maximum deflection of girder

B at mid-span was around 0.18 in.
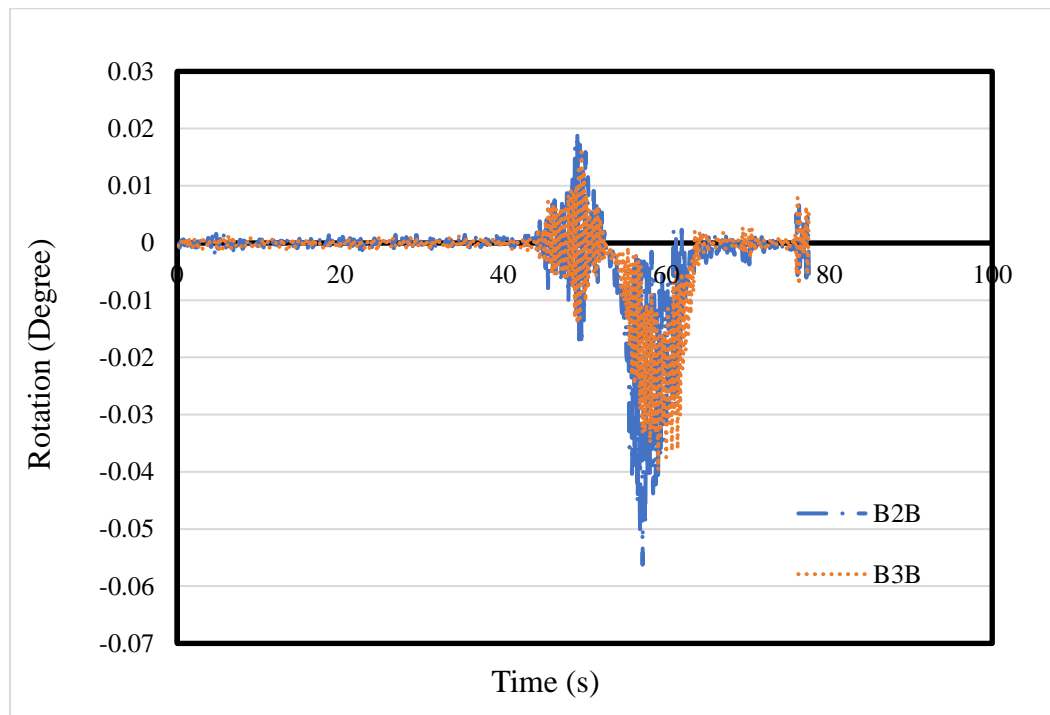
(a)
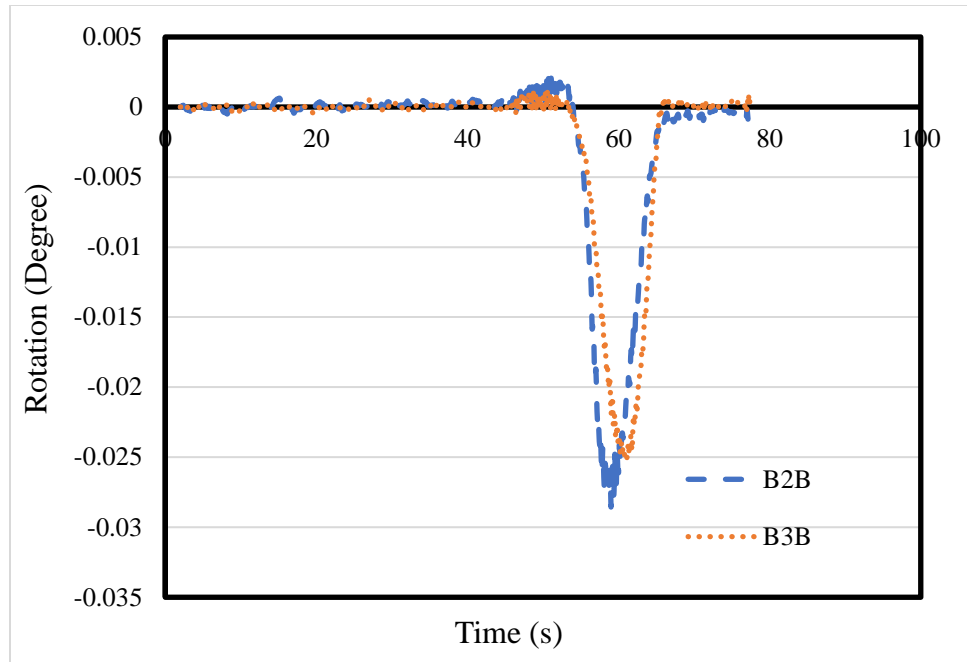
(b)

Figure 6-6 Rotation data vs. time: (a) Raw data; (b) Modified data

6.1.2.2 Phase 2

The objective of EB follow-up load test is to check whether the replaced deck showed an improvement in terms of increased load carrying capacity and DCA. Figure 6-7 shows the strain responses for Path 1 (crawl test). Next, the truck movement across span 2 was at a uniform speed less than 5 mph. The strain responses at girders A and B were maximum as expected, as truck A passed on top of these girders. The strain responses across the other girders were very small. Therefore, these strain responses can be ignored as other girders were located relatively far away from the truck tires.

Figure 6-8 shows the maximum strain responses from bottom gages from all paths for the girders (A-F) for section 1, located at 20 ft. from bent 2. Additionally, the bottom strain gage at girder C has the highest strain value, 53 $\mu\varepsilon$, compared to other girders. The reason for the increment in strain response was due to the existing hairline crack in the PCP located to the right of girder C, which was observed during the follow-up bridge instrumentation process.

89
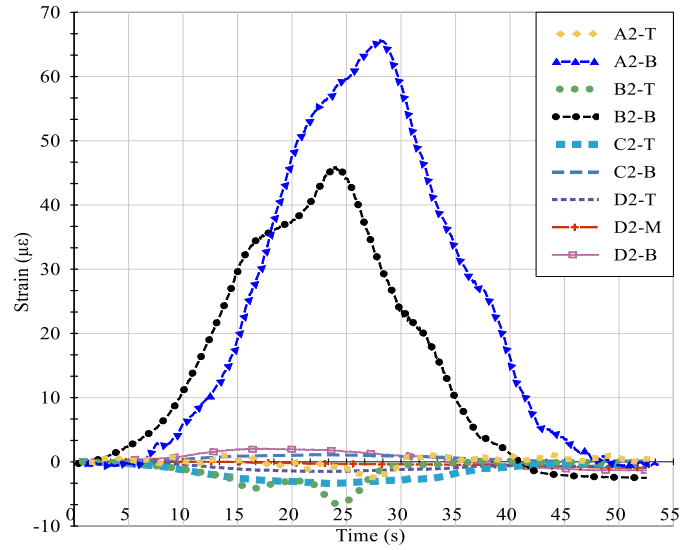
Figure 6-7: Strain data for Path 1
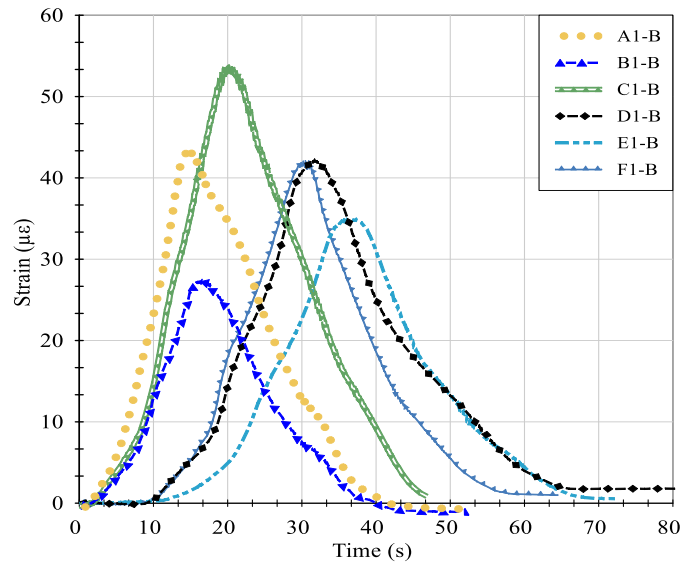
Figure 6-8: Maximum strain data form all paths

Figures 6-9(a) and 6-9(b) show the strain response from gages attached to the PCP near the

construction joint, which is located above girder C. These strain gages were installed on both sides

of girder C. The sides were designated as north (N.) and south (S.) directions based on the traffic

flow direction running east. The N. and S. directions are shown in Figures 6-9(a) and 6-9(b). The

strain gages were attached at three different sections, 20 ft., 35 ft. (mid-span), and 55 ft. measured

from bent 2 (Figure 4-8). Strain gages were designated as follows: 1st two letters denote the strain

gage at construction joint (CJ), the 2nd number shows the location of strain gages (in ft.), and the last letter shows the direction of the strain gages (N-north; S-south) [Figures 6-9(a) and 6-9(b)]. The data suggests that the strain response from the gages near the construction joint in the S. direction are higher than the response of the gages in the N. direction due to the existing PCP crack and the loss in concrete stiffness in the two poured concrete batches. Highly stiff concrete, moreover, exhibited low measured strains during experimental testing. For instance, the loss of stiffness of concrete may be due to the initiation, growth, and coalescence of many micro-cracks. As a result, the S. direction appears to have less concrete stiffness compared to the stiffness of the N. direction.
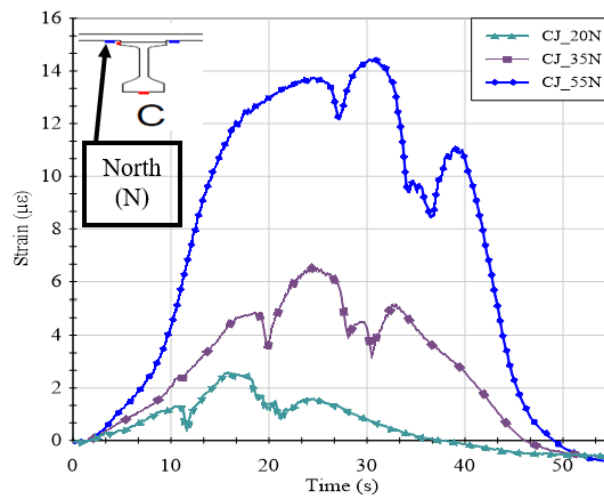
(a)
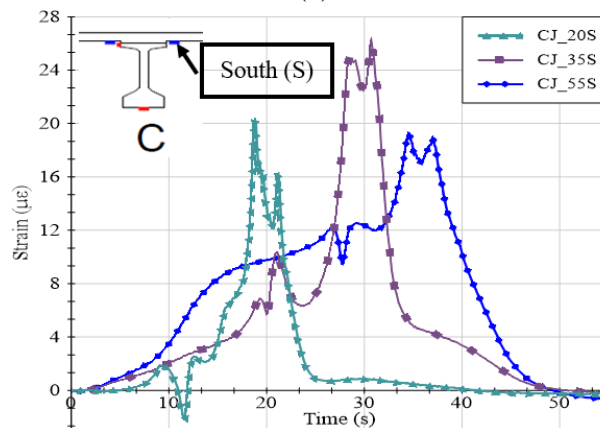
(b)

Figure 6-9 Strain data near construction joint: (a) N. direction; (b) S. direction

The theoretical and load test N.A. locations from the follow-up EB bridge test for different girders are provided in Table 6-2.

Table 6-2: N.A. locations for replaced EB bridge deck

Girder	Theoretical NA from bottom (non-composite), in.	Theoretical NA from bottom (fully composite), in.	Actual NA from retesting (in.)
A	16.85	44.32	37.22
B	16.85	45.24	37.52
C	16.85	45.24	**
D	16.85	45.24	35.12
E	16.85	45.24	**
F	16.85	44.93	35.20
G	18.59	45.33	34.50
H	17.85	44.40	36.76

** Bottom strain gages were damaged while testing.

The actual average NA location for all the girders was around 36.1 in. from the bottom flange, as found from the follow-up load test. The average experimental N.A. was between the average of theoretical fully composite and non-composite with 45 in. and 17.2 in., respectively, which suggests that there is partial composite action between the girders and the composite deck. The corresponding hand calculations are shown in Appendix A. Based on the combined average NA locations, only 68% composite action was calculated between the girders and the deck. The moment capacity of the girders for assumed partial composite action was reduced by about 7.33% because of the loss of composite action. Sanayei et al. (2012) conducted static load test on a newly constructed bridge before the bridge opening. Strain gages were installed at the positive and negative moment regions. The NA locations in girders were calculated for each region. It was concluded that the NA locations were close to the fully composite action only in the positive moment region and not in the negative moment region, due to concrete cracks.

LLDFs found from the follow-up testing of section 2 are shown in Table 6-4. The LLDFs indicate the relative distribution of applied live loads to girders. The average LLDFs for all girders from the bridge retesting is 0.51. To be conservative, LLDF of girder A is used in live load moment

calculation as it produces the highest live moment value. The LLDFs found from the AASHTO Standard Specifications (2002) formula were more than 1.0 (Table 6-3). The equations are based only on girder spacing and the type of bridge girder. On the other hand, the new LLDF equations in AASHTO LRFD (2020) were based on parametric studies and include additional parameters, such as girder length, spacing, longitudinal stiffness, and deck thickness.

The LLDFs from the EB follow-up load test nearly matched calculated LLDFs from AASHTO LRFD (2020) (Table 6-3). Therefore, AASHTO LRFD (2020) LLDFs formulas are considered an accurate representation of bridge behavior (Table 6-3).

Table 6-3: Girder LLDFs for moment

AASHTO- LLDFs for Moment		
LRFD Spec. (2020)		Standard Spec. (2002)
Interior Girder	Exterior Girder	
For one lane loaded: $0.06+\left(\dfrac{S}{14}\right)^{0.4}\left(\dfrac{S}{L}\right)^{0.3}\left(\dfrac{K_g}{12.0Lt_s^3}\right)^{0.1}$	For one lane loaded: Lever Rule	For one lane loaded: $\dfrac{S}{7.0}$
For two or more lane loaded: $0.075+\left(\dfrac{S}{9.5}\right)^{0.6}\left(\dfrac{S}{L}\right)^{0.2}\left(\dfrac{K_g}{12.0\,Lt_s^3}\right)^{0.1}$	For two or more lane loaded: $g = e\, g_{interior}$ $e = 0.77 + \dfrac{d_e}{9.1}$ Use the lesser of the values obtained from the equation above with $N_b = 3$ or the lever rule	For two or more lane loaded: $\dfrac{S}{5.5}$

where:
S = girder spacing (ft.)
L= girder design length (ft.)
K_g = girder longitudinal stiffness
t_s = deck thickness (in.)
g = Live load distribution factor for moment in exterior girder
e = correction factor
g $_{interior}$ = Live load distribution factor for moment in interior girder
d_e = Horizontal distance from the centerline of the exterior girder web to the interior edge of traffic barrier (ft.)

Table 6-4: Live load distribution factors (LLDFs)

Girder	Follow-up Test	LLDFs from AASHTO	
		LFRD (2020)	Standard Specs (2002)
A	0.63	0.81	1.68
B	0.56	0.79	1.68
C	-	0.79	1.68
D	0.59	0.79	1.68
E	-	0.79	1.68
F	0.50	0.79	1.68
G	0.30	0.79	1.45
H	0.46	0.80	1.40

The dynamic allowance impact factors (IMs) found from the follow-up test at Path 3 are shown in Table 6-5. The vehicular live loads are multiplied by an IM to include any dynamic effects in bridges. The data indicates that the IM for girder C section 1 governs (Table 6-5) and should be used in load rating calculation. Therefore, an actual IM value of 24% was used in the load rating calculation. The IM for girder D at section 1 falls below 1.0, based on multiple factors, according to (Benmokrane et al., 2008). These factors included a possible smoother surface of the road which reduces the IMs and lack of accuracy from truck drivers when following the targeted load paths while driving at a high speed. Since bridge deck includes expansion joints, these joints are not leveled properly with deck concrete causing the bridge to exhibit an impact or bumps when the truck moves at high speed. Figure 6-10(a) and 6-10(b) display the strain responses of the dynamic and static load tests at girders C and D, respectively. As the dynamic strain response became high, IM was high as well, as was the case with girder C [Figure 6-10(a)]. The IM can be calculated using Equation 6-2.

Table 6-5: Live load dynamic impact factor (IM)

	Dynamic Impact Factors (IM) (%)			
Girder	Follow-up Test		AASHTO	
	Section 1	Section 2	LFRD (2020)	Standard Specs (2002)
C	24	-	33	26
D	0.87	2		
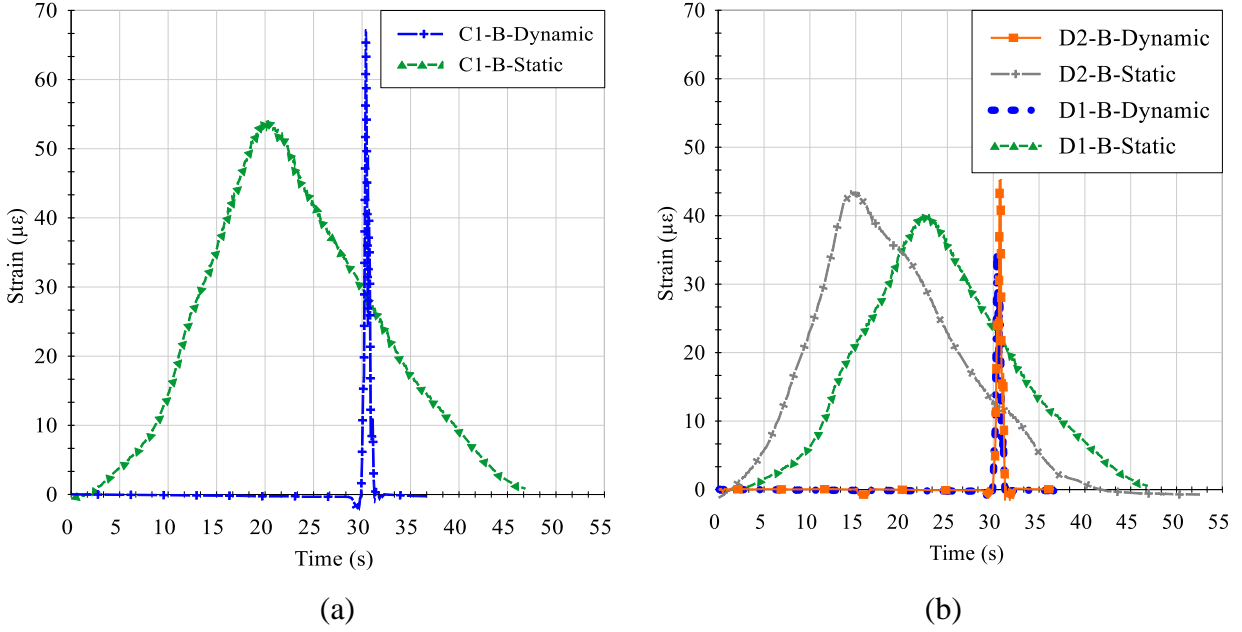
Figure 6-10 Dynamic vs. static strain responses: (a) Girder C; (b) Girder D

$$IM = \frac{\varepsilon_{Dynamic} - \varepsilon_{Static}}{\varepsilon_{Static}} \ (100\%) \qquad\qquad (6\text{-}2)$$

Where:

IM = Dynamic Impact factor (100%)

$\varepsilon_{Dynamic}$ = Maximum dynamic strain response at a specific girder (με)

ε_{Static} = Maximum static strain response at a specific girder (με)

Figures 6-11(a) and 6-11(b) show raw and modified data in the form of rotation vs. time diagrams for girder A due to loading on Path 1, respectively. The average maximum deflection at mid-span of girder A was around 0.17 in.

95
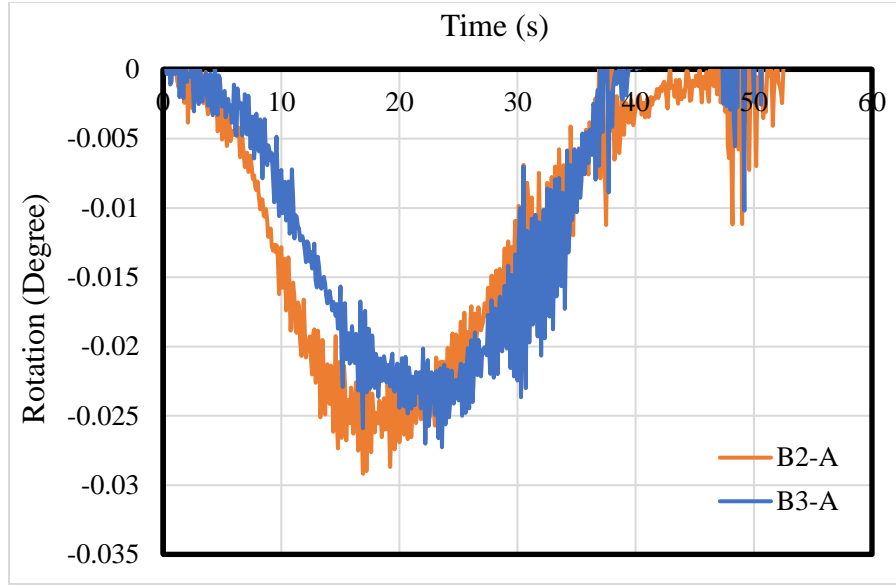
(a)
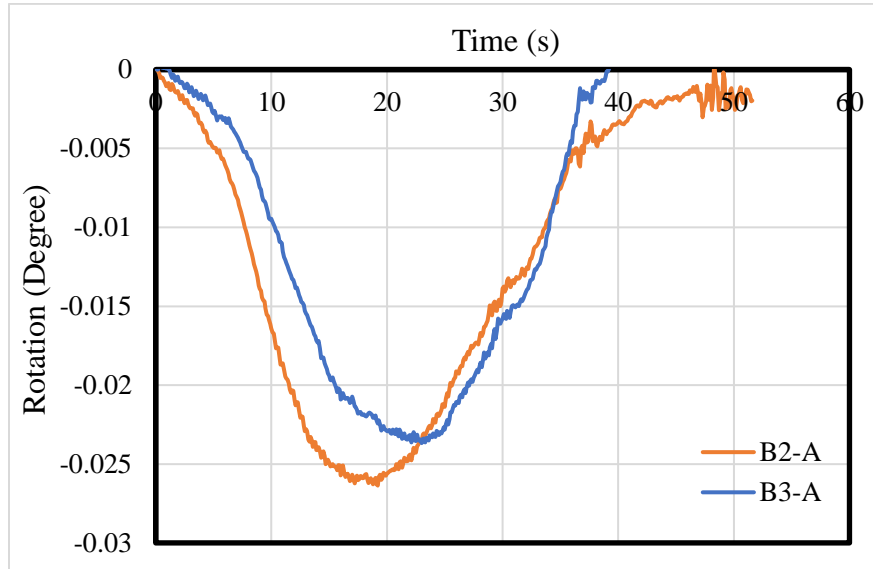
(b)

Figure 6-11 Modified rotation vs. time: (a) Raw data; (b) Modified Data

6.1.2.3 EB Load Tests Comparison

Figures 6-12(a) and 6-12(b) represent the strain responses of both EB bridge deck tests for

Path 2 at sections 1 and 2 (crawl test), as shown in Figures 4-12(a) and 4-13(a). The maximum

measured strains for C1-B were around 53με and 45με [Figures 6-12(a) and 6-12(b)], respectively.

As a result, when compared to the EB follow-up load test, the measured strain was reduced by

15%. In addition, due to composite action loss between the bridge composite deck and the girders,

especially in girders C and D where the failure occurred, the measured top strains, C1-T, were -37 με and -7 με, respectively. Thus, the measured top strain gage decreased by 81% when compared to the follow-up result. The readings from the top and bottom strain attached to girder D in Figures 6-12(c) and 6-12(d) reveal a significant reduction by around 78% and 30% after the bridge re-decking, respectively. From Figure 6-12(e), the top strain readings of girder D at section 1 of the girder diminishes after the bridge re-decking.
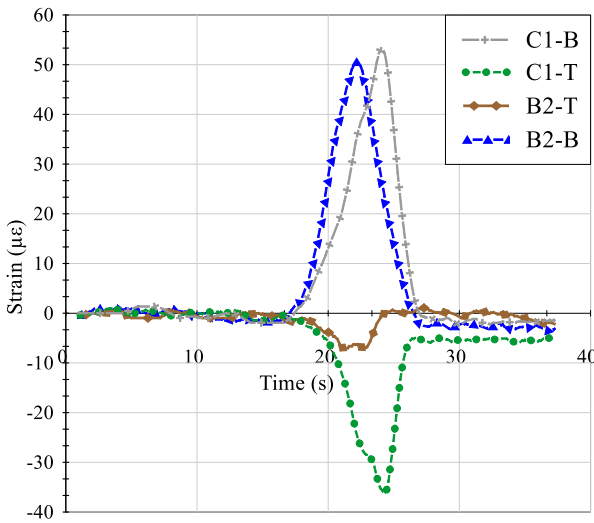
(a) P2-Previous test
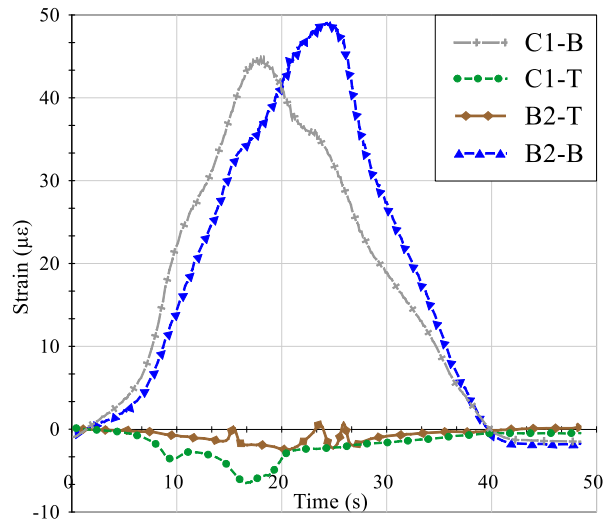
(b) P2-Follow-up test
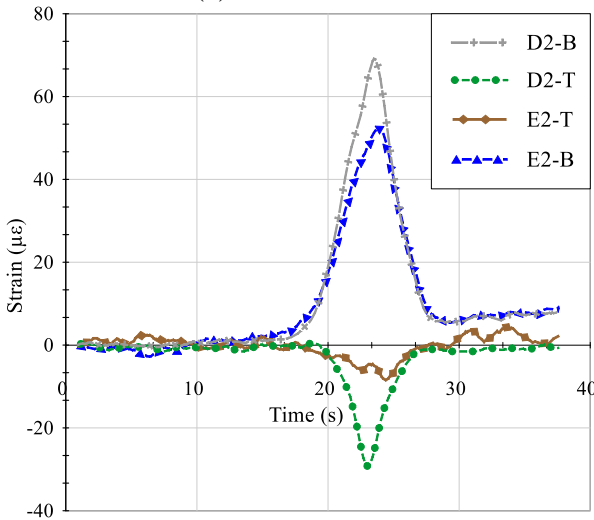
(c) P3-Previous test
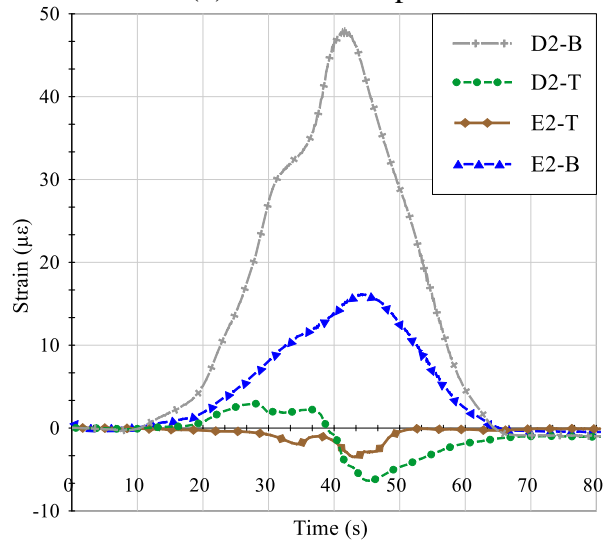
(d) P4-Follow-up test
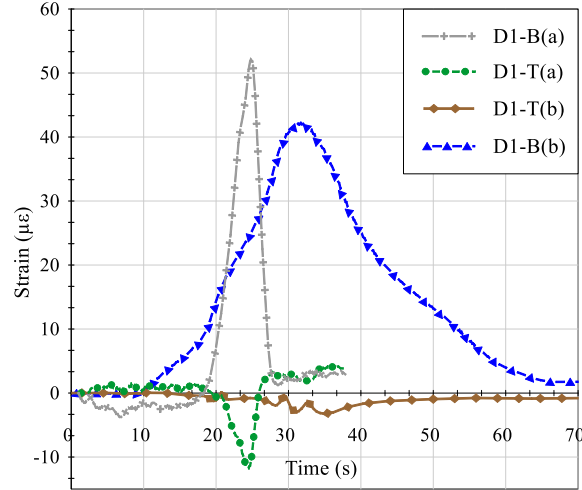
(e) P3-previous and P-4 Follow-up tests

Figure 6-12: Strain response vs. time of previous and follow-up EB Bridge
[legend [(a)]and[(b)] refers to the previous and follow-up tests, respectively]

Table 6-6 shows a summary of the main difference features between the previous and the

follow-up load tests in terms of N.A. locations and composite action between deck-girder interface.

Table 6-6: N.A. locations from original and follow-up EB bridge tests

Parameter	Previous test	Follow-up test
Average theoretical non-composite girder N.A. location from bottom (in.)	17.2	17.2
Average theoretical fully composite girder N.A. location from bottom (in.)	44.64	45.12
Average actual N.A. location from bottom (in.)	30	36.1
Average composite action between deck/girder (%)	46.65	67.25

Figures 6-13(a-d) represent the refined data in the form of maximum rotation vs. time for

girders C, D, E, and F when the truck moved on the top of the girders. As indicated in figures 6-

13(a) and 6-13(b), the maximum rotations from both tests were at girder C with -0.043º and -

0.023º, respectively. As a result, the rotation was reduced by 46.5% after bridge re-decking. Even

though the localized CIP occurred between girders C and D and failure was located below a small

patch, 3ft.x3ft, in the original EB bridge deck, girder C exhibited the largest rotation compared to

the rotation of girder D and other girders. Moreover, the construction joint was located on top of

girder C, which implies that the presence of deck defect near a specific girder where construction

joint exists would increase the negative impact on that girder. This suggests that if a patch area exists near the construction joint, the failure will be limited to this area than the rest of bridge deck as confirmed from strain and rotation data at girder C as well as from the inspection report. The rotations in girders D and E in the previous and replaced decks exhibit the same rotations with a rotational reduction of 18.5% when compared to the retesting results [Figures 6-12(a) and 6-12(b)]. The actual maximum deflection measured at mid-span was at girder C, with a magnitude of 0.28 in., which is less than the 1.05 in permissible live load deflection. Table 6-7 displays a summary of the deflections for girders A-F of previous and follow-up load tests, respectively.

(a) Bent 2-Previous test

(b) Bent 2-Follow-up test

(c) Bent 3-Previous test

(d) Bent 3-Follow-up test
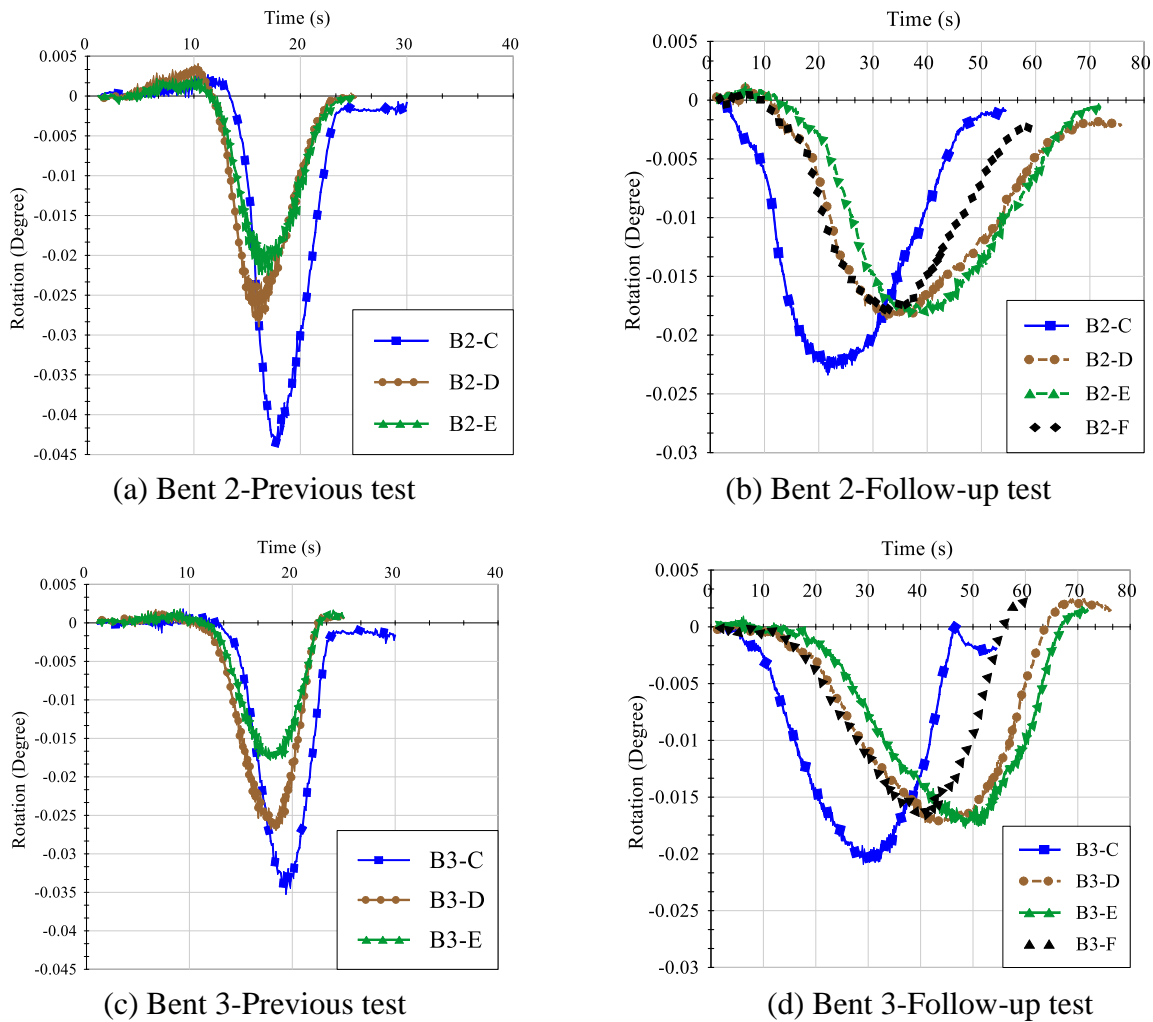
Figure 6-13: Rotational data vs. time of previous and follow-up EB Bridge

Table 6-7: Average estimated deflections from rotational tiltmeters

| Girder | Previous Test | | Follow-up Test | |
| | Deflection (in.) | | | |
	Section 1	Section 2	Section 1	Section 2
A	**	**	0.12	0.17
B	0.13	0.18	**	**
C	0.19	0.28	0.10	0.15
D	0.12	0.17	0.08	0.12
E	0.10	0.13	0.08	0.12
F	**	**	0.08	0.12

** Rotational tiltmeters were not installed on girders.

6.2 NDE Test

The Las Lomas bridge NDE scheme included using GPR and IE, (an overview of each device is presented in Section 4.4; the original WB bridge deck was covered initially). Since the EB bridge had two NDE before and after deck removal, the associated results were divided into two phases, respectively. The GPR scans were post-processed and analyzed with the GPR-SLICE (2018) software. No delamination was observed from the GPR scans, possibly because cracks, voids, or delamination have to be at least 0.25 in. wide to be visible in the B-scans achieved by GPR. The IE data was post-processed and analyzed by WinIE (2018) software. The results of the IE data analysis provided the state of delamination at the given grid points.

6.2.1 Original WB Deck
➢ **GPR:**

A 2-D contour plan GPR scan of spans 3 to 4 measured from the top reinforcement cover depths with (2.6 GHz antenna) is presented in Figures 6-14(a-c). The reinforcement profile was clearly visible and the color legends, as shown in the 2-D contour plan, indicate the areas of different cover depth ranges in inches; the percentages of the cover depth ranges of each area are also shown in Figures 6-14(a-c). The color legends demonstrates that 63% of the bridge deck in lanes 1,2, and 3 has a rebar cover depth between 2 in. to 2.5 in. Therefore, an average of 2.25 in. was used in the load rating discussed later in section 6.3. According to the as-built plans, the

concrete clear top rebar cover was supposed to be 2.0 in. As the top rebar cover might be different

than as-built plans due to construction error, small exploratory cores were drilled at different

locations denoted in red circles. Five small cores were then drilled to calibrate the GPR scanned

contour plots. Next, the small cores were repaired by injecting a quick-setting cement mortar. The

core diameter size was around 0.75 in., and two cores at one spot were needed on numerous

occasions to locate the targeted steel rebar.
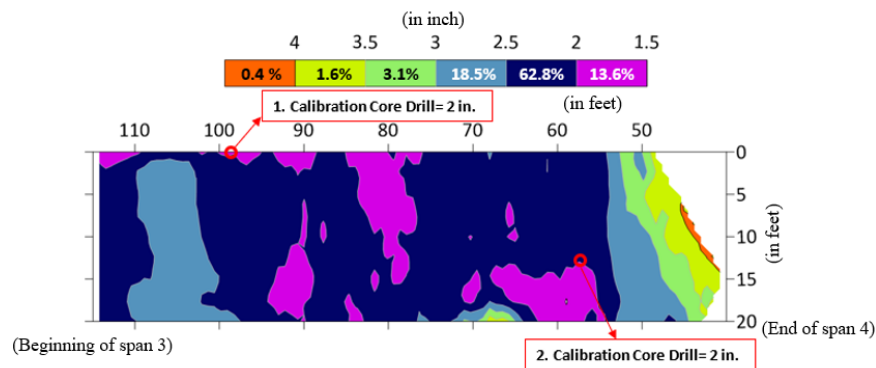
(a)
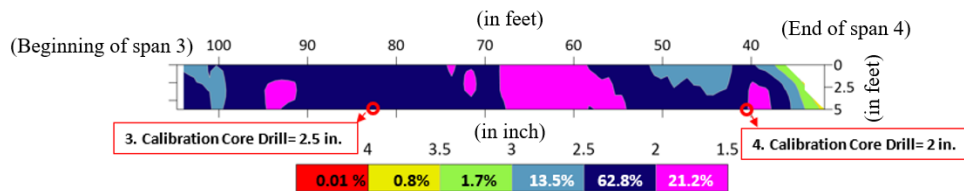
(b)
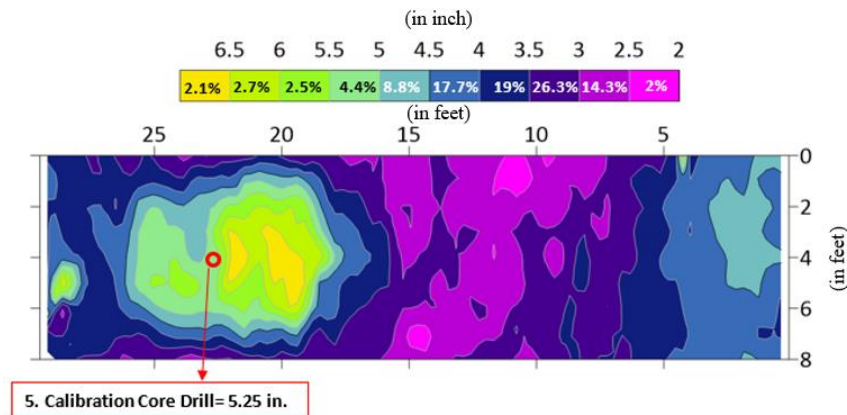
(c)

Figure 6-14 GPR contour of WB bridge: (a) Lanes 1 and 2;(b) Lane 3; (c) Patch area

> **IE:**

The IE results were subsequently plotted on 2-D contour maps. The designation of the colors in the 2-D contour maps of the IE results are presented in Table 6-8. The IE device, however, cannot specify the exact depth of a shallow delamination, occurring within 4 in. of the top of the deck. In contrast, device is only able to determine the presence of delamination at a given grid point.

The assessment of the delamination state was based on discrete discontinuous grid points on the bridge deck; however, the IE results are in the form of continuous contour maps, where linear interpolation was used between the data points.

The delamination of the WB bridge, shown in Table 6-8, appears to be more prevalent in the area starting from the center of span 4 and heading east towards the abutment, especially near the area surrounding the repaired deck panels, which was scanned with a denser grid for greater accuracy. Figure 6-15(b) shows that roughly 50% of the area was severely delaminated.

Table 6-8: Summary of delamination on WB bridge

Levels of Delamination			
Type	Lanes 1E and 2E	Lane 3E	Patch Area
No Delamination (%)	56	56	36
Moderate Delamination (%)	12	4	14
Severe Delamination (%)	32	40	50
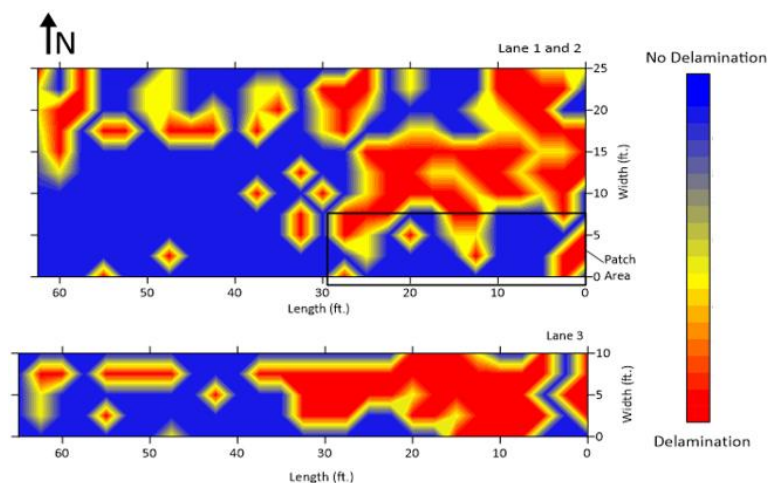
(a)
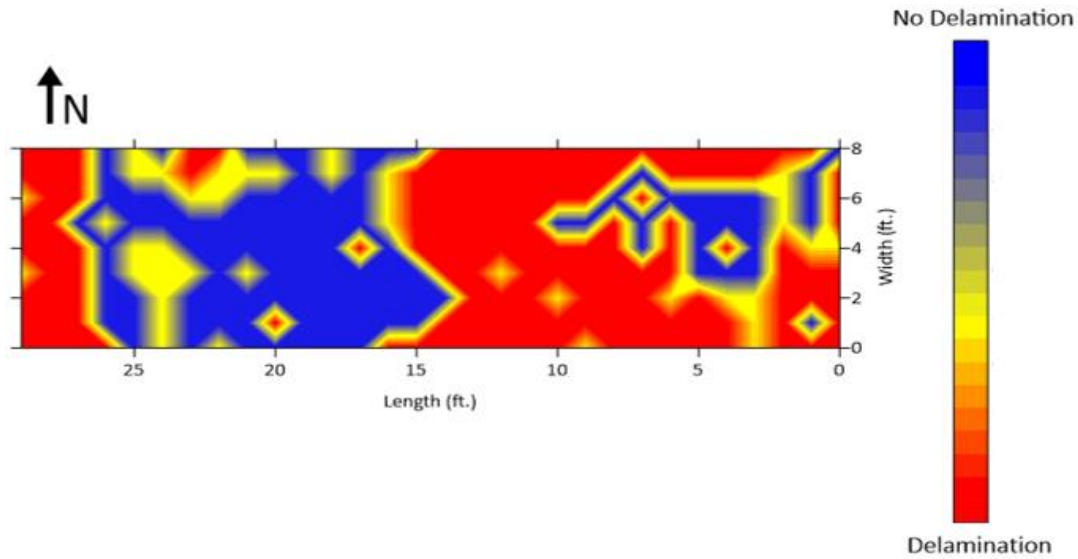
(b)

Figure 6-15 IE plots of WB bridge: (a) Lanes 1, 2, and 3; (b) Patch area

6.2.2 Original and Replaced EB Decks

➤ **Phase 1-GPR and IE:**

2-D contour plan GPR scan of spans 2 to 3 measured from the top reinforcement cover depths with (2.6 GHz antenna) is presented in Figures 6-16(a-c). The reinforcement profile was clearly visible, and the color legends, as shown in the 2-D contour plan, indicate the areas of different cover depth ranges in inches; the percentages of the cover depth ranges of each area are also shown. The color legends additionally indicate that 53% of the bridge deck in lanes 1,2, and 3 has a rebar cover depth between 1 in. to 2 in. Therefore, an average of 1.5 in. was used in the load rating (discussed later in section 6.3).

According to the as-built plans, the clear cover for the deck top layer rebars was supposed to be 2.0 in. Four small cores were drilled to calibrate the GPR scanned contour plots. Two of the drilled cores from the original EB bridge depths are shown in Figures 6-17(a) and 6-17(b) to verify

the accuracy of the GPR readings [Figure 6-16(a) and 6-16(b)], respectively. The locations of the

cores are shown with the red circles in the contour plan.
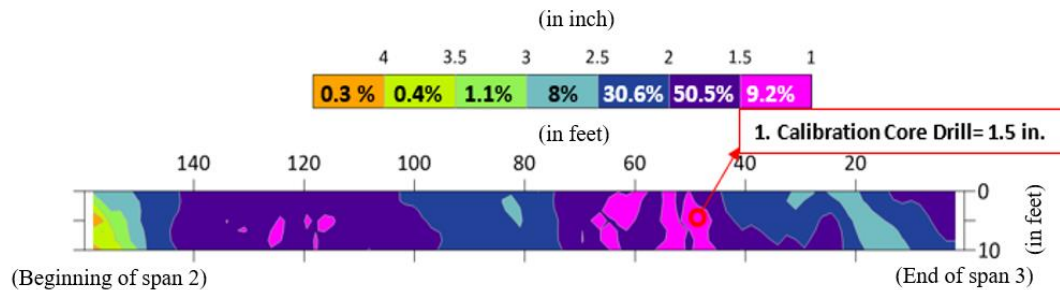
(a)
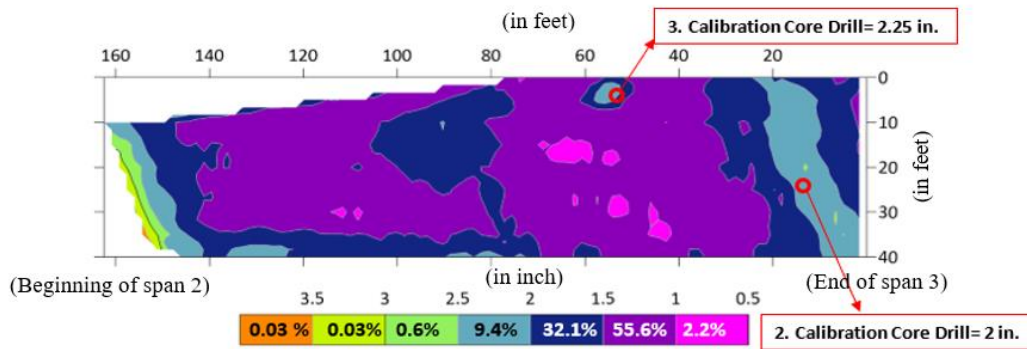
(b)
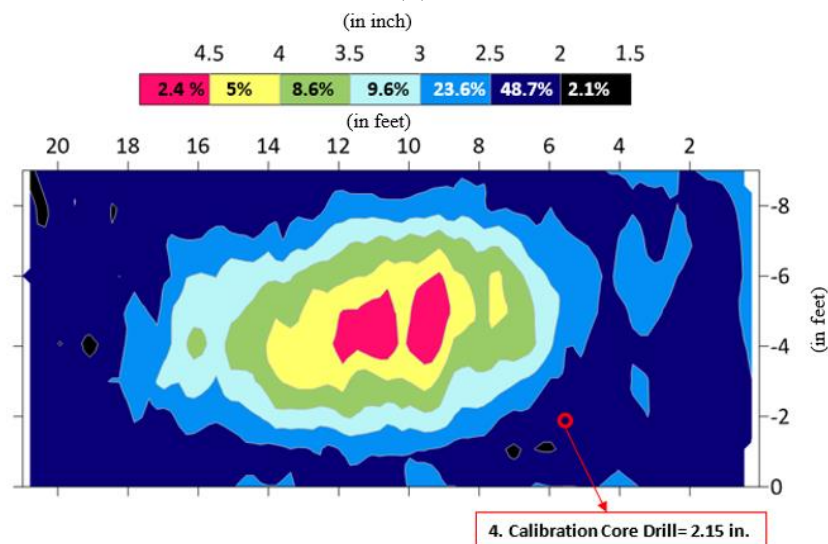
(c)

Figure 6-16 GPR contour of EB bridge: (a) Lane 1;(b) Lanes 2, 3, and Gore area; (c) Patch area

| (a) | (b) |
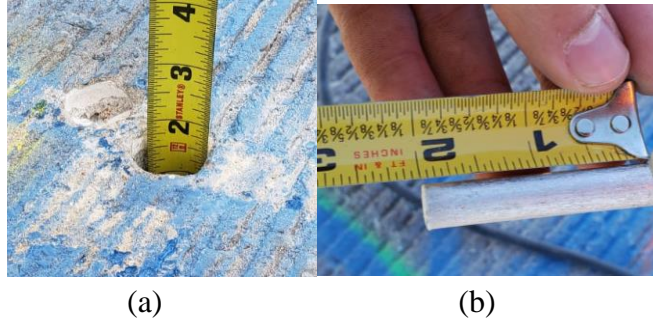
Figure 6-17 Core drill calibration: (a) 1.5 in; (b) 2 in.

The delamination of the EB bridge, shown in Table 6-9, is more prevalent in lanes 2E, 3E, and the gore area of span 2 [Figure 6-18(a)]. In Figure 6-18(b), most of the patch area has severe delamination, even though it was a newly poured concrete. The center portion of the patched area showed no delamination as it was constructed with a full CIP concrete deck, while other areas included poured concrete over PCPs. The patch area of the EB bridge was scanned with a denser grid (1 ft. x 1 ft. squares).

Table 6-9: Summary of delamination on the original EB bridge deck

Level of Delamination	Levels of Delamination		
	Lane 1E	Lanes 2E, 3E, and gore area	Patched Area
No Delamination (%)	44	45	38
Moderate Delamination (%)	44	3	2
Severe Delamination (%)	12	52	60
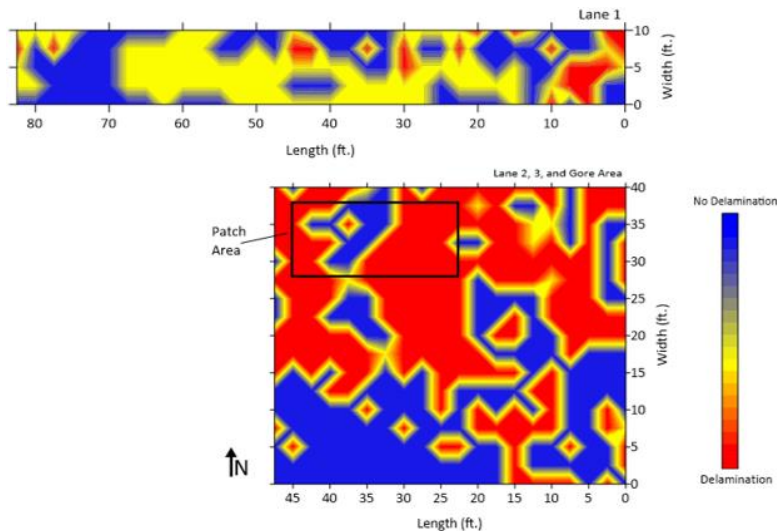
(a)
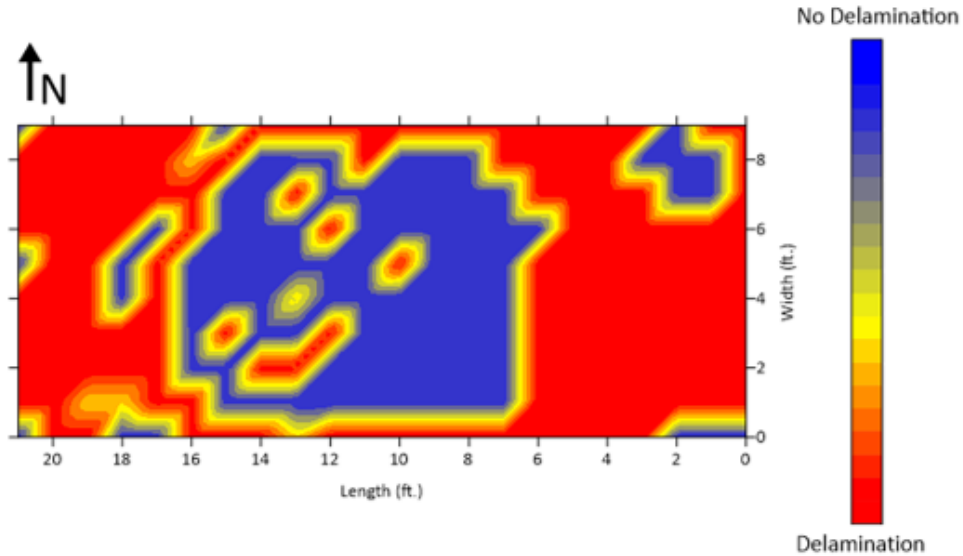
(b)

Figure 6-18 IE plots of original EB deck: (a) Lanes 1, 2, and 3, and gore area; (b) Patch area

➢ **Phase 2-GPR and IE:**

2-D GPR scan contours from span 2 of the EB bridge deck, showing the top reinforcement cover depths, are presented in Figures 6-19(a) and 6-19(b). The reinforcement profile was clearly visible, and the color legends, shown in the 2-D contour plan, indicate the areas of different cover depth ranges in inches. The percentages of the cover depth ranges of each area are also shown. The color legends moreover indicate that 57% of the bridge deck in lanes 1,2, and 3 has a rebar cover depth between 3 in. to 4 in. Therefore, an average of 3.5 in. was used in the load rating (as detailed in section 6.3.2). According to the as-built plans, the concrete cover for the deck top layer rebars was 2.5 in. To verify the top rebar cover, three of the drilled cores are shown in Figures 6-20(a-c) to verify the accuracy of the GPR readings [Figures 6-19(a) and 6-19(b)]. The locations of the cores are also shown with the black circles in the contour plots. A 5 in. core drill is located above the girder where only a full CIP concrete deck exists.
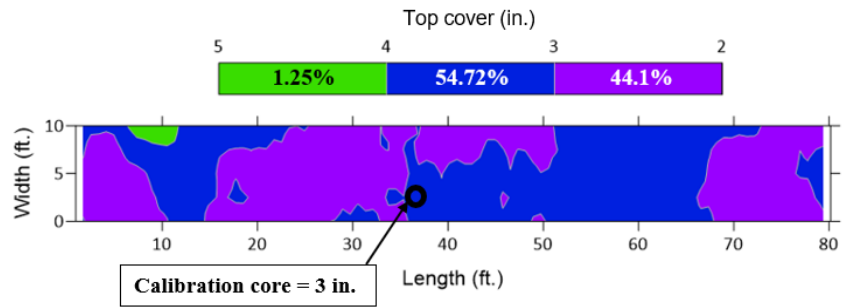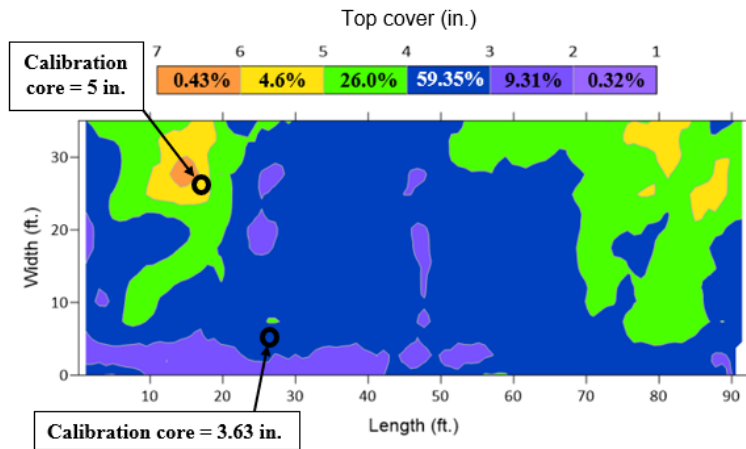
Figure 6-19 GPR contours of replaced deck: (a) Lane 1; (b) Lanes 2, 3, and gore area

Figure 6-20 Core drill calibrations: (a) Lane 1E, 3.0 in; (b) Lane 2E, 3.63 in.;(c) Lane 3E, 5 in.

The delamination of the replaced EB bridge deck, shown in Table 6-10, shows significant improvement of the bridge deck delamination. No severe delamination was detected in lane 1E [Figure 6-21(a)]. Figure 6-21(b) additionally shows a similar same trend as for those of lane 1E; moreover, the severe delamination percentage is negligible.

Table 6-10: Summary of delamination on the replaced EB bridge deck

Level of Delamination	Replaced Deck	
	Lane 1E	Lanes 2E, 3E, and gore area
No Delamination (%)	56	63
Moderate Delamination (%)	44	37
Severe Delamination (%)	0	0.32
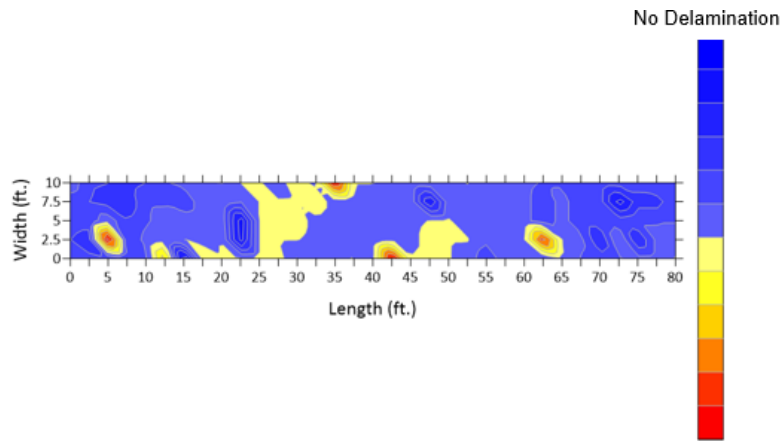
(a)
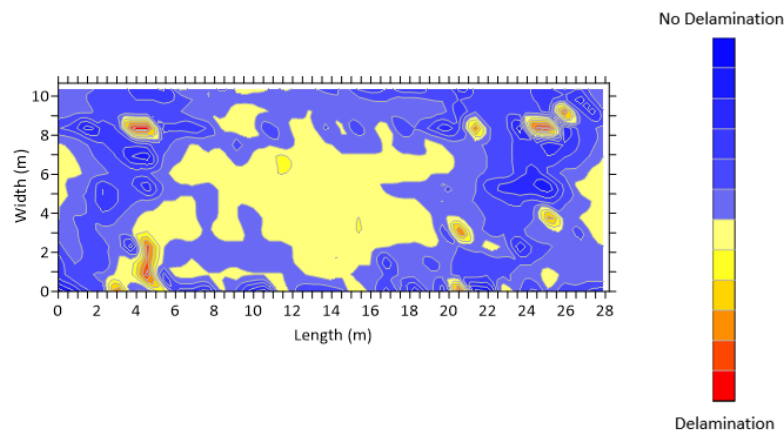
(b)

Figure 6-21 IE plots of replaced EB deck: (a) Lane 1E; (b) Lanes 1, 2,3, and gore area

6.2.3 EB NDE scanning Comparison

The GPR results from the follow-up NDE scanning of the replaced deck were then compared with the results of the previous scanning. Table 6-11 shows the key differences between the NDE scanning results based on the GPR top cover reinforcement in most of the scanned deck area as well as the difference in the core drill calibrations. The data in Table 6-11 confirms that the top rebar cover depth from the follow-up test is significantly higher than the depth from the previous testing. As a result, the negative moment capacity of the deck is significantly reduced.

Since the replaced deck has no severe delamination, especially in the negative moment zone, the girder contribution should be considered as well to resist the live load.

Table 6-11: Key differences in GPR results

Parameters	Previous Test	Follow-up Test
Ranges of top cover in most scanned areas (in.)	1-1.5	3-4
Average top rebar cover depth (in.)	1.25	3.5
First core drill calibration (in.)	1.5	3.0
Second core drill calibration (in.)	2.0	3.63
Third core drill calibration (in.)	2.15	4.0
Fourth core drill calibration (in.)	2.25	5.0

Table 6-12 presents the percentage of the severe delamination from the previous test at 52% for lanes 2E, 3E, and gore area, while in the follow-up test, the percentage of the severe delamination was only 0.32% for the same lanes (Table 6-12). For lane 1E, the severe delamination found from the previous load test was almost removed through the re-decking process.

Table 6-12: Key differences in IE results

	Levels of Delamination			
	Previous Test		Follow-up Test	
Type	Lane 1E	Lanes 2E, 3E, and Gore area	Lane 1E	Lanes 2E, 3E, and Gore area
Severe Delamination (%)	12	52	0	0.32

6.3 Load Rating

The bridge load rating (BLR) is a critical indicator to determine if a bridge requires load posting. MBE represents two methods for bridge load rating as follows: (1) LRFR using HL-93 design truck and (2) LFR utilizing HS-20 design truck. Since TxDOT is currently using HS 20 design truck for load rating and occasionally for bridge design, the LFR method was followed to establish the load rating. Two levels of load rating, inventory and operating, were evaluated. R.F. of 1.0 or higher suggests that the bridge can safely carry the vehicle for which it was rated. The R.F. of the LFR method is given in Equation 6-3, according to [3, 4]. Then, the R.F. is multiplied by the HS-20 truck weight to determine the bridge member rating (BMR) Equation 6-4.

$$\text{R. F.} = \frac{C - A_1 x D}{A_2 x (L + I)} \tag{6-3}$$

$$\text{BMR} = \text{RF x W} \tag{6-4}$$

Where:

R.F. = Rating factor for the live load carrying capacity

C = Nominal capacity of the structural component

D = Dead load effect on the member

L = Live load effect on the member

I = Impact factor to be used with the live load effect

A_1 = Factor for dead loads = 1.3

A_2 = Factor for live load based on rating level (inventory = 2.17 and operating = 1.3)

BMR = Bridge member rating (tons)

W = Weight of nominal truck used in determining the live load effect (tons)

Typically, based on the bridge deck delamination condition, the bridge load rating method is determined. If the bridge deck is severely delaminated, then, two cases can be considered

individually for the load rating of the bridge as follows: (1) positive and negative deck moment capacities in the transverse bridge direction; and (2) composite girder capacity. Otherwise, only positive deck moment capacity and option 2 should be considered. Afterwards, the lowest component rating from options 1 and 2 controls the overall load rating of the bridge.

6.3.1 Original EB and WB Decks

✓ **Deck Capacity**

The deck capacity was calculated, using the GPR and IE data, with the following detailed procedures:

➤ The mild steel rebar size and spacing of the top mat, from the as-built drawing of EB and WB bridges were #5 at 9 in. o.c. The panel dimensions used were 8.6 ft. x 8 ft. x 4 in. and were derived from the TxDOT standard panel drawing. In EB and WB, a total of 16 prestressing steel strands were used with 6 in. spacing, which is the maximum spacing specified by TxDOT. Additionally, 3/8 in. diameter, 270 ksi, low relaxation steel strands were used in the calculation.

➤ The moment capacity of the deck was calculated for a 12 in. wide strip along the length of the girder, and the strip length was assumed to be the spacing of the girders in both bridges.

➤ GPR data was used in the EB and WB bridges to find the concrete cover of the negative mild steel near the girder lines. The negative region was determined to be 2.67 ft. and 2.77 ft., respectively, from both sides of the centerline of the girder and was calculated using the point of contra-flexure in a continuous deck. Furthermore, the negative region was verified using SAP2000 (2016). In the EB and WB bridges, approximately 75% and 70% of the negative moment region had a top cover of 1.5 and 2.25 inches, respectively. Figures 6-22(a) and 6-22(b) show the girder line edges (black lines) and the analyzed negative moment region (hatched area) of the EB and WB bridges, respectively.

5.35'

(a)

5.54'

(b)
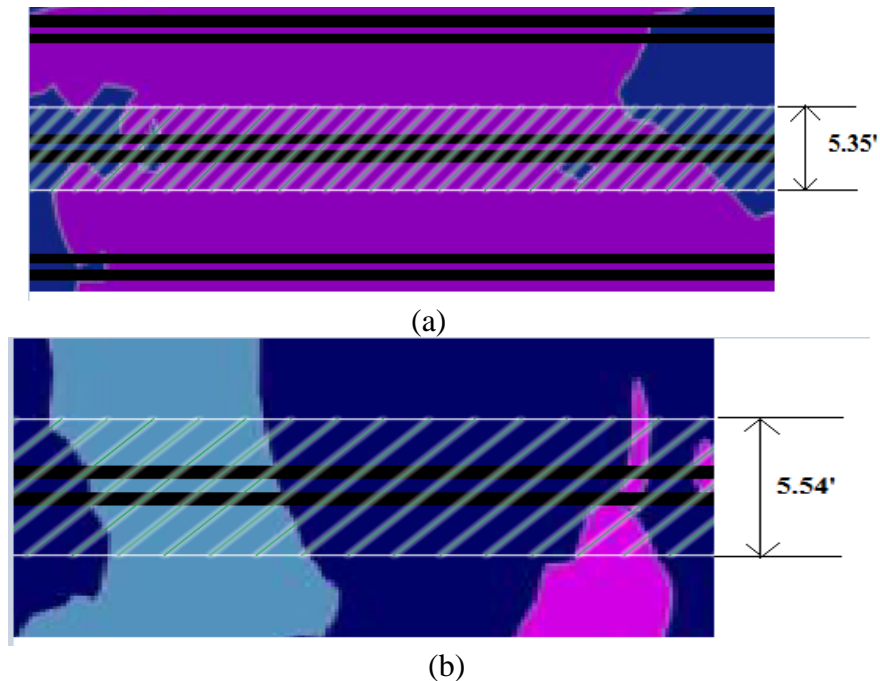
Figure 6-22 Negative moment region from GPR data: (a) EB Bridge; (b) WB bridge

➢ The negative moment capacity of the deck was calculated without using a strength reduction factor (Ø) of 0.9 since letter C in the load rating equation is expressed as the nominal moment capacity. A value of 1.0 was used for the design positive moment capacity.

➢ The GPR data was not used in determining the positive moment capacity of the deck for several reasons. Firstly, the GPR deck scan only determined the location of the top rebars. To determine the location of bottom rebars, the GPR scan had to be conducted from underneath the deck, which would have been difficult and time consuming. A handheld GPR antenna must be used for this purpose. Secondly, the PCPs mainly contribute to the positive deck moment capacity, and the strand placement in PCPs is generally much more uniform than the rebar placement in CIP deck.

➢ The percentages of delamination for the negative and positive moment regions of EB and WB provided by IE data were found. The former was measured at 2.67 ft. and 2.77 ft., respectively, from both sides of the centerline of the girder, while the latter were measured at 4.32 ft. and

112

4.48 ft., respectively. Figures 6-23(a) and 6-23(b) show the positive and negative moment regions (hatched areas) of EB and WB bridges, and the girder line edges (blue lines) show the locations from which the percentage of delamination was extracted.

(a)

(b)
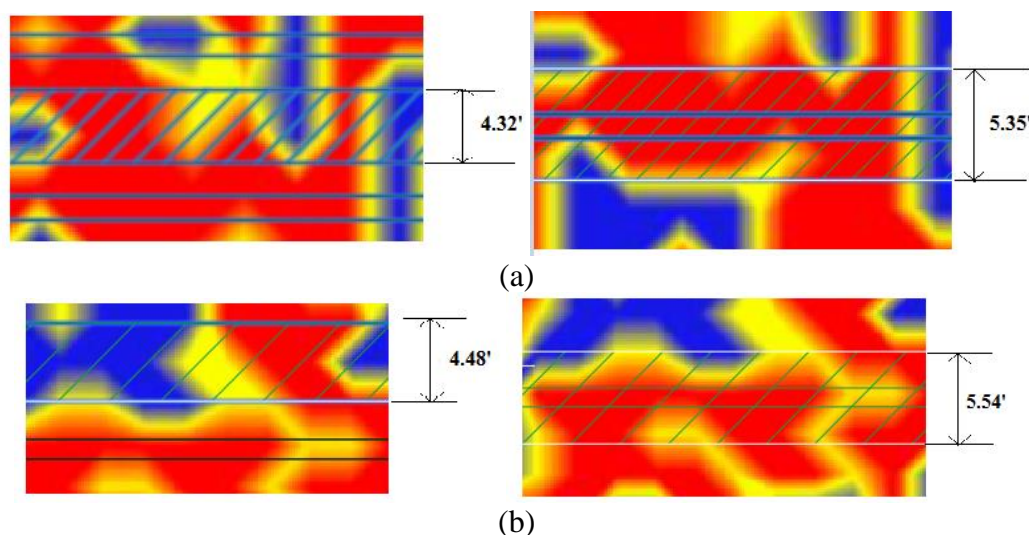
Figure 6-23 Positive (left) and negative (right) moment from IE: (a) EB bridge; (b) WB bridge

The percentage of delamination on EB bridge for the positive region and negative region were found to be 48% and 60%, respectively while the percentage of delamination on WB bridge for the positive and negative regions were 48% and 51%, respectively. To be conservative, an average between the percentage of delamination of both regions in EB and WB bridges was applied to reduce the capacity of both positive and negative moments, as illustrated in Tables 6-13 and 6-14, respectively. Tables 6-13 and 6-14 show the deck moment capacities of the EB and WB bridges calculated from GPR and IE data, respectively.

Table 6-13: Deck moment capacity of the original EB bridge deck

Parameter	Moment Type	
	Positive Moment	Negative Moment
Nominal Moment (k-ft./ft.)	21.30	14.60
Average Delamination (%)	54	54
Reduced Nominal Moment (k-ft./ft.)	10.0	7.0

Table 6-14: Deck moment capacity of original WB bridge deck

Parameter	Moment Type	
	Positive Moment	Negative Moment
Nominal Moment (k-ft./ft.)	20.30	12.60
Average Delamination (%)	49.50	49.50
Reduced Nominal Moment (k-ft./ft.)	10.30	6.40

Since no dynamic load test was performed for the previous load test, the live load moment was determined by using HS-20 loading, including an impact factor of 1.3, according to AASHTO Standard Specification (2002). The detailed hand calculation is provided in Appendix B.

Tables 6-15 and 6-16 show a summary of the ratings for the LFR method of EB and WB bridges, respectively.

Table 6-15: Deck moment rating factor and load posting of original EB bridge deck

Rating Level	Governed Moment Type	
	Negative Moment	
	R.F.	BMR (kip)
Inventory	0.46	33.12
Operating	0.77	55.44

Table 6-16: Deck moment rating factor and load posting of original WB bridge deck

Rating Level	Governed Moment Type	
	Negative Moment	
	R.F.	BMR (kip)
Inventory	0.43	30.96
Operating	0.71	51.12

Figure 6-24(a) displays the negative rebar cover depth variation vs. R.F. of the original EB bridge deck. According to the data, the load rating decreases as the rebar cover depth increases. Moreover, the top rebar cover of the deck was 2 in., according to the bridge as-built drawing. If the cover value was only considered in the rating calculation, the bridge would have carried HS-20, but considering the GPR and IE collected data, the moment capacity was reduced, which accordingly affected the load rating. Figure 6-24(b) then shows the effect of delamination on the bridge load rating in the positive moment location. The deck delamination has the same trend as

the rebar cover, but the data indicates that the bridge deck can still carry the HS-20 truck if the delamination percentage is less than or equal to 35%.
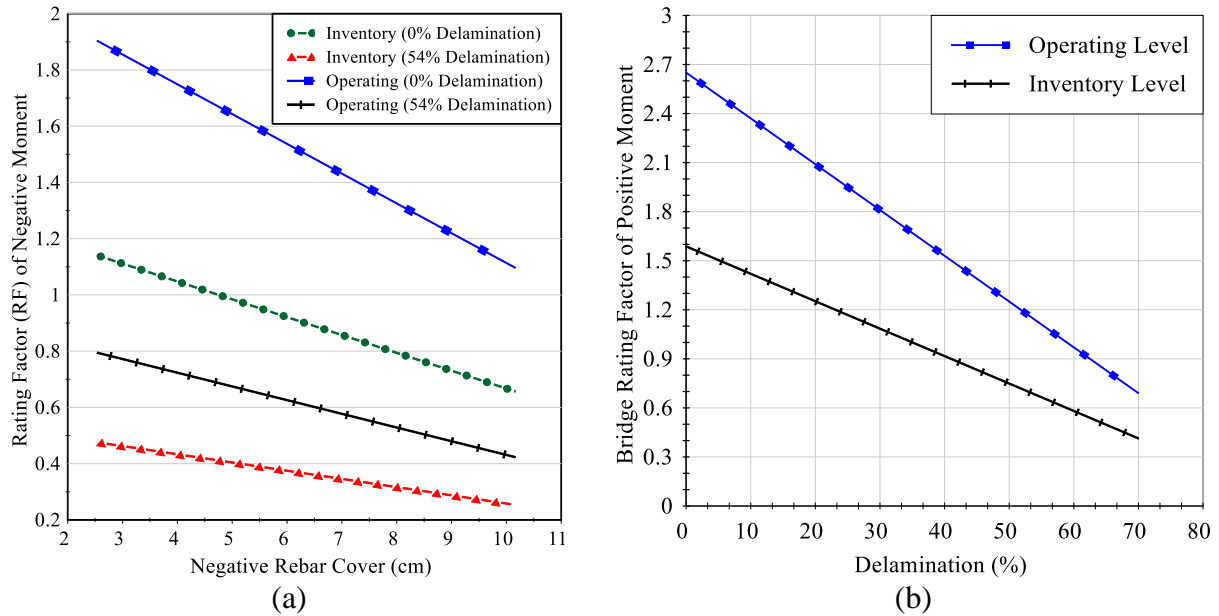
Figure 6- 24 R.F. of the EB deck versus: (a) different cover variations; (b) delamination status

✓ **Composite Girder Capacity**

The load rating of a composite girder and deck was selected to determine the girder capacity. Moreover, the load rating was calculated manually using the LFR method (AASHTO, 2018). Appendix B shows a sample calculation for load rating, and the result of the bridge load rating of EB and WB bridges is shown in Tables 6-17 and 6-18, respectively. When partial-composite action was applied, using the average neutral axis location from the load test, the girders were still safe for HS-20 standard vehicles for both the inventory and operating level. Using the rating factor that assumes partial-composite action was more practical in this case because the load test confirmed partial-composite action and a reduced girder capacity.

Table 6-17: Composite girder moment rating factor and load posting of original EB bridge deck

Composite Girder Rating of EB Original Deck				
Rating Level	R.F. assuming full-composite action	Member Rating (kip) assuming full composite action	R.F. assuming partial-composite action	Member Rating (kip) assuming partial composite action
Inventory level	1.66	119.52	1.57	113.040

| Operating level | 2.76 | 198.72 | 2.63 | 189.36 |

Table 6-18: Composite girder moment rating factor and load posting of original WB bridge deck

Composite Girder Rating of WB Original Deck				
Rating Level	R.F. assuming full-composite action	Member Rating (kip) assuming full composite action	R.F. assuming partial-composite action	Member Rating (kip) assuming partial composite action
Inventory level	1.59	114.48	1.55	111.60
Operating level	2.66	191.52	2.58	185.76

6.3.2 Replaced EB Deck

Since the replaced EB deck was recently re-constructed, and the deck had almost 0% severe delamination in all EB bridge lanes, the bridge load rating was calculated by accounting only the positive moment capacity and the composite girder capacity. The lowest of the two capacities were selected to represent the overall bridge rating.

✓ **Positive Deck Capacity**

Since a GPR scan was only performed on the top of the bridge deck, and PCPs mainly contribute to the positive deck moment capacity, GPR is not beneficial to use in the positive moment zone. From the IE data, the calculation of percentage delamination was based on lanes 1E, 2E, gore area, and 3E. The 2-D IE contour, however, cannot verify the depth of delamination. To be conservative, the average between the delamination of all lanes (15%) was applied to reduce the positive moment capacity. Table 6-19 shows the calculated positive moment capacity of the deck.

Table 6-19: Deck moment capacity from the follow-up test

Parameter	Moment Type
	Positive Moment
Nominal Moment (k-ft./ft.)	22.2
Average Delamination (%)	15
Reduced Nominal Moment (k-ft./ft.)	19.0

Since the follow-up test involved a dynamic load test, the deck R.F. for HS-20 loading was determined using the IM found from the follow-up test and also from the AASHTO Standard Specifications (2002). An IM moment included an impact factor of 1.24 which was determined from the follow-up load test as well as an impact factor of 1.3, according to AASHTO Standard Specifications (2002). Therefore, R.F. of deck was performed twice based on the recent load test results and AASHTO Standard Specifications (2002). Tables 6-20 and 6-21 show a summary of ratings for the LFR Method using HS-20 truck employing IM that was determined using AASHTO Standard Specifications (2002) and a follow-up load test, respectively.

Table 6-20: Deck moment rating factor and load posting from AASHTO standard specs. (2002)

Rating Level	Deck R.F.- HS-20 Truck	
	AASHTO IM	
	R.F.	BMR (kip)
Inventory	1.40	100.80
Operating	2.34	168.48

Table 6-21: Deck moment rating factor and load posting from follow-up load test

Rating Level	Deck R.F.- HS-20 Truck	
	IM from Follow-up Test	
	R.F.	BMR (kip)
Inventory	1.47	105.84
Operating	2.46	177.12

✓ **Composite Girder Capacity**

Both full and partial CIP-girder composite actions were conducted. The data suggests that rating factors utilizing AASHTO Standard Specification (2002), as shown in Table 6-22, greatly differ from the LRFD (2020) and load test data [Tables 6-23 and 6-24], respectively as LLDF in Standard Specification (2002) is expressed only as a function of girder spacing, while in LRFD, LLDF has multiple parameters, as mentioned in Table 3. Therefore, LRFD provides more accurate prediction of LLDF, which is close to the field test data. When partial-composite action was

applied using the average neutral axis location from the load test, the girders were still safe for

HS-20 standard vehicles for the inventory levels and operating levels. Using the R.F. that assumes

partial-composite action was more practical in this case because the load test confirmed partial-

composite action and a reduced girder capacity.

Table 6-22: Composite girder RF and load posting according to AASHTO Standard Spec. (2002)

Composite Girder Rating- AASHTO-Standard Spec. (2002)				
Rating Level	R.F. assuming full-composite action	Member Rating (kip) assuming full composite action	R.F. assuming partial-composite action	Member Rating (kip) assuming partial composite action
Inventory level	1.66	119.52	1.49	107.28
Operating level	2.77	199.44	2.49	179.28

Table 6-23: Composite girder RF and load posting according to AASHTO LRFD Spec.

Composite Girder Rating- AASHTO-LRFD Spec. (2020)				
Rating Level	R.F. assuming full-composite action	Member Rating (kip) assuming full composite action	R.F. assuming partial-composite action	Member Rating (kip) assuming partial composite action
Inventory level	3.26	234.72	2.93	210.96
Operating level	5.44	391.68	4.89	352.08

Table 6-24: Composite girder RF and load posting according to follow-up test data

Composite Girder Rating- Follow-up Test				
Rating Level	R.F. assuming full-composite action	Member Rating (kip) assuming full composite action	R.F. assuming partial-composite action	Member Rating (kip) assuming partial composite action
Inventory level	4.5	324.0	4.0	288.0
Operating level	7.5	540.0	6.74	485.28

6.4 FE Modeling

6.4.1 FE Mesh Sensitivity Analysis

A mesh sensitivity analysis was performed using Richardson's extrapolation formula

(Cook et al. 2002) to determine the optimum mesh size. The formula is presented in Equation 6-5.

$$\phi_\infty = \frac{\phi_1 h_2^q - \phi_2 h_1^q}{h_2^q - h_1^q} \tag{6-5}$$

Where:

ϕ_∞ = Quantity from infinite mesh

ϕ_1 = Quantity of stress or deflection from 1st mesh

h_1 = Characteristic length of 1st mesh = $\sqrt{M_n^2 + M_n^2}$

ϕ_2 = Quantity of stress or deflection from 2nd mesh

h_2 = Characteristic length of 2nd mesh

q = Optimal extrapolation exponent (q value that leads to linear curve with $R^2 = 1.0$)

M_n = mesh size of 1st, 2nd, or 3rd selection

A convergence study was initially conducted by varying the mesh sizes from 3 to 7 inches. The study considered the mid-span deflection of the girders as a parameter. However, the deflection- characteristic length (h^q) graph did not yield a linear curve ($R^2 = 1.0$) because the values of the mesh size were nearly identical. The analysis was also not continued for the 3-inch size due to insufficient computer memory. Another study was conducted by varying the mesh sizes from 4 to 16 inches. Table 6-25 shows the calculated Richardson's formula parameters and deflection values of each mesh size from the FEM model. As shown in Figure 6-25, the graph yields a linear curve, and the optimal value of extrapolation exponent (q) is equal to 0.65. Next, the deflection values of each mesh size were compared to the actual deflection from the infinite mesh obtained from Equation 6-5, and the data indicates that 8 inches is the optimum mesh size.

Table 6-25: Parameters for Richardson's extrapolation formula

Length (Mesh Size) (in.)	Deflection (in.)	Char. Length (h) (in.)	Char. Length (h^q)
4	0.241	5.65	3.08
8	0.245	11.31	4.83
16	0.250	22.62	7.59
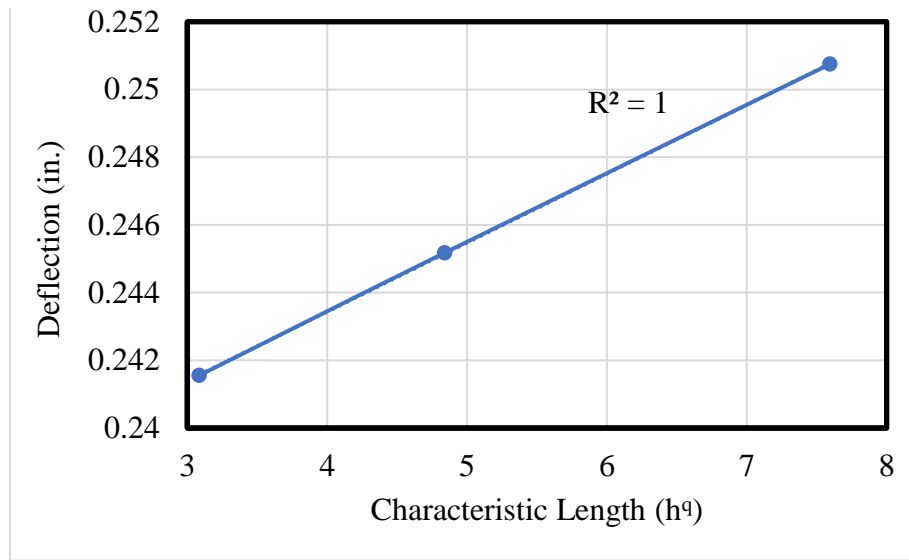
Figure 6-25: Deflection-characteristic length (hq) graph

6.4.2 FE Model Calibration

The calibration of the original EB bridge with field test data was initially based on the tie constraint option between the girder and CIP deck in FE. The strain value at mid-span of the girder was additionally used as a basis for the primary calibration. The measured strain determined from FE was lower than the experimental strain, as tie constraint tends to provide full composite action, as shown in Table 6-26. The result from the previous load test suggests that partial composite action was achieved. Therefore, the tie constraint option was not a valid option. As the bridge decks suffered from severe delamination as well as cracks, the deck stiffness was reduced to account for the defect, and then the strain response was compared to the field load test data (Table 6-27). The measured strain accordingly increased when the deck stiffness was reduced at the patched area, as well as at 50% reduction of entire deck.

Table 6-26: Model calibration using Tie Constraint

EB Bridge strain calibration data, old deck – Path 2, section 2 = 35 ft.		
Designated Girder	Experimental Data (με)	FEM Data (με)
Girder B	50.6	28.14

Table 6-27: Calibration using deck stiffness

EB Bridge strain calibration data, old deck – Path 2, section 2 = 35 ft.		
Deck reduction at Patched Area		
Designated Girder	Experimental Data (µε)	FEM Data (µε)
Girder B	50.6	29.61
50% Deck reduction		
Girder B	50.6	31.4

To further refine the model and account for partial composite action, cohesive contact behavior between the CIP/PCP and CIP/girder surfaces was considered along with deck stiffness. The CIP/PCP and CIP/girder surfaces were assigned as master and slave, respectively. The consideration of cohesive contact behavior was also based on the previous load test result, which showed that 48% composite action was achieved. Furthermore, the shear stiffness parameters (K_{ss} and K_{tt}) in ABAQUS were varied between these surfaces while keeping the normal stiffness coefficient as a constant large number (10^9 lb./in^2). Several runs with different shear stiffness parameters ranging from 1000 to 10^6 lb./in^2 were then performed. Table 6-28 shows different shear stiffness coefficients used in the FEM with their corresponding strain values at mid-span of girder B under Path P2. The data in Table 6-28suggests that as the shear stiffness increases, strain reading increases. The increase in shear stiffness coefficient also reduces the interfacial horizontal shear force responsible for the slip between CIP and PCP concrete layers.

Table 6-28: Shear stiffness coefficients used in FEM

Shear stiffness coefficient (K_{ss} and K_{tt})	Strain value (µε)
1000000	34.0
10000	35.97
5000	40.14
1000	42.65

To further calibrate the FE, numerous viscosity parameters ranging from 0.01 to 0.0001 were used. The viscosity parameter in FE moreover plays an important role in softening the structure, which in turn increases the strain. As the viscosity parameter decreases, the strain response and the computational time of the model increase. Table 6-29 shows different viscosity parameters used in FE with their corresponding strain values at mid-span of girder B for Path 2.

Table 6-29: Viscosity parameters used in FEM

Viscosity parameters (μ)	Strain value (με)
0.01	33
0.0005	45
0.0001	50

After the optimal shear coefficient and viscosity parameter were determined, the measured strain values in FE of girders B,C, and D were compared to the field load test data (Figure 6-26). Strain readings at girders B and C exhibited nearly the same strain from the field test as the patch load in FE was above the girders.
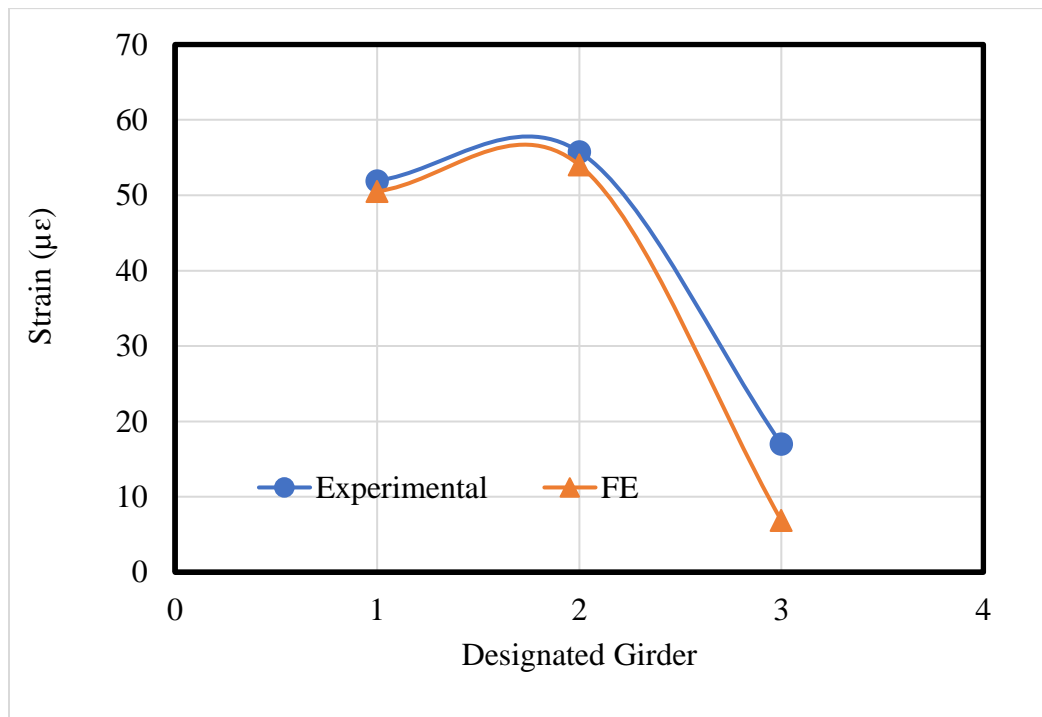
Figure 6-26: Field test vs. FE model strain data

6.5 PCP Failure Mechanism

To investigate the possible causes behind the localized deck failure that occurred on the EB and WB bridges, sufficient information should be collected about the bridge condition prior to the occurrence of the failure. This was achieved by reviewing the TxDOT inspection reports on both bridges. The following bridge comments from the TxDOT inspection reports are related to the previous bridge deck and PCPs.

- *EB Bridge Comments:*

Condition Rating Report

Deck (Item 58)

Min.:

Description:

Rating:

0 - Deck - Rating

5 - Fair Condition (minor section loss)

Top surface of deck has minor abrasion/wear in the wheel paths. Deck has minor transverse cracking where continuous over the supports. Deck soffit has minor transverse cracks with light efflorescence at cast-in-place sections over Bents 2 & 4 from the West. Soffit of deck overhangs have isolated transverse cracks with efflorescence. The soffit of deck at the SW corner has an ~1' x 2' spall with exposed rusted rebar (see photo). The top surface of the deck in Span 2 from the West has an ~10 SF concrete patch in the right lane. The P/S deck panels directly under the concrete patch have water staining and hairline cracks with efflorescence. There are 4 P/S concrete deck panels that show this type of deterioration (see photo). The adjacent bridge had similar deterioration to the P/S deck panels in 2016 and sometime between the 2016 inspection and current inspection, the deck over the P/S deck panels with water staining and hairline to minor cracks with efflorescence had a full-depth concrete repair.
***During our routine inspection on 5/22/18, the area of deck soffit water staining and hairline cracks with efflorescence were photographed and noted in the report. The deterioration was isolated to only 4 P/S deck panels in Span 2 from the West. A concrete patch was previously installed over this area. As the team leader inspected the deck from the outside South shoulder, corners of deck and striped median, the team leader did not observe any signs of distress or deflection on the top side of the deck near or around the previously installed deck patch in Span 2, nor hear any unusual sounds under live loads. The deck was originally rated "6" due to water staining and hairline cracks to deck panels being limited to only 4 panels in Span 2. However, approximately one month after 5/22/2018 inspection, on 6/18/2018 the deck experienced a localized punch-through failure in Span 2 over the subject deck panels. (See TxDOT Photos taken 6/18/2018). Continued below...

123

NOTE: 1. On 5/22/18, four P/S deck panels between beams 3 & 4 from North in Span 2 from West have evidence of water staining and hairline cracks with efflorescence. This deterioration is located below a small patch in top surface of deck.
2. On 6/18/18, the P/S deck panel just West of the mid-span diaphragm fractured and failed causing a localized deck failure (~7' W x 15' L) that required a full-depth repair (see additional photos).

- *WB Bridge Comments:*

Condition Rating Report

Deck (Item 58)

Min.:

Description:

Rating:

0 - Deck - Rating

5 - Fair Condition (minor section loss)

Top surface of concrete deck has minor transverse cracking (mostly over supports) and minor spalls along the joints. Deck has minor abrasion/wear in the wheel paths. Soffit of deck at C-I-P sections and overhangs have hairline to minor transverse cracks with efflorescence. The edge of the deck at the SW corner has minor spalling due to contact with the backwall. In the previous 2016 inspection report, it states widespread hairline to minor alligator cracking with some efflorescence in the P/S deck panels between Beams 3 & 4 from the NW in the center lane of Span 4 from the West. Also, the 2016 inspection report states that 2 concrete deck patches were in place with some minor spalling around the patches. The concrete patches were noted as directly above where the P/S deck panels had widespread hairline to minor alligator cracking with some efflorescence. Sometime between 5/25/2016 (the date of the 2016 inspection report) and 5/22/2018 (the date of most recent inspection report), a full-depth concrete repair was performed to the affected area in Span 4 from the West. The full-depth repair appears to be the size of one P/S deck panel. The steel deck form for full-depth repair is still in place (see photos). However, three other P/S deck panels between beams 3 & 4 adjacent to the full-depth repair remain as previously described (hairline to minor soffit cracks with efflorescence) [NOTE: Based on recent deck failure in adjacent EB Str. – 378, deck rating has been lowered to a 5.] There is no documentation in bridge folder, InspectTech or PONTEX to indicate why or when the deck was repaired and no repair plans or photos.

Comments:

(1) Minor transverse cracking (< 1/16" wide) (predominately over interior Bents where Deck is continuous and construction joints were not installed) on Deck surface (most cracking has been sealed). Patches (~ 3' x 3' and ~ 3' x 8') in place in center lane of Span No. 4 with minor spalling of patches and Deck around the patches. (Photos 8 and 9) Widespread hairline to minor alligator cracking (some with efflorescence) of Deck Panels between Girder Nos. 3 and 4 (from NW) in Span No 4. (This area is directly below patches in Deck surface.) (Photos 10 and 11) Isolated minor spalling at joints on Deck surface. Minor cracking with efflorescence on underside of Deck at cast-in-place portions. Minor cracking at underside of overhangs that extend to the vertical edge of Deck. Minor spalling with exposed reinforcing steel at edges where Deck is in contact with Backwalls. (Photo 12)

(2) Open joints are pinched closed.

(3) Minor accumulation of dirt/gravel in gutterlines.
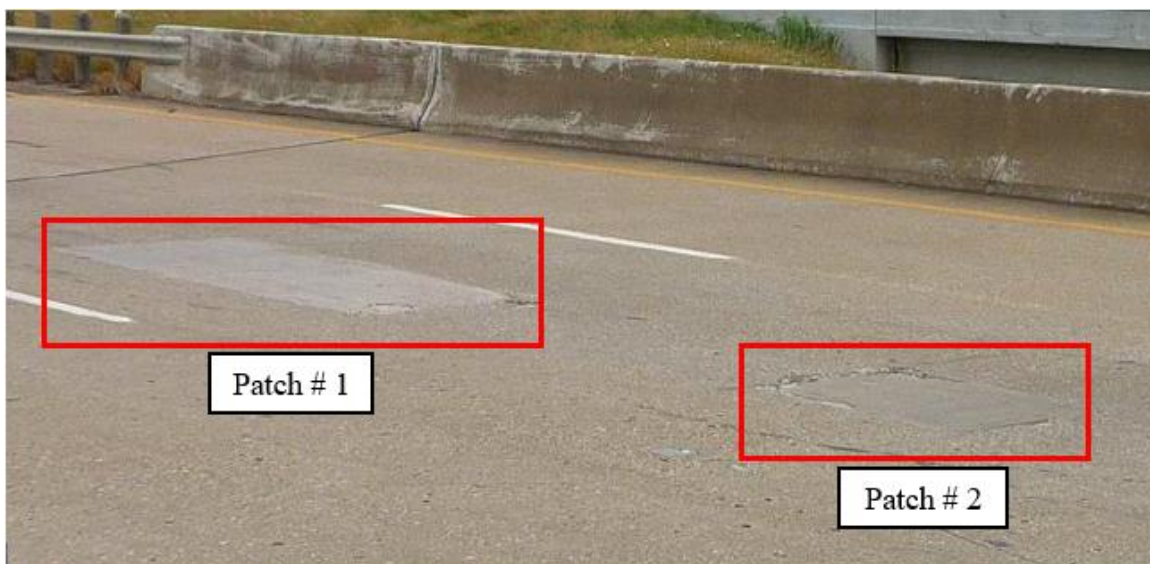
Patch # 1

Patch # 2

125

NOTE: Widespread hairline to minor alligator cracking (some with efflorescence) of Deck Panels between Girder Nos. 3 and 4 (from NW) in Span No 4. (This area is directly below patches in Deck surface.)

NOTE: Widespread hairline to minor alligator cracking (some with efflorescence) of Deck Panels between Girder Nos. 3 and 4 (from NW) in Span No 4. (This area is directly below patches in Deck surface.)

The following flowchart summarizes the inspection report findings which were mentioned above on the PCP's previous condition.

```
                        ┌──────────────────────────┐
                        │  PCP Previous Condition  │
                        └──────────────────────────┘
                                     │
              ┌──────────────────────┴──────────────────────┐
              │                                             │
       ┌─────────────┐                             ┌─────────────┐
       │  EB Bridge  │                             │  WB Bridge  │
       └─────────────┘                             └─────────────┘
              │        ┌──────────────┐                   │       ┌──────────────┐
              │        │ On 5/22/2018 │                   │       │ On 5/25/2016 │
              │        └──────────────┘                   │       └──────────────┘
```

EB Bridge — On 5/22/2018

4 PCPs showed evidence of water staining and **hairline cracks with efflorescence**

↓

This deterioration was located **below a small patch, 3ft.x3ft,** on top surface of deck.

On 6/18/2018

↓

One PCP, located just west of the mid-span diaphragm, **fractured and failed.**

↓

Due to the **fractured PCP**, the deck experienced **a localized punch-through**

↓

Full-depth repair was performed on **all four PCPs**

WB Bridge — On 5/25/2016

4 PCPs showed evidence of water staining, hairline, and **minor alligator cracking**

↓

Two concrete patches measured 3ft. x 3ft. and 3ft. x 8ft. were **directly above these**

↓

Concrete spalling was observed **around some edges of the patch area**

Between 5/25/2016 and 5/22/2018

↓

Full depth repair was performed on **only one PCP with alligator cracking**

Based on all information provided in the inspection reports and IE result of the patch area for both the EB and WB bridges, the PCP failure mechanism is summarized as follows:

- The concrete patch was caused by abrasion/wear in the wheel paths, which is one of the damages/defects that can occur on the top of the deck. If insufficient top concrete clear cover exists, reinforcing steel will be exposed, which, in turn, requires repair. According to TxDOT Section 4: Bridge Deck Repair, regardless of the deck severity, when performing deck repairs in such cases, the cast-in-place portion should be removed to expose the top of the PCP, which then becomes the bonding interface for the repair material.

- PCP failure was localized and only observed directly under the concrete patch. Due to the concrete spalling that occurred around the patch's edges, the affected area was separated or did not act continuously with the rest of the bridge deck.

- Applied live loads from vehicles and trucks were only resisted by PCPs within the affected area. The loads caused PCPs to exhibit water staining, hairline cracking, and minor alligator cracking.

- Once one PCP fractured and failed because of localized punch, it affected the adjacent PCPs as well as the CIP deck portion above, which caused the failure to spread out.

- From the IE data, the patch area exhibited severe delamination [Figures 6-15(b) and 6-18(b)] in portions where new concrete was poured above the PCP. The delamination can occur due to steel corrosion and occurs when the reinforcing steel in the higher layer rusts, causing the steel to separate from the surrounding concrete.

- Considering that the reinforcing steel is coated and protected against corrosion, the next weakest surface is the CIP/PCP interface, according to the IE result. To justify the second weak surface, from Figure 6-18(b), only the center portion of the patched area showed no delamination as it was constructed with full CIP depth, which strongly suggests that the delamination occurred within the interface between CIP and PCP.

128

Chapter 7

BRIDGE RETROFITTING/CONSTRUCTION OPTIONS

The main objective of the retrofitting methods is to enhance the composite action and the live load-carrying capacity of the bridge by satisfying the load rating requirement where R.F. should be equal or greater than 1.0 to be considered a safe bridge. Some of the approaches discussed in this paper have been previously applied in bridge construction but only by following the TxDOT standard drawings as a reference. Chapter 7 presented multiple scenarios for each retrofitting option by conducting parametric studies, which help to establish guidelines while constructing a bridge. The bridge deck retrofitting options were then performed using FE models.

The retrofitting and construction options were divided to two categories in terms of applicable bridge deck systems and whether the bridge deck is already constructed or not, as shown in Table 7-1. The modeling involved a 1 ft. strip of concrete deck for most of the retrofitting or construction options, and one option was modeled using the girder and effective CIP concrete deck width. The 1 ft. strip of concrete deck control/pre-retrofitted model was additionally calibrated with the theoretical positive moment capacity, based on bridge's current condition, which was achieved using the cohesive interaction option in FE to create a slip between the interface of the CIP concrete deck and PCPs. After the optimal shear coefficient was identified, the coefficient was kept the same while conducting the parametric studies for the retrofitting options. As the CIP deck failure was localized and also to estimate the real deck response, only one span was only loaded. The model selection was based on two factors. The first factor was to obtain accurate results if there were any changes between the control and post-retrofitted model. The second factor was to easily acquire the moment capacity of the post-retrofitted models.

Table 7-1: Applicable Bridge deck system and conditions for retrofitting and construction options

Options	Concrete Bridge Deck System		Applicable in	
	Full Depth CIP	CIP over PCP	Existing Bridge	New Bridge
Shear Connectors	NA*	√	NA*	√
SFRC	√	√	√	√
PCP Overhang	NA*	√	NA*	√
Under-cut Anchors	√	√	√	√

*NA: Not applicable

7.1 CIP/PCP Interface Shear Connectors

Shear connectors have been previously used between girder and CIP concrete decks to provide the desired composite action needed to resist the live load. These connectors also decrease the interfacial shear force between two surfaces. Therefore, the connectors were used in the present study between CIP and PCP to increase the composite action as well as the bridge R.F. Additionally, two FE models with shear connectors, which were placed in one row and spaced at 1.5 ft., and 2 ft. in the transverse direction, were considered to mitigate any slippage between CIP and PCP. The shear connectors had a 1 ft. spacing in the longitudinal/traffic direction. Since only a 1 ft. strip of concrete deck was used, the transverse shear connectors were only shown. Figures 7-1(a-b) show the FE models showing the shear connectors at 1.5 ft. and 2 ft. Table 7-2 moreover shows a comparison of nominal moment capacity and R.F. for the control and retrofitted models determined by FE.

The data in Table 7-2 underscores the benefits of applied shear connectors on increasing the moment capacity as well as the shear connectors' ability to provide the mandatory R.F. of 1.0.

Table 7-2: Comparison between the calibrated and retrofitted models using ABAQUS

Model Type / One Row		Nominal Moment (k-ft/ft)	Rating Levels	
			Inventory	Operating
Pre-retrofitted model	Control	10.93	0.77	1.28
Retrofitted models	2 ft. spacing	12.51	0.89	1.49
	1.5 ft. spacing	13.77	1.0	1.66

| (a) | (b) |
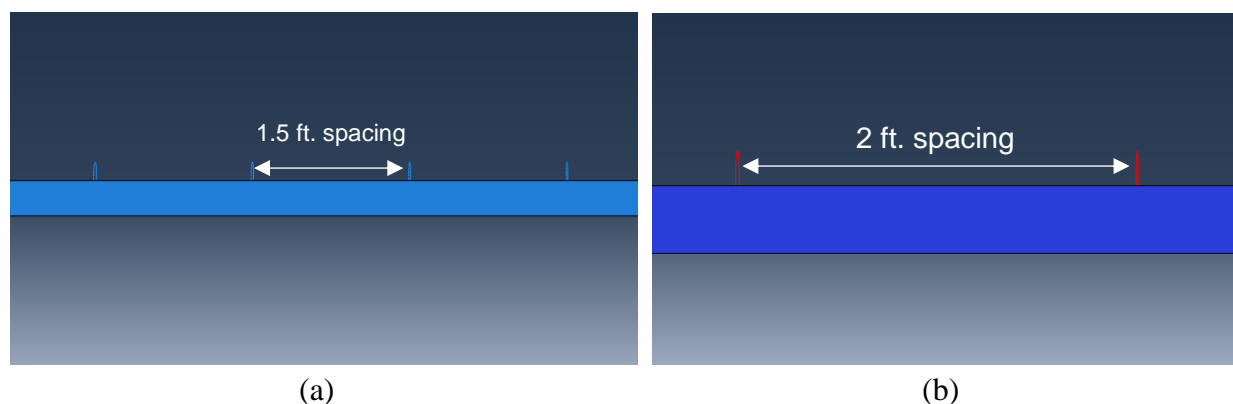
Figure 7-1 FE model view: (a) 1.5 ft. spacing; (b) 2 ft. spacing

The 100%, 0% and partial DCAs of the control can be calculated based on the ultimate load using Equation 7-1.

$$\text{DCA } (100\%) = (1 - \frac{P_{\text{full composite}} - P_{\text{partial}}}{P_{\text{full composite}} - P_{\text{non-composite}}}) \tag{7-1}$$

Where:

$P_{\text{non-composite}}$ = Ultimate load corresponding to 0%

$P_{\text{composite}}$ = Ultimate load corresponding to 100%

P_{partial} = Ultimate load corresponding to partial DCA

Table 7-3 illustrates the DCA based on the ultimate load values for different shear coefficients using the control model to determine 0%, partially composite, and 100% DCA. These values were used as a basis to determine the DCA of all the retrofitted models discussed in Chapter 7.

Table 7-3: Calculated different DCAs based on ultimate load using control model

Degree of composite actions (DCAs)-Pre-retrofitted models		
Shear coefficient ($K_{tt} = k_{ss}$)	Ultimate load (kip)	DCA (%)
10^5	16.75	100
1000 (calibrated/control model)	11.61	46
0	7.40	0

Table 7-4 shows the DCA of the retrofitted models using shear connectors found from ABAQUS. 2 ft. and 1.5 ft. shear connector models showed an increase in composite action of around 35% and 67%, respectively.

Table 7-4: Calculated DCA based on ultimate load for shear connector models

Retrofitted Shear Connector Models			
Model Type	Ultimate Load (kip)	DCA (%)	DCA Increased by (%)
2 ft. spacing	13.18	62	35
1.5 ft. spacing	14.54	76	65

7.2 Recasting the Patched Area with Steel Fiber Reinforced Concrete (SFRC)

According to TxDOT Concrete Repair Manual (2021), bridge deck repairs over relatively small areas are categorized in two ways. The first way is related to the extent of the affected area depths, while the second way is related to the speed of repairing the affected area. According to TxDOT Concrete Repair Manual (2021), regardless of the severity of the distress that occurred in the CIP sections of the deck above the PCPs, the CIP affected portion should be removed to expose the top of the PCP. Then, the area should be cleaned, and new concrete should be poured. Table 7-5 shows different types of concrete used as well as their required time to attain sufficient compressive strength to be open to traffic.

Table 7-5: Bridge concrete deck repair material

Concrete Type	Time (hrs.)	Comments
Type B Ultra-Rapid	2-4	Used a preapproved Type B Ultra-Rapid Repair material meeting the requirements of DMS 4655
Type A Rapid	6-8	Used a preapproved Type A Rapid Repair material meeting the requirements of DMS 4655
Class K	24	Used for accelerated strength gain and return to service
Class C	48-96	Used to cast new bridge decks; offers the greatest likelihood of long-term serviceability

TxDOT Special Specification 4168 (2020) indicates that SFRC can be used in the bridge deck concrete overlay to regain the concrete deck stiffness. In this paper, SFRC was used as

concrete repair material where SFRC concrete was poured immediately above the PCPs. TxDOT

Special Specification 4168 (2020) was also followed to determine the concrete type, fiber dosage,

and aspect ratio (Table 7-6). Table 7-7 then shows the fiber dosages and their corresponding fiber

percentages. Fiber dosage of 70 lb./yd^3 and aspect ratios of 40 and 55 were selected in this study

because of budget constraints. Figure 7-2 shows stress vs. strain of the selected fiber dosage and

their corresponding aspect ratios.

Table 7-6: Concrete type, fiber dosage, and aspect ratio from TxDOT spec.

Parameters	Values
Concrete Type (f_c') (ksi)	Class CO (4.6)
Aspect ratio	40-60
Straight fiber dosage (lb./cy^3 of concrete)	70-80

Table 7-7: Fiber dosage and their calculated fiber percentages

Fiber dosage	Fiber percentage (%)
70	1.73
75	1.85
80	1.98
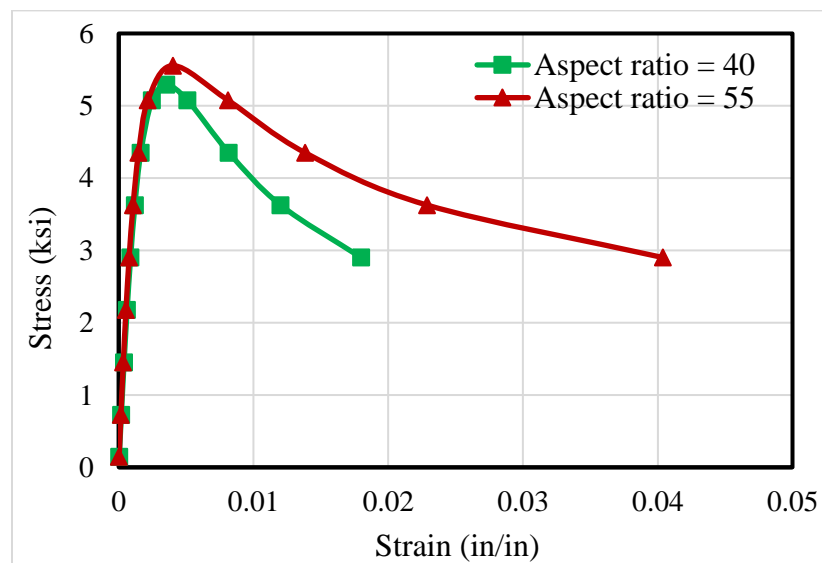
Figure 7-2: Stress vs. strain of the 70 lb./yd^3 and their aspect ratios

The retrofitted models investigated both full and partial composite actions between the

newly SFRC patched area and the PCPs. The assumption of full and partial composite actions was

made to consider the best- and worst-case scenarios. The best case is when the newly SFRC poured concrete provided a full bond with the PCPs, while in the worst case, the SFRC was partially bonded with the PCPs.

Tables 7-8 and 7-9 show a comparison of nominal moment capacity and RF for the control and retrofitted models, respectively, while assuming full and partial composite actions found from FE for the corresponding models. Figures 7-3(a-c) show the FE models of the SFRC patched area with full model, full, and partial composite actions between the CIP and PCP interface. The full composite action was then introduced using a tie constraint while the partial composite utilized cohesive interaction to allow for the interfacial slip between CIP and PCP. Table 7-10 shows the DCA of the retrofitted models of full and partial composite actions found from ABAQUS.

(a)

(b)   (c)
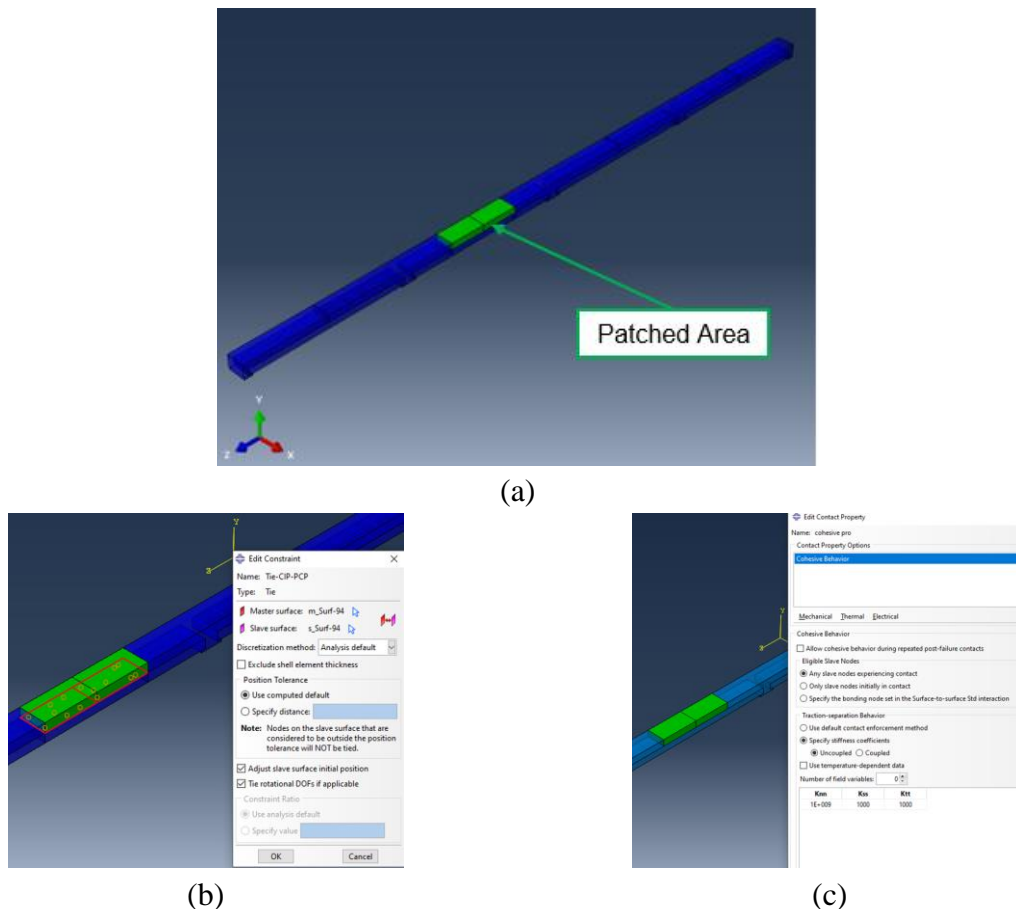
Figure 7-3: SFRC patched area model (a) Full model; (b) Full composite; (c) Partial composite

Table 7-8: Comparison between the calibrated and retrofitted models using ABAQUS

Model Type	70 lb./yd^3 – Full Composite		
	Nominal Moment (k-ft/ft)	Rating Levels	
		Inventory	Operating
Pre-retrofitted model, Control	10.93	0.77	1.28
Retrofitted models with l/d = 40	21.61	1.61	2.69
Retrofitted models with l/d = 55	21.98	1.64	2.74

Table 7-9: Comparison between the calibrated and retrofitted models using ABAQUS

Model Type	70 lb./yd^3 – Partial Composite		
	Nominal Moment (k-ft/ft)	Rating Levels	
		Inventory	Operating
Pre-retrofitted model, Control	10.93	0.77	1.28
Retrofitted models with l/d = 40	15.58	1.14	1.90
Retrofitted models with l/d = 55	15.72	1.15	1.92

Table 7-10: Calculated DCA of retrofitted models using SFRC

Retrofitted SFRC Patched Area Models- Full Composite		
Model type	Ultimate Load (kip)	DCA (%)
l/d = 40	22.20	100
l/d = 55	22.53	100
Retrofitted SFRC Patched Area Models- Partial Composite		
l/d = 40	16.22	94
l/d = 55	16.36	96

7.3 PCP Overhang Extension

To study the effect of PCP overhang extension, TxDOT as-built and standard drawings must be followed. The PCP overhang length (PCP$_L$) depends on the bedding strip width. The bedding strip width ranges can be found from the TxDOT standard drawing available on their website. Figure 7-4 shows the bedding strip width and height ranges. The maximum and minimum PCP$_L$ should also be met, which can found in the TxDOT's fabrication drawing (Figure 7-5).
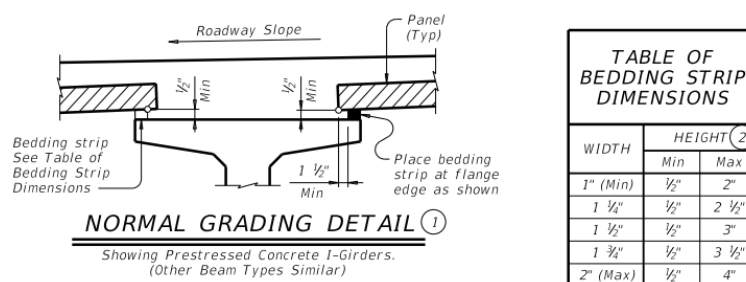
Figure 7-4: Bedding strip dimension range
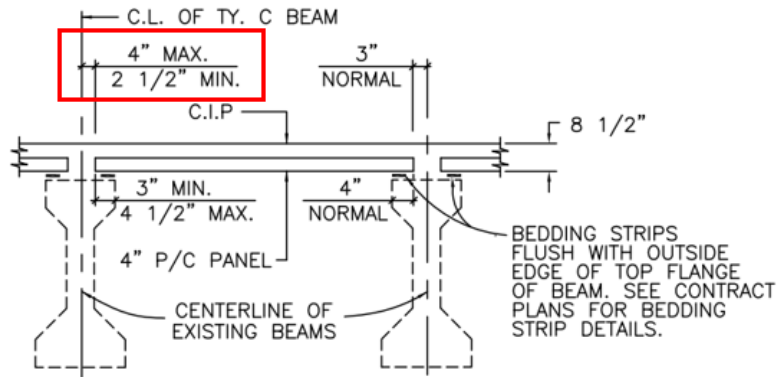
Figure 7-5: CIP/PCP cross section showing PCP overhang

The values of the PCP_L were selected based on different conditions, 2 in., and 3.5 in. and were based on typical overhang used in Type C girder and following the minimum overhang requirement specified in as-built drawing (see the red square in Figure 7-5), respectively. These conditions, along with their own values, are summarized in Table 7-11. The bedding strip height was kept the same because of the haunch of 1 in. Table 7-12 then shows a comparison of nominal moment capacity and RF for the control and retrofitted models found from FE. Next, Figure 7-6(a) represents the full FE model view of the PCPL = 2 in. Figures 7-6(b) and 7-6(c) show a more detailed depiction of the overhang conditions. Table 7-13 shows the DCA of the retrofitted models for retrofitted PCP overhang conditions.

Table 7-11: Summary of investigated PCP overhang conditions

Investigated Condition	Bedding Strip Height (in.)	Bedding Strip Width (in.)	PCP Overhang Length (PCP_L) (in.)
No Overhang	1	2	0
Type I girders, 2 in.	1	2	2
Minimum, 2.5 in.	1	1	3.5

Table 7-12: Comparison between the calibrated and retrofitted models using ABAQUS

Model Type	Nominal Moment (k-ft/ft)	Rating Levels	
		Inventory	Operating
No Overhang, $PCP_L = 0$ in.	10.93	0.77	1.28
Type I girders, $PCP_L = 2$ in.	13.64	0.98	1.64
Maximum Overhang, $PCP_L = 3.5$ in.	14.47	1.10	1.75

Table 7-13: Calculated DCA of retrofitted models using PCP Overhang Extension

Retrofitted PCP Overhang Models			
Model type	Ultimate Load (kip)	DCA (%)	DCA increased by (%)
Type I girders, PCP_L = 2 in.	14.34	74	61
Maximum Overhang, PCP_L = 3.5 in.	15.15	83	80
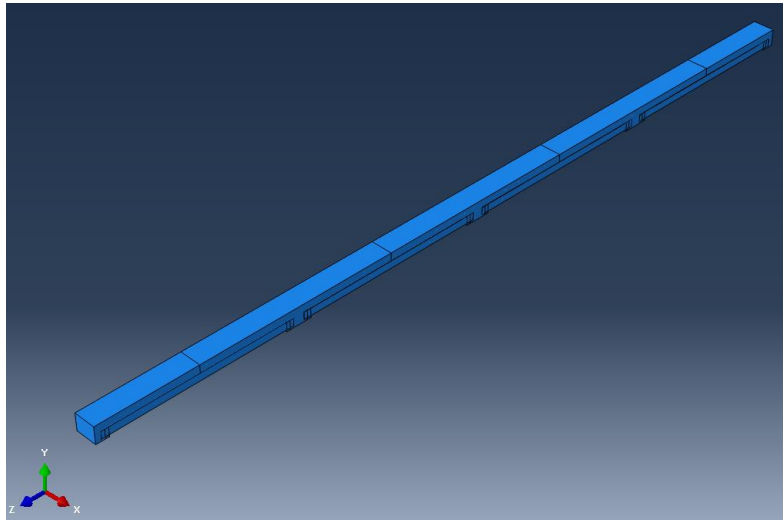
(a)
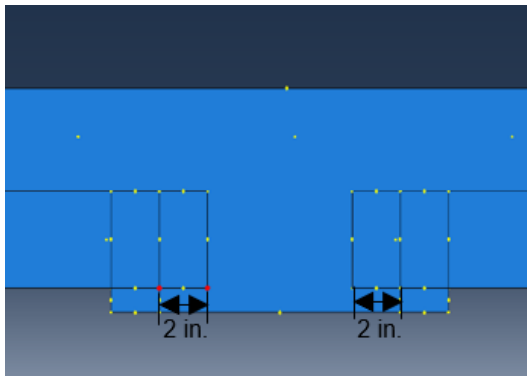
(b)
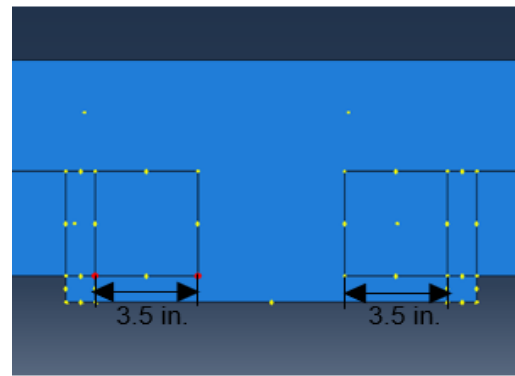
(c)

Figure 7-6 FE model view: (a) Full model; (b) 2 in. overhang; (c) 3.5 in. overhang

7.4 Enhancement of Longitudinal Reinforcement

The objective of longitudinal reinforcement in the bridge deck is to control shrinkage and temperature cracks. Figure 7-7 shows the configuration of the longitudinal reinforcements. In full-depth CIP, two steel rebar mats were placed at two layers, as shown in Figure 7-7. The top longitudinal reinforcement was designed for temperature and shrinkage cracks, while the bottom

reinforcement was designed for load distribution purposes. For the present study, as the bridge included CIP concrete deck over PCPs, the distribution reinforcement was not needed.
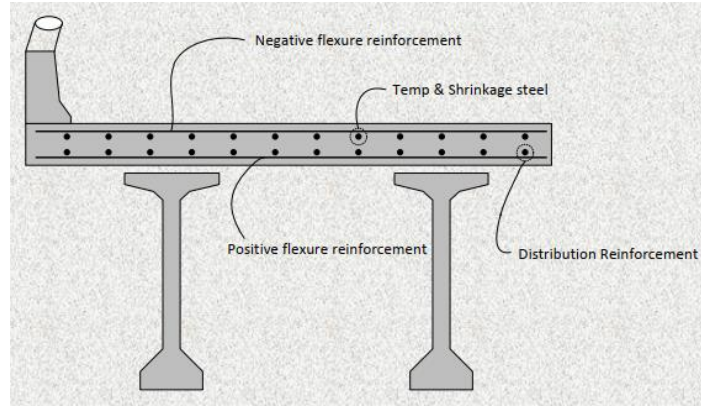
Figure 7-7: Temperature and shrinkage steel reinforcements

The No#4 steel rebar was used as the top longitudinal reinforcement in the investigated bridge. Furthermore, No#4 rebar was kept the same, and the effect of several rebar spacings were examined to check whether rebar spacings would have an impact on the bridge load rating. There are two guidelines that must be followed when selecting the rebar No. and spacing, according to AASHTO (2020). Equation 7-2 represents the rebar No. restriction, while Equation 7-3 illustrates the maximum rebar spacing that should not be exceeded.

$$A_s \left(\frac{in^2}{ft}\right) \geq \frac{1.30*b*h}{2(b+h)*f_y} \quad \text{where} \quad 0.11 \leq A_s \leq 0.60 \qquad (7\text{-}2)$$

$$\text{Least of} \begin{cases} 3 * \text{slab thickness} \\ 18 \text{ in.} \end{cases} \qquad (7\text{-}3)$$

Table 7-14 shows a comparison of nominal moment capacity and RF for the control and retrofitted models found from FE. Figure 7-8 then shows steel rebar spacings vs. inventory bridge rating factor (RF). Next, Table 7-15 presents the DCA of the retrofitted models for the retrofitted models.

Table 7-14: Comparison between the calibrated and retrofitted models using ABAQUS

Rebar Spacing (in.)	Nominal Moment (k-ft/ft)	Rating Levels Inventory
4	13.86	1.0
5	13.82	0.998
6	13.81	0.997
7	13.75	0.993
8	13.72	0.99

Table 7-15: Calculated DCA based on ultimate load

Retrofitted PCP Overhang Models			
Rebar Spacing (in.)	Ultimate Load (kip)	DCA (%)	DCA Increased by (%)
4	14.55	46.80	1.74
5	14.51	46.50	1.10
6	14.50	46.40	0.80
7	14.44	45.85	-
8	14.40	45.50	-
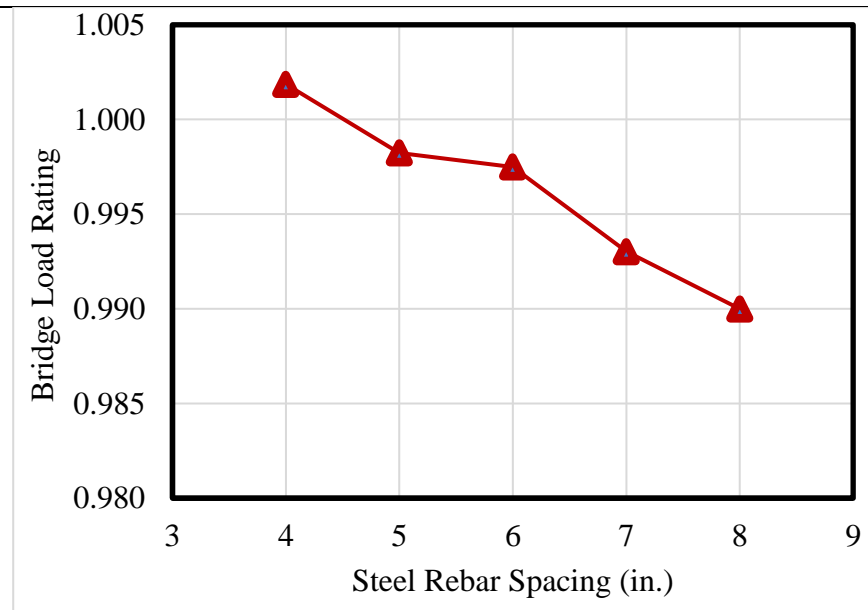
Figure 7-8: Steel rebar spacings vs. inventory R.F.

Figure 7-9(a) represents the full FE model view with the visible longitudinal reinforcement.

Figures 7-9(b) and 7-9(c) show a close look of the reinforcement spaced at 4 in. and 7 in. c/c, respectively.

(a)

(b)

(c)
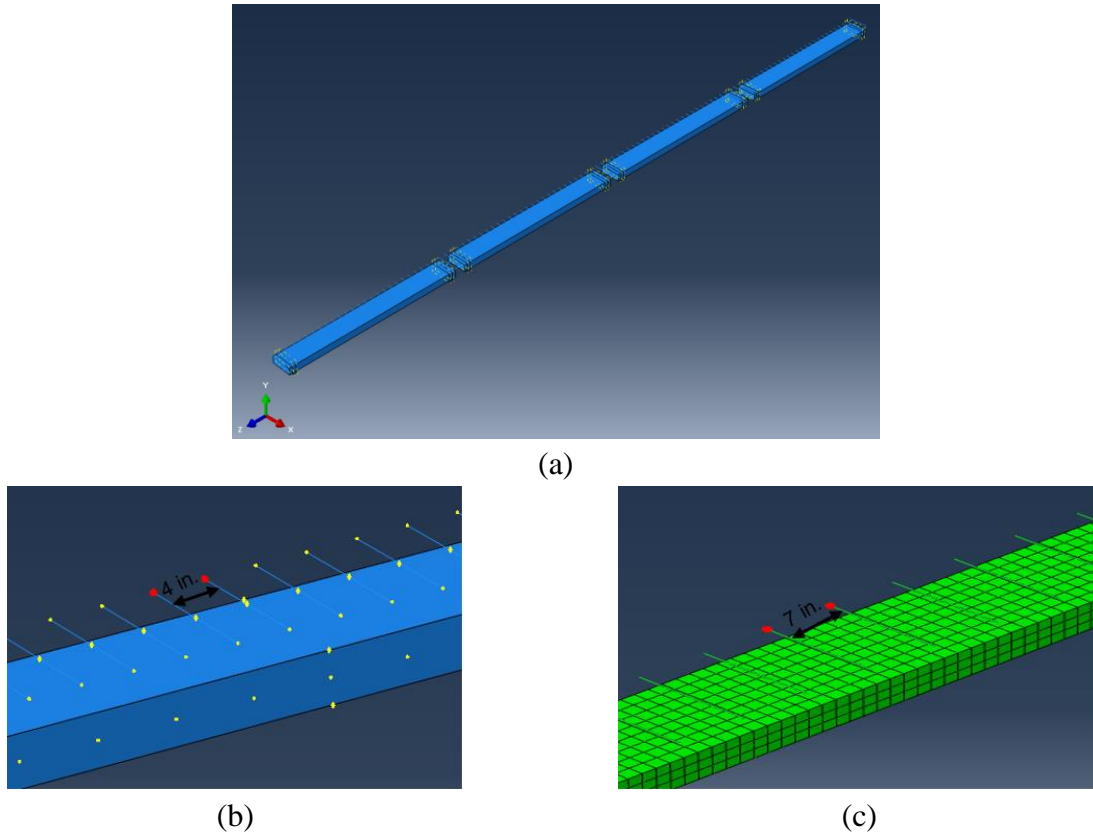
Figure 7-9 FE model view: (a) Full model; (b) 4 in. spacing; (c) 7 in. spacing

7.5 Installation of Under-Cut Anchor

Since undercut anchors are installed in the girder, the predominant applied force due to vehicles driving on the bridge is shear force. Therefore, the undercut anchors were used to help with shear force resistance. Chapter 17 in ACI 318-19 discusses different types of concrete anchorage and the shear failure modes. Shear failure modes related to concrete include concrete breakout failure and concrete pryout (applicable to all anchor types). The breakout failure of both single and group anchor effect is discussed in section 17.7.2.

For the present study, we only considered single anchor effect since the group anchor effect can be ignored as the spacing between two adjacent anchors is more than the critical spacing (3 C_{a1}, as covered in ACI 318-19, Table 17.5.1.3.1).

Figure 7-10 shows the breakout cone for shear. C_{a1} value was then determined to be used for a Type C girder and also to meet the critical edge distance requirement.

140

The critical edge distance for headed studs, headed bolts, expansion anchors, screw anchors, and undercut anchors is $1.5c_{a1}$

$\approx 35°$

$1.5c_{a1}$

$1.5c_{a1}$

c_{a1}

V

Edge of concrete

Plan

$1.5c_{a1}$ $1.5c_{a1}$

c_{a1}

V

$\approx 35°$

$1.5c_{a1}$

h_{ef}

Elevation

Side section

$A_{Vco} = 2(1.5c_{a1}) \times (1.5c_{a1}) = 4.5c_{a1}^2$
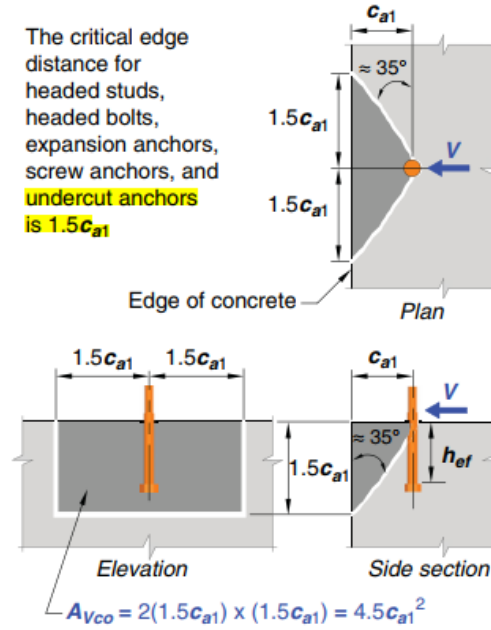
Figure 7-10: Breakout cone in shear

The typical bedding strip width for a Type C girder is 2 inches, and the distance between the edge of a Type C top flange to the edge of Type C web is 3.5 inches. Therefore, the location of the undercut anchor should be between 2 in. and 3 in., which was measured at 2.75 inches measured from the edge of top flange. As a result, either of the distances on the right or left of undercut anchor, 1.5 C_{a1} should not exceed 2.75 inches. Accordingly, the final C_{a1} is 1.83 inches.

The maximum spacing between the two adjacent anchors to provide a fully bond between the girder-deck interface per side is 5.5 inches. To perform this perfect bond, the maximum number of anchors required for a 70 ft. girder is 153 anchors. Table 7-16 shows the different number of anchors per side per girder modeled in ABAQUS.

Table 7-16: Different number of anchors per side modeled in ABAQUS

No. of Undercut Anchors per side per girder	Provided Anchors (%)
153	100%
115	75%
77	50%
38	25%
0 (control)	0%

Table 7-17 shows a comparison of nominal moment capacity and RF for the control and retrofitted models found from FE. Figures 7-11(a-c) show the modeled under-cut anchor based on anchor numbers in ABAQUS.

Table 7-17: Comparison between the calibrated and retrofitted models using ABAQUS

No. of Undercut Anchors	Nominal Moment (k-ft)	Rating Level Inventory
153	4895	1.55
115	4832	1.52
77	4769	1.49
38	4707	1.47
0 (control)	4644	1.44
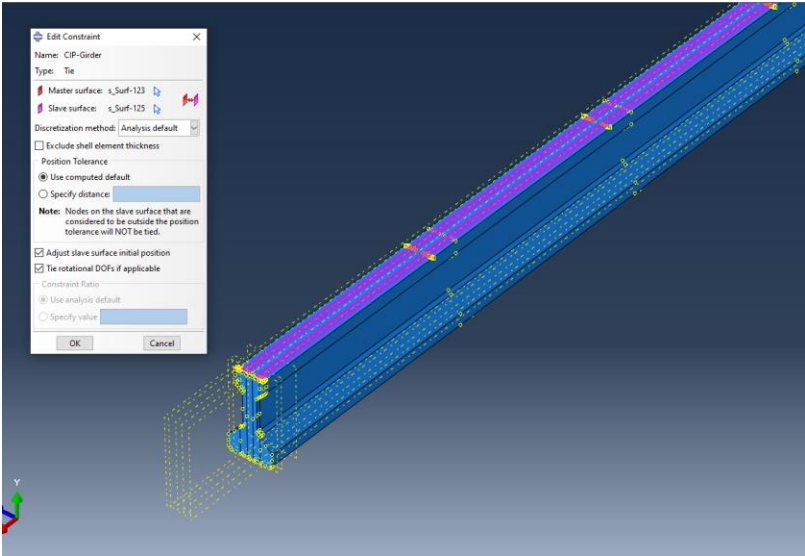
(a)
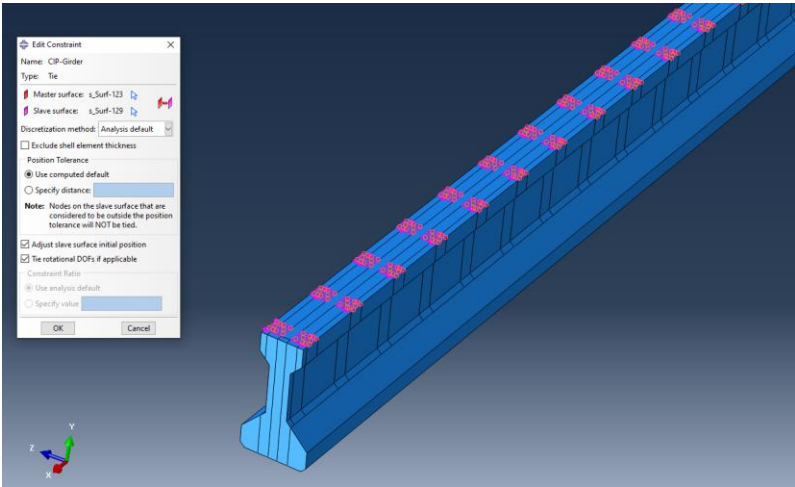
(b)
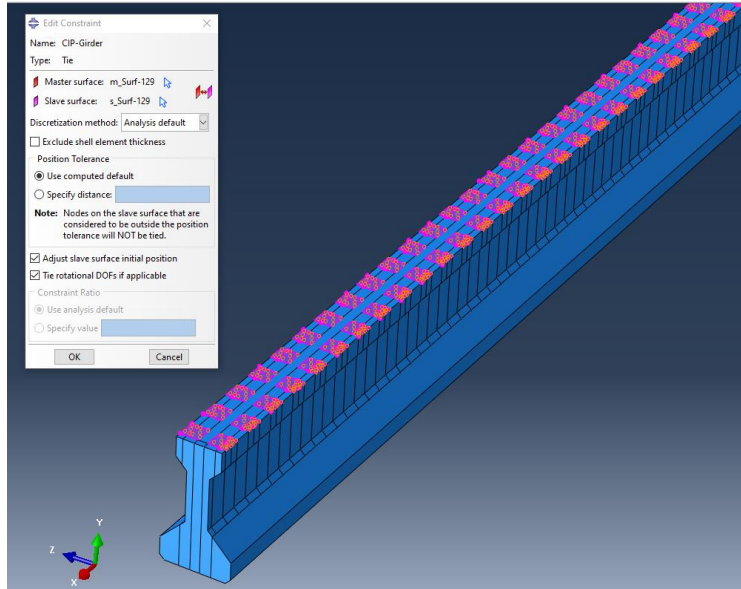
(c)

Figure 7-11 Modeled under-cut anchors: (a) 153 anchors; (b) 38 anchors; (c) 77 anchors

Figures 7-12(a) and 7-12(b) shows the flexural cracks caused by tensile stress FE results

of the control specimen and 153 under-cut anchors, respectively.
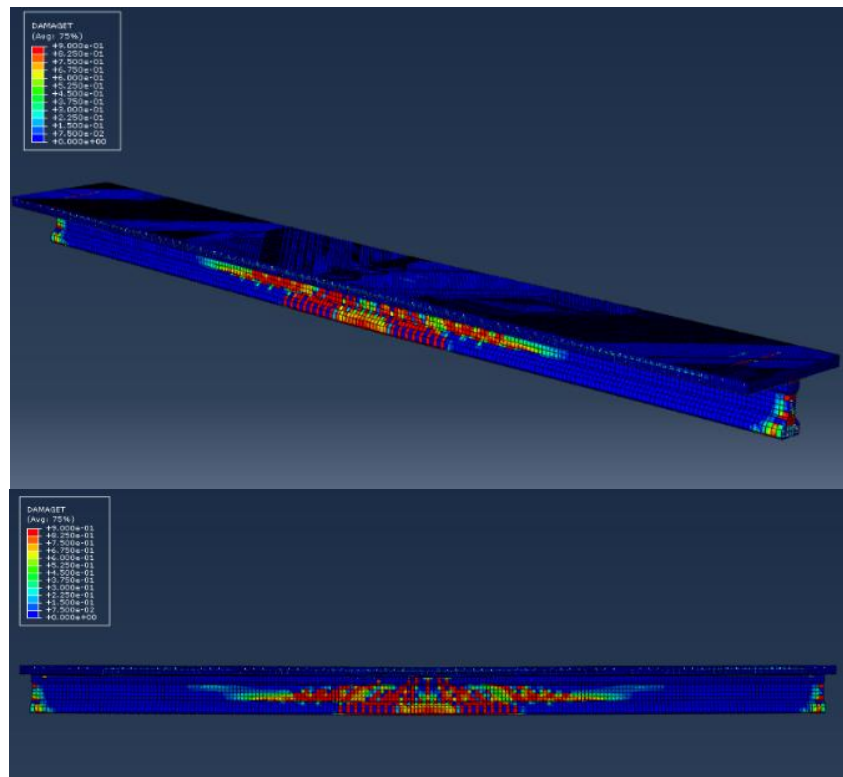
(a)
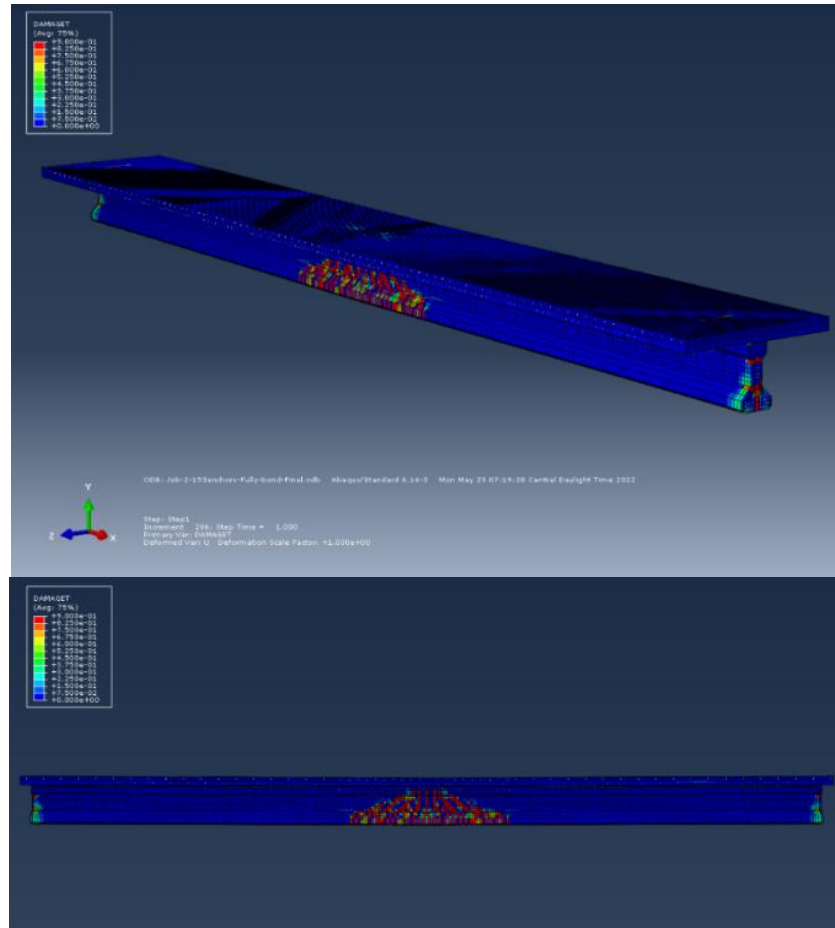
(b)

Figure 7-12 Induced flexural cracks: (a) control specimen; (b) 153 anchors

7.6 Cost Analysis

The bridge maintenance/ rehabilitation is of great importance to ensure the structural integrity. Once a certain bridge has a defect, the bridge is shut down until the required repair are done. This temporary closure is costly, and the closure adds up to the overall repair costs that includes material and labor. The overall cost and necessary equipment of each suggested retrofitting option are different. Table 7-18 shows the proposed retrofitting options with its corresponding required traffic closure and cost condition.

Table 7-18: Traffic closure of each retrofitted option

Retrofitting methods	Traffic closure	Cheap/Expensive
Installation of shear connectors	Required	Very Expensive
Recasting bridge deck partially with SFRC	Required	Expensive
PCP overhang length extension	Required	Moderate
Undercut Anchors	Not required	Moderate

To select the optimal retrofitting option, a benefit-cost analysis was performed. The cost analysis involved only the inventory rating in the benefit scale, whereas the cost scale involved the initial cost of each retrofitted model. Operating rating was not used in the cost analysis as operating level is automatically satisfied if the inventory level is ≥ 1.0. Table 7-19 summarizes the initial cost and inventory rating as the benefit of each deck retrofitted option. Table 7-20 shows the initial cost and inventory rating of the girder retrofitted models. Cost analysis calculation is provided in Appendix D.

Table 7-19: Initial cost and inventory rating of deck retrofitted models

Deck Retrofitting methods	Initial Cost ($)	Inventory Rating
Installation of shear connectors	178944	1.0
SFRC-Full composite (aspect ratio = l/d =40)	148128	1.61
SFRC-Full composite (aspect ratio = l/d =55)	148128	1.64
SFRC-Partial composite (aspect ratio = l/d =40)	148128	1.14
SFRC- Partial composite (aspect ratio = l/d =55)	148128	1.15
Deck Design/Construction Method	**Initial Cost ($)**	**Inventory Rating**
PCP overhang length extension	206592	1.10

Table 7-20: Initial cost and inventory rating of under-cut anchor models in girders

Under-cut Anchor- Total cost including GPR and Labor cost			
No of Anchors/girder side/one girder	1 Girder ($)**	8 Girders ($)**	Inventory Rating
38	9,178	73,424	1.47
77	13,456	107,648	1.49
115	17,734	141,872	1.52
153	22,012	176,096	1.55

** A $ 2000 boom lift rent will be added with each final cost.

Figure 7-13 represents the benefit-cost index of each retrofitting options. The benefit-cost ratio was normalized to a maximum value of 10. The largest ratio results in a more optimal selection of one of the examined retrofitted options. From Figure 7-13, most of the retrofitted options have orange and blue colors. The blue color represents a minimum R.F. of 1.0 where the bridge considers safe and does not need load posting, while the orange colors represent the residual R.F. that exceeding the required R.F. of 1.0.
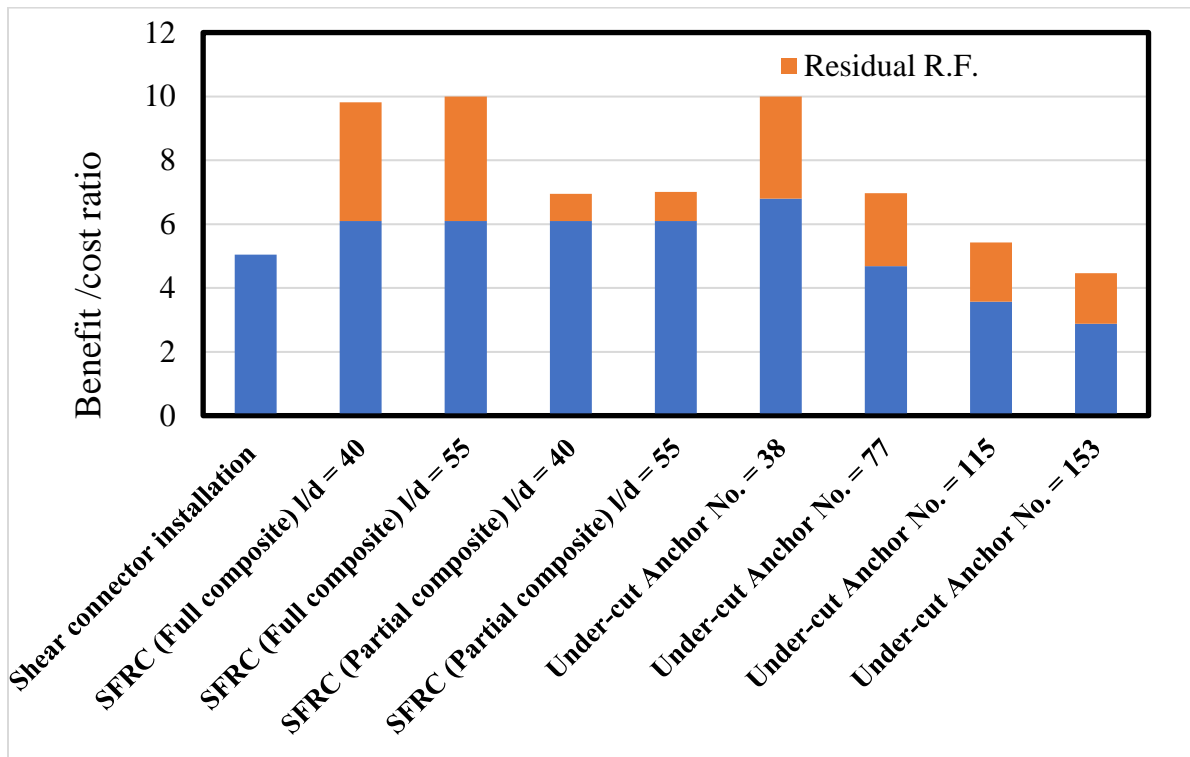
Figure 7-13: Benefit-cost index

Chapter 8

CONCLUSIONS AND RECOMMENDATIONS

8.1 Summary

Las Lomas bridge EB and WB exhibited localized deck failure due to failure of four PCPs. The failure occurred on June 18, 2018 and it was located near the mid-span diaphragm of spans 2 and 4 of EB and WB bridges, respectively. The localized deck failure received an emergency repair with full CIP depth. Furthermore, TxDOT contacted The University of Texas at Arlington (UTA) research team to perform a bridge evaluation that included a load diagnostic test and NDE. As the bridge was built in 1980's, there was significant and severe bridge deck delamination, as detected by IE. Comprehensive studies including field load testing, NDE evaluation, numerical modeling, and model calibration with field load test data were conducted. Retrofitting options were then carried out to increase the bridge load-carrying capacity. Both composite action between CIP and PCPs and bridge rating factors were the two main scales used to determine the effectiveness of the proposed retrofitting options.

The bridge instrumentation involved only spans 2 and 4, as those were the sites of the CIP failure. Non-reusable, reusable strain gages, and rotational tiltmeters were attached to the girder surfaces at different sections to assess the bridge response due to truck movement. NDE using GPR and IE was also incorporated to conduct an accurate assessment of the bridge performance. To perform a more comprehensive study, numerical analysis using ABAQUS was used to run several retrofitting models that could improve the bridge life service by enhancing the load carrying capacity and degree of composite action.

8.2 Findings and Conclusions

This section includes the findings from the experimental/field load test data and numerical analysis conducted in the investigation of the bridge behavior.

8.2.1 Load Tests and NDE

The following conclusions and recommendations are based on the results of the present study:

❖ **Phase 1- Original EB and WB Bridges**

- The average N.A. locations of the EB and WB bridges from the load test were 30 in. and 28 in., respectively. The EB and WB bridges revealed lower N.A. value as the recorded top strain gages in girders C and D varied from 40 to 60 $\mu\varepsilon$ (see Figures 6-1, 6-2(a), 6-5(b) and 6-5(c)], which suggests that partial composite exists, and the degree of composite action relies on the measured top gage. As the top gage reading increases, low partial composite action will be observed. The main reason behind the increase was the localized failure that occurred between girders C and D.

- The EB and WB bridges exhibited a composite action between the girder-CIP concrete deck of 41% and 48%, which implies that both decks had nearly similar performance. The reason behind this similarity is that both bridges had the same localized failure issue, and both decks were severely delaminated, as detected from IE data.

- Even though the localized CIP occurred between girders C and D in the original EB bridge deck, girder C exhibited the largest rotation compared to the rotation of girder D and other girders. Moreover, the construction joint was located on top of girder C, which implies that the presence of deck defect near a specific girder where construction joint exists would increase the negative impact on that girder.

- The GPR data, indicates that around 53% and 63% of the scanned deck areas for the EB and WB bridges had an average top rebar cover of 1.5 in. and 2.25 in., respectively. Additionally, the top rebar cover below 2 in. may be a concern for deck top rebar corrosion.

- The IE data indicates that there was 48% delamination in the positive moment region for the original EB and WB decks while there was 60% and 51% delamination in the negative moment region, respectively.

- The positive moment region of the original EB bridge deck with ≤ 35% deck delamination was able to achieve the minimum load rating of 1.0 [Figure 6-24(b)].

- The negative top rebar cover with 0% delamination had a significant drawback on the bridge load rating [Figure 6-24(a)] as observed in the original EB bridge deck, where the bridge was rated based on the deck negative moment capacity alone. The optimal value of rebar cover, which provides a load rating of 1.0 and protection against corrosion, is 2 in.

- NDE appeared to be a useful tool in finding the suitable load rating approach. If the deck is severely delaminated, it is conservative to evaluate the CIP concrete deck and composite girder individually during the bridge load rating calculation. The lowest load rating between these two components controls the overall bridge performance.

- Combining the GPR and IE data, the deck capacity of the original EB and WB decks was found to be 10 k-ft./ft. and 10.3 k-ft./ft. for positive moment capacity and 7 k-ft./ft. and 6.4 k-ft./ft. for negative moment capacity, respectively.

- The deck is not able to carry the HS-20 loads due to the high level of delamination between the girders and panels/deck. The neutral axis location from the load test confirmed the delamination by showing partial composite action. The inventory member rating is 33.12 kip and 30.96 kip for the original EB and WB decks, respectively.

- According to LFR Method (AASHTO Manual for Bridge Evaluation, 2018), the girders were able to carry the HS-20 loads even after considering the loss of composite action for both bridge decks.

149

❖ **Phase 2 EB Original and Replaced Decks**

- The average neutral axis of the replaced deck was improved compared to the previous deck, as the top strain gages on girders provide very small readings.

- Girder C exhibited the largest rotation compared to other girders before the deck replacement, while the rotation was reduced by 46.5% after deck replacement. Also, all other girders showed the same rotations in the replaced deck, with the exception of girder C.

- The maximum vertical deflection at mid-span was recorded to be at girder C, with a value of 0.28 in., which is less than the maximum permissible deflection of 1.05 in.

- Most of the scanned area of the original and replaced EB decks revealed an average top rebar cover of 1.5 in. and 3.5 in, respectively, suggesting that the top rebar cover mentioned in the as-built drawing is not always satisfied during bridge construction, which will lead to inaccurate prediction of the bridge live load capacity.

- The replaced EB deck showed almost 0% severe delamination, while 54% of the scanned area was severely delaminated in the original deck.

- Since the replaced deck had no severe delamination, the girders' contribution was included to increase the negative moment capacity.

- The positive replaced deck moment region met the load rating requirement as the severe deck delamination was negligible.

- The composite girder rating was satisfactory for both full and partial composite action between the girder and CIP concrete replaced deck.

8.2.2 Bridge Retrofitting

- FE models retrofitted with 1.5 ft. and 0.1 in. shear connector mesh size provided the minimum required R.F. for the bridge to be considered safe. DCA was determined based on the ultimate load method, and DCA achieved 76% compared to 46% for the pre-retrofitted model. Based

on the results, shear connectors were helpful in increasing the interfacial shear force, thus reducing the slip between the CIP and PCP interface. To further increase the composite action and R.F., this post-retrofitted model can be combined with other retrofitting options.

- Using SFRC as repairing material would greatly increase the bridge R.F. up to 1.61 and 1.14 for aspect ratio of 40 of full and partial composite action, respectively. SFRC also increases the composite action to reach to 94%. SFRC proved to be the most superior retrofitting option compared to all other options. SFRC can minimize the concrete spalling as well.

- The retrofitted model which employed the 3.5 in. PCP overhang extension measured from PCP edge to the interior face of the bedding strip had two advantages: cost-effectiveness and an increase in the composite action by 80%.

- The least effective retrofitting option, in terms of increased composite action and bridge R.F., was the addition of longitudinal reinforcement. The maximum increased DCA was 1.74%. Even though longitudinal reinforcement was not effective, the approach might still be helpful in controlling and reducing the shrinkage and temperature cracks.

- The controlled and retrofitted under-cut anchor models bridge R.F. were already more than 1.0, and the bridge considered to be safe. As the girder was stiffer than the deck, the girder contribution was observed in the control or pre-retrofitted model. Therefore, composite action can be used as an indicator to determine the effectiveness of under-cut retrofitting.

8.3 Future Research

- All retrofitting options were performed using FE. Future lab experimental studies can be conducted to verify the output.

- Some of the retrofitting models were modeled using a small-scale specimen to accurately calculate moment capacity. The models were also selected due to computational time constraint and convergence issues.

- The FE used a static model option. Therefore, the live load was applied as a patch area. It will be more realistic to use dynamic model to apply the moving load to account for the real situation where vehicles are driven on the bridge at various speeds.

Appendix A:

Neutral Axis (N.A) Calculation for Original EB, WB Bridges, and Replaced EB Bridge

For Original EB Bridge Deck:

Theoretical NA Location (Non-Composite)

For girders (A-F):

The following parameters are shown in Figure 3-2(c) and Tables 3-1, 3-2, and 3-3.

No. of strand = 36   Diameter of strand = 0.5 in.

$f_u = 270$ ksi $\qquad\qquad e_{mid} = 12.42$ in. $\qquad\qquad f_c' = 5.8$ ksi

Spacing of girders = 9.25 ft.

Type C girder properties:

$\quad y_t = 22.91$ in. $\qquad y_b = 17.09$ in. $\qquad A = 494.9$ in^2 $\qquad\qquad I = 82602$ in^4

$A_{ps} = 36 * 0.153 = 5.508$ in^2

$\beta_1 = 0.76$

$d_p = y_t + c = 22.91 + 12.42 = 35.33$ in

$$C = \frac{A_{sp}f_{pu}}{0.85f_c'\beta_1 b + kA_{ps}\dfrac{f_{pu}}{d_p}} = \frac{5.508 * 270}{0.85 * 5.8 * 0.76 * 14 + 0.28 * 5.508 * \dfrac{270}{35.33}} = 23.15 \text{ in. [from top]}$$

∴ Location of NA from bottom = 40 in − 23.15 in = 16.85 in

For girder (G):

No. of strand = 30   Diameter of strand = 0.5 in.

$f_u = 270$ ksi $\qquad\qquad e_{mid} = 13.09$ in. $\qquad\qquad f_c' = 5.1$ ksi

Spacing of girders = 9.25 ft.

Type C girder properties:

$\quad y_t = 22.91$ in. $\qquad y_b = 17.09$ in. $\qquad A = 494.9$ in^2 $\qquad\qquad I = 82602$ in^4

$A_{ps} = 30 * 0.153 = 4.59$ in^2

$\beta_1 = 0.8$

$d_p = y_t + c = 22.91 + 13.09 = 36$ in

$$C = \frac{A_{sp}f_{pu}}{0.85f_c'\beta_1 b + kA_{ps}\dfrac{f_{pu}}{d_p}} = \frac{4.59 * 270}{0.85 * 5.1 * 0.8 * 14 + 0.28 * 4.59 * \dfrac{270}{36}} = 21.4 \text{ in. [from top]}$$

∴ Location of NA from bottom = 40 in − 21.3 in = 18.59 in

No. of strand $= 32$ Diameter of strand $= 0.5$ in.

$f_u = 270$ ksi $e_{mid} = 12.84$ in. $f_c' = 5.27$ ksi

Spacing of girders $= 9.25$ ft.

Type C girder properties:

$y_t = 22.91$ in. $y_b = 17.09$ in. $A = 494.9$ in^2 $I = 82602$ in^4

$A_{ps} = 32 * 0.153 = 4.896$ in^2

$\beta_1 = 0.79$

$d_p = y_t + c = 22.91 + 12.84 = 35.75$ in

$$C = \frac{A_{sp}f_{pu}}{0.85f_c'\beta_1 b + kA_{ps}\frac{f_{pu}}{d_p}} = \frac{4.896 * 270}{0.85 * 5.27 * 0.79 * 14 + 0.28 * 4.896 * \frac{270}{35.75}} = 22.15 \text{ in. [from top]}$$

$$\therefore \text{ Location of NA from bottom} = 40 \text{ in} - 22.15 \text{ in} = 17.85 \text{ in}$$

Theoretical NA Location (Fully Composite)

For an interior girder C as an example:

$d_p = y_t + e + 9.25''(\text{thickness} + \text{haunch})$

$d_p = 22.91 + 12.42 + 9.25 = 44.58 \; in$

$$C_{com} = \frac{A_{sp}f_{pu}}{0.85f_c'\beta_1 b + kA_{ps}\frac{f_{pu}}{d_p}} = \frac{5.508 * 270}{0.85 * 4.0 * 0.85 * (9.25 * 12) + 0.28 * 5.508 * \frac{270}{44.58}}$$

$$= 4.50 \text{ in. [from top]}$$

$$\therefore \text{ Location of NA from bottom} = 40 \text{ in} + 9.25 \text{ in} - 4.50 \text{ in} = 44.75 \text{ in}$$

Assume,

NA Location from bottom $= 16.85$ in. [means 0% Composite Action]

NA Location from bottom $= 44.75$ in. [means 100% Composite Action]

$\therefore$ Average NA Location from bottom from load test 30 in. [means 47.13% Composite Action]

$$\therefore \text{ From Load Test, girder C has a 47.13\% Composite Action}$$

For Original WB Bridge Deck:

Theoretical NA Location (Non-Composite)

For girders (A-F):

No. of strand = 34

$f_u = 270$ ksi $\qquad e_{mid} = 12.62$ in. $\qquad f'_c = 5.5$ ksi

Spacing of girders = 9.1 ft.

Type C girder properties:

$y_t = 22.91$ in. $\qquad y_b = 17.09$ in. $\qquad A = 494.9$ in^2 $\qquad I = 82602$ in^4

$A_{ps} = 34 * 0.153 = 5.202$ in^2

$\beta_1 = 0.78$

$d_p = y_t + c = 22.91 + 12.62 = 35.53$ in.

$$C = \frac{A_{sp}f_{pu}}{0.85f'_c\beta_1 b + kA_{ps}\frac{f_{pu}}{d_p}} = \frac{5.202 * 270}{0.85 * 5.5 * 0.78 * 14 + 0.28 * 5.202 * \frac{270}{35.53}} = 22.73 \text{ in. [from top]}$$

$$\therefore \text{ Location of NA from bottom} = 40 \text{ in} - 22.73 \text{ in} = 17.30 \text{ in}$$

Theoretical NA Location (Fully Composite)

For an interior girder:

$d_p = y_t + e + 9$ in. (thickness + haunch)

$= 22.91 + 12.62 + 9 = 44.53$ in.

$$C_{com} = \frac{A_{sp}f_{pu}}{0.85f'_c\beta_1 b + kA_{ps}\frac{f_{pu}}{d_p}} = \frac{5.202 * 270}{0.85 * 4.0 * 0.85 * (9.1 * 12) + 0.28 * 5.202 * \frac{270}{44.53}}$$

$$= 4.33 \text{ in. [from top]}$$

$$\therefore \text{ Location of NA from bottom} = 40 \text{ in.} + 9 \text{ in.} - 4.33 \text{ in} = 44.67 \text{ in}$$

Assume,

NA Location from bottom = 17.30 in. [means 0% Composite Action]

NA Location from bottom = 44.67 in. [means 100% Composite Action]

$\therefore$ NA Location from bottom = 28 in. [means 39.1% Composite Action]

$$\therefore \text{ From Load Test, an interior girder has a 39.1\% Composite Action}$$

For Replaced EB Bridge Deck:

Theoretical NA Location (Non-Composite)

N.A. location of non-composite action is the same N.A. location of original EB bridge deck as the girders were not replaced or changed.

Theoretical NA Location (Fully Composite)

For an interior girder C as an example:

$d_p = y_t + e + 9.5''(\text{thickness} + \text{haunch})$

$d_p = 22.91 + 12.42 + 9.5 = 44.83 \ in$

$$C_{com} = \frac{A_{sp}f_{pu}}{0.85f_c'\beta_1 b + kA_{ps}\dfrac{f_{pu}}{d_p}} = \frac{5.508 * 270}{0.85 * 4.0 * 0.85 * (9.25 * 12) + 0.28 * 5.508 * \dfrac{270}{44.83}}$$

$$= 4.51 \ in. \, [\text{from top}]$$

∴ Location of NA from bottom = 40 in + 9.5 in − 4.51 in = 45.0 in

Assume,

NA Location from bottom = 16.85 in. [means 0% Composite Action]

NA Location from bottom = 45.0 in. [means 100% Composite Action]

∴ Average NA Location from bottom from load test 36.1 in. [means 68.4% Composite Action]

∴ From Load Test, girder C has a 68.4% Composite Action

Appendix B:

Moment Capacity and Load Rating Calculations of Original and Replaced EB Bridges

❖ **For Original EB Bridge:**

➢ **Deck Capacity (EB) Bridge**

• *Positive Deck Moment Capacity:*

Precast panels width $= 9.25' - \dfrac{14"}{12} + \dfrac{4" * 2}{12} = 8.75$ ft.

Length of panel $= 8$ ft.

Panel thickness $= 4$ in.

Number of strands:

$n = 16 \quad \Phi = 3/8$ in.

$\therefore M_n = A_{ps} f_{ps} \left(d_p - \dfrac{a}{2} \right)$

$A_{ps} = 16 * 0.085 = 1.36 \text{ in}^2$

$d_p = 8.25 - \dfrac{4}{2} = 6.25$ in

$\beta_1 = 0.85$

$c = \dfrac{A_{ps} f_{pu}}{0.85 * f'_c \beta_1 b + k A_{ps} \dfrac{f_{pu}}{d_p}} = \dfrac{1.36 * 270}{0.85 * 4.0 * 0.85 * (8.75 * 12) + 0.28 * 1.36 * \dfrac{270}{6.25}} = 1.15$ in.

$a = \beta_1 c = 0.85 * 1.15 = 0.976$ in.

$\therefore f_{ps} = f_{pu} \left(1 - k \dfrac{c}{d_p} \right) = 270 \left(1 - 0.28 * \dfrac{1.15}{6.25} \right) = 256.1$ ksi

$M_n = 1.36 * 256.1 * \left(6.25 - \dfrac{0.976}{2} \right) = 2007.1 \text{ }^{k-in}/_{panel} = 167.3 \text{ }^{k-ft}/_{panel}$

For a 1 ft strip:

$M_n = \dfrac{167.3}{8} = 21.0 \text{ }^{k-ft}/_{ft}$

Applying 54% delamination

$M_n = 21 * 0.46$

$M_n = 9.6 \text{ }^{k-ft}/_{ft} \cong \boxed{10 \text{ }^{k-ft}/_{ft}}$

• *Negative Deck Moment Capacity:*

157

From GPR, top cover in negative zone = 1.5 in

$$d = 9.25 - 1.5 - \frac{5}{8 * 2} = 7.44 \text{ in.}$$

#5 @ 9 in. O.C.

$$a = \frac{A_s f_y}{0.85 f_c' b} = \frac{0.41 * 60}{0.85 * 4.0 * 12} = 0.603 \text{ in.}$$

$$\therefore M_n = A_s f_y \left(d - \frac{a}{2}\right) = 0.41 * 60 * \left(7.44 - \frac{0.603}{2}\right) = 175.61 \; ^{k-in}/_{ft} = 14.6 \; ^{k-ft}/_{ft}$$

Apply 54% delamination:

$$M_n = 14.6 * 0.46 = 6.72 \; ^{k-ft}/_{ft} \cong 7 \; ^{k-ft}/_{ft}$$

∴ The governed nominal deck moment capacity is 7 k-ft/ft

➢ **Deck Load Rating of Original EB Bridge:**

$$DL = 0.1 * \left(\frac{8.25}{12} * 1' * 0.15\right) * 9.25^2 = 0.88 \; k - ft$$

LL equation is for continuous slab, P=16 kip for HS-20.

$$LL = 0.8 * \left(\frac{S+2}{32}\right) * P = 0.8 * \left(\frac{9.25+2}{32}\right) * 16 = 4.5 \; ^{k-ft}/_{ft}$$

$$LL + IM = 1.3 * 4.5 \; ^{k-ft}/_{ft} = 5.85 \; ^{k-ft}/_{ft}$$

R.F. For HS-20 (Inventory level):

$$\text{Rating Factor} = R.F. = \frac{C - A_1 \, XDL}{A_2 \, x \, (LL + IM)} = \frac{7.0 - 1.3 * 0.88}{2.17 * 5.85} = 0.46$$

Bridge Member rating = 36 x 0.46 = 16.56 tons = 33120 lb.

R.F. For HS-20 (Operating level):

$$\text{Rating Factor} = R.F. = \frac{C - A_1 \, XDL}{A_2 \, x \, (LL + IM)} = \frac{7.0 - 1.3 * 0.88}{1.3 * 5.85} = 0.77$$

Bridge Member rating = 36 x 0.77 = 27.72 tons = 55440 lb.

➢ **Composite Girder Capacity of Original EB Bridge**

● *Flexural resistance at mid span [full composite action assumed]:*

$$d_p = y_t + \text{haunch} + t_s + C_m = 22.91 + 9.25 + 12.42 = 44.58 \text{ in.}$$

$$C = \frac{A_{ps} f_{pu}}{0.85 f_c' \beta_1 b + k A_{ps} \dfrac{f_{pu}}{d_p}} = \frac{5.508 * 270}{0.85 * 4.0 * 0.85 * (9.25 * 12) + 0.28 * 5.508 * \dfrac{270}{44.58}} = 4.51 \text{ in.}$$

$$a = \beta_1 C = 0.85 * 4.51 = 3.83 \text{ in.} < t_s$$

Rectangular section behavior

$$f_{ps} = 270 \left(1 - 0.28 * \frac{4.51}{44.58}\right) = 262.36 \text{ ksi}$$

$$\therefore M_n = A_{ps}f_{ps}\left(d_p - \frac{a}{2}\right) = 5.508 * 262.36 * \left(44.58 - \frac{3.83}{2}\right) = \text{5137.85 k} - \text{ft}$$

- ***Flexural resistance at mid span [Partial composite action]:***

$$C = 40'' + 9.25'' - 30'' = 19.25'' \ [from\ top]$$

$$a = \beta_1 C = 0.85 * 19.25 = 16.36''$$

$$f_{ps} = 270 \left(1 - 0.28 * \frac{19.25}{44.58}\right) = 237.36 \text{ ksi}$$

$$M_n = A_{ps}f_{ps}\left(d_p - \frac{a}{2}\right) + \alpha_1 f_c'(b - b_w)h_f \left(\frac{a}{2} - \frac{h_f}{2}\right)$$

$$M_n = 5.508 * 237.36 * \left(44.58 - \frac{16.36}{2}\right) + 0.85 * 4.0 * (9.25 * 12 - 7) * 8.25 * (\frac{16.36}{2} - \frac{8.25}{2})$$

$$M_n = 59417.84 \text{ k} - \text{in} = \text{4951.5 k} - \text{ft}$$

Loss of moment capacity $= \frac{5137.85 - 4951.5}{5137.85} * 100 \cong 4\%$

> ## Composite Girder Load Rating of Original EB Bridge:

<u>Dead Load Analysis:</u>

SW of girder $= \dfrac{494.9}{144} * 0.15 = 0.516 \ \text{k}/_\text{ft}$

Weight of slab + haunch $= \left[\dfrac{8.25}{12} * 9.25 + \dfrac{1 * 14}{144}\right] * 0.15 = 0.97 \ \text{k}/_\text{ft}$

$\therefore DC_1 = 1.486 \ \text{k}/_\text{ft}$

$M_{DC_1} = \dfrac{1.486 * 70.4^2}{8} = 920.61 \text{ k} - \text{ft}$

Type Type T501 barrier $= 0.326 \ (\dfrac{k}{ft}) * 2 = 0.652 \text{ k/ft}$

$\therefore$ barrier load per beam $= \dfrac{0.652}{3} = 0.22 \text{ k/ft}$

$M_{DC_2} = \dfrac{0.22 * 70.4^2}{8} = 136.30 \text{ k} - \text{ft}$

$M_{Total} = 920.61 + 136.30 = \text{1056.91 k} - \text{ft}$

<u>Live Load Analysis:</u>

Two or more land loaded:

$$g_{m_1} = \frac{S}{5.5} = \frac{9.25}{5.5} = 1.68$$

Maximum LL effect for HS –20:

HS-20 live moment = 496.4 k-ft. [From AASHTO Manual for Bridge Evaluation (2018), Page 6-158]

$$I = \frac{50}{L+125} \leq 0.3$$

$$I = \frac{50}{70.4 + 125} = 0.256$$

$$\therefore m_{LL+I} = 496.4 * 1.256 * 1.68 = \boxed{1048.5 \, k-ft}$$

A- Load Rating Assuming Full Composite Action:

R.F. For HS-20 (Inventory level):

$$RF = \frac{C - A_1 \, x \, DL}{A_2 \, x \, (LL + IM)} = \frac{5137.85 - 1.3 * 1056.91}{2.17 * 1048.5} = \boxed{1.66}$$

Bridge Member rating = 36 x 1.66 = 59.76 tons = 119520 lb.

R.F. For HS-20 (Operating level):

$$RF = \frac{C - A_1 \, x \, DL}{A_2 \, x \, (LL + IM)} = \frac{5137.85 - 1.3 * 1056.91}{1.3 * 1048.5} = \boxed{2.76}$$

Bridge Member rating = 36 x 2.76 = 99.36 tons = 198720 lb.

B- Rating Assuming Partial Composite Action

R.F. For HS-20 (Inventory level):

$$RF = \frac{C - A_1 \, x \, DL}{A_2 \, x \, (LL + IM)} = \frac{4951.5 - 1.3 * 1056.91}{2.17 * 1048.5} = \boxed{1.57}$$

Bridge Member rating = 36 x 1.09 = 39.24 tons = 78480 lb.

R.F. For HS-20 (Operating level):

$$RF = \frac{C - A_1 \, x \, DL}{A_2 \, x \, (LL + IM)} = \frac{4951.5 - 1.3 * 1056.91}{1.3 * 1048.5} = \boxed{2.63}$$

Bridge Member rating = 36 x 2.63 = 94.68 tons = 189360 lb.

❖ **For Original WB Bridge:**

➢ **Deck Capacity (WB) Bridge**

• *Positive Deck Moment Capacity:*

$$\text{Precast panels width} = 9.1' - \frac{14"}{12} + \frac{4" * 2}{12} = 8.6 \text{ ft.}$$

Length of panel = 8 ft.

Panel thickness = 4 in.

Number of strands:

$n = 16 \qquad \Phi = 3/8$ in.

$\therefore M_n = A_{ps}f_{ps}\left(d_p - \dfrac{a}{2}\right)$

$A_{ps} = 16 * 0.085 = 1.36$ in^2

$d_p = 8 - \dfrac{4}{2} = 6$ in

$\beta_1 = 0.85$

$c = \dfrac{A_{ps}f_{pu}}{0.85 * f'_c\beta_1 b + kA_{ps}\dfrac{f_{pu}}{d_p}} = \dfrac{1.36 * 270}{0.85 * 4.0 * 0.85 * (8.6 * 12) + 0.28 * 1.36 * \dfrac{270}{6}} = 1.16$ in.

$a = \beta_1 c = 0.85 * 1.16 = 0.99$ in.

$\therefore f_{ps} = f_{pu}\left(1 - k\dfrac{c}{d_p}\right) = 270\left(1 - 0.28 * \dfrac{1.16}{6}\right) = 255.3$ ksi

$M_n = 1.36 * 255.3 * \left(6 - \dfrac{0.99}{2}\right) = 1911.4 \; {}^{k-in}\!/_{panel} = 159.3 \; {}^{k-ft}\!/_{panel}$

For a 1 ft strip:

$M_n = \dfrac{159.3}{8} = 20 \; {}^{k-ft}\!/_{ft}$

Applying 49.5% delamination

$M_n = 20 * 0.505$

$M_n = 10.3 \; {}^{k-ft}\!/_{ft}$

- ***Negative Deck Moment Capacity:***

From GPR, top cover in negative zone = 2.25 in

$d = 9 - 2.25 - \dfrac{5}{8 * 2} = 6.44$ in.

#5 @ 9 in. O.C.

$a = \dfrac{A_s f_y}{0.85 f_c' b} = \dfrac{0.41 * 60}{0.85 * 4.0 * 12} = 0.603$ in.

$\therefore M_n = A_s f_y\left(d - \dfrac{a}{2}\right) = 0.41 * 60 * \left(6.44 - \dfrac{0.603}{2}\right) = 150.62 \; {}^{k-in}\!/_{ft} = 12.55 \; {}^{k-ft}\!/_{ft}$

Apply 49.5% delamination:

$M_n = 12.55 * 0.505 = 6.4 \; {}^{k-ft}\!/_{ft}$

$\therefore$ The governed nominal deck moment capacity is 6.4 k-ft/ft

➢ **Deck Load Rating of Original WB Bridge:**

$$DL = 0.1 * \left(\frac{8}{12} * 1' * 0.15\right) * 9.1^2 = \boxed{0.828 \; k - ft}$$

LL equation is for continuous slab, P=16 kip for HS-20.

$$LL = 0.8 * \left(\frac{S + 2}{32}\right) * P = 0.8 * \left(\frac{9.1 + 2}{32}\right) * 16 = 4.44 \; {}^{k-ft}/_{ft}$$

$$LL + IM = 1.3 * 5.55 \; {}^{k-ft}/_{ft} = \boxed{5.77 \; {}^{k-ft}/_{ft}}$$

R.F. For HS-20 (Inventory level):

$$\text{Rating Factor} = R.F. = \frac{C - A_1 \, x \, DL}{A_2 \, x \, (LL + IM)} = \frac{6.4 - 1.3 * 0.828}{2.17 * 5.77} = \boxed{0.43}$$

Bridge Member rating = 36 x 0.43 = 15.48 tons = 30960 lb.

R.F. For HS-20 (Operating level):

$$\text{Rating Factor} = R.F. = \frac{C - A_1 \, x \, DL}{A_2 \, x \, (LL + IM)} = \frac{6.4 - 1.3 * 0.828}{1.3 * 5.77} = \boxed{0.71}$$

Bridge Member rating = 36 x 0.71 = 25.56 tons = 51120 lb.

➢ **Composite Girder Capacity of Original WB Bridge**

- *Flexural resistance at mid span [full composite action assumed]:*

$$d_p = y_t + \text{haunch} + t_s + C_m = 22.91 + 9 + 12.62 = 44.53 \text{ in.}$$

$$C = \frac{A_{ps} f_{pu}}{0.85 f'_c \beta_1 b + k A_{ps} \dfrac{f_{pu}}{d_p}} = \frac{5.202 * 270}{0.85 * 4.0 * 0.85 * (9.1 * 12) + 0.28 * 5.202 * \dfrac{270}{44.53}} = 4.33 \text{ in.}$$

$$a = \beta_1 C = 0.85 * 4.33 = 3.68 \text{ in.} < t_s$$

Rectangular section behavior

$$f_{ps} = 270 \left(1 - 0.28 * \frac{4.33}{44.53}\right) = 262.65 \text{ ksi}$$

$$\therefore M_n = A_{ps} f_{ps} \left(d_p - \frac{a}{2}\right) = 5.202 * 262.65 * \left(44.53 - \frac{3.68}{2}\right) = \boxed{4860.63 \; k - ft}$$

- *Flexural resistance at mid span [Partial composite action]:*

$$C = 40'' + 9'' - 28'' = 21'' \; [from \; top]$$

$$a = \beta_1 C = 0.85 * 21 = 17.85''$$

$$f_{ps} = 270 \left(1 - 0.28 * \frac{21}{44.53}\right) = 234.35 \text{ ksi}$$

$$M_n = A_{ps} f_{ps} \left(d_p - \frac{a}{2}\right) + \propto_1 f'_c (b - b_w) h_f \left(\frac{a}{2} - \frac{h_f}{2}\right)$$

$$M_n = 5.202 * 234.35 * \left(44.53 - \frac{17.85}{2}\right) + 0.85 * 4.0 * (9.1 * 12 - 7) * 8 * \left(\frac{17.85}{2} - \frac{8}{2}\right)$$

$M_n = 57095.93 \text{ k} - \text{in} = $ <mark>4758 k − ft</mark>

Loss of moment capacity $= \frac{4860.63 - 4758}{4860.63} * 100 \cong 2\%$

➤ **Composite Girder Load Rating of Original WB Bridge:**

Dead Load Analysis:

SW of girder $= \dfrac{494.9}{144} * 0.15 = 0.516 \;^{\text{k}}/_{\text{ft}}$

Weight of slab + haunch $= \left[\frac{8}{12} * 9.1 + \frac{1*14}{144}\right] * 0.15 = 0.92 \;^{\text{k}}/_{\text{ft}}$

$\therefore DC_1 = 1.44 \;^{\text{k}}/_{\text{ft}}$

$M_{DC_1} = \frac{1.44*70^2}{8} = 882 \text{ k} - \text{ft}$

Type Type T501 barrier $= 0.326 \left(\dfrac{k}{ft}\right) * 2 = 0.652 \text{ k/ft}$

$\therefore$ barrier load per beam $= \dfrac{0.652}{3} = 0.22 \text{ k/ft}$

$M_{DC_2} = \dfrac{0.22 * 70^2}{8} = 133.12 \text{ k} - \text{ft}$

$M_{Total} = 882 + 133.12 = $ <mark>1015.2 k − ft</mark>

Live Load Analysis:

Two or more land loaded:

$g_{m_1} = \frac{S}{5.5} = \frac{9.1}{5.5} = 1.65$

Maximum LL effect for HS –20:

HS-20 live moment = 492.8 k-ft. [From AASHTO Manual for Bridge Evaluation (2018), Page 6-158]

$I = \frac{50}{L+125} \leq 0.3$

$I = \dfrac{50}{70 + 125} = 0.256$

$\therefore m_{LL+I} = 492.8 * 1.256 * 1.65 = $ <mark>1024.43 k − ft</mark>

A- Load Rating Assuming Full Composite Action:

R.F. For HS-20 (Inventory level):

$RF = \dfrac{C - A_1 \text{ x DL}}{A_2 \text{ x (LL + IM)}} = \dfrac{4860.63 - 1.3 * 1015.2}{2.17 * 1024.43} = $ <mark>1.59</mark>

Bridge Member rating = 36 x 1.59 = 57.24 tons = 114480 lb.

R.F. For HS-20 (Operating level):

$$RF = \frac{C - A_1 \times DL}{A_2 \times (LL + IM)} = \frac{4860.63 - 1.3 * 1015.2}{1.3 * 1024.43} = \boxed{2.66}$$

Bridge Member rating = 36 x 2.66 = 95.76 tons = 191520 lb.

B- Rating Assuming Partial Composite Action

R.F. For HS-20 (Inventory level):

$$RF = \frac{C - A_1 \times DL}{A_2 \times (LL + IM)} = \frac{4758 - 1.3 * 1015.21}{2.17 * 1024.43} = \boxed{1.55}$$

Bridge Member rating = 36 x 1.55 = 55.8 tons = 111600 lb.

R.F. For HS-20 (Operating level):

$$RF = \frac{C - A_1 \times DL}{A_2 \times (LL + IM)} = \frac{4758 - 1.3 * 1015.2}{1.3 * 1024.43} = \boxed{2.58}$$

Bridge Member rating = 36 x 2.58 = 92.88 tons = 185760 lb.

❖ **For Replaced EB Bridge:**

➢ **Replaced Deck Capacity (EB) Bridge**

• *Positive Deck Moment Capacity:*

Precast panels width $= 9.25' - \dfrac{14"}{12} + \dfrac{4" * 2}{12} = 8.75$ ft.

Length of panel = 8 ft.

Panel thickness = 4 in.

Number of strands:

$n = 16 \qquad \Phi = 3/8$ in.

$$\therefore M_n = A_{ps} f_{ps} \left(d_p - \frac{a}{2} \right)$$

$A_{ps} = 16 * 0.085 = 1.36 \text{ in}^2$

$d_p = 8.5 - \frac{4}{2} = 6.5$ in

$\beta_1 = 0.85$

$$c = \frac{A_{ps} f_{pu}}{0.85 * f'_c \beta_1 b + k A_{ps} \dfrac{f_{pu}}{d_p}} = \frac{1.36 * 270}{0.85 * 4.0 * 0.85 * (8.75 * 12) + 0.28 * 1.36 * \dfrac{270}{6.5}} = 1.25 \text{ in.}$$

$a = \beta_1 c = 0.85 * 1.25 = 1.064$ in.

$$\therefore f_{ps} = f_{pu} \left(1 - k \frac{c}{d_p} \right) = 270 \left(1 - 0.28 * \frac{1.25}{6.5} \right) = 255.4 \text{ ksi}$$

$$M_n = 1.36 * 255.4 * \left(6.5 - \frac{1.064}{2} \right) = 2073.2 \, {}^{k-in}/_{panel} = 172.8 \, {}^{k-ft}/_{panel}$$

For a 1 ft strip:

$$M_n = \frac{172.8}{8} = 21.6 \; {}^{k-ft}/_{ft} \cong 22 \; {}^{k-ft}/_{ft}$$

Applying 15% delamination

$$M_n = 22 * 0.85$$

$$M_n = 18.7 \; {}^{k-ft}/_{ft} \cong 19 \; {}^{k-ft}/_{ft}$$

Since there was no severe delamination in the replaced EB deck, the negative moment region was not calculated and was included in composite girder calculation.

➢ **Deck Load Rating of Replaced EB Bridge:**

$$DL = 0.1 * \left(\frac{8.5}{12} * 1' * 0.15 \right) * 9.25^2 = 0.91 \; k-ft$$

LL equation is for continuous slab, P=16 kip for HS-20.

$$LL = 0.8 * \left(\frac{S+2}{32} \right) * P = 0.8 * \left(\frac{9.25+2}{32} \right) * 16 = 4.5 \; {}^{k-ft}/_{ft}$$

$$LL + IM = 1.3 * 4.5 \; {}^{k-ft}/_{ft} = 5.85 \; {}^{k-ft}/_{ft}$$

LL+IM from the follow-up load test = 1.24 x 4.5 = 5.58 k-ft/ft

R.F. For HS-20 (Inventory level) According to AASHTO Standard Spec. (2002):

$$\text{Rating Factor} = R.F. = \frac{C - A_1 \, XDL}{A_2 \, x \, (LL + IM)} = \frac{19 - 1.3 * 0.91}{2.17 * 5.85} = 1.40$$

Bridge Member rating = 36 x 1.40 = 50.4 tons = 100800 lb.

R.F. For HS-20 (Operating level) According to AASHTO Standard Spec. (2002):

$$\text{Rating Factor} = R.F. = \frac{C - A_1 \, XDL}{A_2 \, x \, (LL + IM)} = \frac{19 - 1.3 * 0.91}{1.3 * 5.85} = 2.34$$

Bridge Member rating = 36 x 2.34 = 84.24 tons = 168480 lb.

R.F. For HS-20 (Inventory level) According to Follow-up Load Test:

$$\text{Rating Factor} = R.F. = \frac{C - A_1 \, XDL}{A_2 \, x \, (LL + IM)} = \frac{19 - 1.3 * 0.91}{2.17 * 5.58} = 1.47$$

Bridge Member rating = 36 x 1.47 = 52.92 tons = 105840 lb.

R.F. For HS-20 (Operating level) According to Follow-up Load Test:

$$\text{Rating Factor} = R.F. = \frac{C - A_1 \, XDL}{A_2 \, x \, (LL + IM)} = \frac{19 - 1.3 * 0.91}{1.3 * 5.58} = 2.46$$

Bridge Member rating = 36 x 2.46 = 88.56 tons = 177120 lb.

➢ **Composite Girder Capacity of Replaced EB Bridge**

- *Flexural resistance at mid span [full composite action assumed]:*

$d_p = y_t + \text{haunch} + t_s + C_m = 22.91" + 1.25 + 8.5" + 12.42" = 45.1$ in.

$$c_{com} = \frac{A_{ps}f_{pu}}{0.85f_c'\beta_1 b + kA_{ps}\dfrac{f_{pu}}{d_p}} = \frac{5.508 * 270}{0.85 * 4.0 * 0.85 * (9.25 * 12) + 0.28 * 5.508 * \dfrac{270}{45.1}} = 4.51 \text{ in.}$$

$a = \beta_1 c_{com} = 0.85 * 4.51 = 3.83$ in. $< t_s$

Rectangular section behavior

$$f_{ps} = 270\left(1 - k * \frac{c}{d_p}\right)$$

$$f_{ps} = 270\left(1 - 0.28 * \frac{4.51}{45.1}\right) = 262.4 \text{ ksi}$$

$$\therefore M_n = A_{ps}f_{ps}\left(d_p - \frac{a}{2}\right) = 5.508 * 262.4 * \left(45.1 - \frac{3.83}{2}\right) = \boxed{5200 \text{ k} - \text{ft}}$$

- *Flexural resistance at mid span [Partial composite action]:*

$C = 40'' + 1.25'' + 8.5'' - 36.1''(\text{from load test}) = 13.65''$ [from top]

$a = \beta_1 C = 0.85 * 13.65 = 11.60'' > t_s$

$$f_{ps} = 270\left(1 - 0.28 * \frac{13.65}{45.1}\right) = 247.12 \text{ ksi}$$

$$M_n = A_{ps}f_{ps}\left(d_p - \frac{a}{2}\right) + \propto_1 f_c'(b - b_w)h_f\left(\frac{a}{2} - \frac{h_f}{2}\right)$$

$$M_n = 5.508 * 247.12 * \left(45.1 - \frac{11.60}{2}\right) + 0.85 * 4.0 * (9.25 * 12 - 7) * 8.5 * \left(\frac{11.60}{2} - \frac{8.5}{2}\right)$$

$M_n = 58123.75 \text{ k} - \text{in} = \boxed{4843.65 \text{ k} - \text{ft}}$

Loss of moment capacity $= \dfrac{5200 - 4843.65}{5200} \text{x } 100 = 6.85 \% \cong 7.0 \%$

➢ **Composite Girder Load Rating of Replaced EB Bridge:**

Dead Load Analysis:

SW of girder $= \dfrac{494.9}{144} * 0.15 = 0.516 \text{ }^k/_{ft}$

Weight of slab + haunch $= \left[\dfrac{8.5}{12} * 9.25 + \dfrac{1.25 * 14}{144}\right] * 0.15 = 1.0 \text{ }^k/_{ft}$

$\therefore DC_1 = 1.516 \text{ }^k/_{ft}$

$M_{DC_1} = \dfrac{1.516 * 70.4^2}{8} = 939.54 \text{ k} - \text{ft}$

Type Type SSTR barrier $= 0.376 \left(\dfrac{k}{ft}\right) * 2 = 0.752 \text{ k/ft}$

$$\therefore \text{ barrier load per beam} = \frac{0.752}{3} = 0.251 \text{ k/ft}$$

$$M_{DC_2} = \frac{0.251 * 70.4^2}{8} = 155.5 \text{ k} - \text{ft}$$

$$M_{Total} = 939.54 + 155.5 = \boxed{1095 \text{ k} - \text{ft}}$$

Live Load Analysis:

Maximum LL effect for HS –20:

HS-20 live moment = 496.4 k-ft. [From AASHTO Manual for Bridge Evaluation (2018), Page 6-158]

Distribution Factor (DF):

$$g_{m_1} = 0.63 \text{ (Load Test)} \quad \text{and} \quad g_{m_1} = \frac{S}{5.5} = \frac{9.25}{5.5} = 1.68 \text{ [Standard AASHTO (HS} - 20)]$$

Impact Factor (IM):

IM = 1.24 (Load Test) and $I = \frac{50}{L+125} \leq 0.3$ [Standard AASHTO] $\rightarrow$ $I = \frac{50}{70.4+125} = 0.256$

Live moment including Impact Factor:

From load test:

$$\therefore M_{LL+I} = 496.4 * 1.24 * 0.63 = \boxed{387.80 \text{ k} - \text{ft}}$$

From AASHTO Standard Specs (2002):

$$\therefore M_{LL+I} = 496.4 * 1.256 * 1.68 = \boxed{1048.5 \text{ k} - \text{ft}}$$

A- Load Rating Assuming Full Composite Action According to AASHTO Standard Spec. (2002):

R.F. For HS-20 (Inventory level):

$$RF = \frac{C - A_1 \text{ x DL}}{A_2 \text{ x (LL + IM)}} = \frac{5200 - 1.3 * 1095}{2.17 * 1048.5} = \boxed{1.66}$$

Bridge Member rating = 36 x 1.66 = 59.76 tons = 119520 lb.

R.F. For HS-20 (Operating level):

$$RF = \frac{C - A_1 \text{ x DL}}{A_2 \text{ x (LL + IM)}} = \frac{5200 - 1.3 * 1095}{1.3 * 1048.5} = \boxed{2.77}$$

Bridge Member rating = 36 x 2.76 = 99.72 tons = 199440 lb.

A- Load Rating Assuming Full Composite Action According to Follow-up Load Test:

R.F. For HS-20 (Inventory level):

$$RF = \frac{C - A_1 \text{ x DL}}{A_2 \text{ x (LL + IM)}} = \frac{5200 - 1.3 * 1095}{2.17 * 387.80} = \boxed{4.5}$$

Bridge Member rating = 36 x 4.5 = 162 tons = 324000 lb.

R.F. For HS-20 (Operating level):

$$RF = \frac{C - A_1 \text{ x DL}}{A_2 \text{ x (LL + IM)}} = \frac{5200 - 1.3*1095}{1.3*387.80} = 7.5$$

Bridge Member rating = 36 x 7.5 = 270 tons = 540000 lb.

B- Rating Assuming Partial Composite Action According to AASHTO Standard Spec. (2002):

R.F. For HS-20 (Inventory level):

$$RF = \frac{C - A_1 \text{ x DL}}{A_2 \text{ x (LL + IM)}} = \frac{4843.65 - 1.3*1095}{2.17*1048.5} = 1.50$$

Bridge Member rating = 36 x 1.50 = 54 tons = 108000 lb.

R.F. For HS-20 (Operating level):

$$RF = \frac{C - A_1 \text{ x DL}}{A_2 \text{ x (LL + IM)}} = \frac{4843.65 - 1.3*1095}{1.3*1048.5} = 2.51$$

Bridge Member rating = 36 x 2.51 = 90.36 tons = 180720 lb.

B- Rating Assuming Partial Composite Action According to Follow-up Load Test:

R.F. For HS-20 (Inventory level):

$$RF = \frac{C - A_1 \text{ x DL}}{A_2 \text{ x (LL + IM)}} = \frac{4843.65 - 1.3*1095}{2.17*387.80} = 4.10$$

Bridge Member rating = 36 x 4.10 = 147.6 tons = 295200 lb.

R.F. For HS-20 (Operating level):

$$RF = \frac{C - A_1 \text{ x DL}}{A_2 \text{ x (LL + IM)}} = \frac{4843.65 - 1.3*1095}{1.3*387.80} = 6.78$$

Bridge Member rating = 36 x 6.78 = 244.1 tons = 488200 lb.

Appendix C:

Calculation of Losses in Prestressing Strand

Prestress Losses of Type C Girders			
Short Term Prestress Losses			
Parameters	Girder (A-F)	Girder (G)	Girder (H)
No. of strands	36	30	32
Area of strand (A_s) (in^2)	0.153	0.153	0.153
Total area of strand (A_{sp}) (in^2)	5.51	4.59	4.90
Prestress force (kips)	31	31	31
Initial strand stress (F_{pi}) (ksi)	202.6	202.6	202.6
Eccentricity (e_m)(in)	12.42	13.09	12.84
Moment of inertia (I_g) (in^4)	82602	82602	82602
Girder area (A_g) (in^2)	494.9	494.9	494.9
Girder span-length (ft.)	69.86	71.184	72.5
Normal concrete weight (lb/ft^3)	150	150	150
W_u (distributed load due to self-weight of girder (k/ft)	0.516	0.516	0.516
Mid-span moment due to self-weight of girder (M_u) (k-ft)	314.49	326.53	338.71
Compressive strength of concrete (f'$_c$) (psi)	5800.000	4770.000	5050.000
Modulus of elasticity of concrete during release (E_{ci}) (ksi)	4341.0	3936.7	4050.6
Modulus of elasticity of prestressing strands (E_p) (ksi)	28500.000	28500.000	28500.000
A_{ps} (I_g+em^2*A_g) (in^6)	875460.76	768375.98	803893.75
(A_g*I_g*E_{ci})/E_p (in^6)	6226615	5646732	5810101
Short term prestress losses (ΔF_{PES}) (ksi)	21.71	20.31	20.72
Long Term Prestress Losses			
Humidity (H) (%)	69.80	69.80	69.80
Humidity factor (γ_h)	1.0	1.0	1.0
Humidity factor (γ_{st})	0.74	0.87	0.83
ΔF_{PR} (low relaxation strands) (ksi)	2.50	2.50	2.50
Long Term prestress losses (ΔF_{PLT}) (ksi)	27.96	29.24	29.04
Total prestress losses (ksi)	49.66	49.55	49.76
Applied prestress stress/strand (ksi)	152.94	153.05	152.84

Appendix D:
Calculation of Cost Analysis

➤ *Installation of Shear Connectors:*

TxDOT specification Item 429 (2021) **"Concrete Structure Repair"** includes remove and repair of unsound, delaminated, or spalled concrete. For deck, the re-casted concrete should be Type S concrete. The following quotation was taken from Item 429 that said *" The work performed, and materials furnished in accordance with this Item and measured as provided under "Measurement" will be paid for at the unit price bid for "Concrete Structure Repair" of the kind specified. This price is full compensation for furnishing, placing, and curing all repair materials; removing concrete; saw cutting; cleaning reinforcing steel; supplying and installing replacement or supplemental reinforcing steel, drive pins, studs, or expansion bolts; and equipment, labor, and incidentals".*

Item Cost: Statewide Maximum: $288/SF (Average low bid Price Excel)

For Las Lomas EB Bridge (Span 2):

Total amount of concrete to be removed = (9 ft. x 8 ft. for one PCP) = 72 SF = 8 SY

• Gross Cost = (72 x 288) = $ 20736

The gross cost includes providing supplemental reinforcing steel, equipment, and labor as mentioned in item 429 (2021) in the payment section.

Traffic closure:

Cost= $ 500/hr. (Include freeway + normal lane closure)

Time to install PCP with connectors and concrete casting = 48 hrs.

Total cost for lane closure= 48 x 500 = $ 24000

Total cost = $ 20736 + $ 24000 = $ 44736

• *For 4 PCPs:*

Total cost = 4 x $ 44736 = $ 178944

➢ *Casting the Affected Area with Steel Fiber Reinforced Concrete (SFRC) :*

According to TxDOT Special Specification 4168 (2020) **"Bridge Deck Overlay with Steel Fiber Reinforced Concrete"** includes Furnish and place steel fiber reinforced concrete (FRC) as bridge deck overlay where shown on the plans.

TxDOT Special Specification 4168 (2020) mentioned that "The work performed, and materials furnished in accordance with this item and measured as provided under "Measurement" will be paid for at the unit price bid for "Steel Fiber Reinforced Concrete Overlay." Payment for "Steel Fiber Reinforced Concrete Overlay" is full compensation for final cleaning surface and preparing surface for overlay, cleaning and restoration of reinforced steel; furnishing and placing reinforcing steel; furnishing, placing, finishing and curing the steel fiber concrete overlay; and final surface finish. These prices are full compensation for materials, tools, equipment, labor, and incidentals. Repair of deteriorated concrete below the level of scarification will be paid for in accordance with Item 429, "Concrete Structure Repair." Concrete removal and surface preparation utilizing hydro-demolition will be paid for in accordance with item 483, "Concrete Bridge Deck Surfacing."

Item Cost: Statewide Maximum: $181/SF. (Average low bid Price Excel)

For Las Lomas EB Bridge (Span 2):

Total amount of concrete to be removed = (9 ft. x 8 ft. for one PCP) = 72 SF = 8 SY

Cost of SFRC concrete/S.F.= $ 181 [Based on California Department of Transportation (Caltrans)]

- Total Cost = (72 x 181) = $ 13,032

The total cost includes providing material, equipment, tools, and labor as mentioned in item 4168 (2020) in the payment section.

Traffic closure:

Cost= $ 500/hr. (Include freeway + normal lane closure)

Time to install connector and concrete casting = 48 hrs.

Total cost for lane closure= 48 x 500 = $ 24000

- Total cost = $ 13,032 + $ 24000 = $ 37032

- *For 4 PCPs:*

Total cost = 4 x $ 37032 = $ 148128

➤ *PCP Overhang Length Extension:*

Item Cost: Statewide Maximum: $288/S.F. (Average low bid Price Excel)

For Las Lomas EB Bridge (Span 2):

Total amount of normal weight concrete to be casted = (12 ft. x 8 ft. for one PCP) = 96 SF

- Gross Cost = (96 x 288) = $ 27648

The gross cost includes providing supplemental reinforcing steel, equipment, and labor as mentioned in item 429 (2021) in the payment section.

Traffic closure:

Cost= $ 500/hr. (Include freeway + normal lane closure)

Time to install connector and concrete casting = 48 hrs.

Total cost for lane closure= 48 x 500 = $ 24000

Total cost = $ 27648 + $ 24000 = $ 51648

- *For 4 PCPs:*

Total cost = 4 x $ 51648 = $ 206592

➤ *Installation of Undercut Anchor:*

Under-cut anchor installation required some equipment. All equipment is included in the overall cost. The cost was obtained from Hilti company.

For 1 pack of under-cut anchors and their necessary equipment:

- Undercut anchor Type HAD-P M10 x 100/20 1 pack (12 pc)- Price $ 713.0
- TE-C-HDA-ST SETTING TOOL (1 pc)- Price $ 111.0
- Stop drill bit TE-C-HDA-B 20 x 100 (1 pc)- Price $ 557.0
- Blow-out-pump (1 Pc) Price $ 69.0
- Total cost = 713+ 111+ 557+ 69 = $ 1450.0

For 153 under-cut anchors, 13 packs are needed:

- Undercut anchor Type HAD-P M10 x 100/20 13 pack (156 pc)- Price $ 9269
- Total cost = 9269+ 111+ 557+ 69 = $ 10,006

For 115 under-cut anchors, 10 packs are needed:

- Undercut anchor Type HAD-P M10 x 100/20 10 pack (120 pc)- Price $ 7130
- Total cost = 7130+ 111+ 557+ 69 = $ 7867

For 77 under-cut anchors, 7 packs are needed:

- Undercut anchor Type HAD-P M10 x 100/20 7 pack (84 pc)- Price $ 4991
- Total cost = 4991+ 111+ 557+ 69 = $ 5728

For 38 under-cut anchors, 7 packs are needed:

- Undercut anchor Type HAD-P M10 x 100/20 4 pack (48 pc)- Price $ 2852
- Total cost = 2852+ 111+ 557+ 69 = $ 3589

To install the under-cut anchor, GPR is needed to determine the optimal location by avoiding the girder reinforcing steel. GPR requires at least two qualified persons. The GPR rental is one-time payment. The estimated scanning cost per hour is as follows. Boom lift is also required.

- GPR rental + scanning cost = $ 1500 + $ 250/hr. = $ 1750

Total cost including GPR and Labor cost		
No of Anchors/girder side/one girder	1 Girder ($)**	8 Girders ($)**
38	9,178	73,424
77	13,456	107,648
115	17,734	141,872
153	22,012	176,096

** A $ 2000 boom lift rent will be added with each final cost.

References

1. AASHTO (2017). Load resistance and factor design: Bridge design specifications, 8th ed., American Association of State Highway and Transportation Officials, Washington, D.C.

2. AASHTO. (2002). Standard Specifications for Highway Bridges, 17th Edition.

3. AASHTO (2018). The Manual for Bridge Evaluation, 3rd Edition, American Association of State Highway and Transportation Officials, Washington, D.C.

4. Aboelseoud, M. A., and Myers, J. J. (2015). "Finite-element modeling of hybrid composite beam bridges in Missouri." Journal of Bridge Engineering, 20(1), 1–11.

5. Alvi, A. H., Gualtero, I., Sen, R., and Mullins, G. (2012). "Repair of construction-related deterioration in precast deck-panel bridges." Transportation Research Record, (2292), 104–112.

6. American Association of State Highway and Transportation Officials. (2016). "Manual for Bridge Evaluation, 2nd Edition, with 2011, 2013, 2014, 2015, and 2016 Interim Revisions." C3, Washington, DC.

7. American Society of Civil Engineers. (2013). "Released March 2013 About the American Society of Civil Engineers." (March), 1–119.

8. Barker, J. M. (1975). "Research, Application, and Experience With Precast Prestressed Bridge Deck Panels." J Prestressed Concr Inst, 20(6), 66–85.

9. Bayrak, O., Chao, S.-H., Jirsa, J. O., Klingner, R. E., Azimov, U., Foreman, J., Foster, S., Karki, N., Kwon, K. Y., and Woods, A. (2013). "Bridge Deck Reinforcement and PCP Cracking: Final Report." 7.

10. Benmokrane, B., El-salakawy, E., El-gamal, S., and Goulet, S. (2008). "Construction and Testing of an Innovative Concrete Bridge Deck Totally Reinforced with Glass FRP Bars: Val-Alain Bridge on Highway 20 East." 12(5), 632–645.

11. CSiBridge (2015). "Introduction to CSiBridge." Computer & Structures, Inc.

12. Deshmukh, G. (2004). "Replacement Prioritization of Precast Deck Panel Bridges in Florida."

13. Dinh K, Gucunski N, Duong TH. An algorithm for automatic localization and detection of rebars from GPR data of concrete bridge decks. Autom ConStruct 2018;89:292–8. https://doi.org/10.1016/j.autcon.2018.02.017

14. Dong, C., Bas, S., Debees, M., Alver, N., and Catbas, F. N. (2020). "Bridge Load Testing for Identifying Live Load Distribution, Load Rating, Serviceability and Dynamic Response." Frontiers in Built Environment, 6(May), 1–14.

15. Durham, S. A., Heymsfield, E., Schemmel, J. J., and Jones, J. X. (2004). "The Structural evaluation of Precast Concrete - Slab Panels in Bridge Superstructures." Arkansas State Highway and Transportation Department.

16. Fang, I. K., Tsui, C. K. T., Burns, N. H., and Klingner, R. E. (1990). "Load capacity of isotropically reinforced, cast-in-place and precast panel bridge decks." PCI Journal, 35(4), 104–113.

17. Gar, S. P., Head, M., Hurlebaus, S., and Mander, J. B. (2013). "Comparative experimental performance of bridge deck slabs with AFRP and steel precast panels." Journal of Composites for Construction, 17(6), 1–9.

18. Goldberg, D., Ashwill, T. D., Aswad, A., Barker, J. M., Barnoff, R. M., Bassi, K. G., Behar-Ybarra, E., Burns, N. H., Collier, J., Gates, J. H., Grinstead, W. G., Guarre, J. S., Haven, P., Henneberger, W., and Imper, R. R. (1987). "Precast Prestressed Concrete Bridge Deck Panels." PCI Journal, 32(2), 26–45.

19. GPR-SLICE (2018). "GPR-SLICE v7.0 User's Manual." Geophysical Archeometry Laboratory Inc., 20014 Gypsy Ln, Woodland Hills, CA 91364, USA.

20. Gregory S. Rajek A. (2010). "Numerical Modeling of the Performance of Highway Bridge Approach Slabs." International Journal of Heritage Studies, 16(1), 1689–1699.

21. Gualtero, I. A. (2004). "Deterioration process and deck failure mechanism of Florida's precast deck panel bridges."

22. Gucunski, N., et al. (2016). "Capture and Quantification of Deterioration Progression in Concrete Bridge Decks through Periodical NDE Surveys." Journal of Infrastructure Systems, © ASCE, ISSN 1076-0342.

23. Hays, C., Fagundo, F. E., and Callis, E. C. (1976). "Study of Cracking of Composite Deck Bridge on I-7 5 over Peace River."

24. Hsu, L. S., and Hsu, C.-T. T. (1994). "Complete stress — strain behaviour of high-strength concrete under compression." Magazine of Concrete Research, 46(169), 301–312.

25. Issa, M. A., Yousif, A. A., Issa, M. A., Kaspar, I. I., and Khayyat, S. Y. (1995). "Field performance of full depth precast concrete panels in bridge deck reconstruction." PCI Journal, 40(3), 82–108.

26. LEY, T., and PATIL, M. G. S. (2010). INVESTIGATIONS OF A PRECAST BRIDGE DECK SYSTEM. Oklahoma Transportation Center.

27. Mander, T. J. (2009). "Structural Performance of a Full-Depth Precast Concrete Bridge Deck System Structural Performance of a Full-Depth." (August), 168.

28. Mander, T. J., Henley, M. D., Scott, R. M., Head, M. H., Mander, J. B., and Trejo, D. (2010). "Experimental performance of full-depth precast, prestressed concrete overhang, bridge deck panels." Journal of Bridge Engineering, 15(5), 503–510.

29. Merrill, B. D. (2002). "Texas' Use of Precast Concrete Stay-In-Place Forms for bridge Decks." Concrete Bridge Coference, 8–11.

30. Michael Schwarz and Jeffrey A. Laman. (2001). "RESPONSE OF PRESTRESSED CONCRETE I-GIRDER BRIDGES TO LIVE LOAD." Journal of Bridge Engineering, 6(February), 1–8.

31. Moore, M., Phares, B., Graybeal, B., Rolander, D., and Washer, G. (2001). "Reliability of visual inspection for highway bridges." Rep. Prepared for the Federal Highway Administration,Washington, DC.

32. Okumus, P., Oliva, M. G., and Becker, S. (2012). "Nonlinear finite element modeling of cracking at ends of pretensioned bridge girders." Engineering Structures, Elsevier Ltd, 40, 267–275.

33. Pai, N., Gualtero, I., Alvi, A., Sen, R., and Mullins, G. (2016). "Prioritization strategy for replacing deteriorating partial-depth precast concrete deck panels in Florida." Journal of Bridge Engineering, 21(6), 1–10.

34. Parrillo, R., Roberts, R.L., and Haggan, A., 2005, Bridge Deck Condition Assessment Using Ground Penetrating Radar, International Bridge Conference, June 13-15, 2005, Pittsburgh, PA.

35. Peiris, A., and Harik, I. (2016). "Load testing of bridges for load rating." The 7th International Conference on Sustainable Built Environment, (12), 8.

36. Pirayeh Gar, S., Head, M., Hurlebaus, S., and Mander, J. B. (2014). "Experimental performance of AFRP concrete bridge deck slab with full-depth precast prestressed panels." Journal of Bridge Engineering, 19(4), 1–10.

37. Ren, W., Sneed, L. H., Yang, Y., and He, R. (2015). "Numerical Simulation of Prestressed Precast Concrete Bridge Deck Panels Using Damage Plasticity Model." International Journal of Concrete Structures and Materials, 9(1), 45–54.

38. Sanayei, M., Phelps, J. E., Sipple, J. D., Bell, E. S., and Brenner, B. R. (2012).

"Instrumentation, Nondestructive Testing, and Finite-Element Model Updating for Bridge Evaluation Using Strain Measurements." Journal of Bridge Engineering, 17(1), 130–138.

39. Sanayei, M., Reiff, A. J., Brenner, B. R., and Imbaro, G. R. (2016). "Load Rating of a Fully Instrumented Bridge: Comparison of LRFR Approaches." Journal of Performance of Constructed Facilities, 30(2), 04015019.

40. SAP2000 (2016). "CSI Analysis Reference Manual." Computer & Structures, Inc.

41. Sim, J., Oh, H., and Meyer, C. (2006). "Structural assessment of externally strengthened bridge deck panels." Applied Composite Materials, 13(2), 99–114.

42. WinIE (2018). "Windows Impact Echo (IE) v2.8." Olson Instruments, Inc.